Science and Technology of Nuclear Installations

Severe Accident Analysis in Nuclear Power Plants

Guest Editors: Gilberto Espinosa–Paredes, Lluís Batet, Alejandro Nuñez–Carrera, and Jun Sugimoto

Severe Accident Analysis in Nuclear Power Plants

Science and Technology of Nuclear Installations

Severe Accident Analysis in Nuclear Power Plants

Guest Editors: Gilberto Espinosa-Paredes, Lluís Batet, Alejandro Nuñez-Carrera, and Jun Sugimoto

Editorial Board

Contents

Hindawi Publishing Corporation
Science and Technology of Nuclear Installations
Volume 2012, Article ID 430471, 2 pages
doi:10.1155/2012/430471

Editorial

Severe Accident Analysis in Nuclear Power Plants

Gilberto Espinosa-Paredes,[1] Lluís Batet,[2] Alejandro Nuñez-Carrera,[3] and Jun Sugimoto[4]

[1] *Departamento de Ingeniería de Procesos e Hidráulica, Universidad Autónoma Metropolitana-Iztapalapa, Avenida San Rafael Atlixco 186 Col. Vicentina, 09340 México, DF, Mexico*
[2] *Department of Physics and Nuclear Engineering, Universitat Politècnica de Catalunya (BarcelonaTECH), Av. Diagonal 647, 08028 Barcelona, Spain*
[3] *Comisión Nacional de Seguridad Nuclear y Salvaguardias, Doctor Barragán 779, Col. Narvarte, México City, DF, Mexico*
[4] *Department of Nuclear Engineering, Graduate School of Engineering, Kyoto University, Yoshida, Sakyo, Kyoto 606-8501, Japan*

Correspondence should be addressed to Gilberto Espinosa-Paredes, gepe@xanum.uam.mx

Received 9 September 2012; Accepted 9 September 2012

Safety of nuclear power plants is essential and safety standards are continuously reviewed and upgraded as new developments and research are performed. Continuous research regarding this subject is fundamental for the nuclear industry. Although severe accident analysis and research have been performed throughout the evolution of nuclear industry, it has not yet considered all plausible scenarios. Adequate analyses are needed for all phases of severe accidents in order to maintain or improve safety margins. Hence, it is essential to encourage researchers to keep performing and developing research, codes, and simulations of these potentially hazardous events. The original works published in this special issue can help to improve safety and understand the phenomena involved in severe accidents and their consequences in existing generation II nuclear power plants (NPP) as well as in generation III NPP being built and in generation III+ and IV NPP being developed.

In this special issue ten research articles were published. J. Arndt et al. describe a method to perform simplified analyses concerning integrity of the components of the primary cooling circuit during a severe accident. A second method, using complex calculation models, was used to analyze a postulated high-pressure core melt accident scenario in a PWR caused by a station blackout. Authors found that temperature values of more than 800°C can be reached in the reactor coolant line and the surge line before the bottom of the reactor pressure vessel experience a significant temperature increase due to core melting.

K.-M. Koo et al. presented a response analysis on electrical pulses under severe accident temperature conditions using an abnormal signal simulation analysis. These authors obtained a special function for abnormal pulse signal patterns through a characteristic response under severe accident temperature conditions, which in turn makes it possible to analyze the abnormal output pulse signals through a characteristic response of a 4∼20 mA circuit model and a range of the elements changing with temperature under an accident condition.

G. Espinosa-Paredes et al. presented the simulation and analysis of the loss-of-coolant accident (LOCA) in the boiling water reactor (BWR) of Laguna Verde Nuclear Power Plant (LVNPP) at 105% of rated power. The simulation considers a LOCA in the recirculation loop of the reactor with and without cooling water injection. The LVNPP model was developed using the RELAP/SCDAPSIM code. The lack of cooling water after the LOCA leads the LVNPP to core melting that exceeds the design basis of the nuclear power plant (NPP) sufficiently to cause failure of structures, materials, and systems that are needed to ensure proper cooling of the reactor core by normal means. Faced with a severe accident, the first response is to maintain the reactor core cooling by any means available, but in order to carry out such an attempt it is necessary to fully understand the progression of core damage, since such action has effects that may be decisive in accident progression. During the progression of core damage, these authors analyzed the cooling water

injection at different times and the results show that there are significant differences in the level of core damage and hydrogen production, among other variables analyzed such as maximum surface temperature, fission products released, and debris bed height.

A description of the results for a Station Blackout analysis for Atucha 2 Nuclear Power Plant is presented by A. Bonelli et al. Calculations were performed with MELCOR 1.8.6 YV3165 Code. Atucha 2 is a pressurized heavy water reactor, cooled and moderated with heavy water, by two separate systems, presently under final construction in Argentina. The initiating event is loss of power, accompanied by the failure of four out of four diesel generators. All remaining plant safety systems are supposed to be available. It is assumed that during the station blackout sequence the first pressurizer safety valve fails stuck to open after 3 cycles of water release. During the transient, the water in the fuel channels evaporates first while the moderator tank is still partially full. The moderator tank inventory acts as a temporary heat sink for the decay heat, which is evacuated through conduction and radiation heat transfer, delaying core degradation. These authors found that this feature, together with the large volume of the steel filler pieces in the lower plenum and a high primary system volume to thermal power ratio, derives in a very slow transient in which RPV failure time is four to five times larger than those of German PWRs.

R. P. Martin presented a general evaluation methodology development and application process (EMDAP) paradigm for the resolution of severe accident safety issues. For the broader objective of complete and comprehensive design validation, severe accident safety issues are resolved by demonstrating comprehensive severe accident-related engineering through applicable testing programs, process studies demonstrating certain deterministic elements, probabilistic risk assessment, and severe accident management guidelines. The basic framework described in this paper extends the top-down, bottom-up strategy described in the US Nuclear Regulatory Commission Regulatory Guide 1.203 to severe accident evaluations addressing US NRC expectation for plant design certification applications.

The numerical analysis of heat and mass transfer during hydrogen generation in an array of fuel cylinder rods, each coated with a cladding and a steam current flowing outside the cylinders, is presented by H. Romero-Paredes et al. The analysis considers the fuel element without mitigation effects. The system consists of a representative periodic unit cell where the initial and boundary value problems for heat and mass transfer were solved. In this unit cell, it is considered that a fuel element is coated by a cladding with steam surrounding it as a coolant. The numerical simulations allow describing the evolution of temperature and concentration profiles inside the nuclear reactor and could be used as a basis for hybrid upscaling simulations.

R. Kapulla et al. presented validation experiments, conducted in the frame of the OECD/SETH-2 Project. These experiments address the combined effects of mass sources and heat sinks related to gas mixing and hydrogen transport within containment compartments. A wall jet interacts with an operating containment cooler located in the middle (M-configuration) and the top (T-configuration) of the containment vessel. The experiments are characterized by a 3-phase injection scenario. In Phase I, pure steam is injected, while in Phase II, a helium-steam mixture is injected. Finally, in Phase III, pure steam is injected again. For the M-configuration, a strong degradation of the cooler performance was observed for these authors during the injection of the helium/steam mixture (Phase II). For the T-configuration, we observe a mainly downwards acting cooler resulting in a combination of forced and natural convection flow patterns. The cooler performance degradation was much weaker compared with the M-configuration and a good mixing was ensured by the operation of the cooler.

Forty-three organizations from 22 countries networking their capacities of research in SARNET (Severe Accident Research NETwork of excellence) to resolve the most important remaining uncertainties and safety issues on severe accidents in existing and future water-cooled nuclear power plants (NPP) are discussed by J. P. Van Dorsselaere et al. According to these authors, the first project in the 6th Framework Programme (FP6) of the European Commission, the SARNET2 project, coordinated by IRSN, started in April 2009 for 4 years in the FP7 frame. After 2.5 years, some main outcomes of joint research (modeling and experiments) by the network members on the highest priority issues are presented: in-vessel degraded core coolability, molten-corium-concrete interaction, containment phenomena (water spray, hydrogen combustion), and source-term issues (mainly iodine behavior). The ASTEC integral computer code, jointly developed by IRSN and GRS to predict the NPP SA behavior, capitalizes in terms of models the knowledge produced in the network: a few validation results are presented.

C. M. Allison et al. focused on the Fukushima Daiichi accident; they present an assessment which includes a brief review of relevant severe accident experiments and a series of detailed calculations using the RELAP/SCDAPSIM model which were provided by the Comision Nacional de Seguridad Nuclear y Salvaguardias, the Mexican nuclear regulatory authority. The authors concluded that detailed analysis for realistic bounding scenarios can provide general guidance of timing of important events and that the responses to the accident once the accident is underway can make a significant difference in the consequences of the accident.

Finally, A. Núñez-Carrera et al. presented the analysis of the Boiling Water Reactor (BWR) lower head during a severe accident using SCDAPSIM/RELAP5 3.2. The computer code was used in this work to model the heatup of the reactor core material that slumps in the lower head of the reactor pressure vessel due to a loss-of-coolant accident (LOCA) with simultaneous loss of off-site power and without injection of cooling water. The authors conclude that SCDAPSIM/RELAP5 has the capability to predict the melting of the core, control rod, and some structures, with an estimation of the main parameter of the molten pool until the failure of the crust.

Gilberto Espinosa-Paredes
Lluís Batet
Alejandro Nuñez-Carrera
Jun Sugimoto

Hindawi Publishing Corporation
Science and Technology of Nuclear Installations
Volume 2012, Article ID 646327, 25 pages
doi:10.1155/2012/646327

Research Article

Preliminary Assessment of the Possible BWR Core/Vessel Damage States for Fukushima Daiichi Station Blackout Scenarios Using RELAP/SCDAPSIM

C. M. Allison,[1] J. K. Hohorst,[1] B. S. Allison,[1] D. Konjarek,[2] T. Bajs,[2] R. Pericas,[3] F. Reventos,[3] and R. Lopez[4]

[1] *Innovative Systems Software, 1242 South Woodruff Avenue, Idaho Falls, ID 83404, USA*
[2] *ENCONET, Miramarska 20, 10000 Zagreb, Croatia*
[3] *ETSEIB, Universitat Politècnica de Catalunya, Avenida Diagonal 647, 08028 Barcelona, Spain*
[4] *Comision Nacional de Seguridad Nuclear y Salvaguardias, Dr. Barragan 779, Cuarto piso, Colonia Vertiz Narvarte, Delegacion Benito Juarez, 03020 Ciudad de México, DF, Mexico*

Correspondence should be addressed to C. M. Allison, iss@srv.net

Received 11 January 2012; Accepted 6 March 2012

Academic Editor: Alejandro Nuñez-Carrera

Immediately after the accident at Fukushima Daiichi, Innovative Systems Software and other members of the international SCDAP Development and Training Program started an assessment of the possible core/vessel damage states of the Fukushima Daiichi Units 1–3. The assessment included a brief review of relevant severe accident experiments and a series of detailed calculations using RELAP/SCDAPSIM. The calculations used a detailed RELAP/SCDAPSIM model of the Laguna Verde BWR vessel and related reactor cooling systems. The Laguna Verde models were provided by the Comision Nacional de Seguridad Nuclear y Salvaguardias, the Mexican nuclear regulatory authority. The initial assessment was originally presented to the International Atomic Energy Agency on March 21 to support their emergency response team and later to our Japanese members to support their Fukushima Daiichi specific analysis and model development.

1. Introduction

Immediately after the accident at Fukushima Daiichi, Innovative Systems Software (ISS) and other members of the international SCDAP Development and Training Program (SDTP) [1, 2] started an assessment of the possible core/vessel damage states of the Fukushima Daiichi Units 1–3. The assessment included a brief review of relevant severe accident experiments and a series of detailed calculations using RELAP/SCDAPSIM [3, 4] for a representative BWR vessel and related cooling systems.

As described briefly in Section 2, the experimental review presented to the IAEA emergency response team included representative highlights and phenomena identified from separate effects experiments BWR specific and other bundle experiments [5, 6], performed by the Karlsruhe Institute of Technology (KIT), and selected in-pile experiments [7, 8]. The KIT experiments were limited to peak temperatures less than 2600 K and thus covered the initial stages of core heat up and melting including the liquefaction and relocation of BWR control blades, structural material, and fuel rod cladding. The in-pile experiments reached higher peak temperatures and included the liquefaction of the fuel and other oxidized cladding materials and the formation of ceramic melts and blockages.

As described in Section 3, a combination of RELAP/SCDAPSIM/MOD3.4 and RELAP/SCDAPSIM/MOD3.5 was used to perform the detailed calculations. Both versions use publically available RELAP5/MOD3.2 and MOD3.3 thermal hydraulic models and correlations in combination with the detailed fuel behaviour and severe accident (SCDAP) models and correlations [9, 10]. The RELAP/SCDAPSIM code is designed to predict the behavior of reactor systems during normal and accident conditions including severe accidents

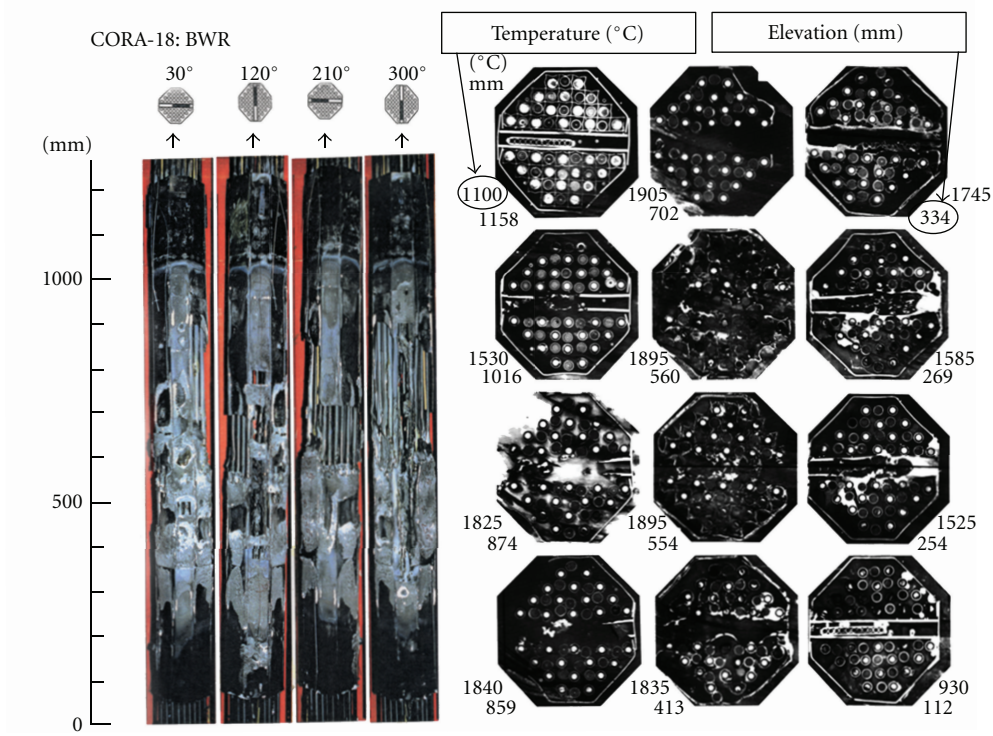

Figure 1: Posttest vertical view and horizontal metallographic cross-sections for CORA-18.

up to the point of reactor vessel failure. MOD3.4, the current production version, has been used by member organizations and licensed users to support a variety of applications including the design and analysis of severe accident experiments. MOD3.5, an experimental version of the code, has been used to support the design and analysis of the French PHEBUS-FP [11, 12], German QUENCH [13], and Russian PARAMETER [14] experiments and incorporates the latest SCDAP model improvements. It is the main version now being used by SDTP members and selected licensed users for Fukushima analysis and assessment.

As described in Section 4, the initial Laguna Verde RELAP/SCDAPSIM input models were provided by the Comision Nacional de Seguridad Nuclear y Salvaguardias (CNSNS), the Mexican nuclear regulatory authority. The Laguna Verde BWRs are BWR5 designs with thermal power of ~2370 MW and 444 fuel assemblies with an average core burnup of 3.57×10^5 MWs/Kg. For comparison, Fukushima Daiichi Unit 1 has a thermal power of 1380 MW from 400 assemblies. Units 2 and 3 have thermal powers of 2381 MW from 548 assemblies.

The initial RELAP/SCDAPSIM calculations performed prior to March 21st included a series of station blackout transients with a variety of emergency core cooling and depressurization strategies. Representative results are provided in Section 5. Additional calculations performed between March 21st and 25th to support the IAEA emergency response team included a variety of scenarios with loss of emergency core cooling ranging from 0 to 70 hours after scram. Representative results from these additional calculations are presented in Section 6.

As discussed in Section 7, these calculations which showed the core uncovery, fuel melting, and relocation of the fuel and other molten materials into the lower plenum can occur rather quickly once emergency cooling is no longer available. The timing of such events depends on the delays in the loss of emergency cooling as well as the specific details of an accident scenario such as the opening of safety relief valves to depressurize the vessel or the addition of water after partial or complete core uncovery.

The conclusions from the results and discussions presented in Sections 2, 3, 4, 5, 6 and 7 are presented in Section 8. This section first presents initial conclusions regarding possible core/vessel damage in Fukushima Daiichi Units 1–3. These initial conclusions are based on the information published and calculations performed in late March of 2011 immediately after the accident. Next, general conclusions for a typical BWR, Laguna Verde, subjected to "Fukushima-Daiichi-like" scenarios (short to extended periods of emergency core cooling after reactor scram, variation in vessel pressure, and water injection after core uncovery and start of core heat up) are presented. Finally the conclusions for severe accident management strategies are presented.

2. Highlights of Relevant Experiments and Phenomena

The existing data base and severe accident code and models developed over the past 40 years since the accident at TMI-2 are considered to be adequate to predict the likely states of a BWR core and vessel during "Fukushima-Daiichi-like"

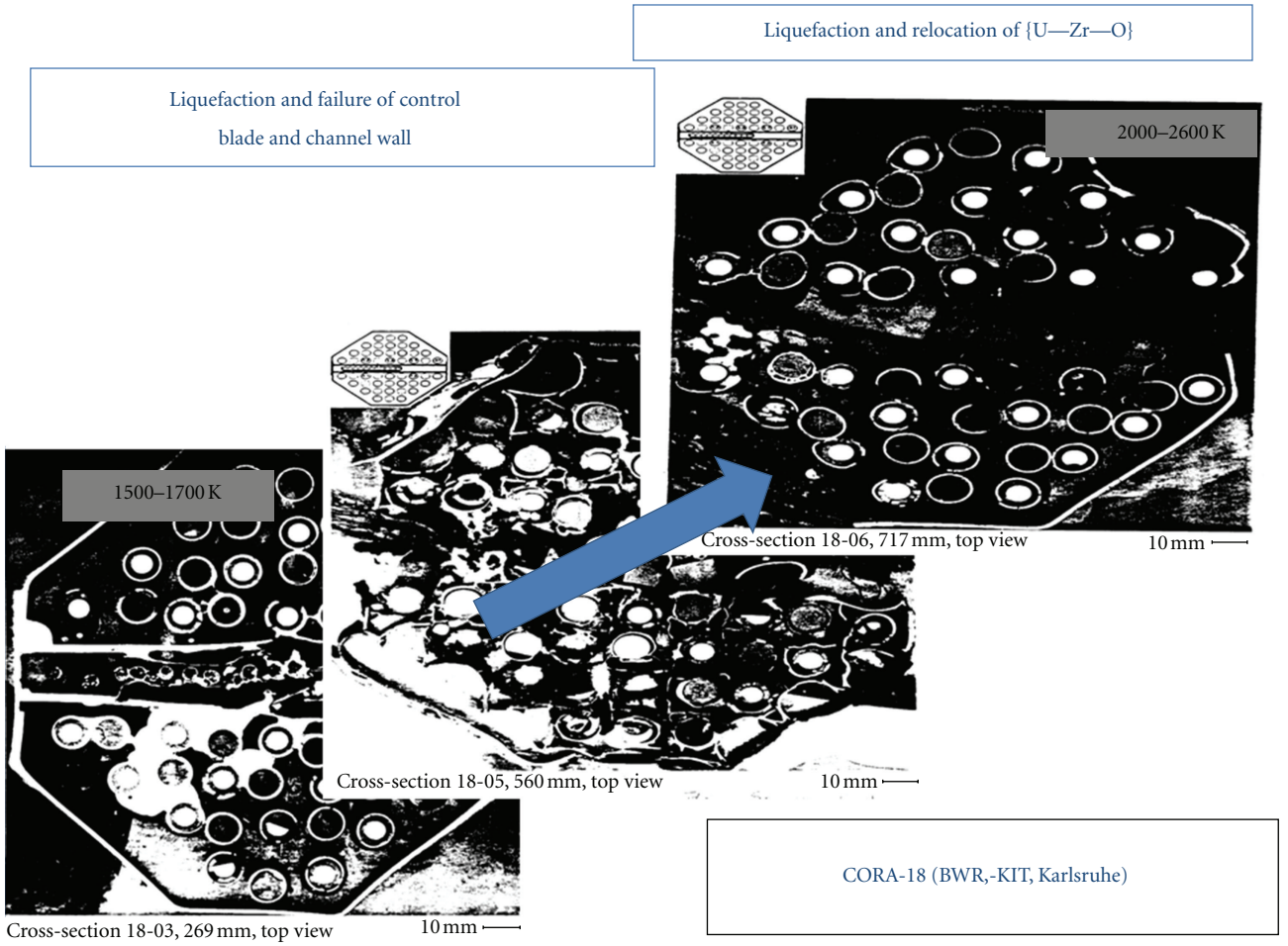

Figure 2: Horizontal metallographic cross-sections for CORA-18 showing destruction of control blade and channel box at temperatures between 1500–1700 K.

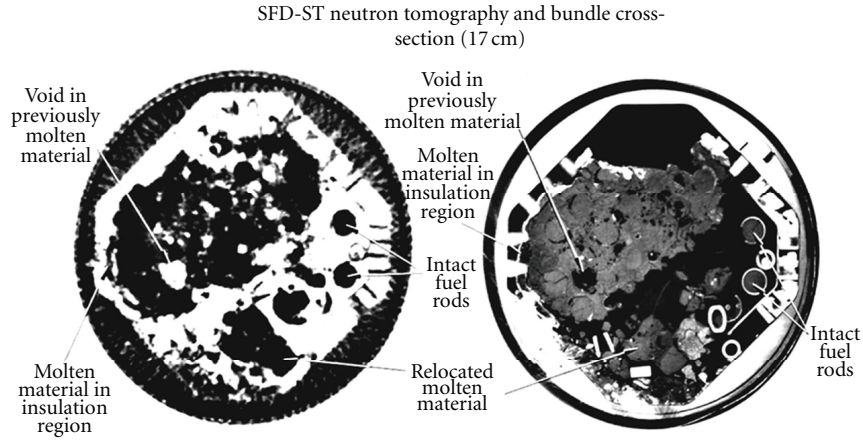

Figure 3: Horizontal metallographic cross-sections from PBF-SFD-ST showing blockage formation after {U-Zr}-O_2 melting and relocation.

scenarios. For Fukushima Daiichi Units 1–3, the dominant uncertainties in the predicted core/vessel states are associated with a lack of knowledge of actual operator actions as well as the possible damage to the reactor cooling systems caused by the earthquake. In particular, as noted in Section 7, operator actions to (a) activate or deactivate the emergency cooling systems, (b) depressurize the reactor vessel, and (c) initiate the addition of water to the vessel will have a significant impact on the heat up and melting of the core. Although it is likely that the analysis and final examination of the

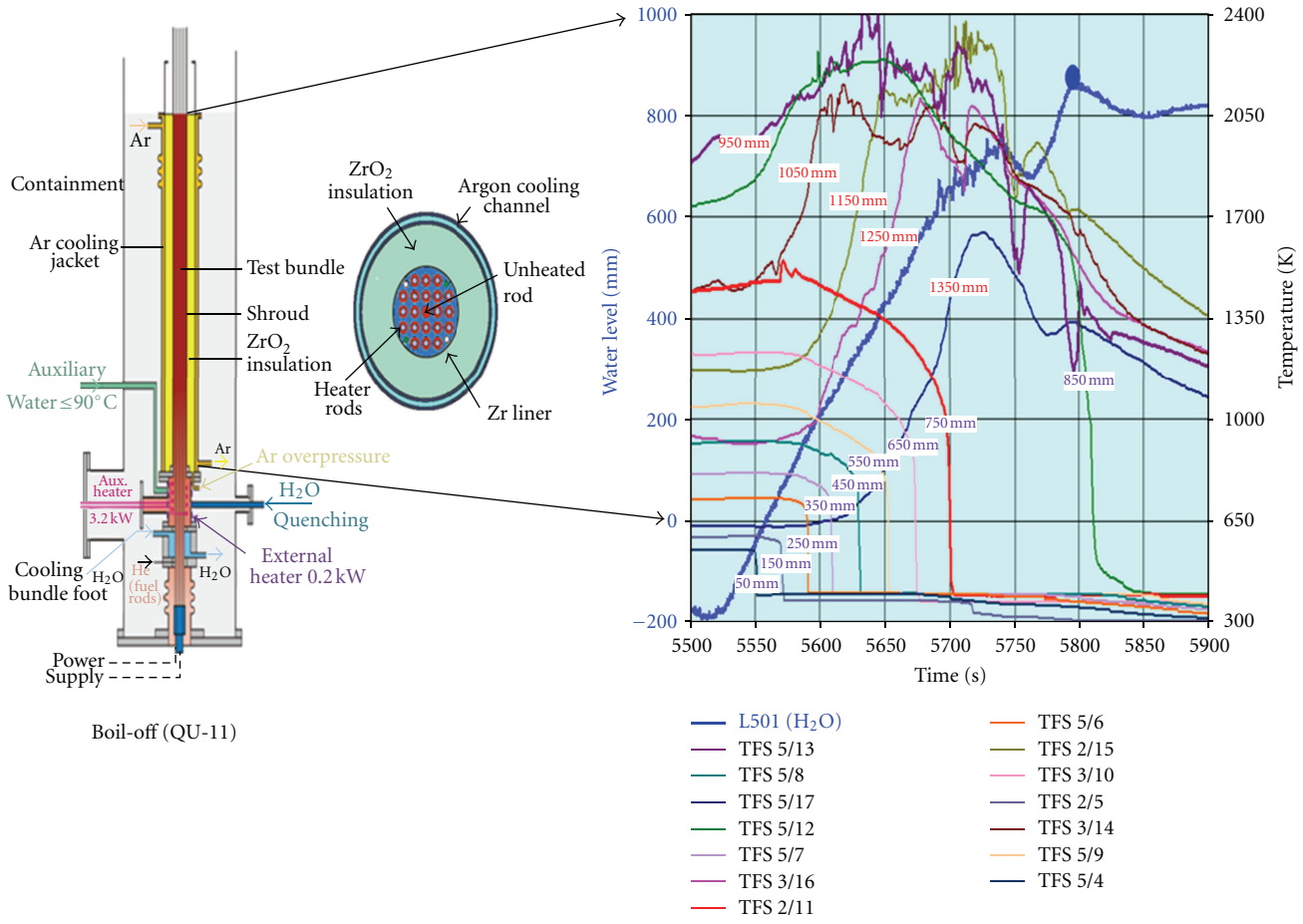

Figure 4: Measured temperatures and collapsed water level during the reflood phase in the Quench 11 experiment.

Fukushima Daiichi cores, vessels, and containments will identify gaps in our data base and models, it would be quite surprising if unexpected trends or phenomena are identified.

For now, it has to be concluded that the existing data base, including BWR specific bundle heating and quenching experiments, provides a good technical basis for the prediction of the progression of damage in a BWR core up to and including fuel melting or liquefaction ($T > 2800$ K). For example, Figures 1 and 2 show the progression of damage in a BWR bundle subjected to temperatures above 2200 K. These figures show metallographic cross-sections taken from the KIT CORA-18 experiment [15], a large BWR bundle subjected to a heat up to peak temperatures ranging from 1200 to 2200 K. The cross-sections of the more than 1 meter long bundle show the (a) liquefaction and failure of a control blade and channel wall (1500–1700 K), (b) liquefaction and relocation of {U—Zr—O} (2000–2200 K), and (c) formation of metallic blockages (1500–2200 K). At higher temperatures, since BWR specific materials and structures are destroyed at the lower temperatures, other in-pile experiments for PWR and BWR designs, as well as TMI-2, address the liquefaction and formation of {U-Zr}-O_2 molten pool(s) (2600–2800 K). For example, Figure 3 shows a metallographic cross-section at the upper part of the bundle where a previously molten mixture of {U-Zr}-O_2 had frozen for PBF-SFD-ST [16], a slowly heated (~0.5 K/s before the start of oxidation) fuel rod assembly of 914 mm.

The existing experiments also show clearly the impact of the addition of water once severe fuel damage has started. Experiments in the United States OECD LOFT-FP [8], German CORA and QUENCH, and Russian PARAMETER programs have shown the influence of water addition under a variety of conditions including flooding from the bottom, from the top, and flooding after the hot bundles have been exposed to air. For example, at heating rates typical of a station blackout with early loss of cooling, the addition of water can result in the accelerated oxidation of the Zircaloy cladding (and B_4C when present), significant increases in hydrogen generation, and the accelerated liquefaction and slumping of {U-Zr}-O_2. Figure 4 shows the results from one such experiment, the Quench 11 experiment [17], where the addition of water to the bottom of the assembly resulted in accelerated heating in the portions of the bundle where peak temperatures are above 1500 K.

3. RELAP/SCDAPSIM

RELAP/SCDAPSIM is designed to describe the overall reactor coolant system (RCS) thermal hydraulic response

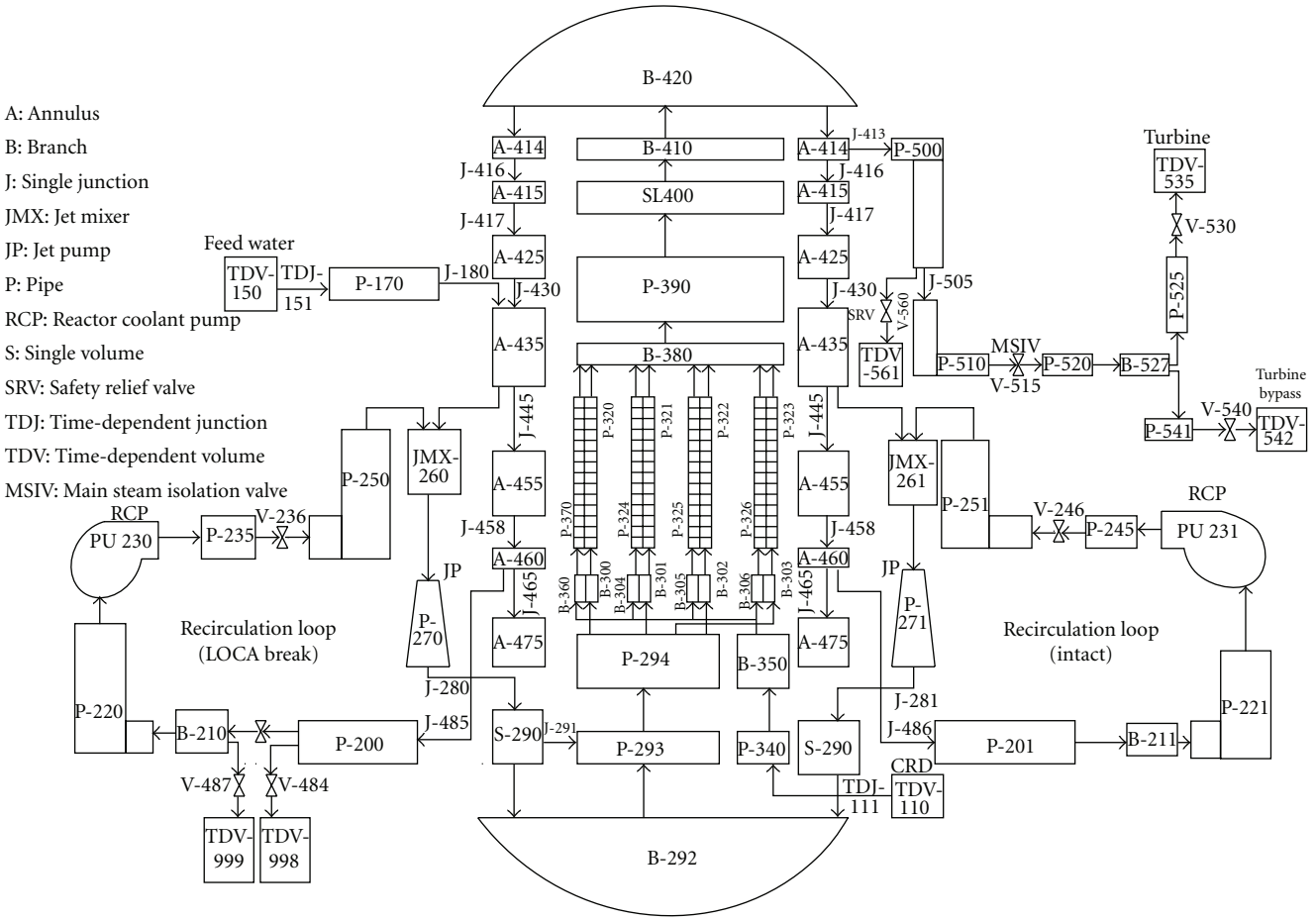

Figure 5: Overall Laguna Verde RELAP/SCDAPSIM thermal hydraulic component nodalization.

and core behaviour under normal operating conditions or under design basis or severe accident conditions. The RELAP5 models calculate the overall RCS thermal hydraulic response, control system behaviour, reactor kinetics, and the behaviour of special reactor system components such as valves and pumps. The SCDAP models calculate the behaviour of the core and vessel structures under normal and accident conditions. The SCDAP portion of the code includes user-selectable reactor component models for LWR fuel rods, Ag-In-Cd and B_4C control rods, BWR control blade/channel boxes, electrically heated fuel rod simulators, and general core and vessel structures. The SCDAP portion of the code also includes models to treat the later stages of a severe accident including debris and molten pool formation, debris/vessel interactions, and the structural failure (creep rupture) of vessel structures. The latter models are automatically invoked by the code as the damage in the core and vessel progresses.

RELAP/SCDAPSIM/MOD3.5 is the first release with the new QUENCH/PARAMETER-experiment-driven SCDAP modelling improvements. The new SCDAP modelling options include (a) an improved fuel rod gap conductance model, (b) improvements in the electrically heated fuel rod simulator model, (c) improvements in the shroud model, and (d) models to treat the influence of air ingression. The improved electrically heated fuel rod simulator model now includes the option to model tantalum heater elements in addition to the tungsten heater elements historically used in the QUENCH and other European bundle experiments. The improved shroud models include enhanced user options to simulate some of the unique features of experimental facilities including options to better simulate the influence of the thermal-mechanical failure of the experimental shrouds during high temperature and quenching conditions. The air ingression modelling options account for the changes in Zircaloy oxidation kinetics and uptake of nitrogen due to the presence of air.

4. Laguna Verde Input Model

The overall thermal hydraulic nodalization for the RELAP/SCDAPSIM model is presented in Figure 5. The plant model, developed by CNSNS, has a high level of detail. It represents the important features of the core, vessel, associated emergency cooling systems, and containment. The nodalization includes the reactor pressure vessel (RPV), Figure 6, the water (safety) injection components of the emergency core cooling system (see Figures 6 and 7) and main steam line(s) (see Figure 8).

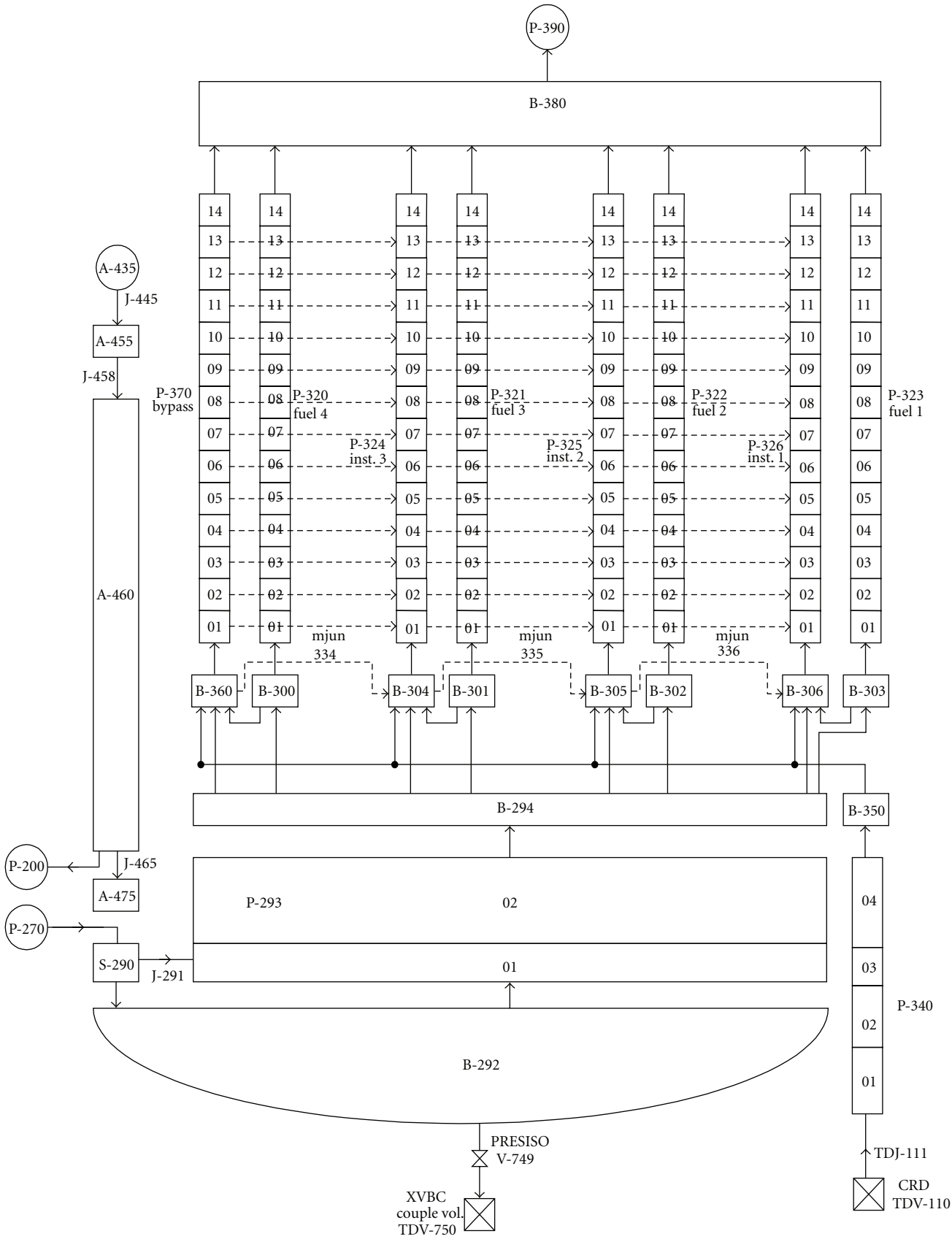

Figure 6: Laguna Verde: reactor pressure vessel and control rod drive (CRD) cooling system detailed nodalization.

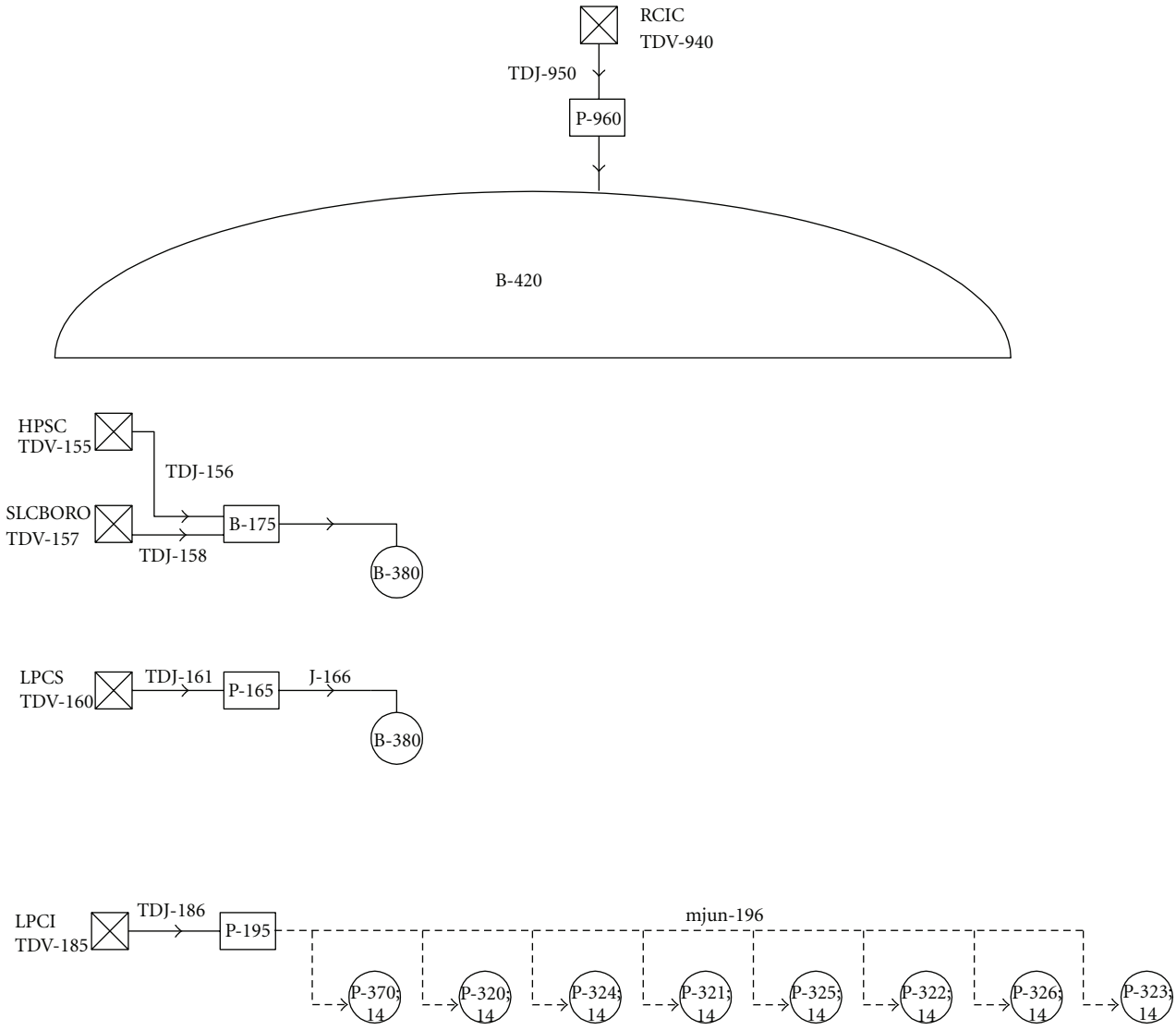

Figure 7: Laguna Verde: emergency cooling system water injection components.

Table 1: Timing of major damage progression events for a scenario with depressurization and termination of emergency water injection at 4.2 hours after reactor scram (CRD flows maintained).

Events	Time (s)	Time (hr)	Time after start of depressurization (hr)
Depressurization and termination of water injection in RPV	15000	4.2	
Initial fuel melting {U-Zr}-O_2	18000	5.0	0.8
Initial relocation of metallics (SS/Zr/B_4C) into LP	19500	5.4	1.3
Initial relocation of fuel {U-Zr}-O_2 into LP	20000	5.6	1.4

The core is described using four groups of representative BWR assemblies and associated control blade/channel boxes at different power levels and burnup histories (see Figure 6). Four vertical flow channels describe the flow within each of the four groups of BWR fuel assemblies (inside the fuel channels). An additional four vertical flow channels describe the flow in the bypass regions outside the channel boxes and surrounding the control blades. Each representative assembly in each group includes a representative fuel rod bundle, Zircaloy channel box, and B_4C control blade element, Figure 9. The fuel rods in each assembly are described by a representative SCDAP fuel rod component. The channel box and control blade segment in each assembly is described by a representative SCDAP BWR channel box/control blade component. The radial and axial power peaking for the four representative fuel rod groups are provided in Figure 10. The fuel rods in groups 1 and 2 (labelled components 1 and 2 in the figure) have average burnup levels of 4.34×10^5 MWs/kg.

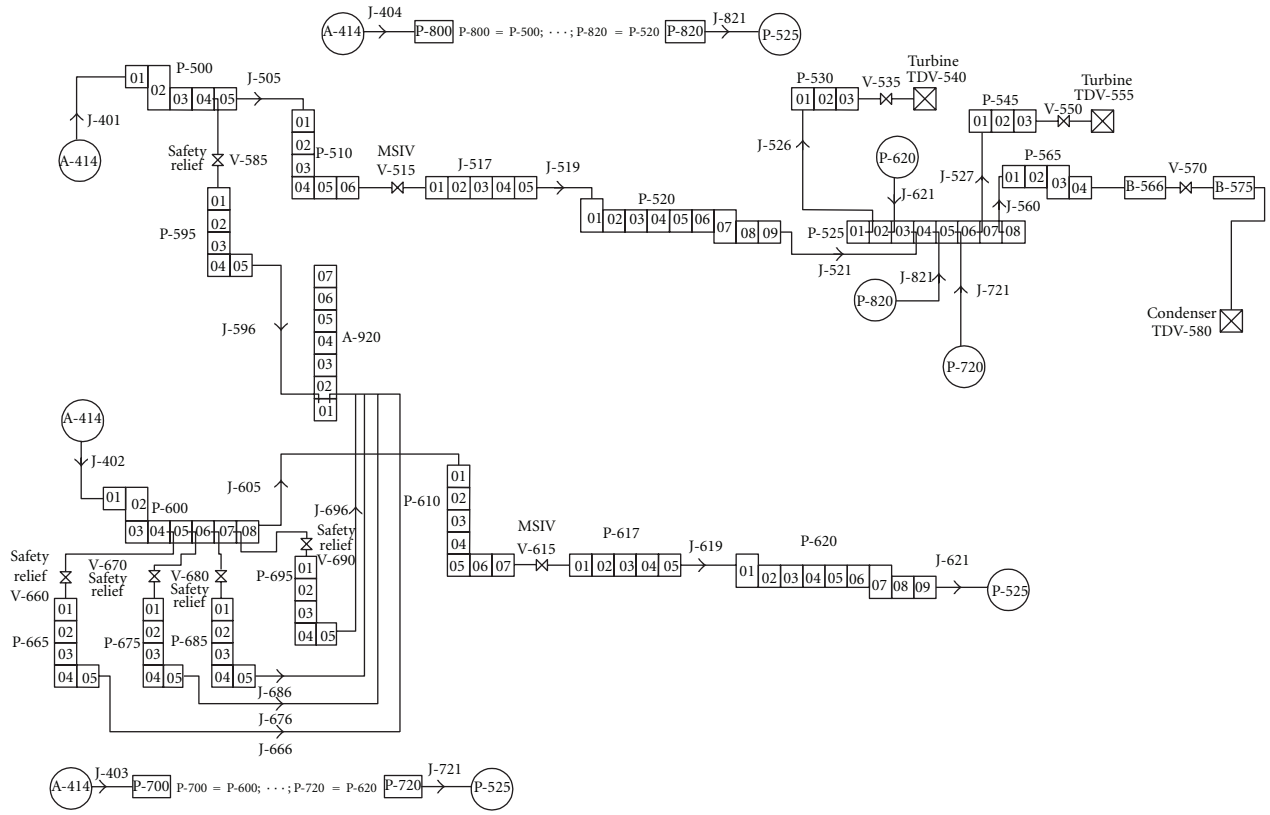

Figure 8: Laguna Verde: main steam line detailed nodalization.

Fuel rods in groups 3 and 4 have average burnup levels of 3.74×10^5 and 1.88×10^5 MWs/kg, respectively.

5. Initial Calculations in Support of IAEA Emergency Response Team (through March 24, 2011)

The initial calculations were performed by CNSNS using RELAP/SCDAPSIM for station blackout conditions with different scenarios after loss of emergency cooling including boil-off at high pressure and low pressure (opening of two safety relief valves (SRVs) after loss of emergency cooling). Additional calculations were then performed by ISS on March 21 to provide bounding results for the IAEA emergency response team. Since, at this time, it was not known what accident management strategies were possible or being performed, a series of calculations were initiated assuming that emergency water injection to the RPV was terminated, and only limited (2.33 kg/s) water injection to the core from the control rod drive (CRD) cooling system was continued for a range of times starting from 4 hours to 20 hours after reactor scram. The following results are from calculations where the reduction in emergency water injection was initiated ~4.2 hours after reactor scram. The reduction of water injection was initiated following the depressurization of the reactor by opening two SRVs. Table 1 shows the event timing in this case. Figure 11 shows the peak assembly temperatures, collapsed water level (relative to the bottom of the vessel), the growth of the {U-Zr}-O_2 molten pool in the core region (radius of a sphere of the same volume), and the height of the debris bed in the lower plenum. The water level shown is relative to the bottom of the lower plenum with the top of the fuel at ~9.0 m. Figures 12, 13, and 14 show the core temperature distributions at times between 5.0 to 5.6 hours after reactor scram. Figure 15 shows integral hydrogen production and collapsed water level. Figures 16, 17 and 18 show the lower plenum debris bed and lower head vessel wall temperatures after the relocation of molten {U-Zr}-O_2 into the lower plenum with detailed snapshots at 6.9 and 7.5 hours after scram.

Additional calculations were then performed from March 22 to 24 to determine the influence of delays in the reduction of emergency water injection (CRD flows were continued at 2.33 Kg/s). The results are shown below. Table 2 shows the comparison of event timing with depressurization and reduction in water injection starting periods ranging from ~4–20 hours after reactor scram. Figure 19 shows the water level and maximum core temperature for the different scenarios with the time referenced to the start of the depressurization. The water level shown is relative to the bottom of the lower plenum with the top of the fuel at ~9.0 m. Figure 20 shows the corresponding hydrogen generation.

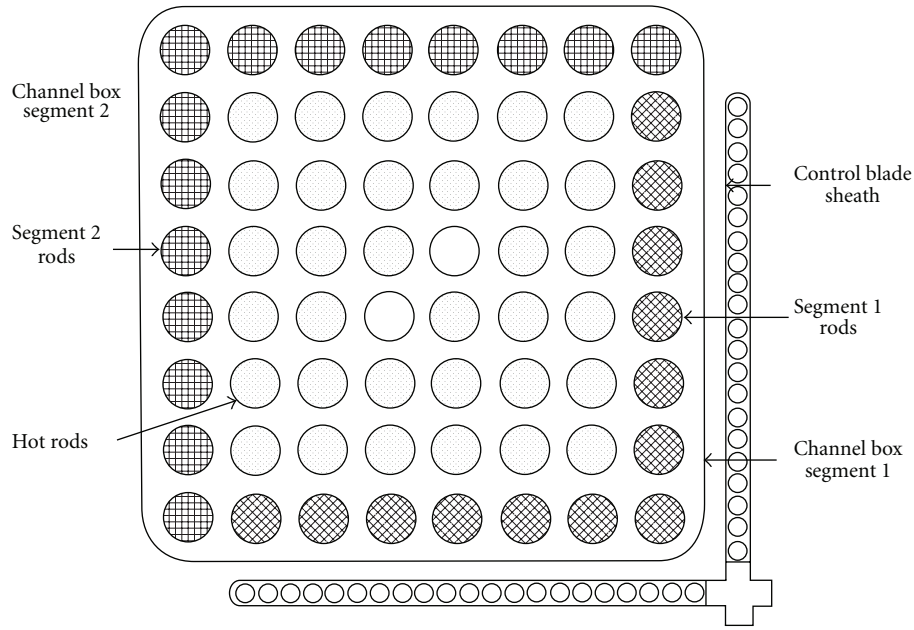

Figure 9: Representative RELAP/SCDAPSIM BWR assembly for Laguna Verde.

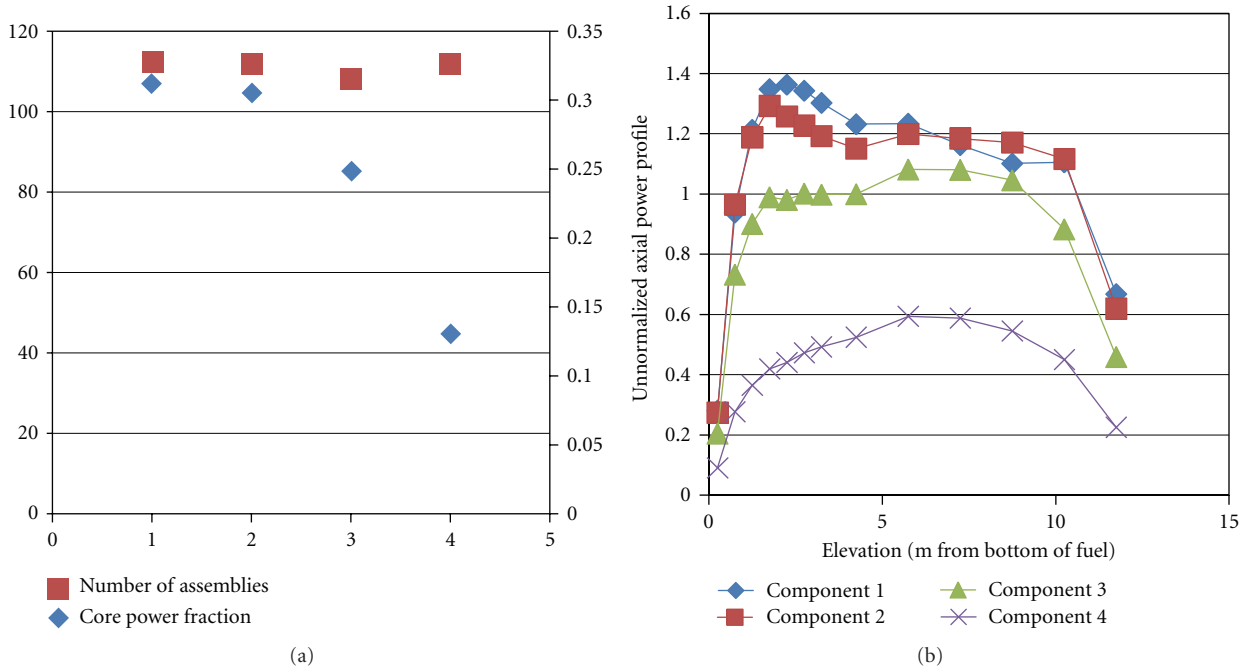

Figure 10: Description of the four representative assemblies used in the Laguna Verde input model.

6. Additional Calculations (March 25–April 24)

After March 25, additional calculations were initiated looking at a variety of different accident scenarios. These calculations included station blackout transients.

(1) Loss of cooling immediately after scram with depressurization and no emergency water injection.

(2) With different water addition scenarios with no or limited emergency cooling water starting 4.2 hours after scram including;

(a) Depressurization by opening 2 SRVs with variations in flow including the following;

(i) Termination of all water addition through emergency cooling systems.

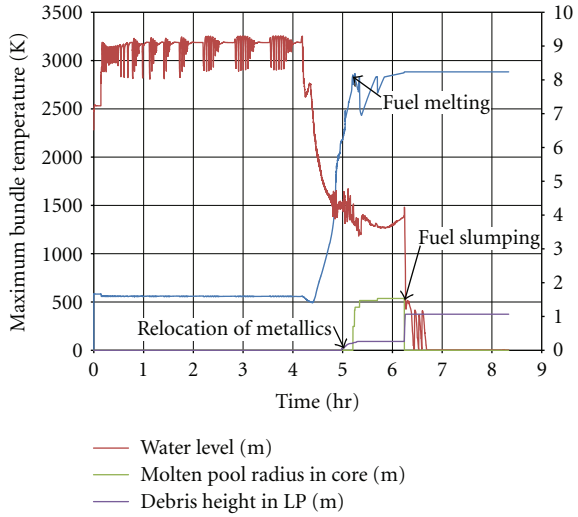

Figure 11: Maximum bundle temperature, water level, effective molten pool radius, and lower plenum debris height for a scenario with depressurization and termination of emergency water injection at 4.2 hours after reactor scram (CRD flows maintained).

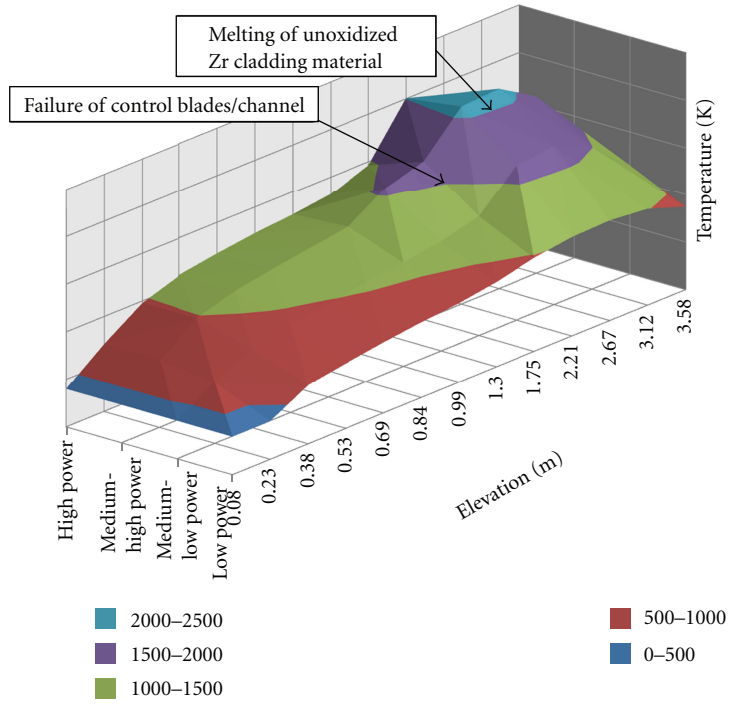

Figure 12: Core temperature distribution at 5.0 hours after reactor scram for a scenario with depressurization and termination of emergency water injection at 4.2 hours after reactor scram (CRD flows maintained).

(ii) Nominal CRD flows of 2.3 kg/s (base case from March 21st).
(iii) Doubled CRD flows of 4.6 kg/s.
(iv) Termination of all water addition for period of time followed by water injection at 4.7 and 5.3 hours after reactor scram.

(b) SRVs remained closed—high pressure varying between relief valve set points.

(3) With comparison of different scenarios initiated at 0, 4, 20, 40, and 70 hours after reactor scram.

As expected, the station blackout scenario immediately after scram resulted in the most rapid core uncovery, melting of the fuel, relocation of the fuel into the lower plenum, and likely lower head failure. In these calculations, the fuel in the reactor core was calculated to start liquefying at the time of 1.5 hours. By 2.2 hours, the molten pool extended to the periphery of the core. A molten pool

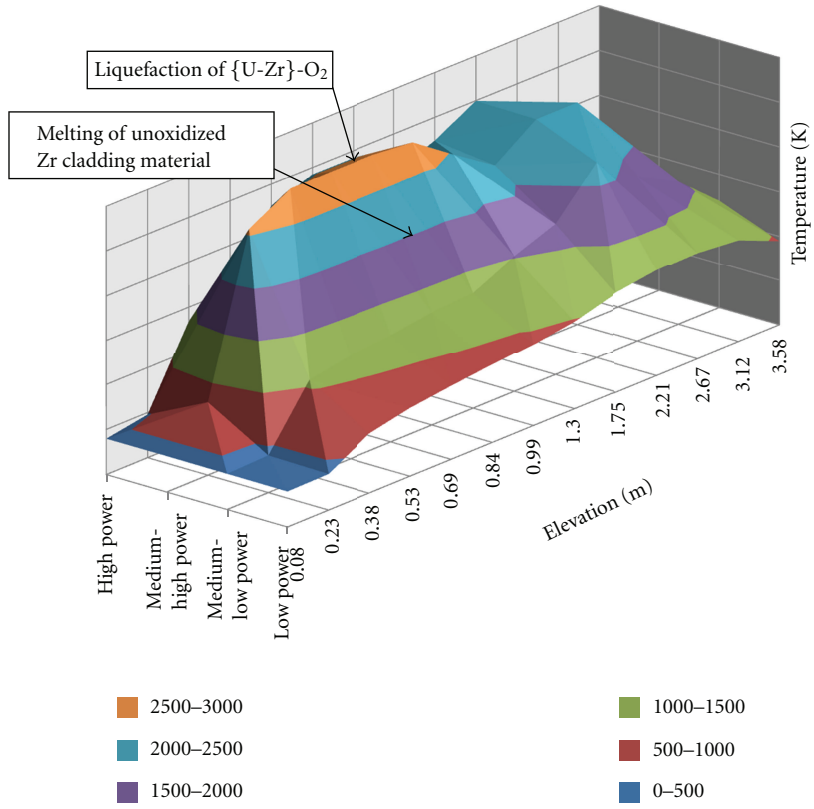

Figure 13: Core temperature distribution at 5.1 hours after reactor scram for a scenario with depressurization and termination of emergency water injection at 4.2 hours after reactor scram (CRD flows maintained).

containing 69,000 kg of liquefied {U-Zr}-O_2 was calculated to slump to the lower head at the time of 3.4 hours. At that time, the cumulative hydrogen production was 465 kg. The steam generated by the slumping caused another 150 kg of hydrogen to be produced in the next several hundred seconds. The maximum temperature in the lower head vessel wall had exceeded the melting point of steel within 4.3 hours.

The study of the influence of different water addition scenarios with no or limited emergency cooling water starting 4.2 hours after scram was a variation of the base calculations performed prior to and on March 21st. Figure 21 shows the influence of reactor vessel pressure on water level and maximum bundle temperature. In this case, the calculations considered a scenario where two safety relief valves (SRVs) were opened allowing the pressure to decrease to a value determined by the containment pressure versus a scenario where the SRVs were not opened and the vessel pressures were determined by the set points on the normal relief valves. Figure 22 shows the corresponding hydrogen generation rate and integral hydrogen production. Figures 23 and 24 show the influence of different scenarios of water injection once the core was starting to uncover. All of these scenarios maintained flow through the CRDs of 2.33 kg/s. Figure 23 shows the maximum bundle temperature, water level, and reactor vessel pressure. Figure 24 shows the corresponding hydrogen generation rate and integral hydrogen production.

The comparisons of different scenarios initiated at different times varying from 0 up to 70 hours after reactor scram included a significant variation in the decay heat levels at the time of core uncovery as well as variations in the reactor system pressure and water injection. The variation in decay heat for the Laguna Verde model is shown in Figure 25. Figure 26 shows the maximum bundle temperatures and water levels for high-pressure scenarios (SRVs remain closed) for scenarios where all of the emergency water injection was terminated at a time varying from 0 hours after scram to 70 hours after scram. Figure 27 shows the corresponding hydrogen production for these scenarios. Figures 28 and 29 show the influence of different scenarios at reduced decay heats with loss of emergency cooling at 40 and 70 hours. The scenarios start out similarly with a high-pressure scenario, but in the 70 hour scenario, the two SRVs were opened approximately 2 hours after the loss of emergency cooling.

7. Discussion of Results

The calculations for a wide range of station blackout scenarios showed that the core uncovery, fuel melting, and relocation of the fuel and other molten materials into the lower plenum can occur rather quickly once emergency cooling is no longer available. For the scenarios with the loss of emergency cooling occurring within 2 or 3 days after reactor scram followed by the opening of the SRVs and

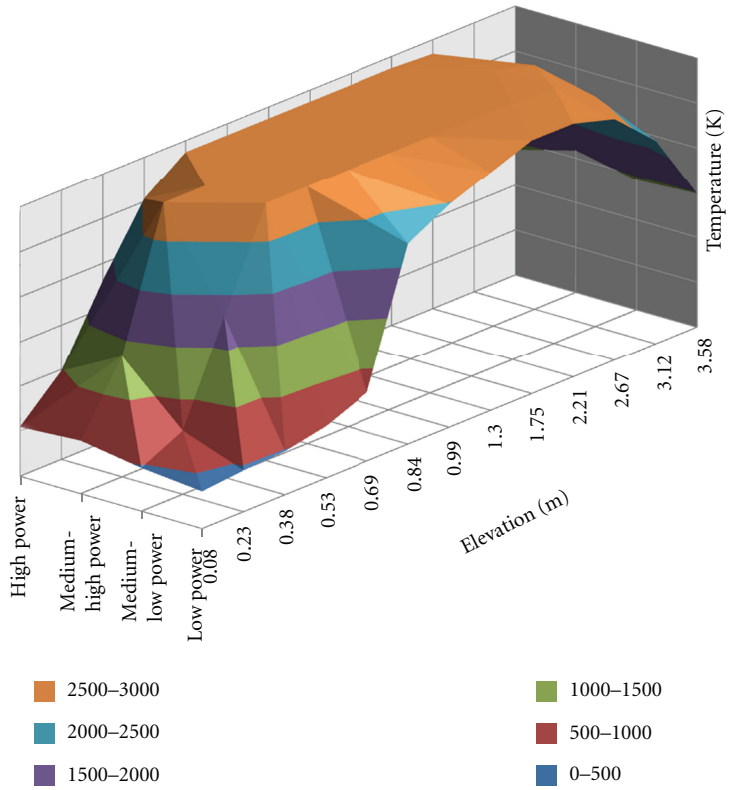

Figure 14: Core temperature distribution at 5.6 hours after reactor scram for a scenario with depressurization and termination of emergency water injection at 4.2 hours after reactor scram (CRD flows maintained).

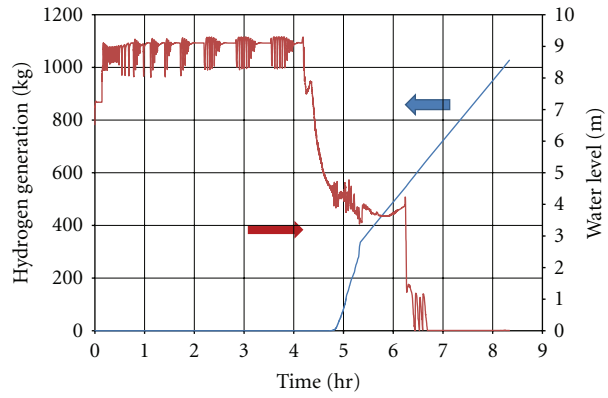

Figure 15: Hydrogen generation and water level for a scenario with depressurization and termination of emergency water injection at 4.2 hours after reactor scram (CRD flows maintained).

Table 2: Timing of initial fuel melting for scenarios with depressurization and termination of emergency water injection at 4.2, 11.8, and 19.6 hours after reactor scram (CRD flows maintained).

Depressurization and termination of water injection in RPV (hr)	Initial fuel melting {U-Zr}-O_2 Time after start of depressurization (hr)
4.2	0.8
11.8	1.5
19.6	1.9

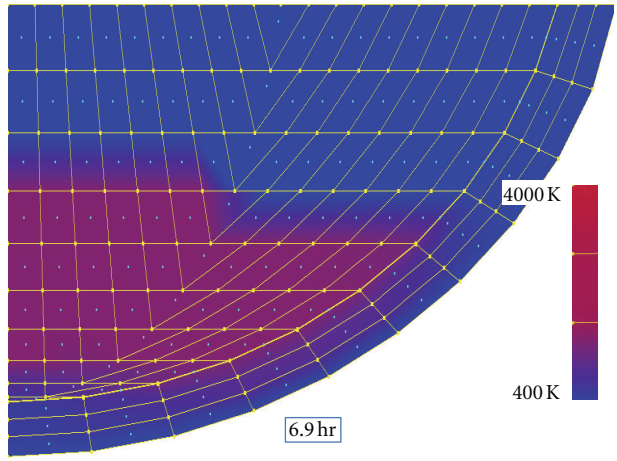

Figure 16: Temperatures in lower plenum at 6.9 hours for a scenario with depressurization and termination of emergency water injection at 4.2 hours after reactor scram (CRD flows maintained).

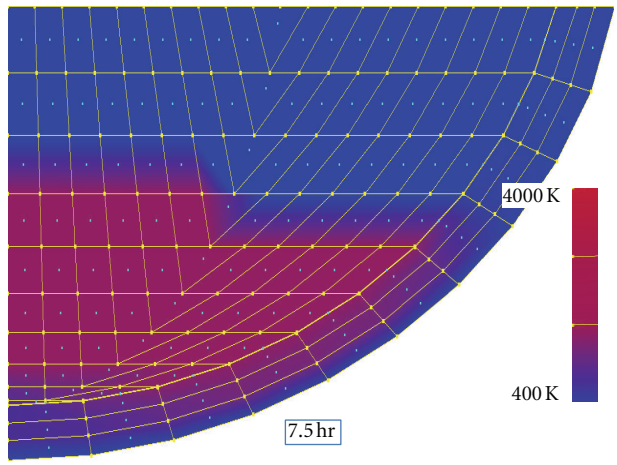

Figure 17: Temperatures in lower plenum at 7.5 hours for a scenario with depressurization and termination of emergency water injection at 4.2 hours after reactor scram (CRD flows maintained).

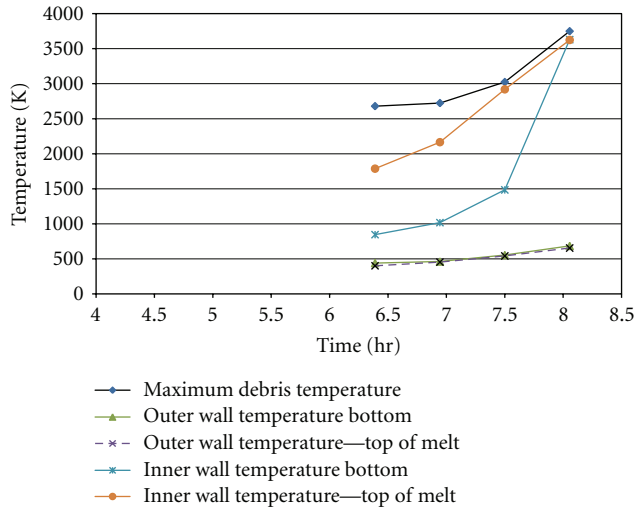

Figure 18: Temperatures in lower plenum wall and debris after melt relocation for a scenario with depressurization and termination of emergency water injection at 4.2 hours after reactor scram (CRD flows maintained).

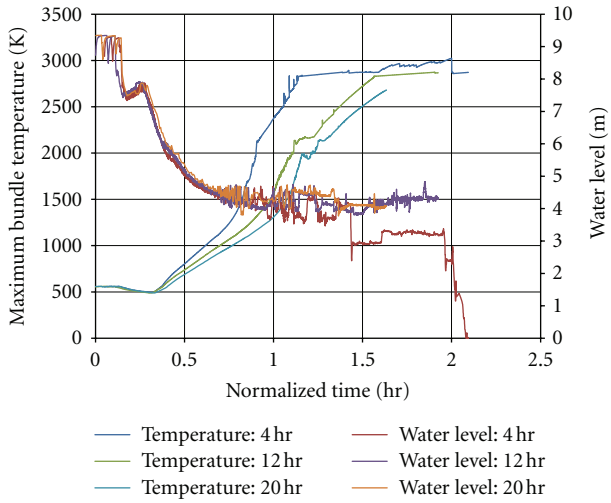

Figure 19: Maximum bundle temperature and water levels for scenarios with depressurization and termination of emergency water injection at 4.2, 11.8, and 19.6 hours after reactor scram (CRD flows maintained).

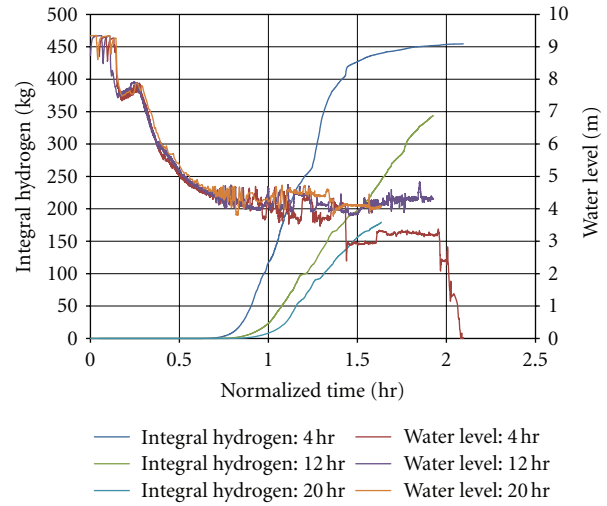

Figure 20: Integral hydrogen production and water levels for scenarios with depressurization and termination of emergency water injection at 4.2, 11.8, and 19.6 hours after reactor scram (CRD flows maintained).

depressurization, fuel melting can be reached within 2 hours of the loss of core cooling. For the same scenarios but keeping the SRVs closed (high-pressure scenarios), fuel melting can be delayed for some hours (approximately 2 hours for a scenario with loss of cooling about 4 hours after scram). This delay is more pronounced for scenarios with a loss of cooling after 2 or 3 days. See Table 2 and Figures 19, 21, and 26, for example.

Although the timing of core damage is impacted by the timing of the loss of emergency cooling, the pattern of the radial and axial extent of the damage in the core does not change significantly. This can be seen by comparing the temperature distributions in the core for the two scenarios where the vessel is depressurized in conjunction with loss of emergency cooling at 4.2 and 40 hours after scram, respectively. Figures 30 and 31 show the temperature distributions after failure of the control blades and channel boxes at temperatures near 1500 K and after the start of the melting of the unoxidized cladding material at temperatures near 2000 K in the hottest regions of the core. The pattern is quite similar even though the 4.2 hour scenario still has limited cooling with the injection of water through the CRD cooling system, while the 40 hour scenario has no water injection. The limited CRD flow in the 4.2 hour scenario results in the bottom of the core remaining relatively cool compared to the rest of the core.

The impact of the axial power distribution in the core is also apparent in the radial and axial extent of core damage. As identified in Figure 10, the axial power distribution for the high and medium-to-high power assemblies actually has a double axial power peak even though the bottom peak is much higher. In contrast, the medium-to-low and low-power assemblies have a cosine power profile with the peak near the center of the core height. The impact of the variation in the

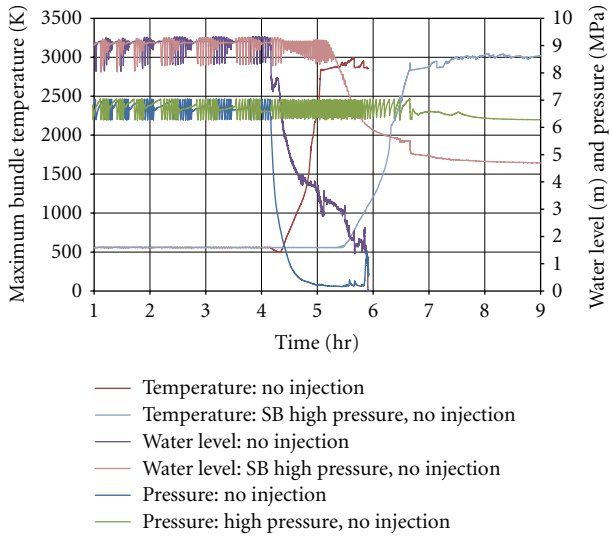

Figure 21: Maximum bundle temperature, water level, and reactor vessel pressure for scenarios with and without water injection after the start of core uncovery (all emergency water injection was terminated at 4.2 hours after reactor scram).

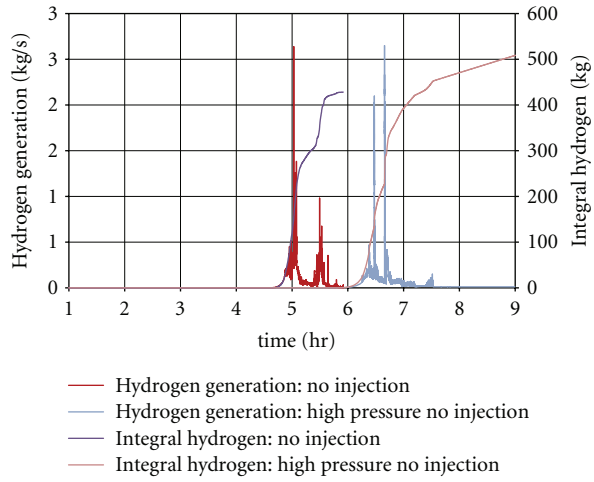

Figure 22: Hydrogen generation rate and integral hydrogen for scenarios with and without water injection after the start of core uncovery (all emergency water injection was terminated at 4.2 hours after reactor scram).

power profile from the high-to-low power assemblies shows up in the noticeable double hump in the temperatures for the higher-power assemblies visible in Figures 30 and 31.

The radial and axial extent of the damage in the core is much more impacted by the changes in thermal hydraulic conditions associated with the opening (or lack of opening) of the SRVs. Figures 32 and 33 show the core temperature distributions at differing times after the start of core uncovery for the scenarios where the emergency core cooling is terminated at 4.2 hours after reactor scram. Figure 32 shows the scenario where the SRVs are opened resulting in a depressurization of the vessel. Figure 33 shows the scenario where the SRVs are not opened, so the vessel pressure cycles between the normal relief valve set points but remains high through the scenario. As shown in Figure 21, the main contributor to the difference in the temperature distributions in these two scenarios is the much higher water level at the time of initial core heating and melting for the high-pressure scenario. That is why the higher temperatures and associated damage are limited to the upper portion of the core in the high-pressure scenario. A secondary factor, also identified in Figure 21, is that the cycling of the pressure due to the opening and closing of the normal relief valve impacts the oxidation in the core. That is, as the relief valve opens and the pressure drops, the steam generation rate and associated oxidation rate increase (in the higher temperature and higher elevation regions where oxidation is limited by the availability of steam).

The influence of water addition can be seen by comparing the results shown in Figures 34–38. Figure 34 shows the maximum core temperature, water level, and pressure for two scenarios where the emergency water cooling was terminated and the vessel was depressurized. The core uncovery and heat up was initiated by the termination of

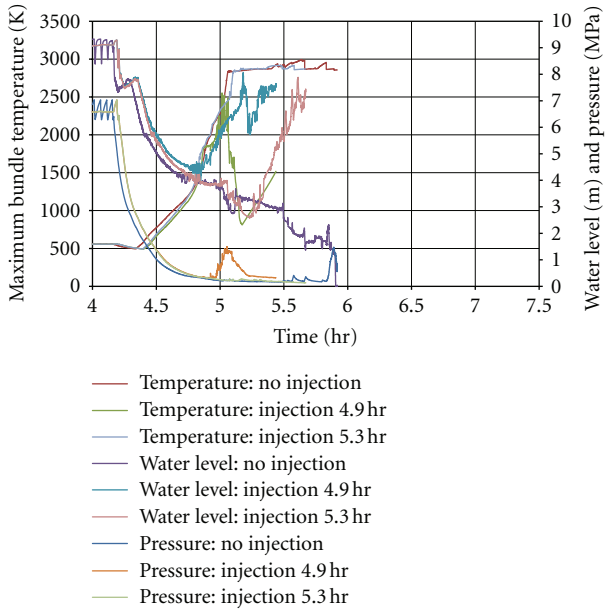

Figure 23: Maximum bundle temperature, water level, and reactor vessel pressure for scenarios with and without water injection after the start of core uncovery (all emergency water injection was terminated at 4.2 hours after reactor scram).

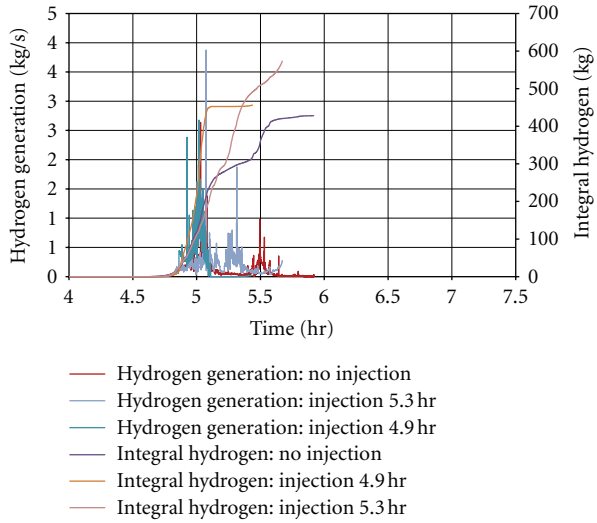

Figure 24: Hydrogen generation rate and integral hydrogen for scenarios with and without water injection after the start of core uncovery (all emergency water injection was terminated at 4.2 hours after reactor scram).

cooling and opening of two SRVs at 4.2 hours after scram. One of the scenarios allowed the core to continue to uncover, while the other scenario included the injection of water into the vessel starting at 4.7 hours after a portion of the core has reached temperatures in excess of 1500 K. Although water level in the core immediately started to increase at 4.9 hours in the scenario with water injection, the maximum core temperatures continue to climb to temperatures above 2500 K before starting to decrease. As shown in Figures 35–36, during the scenario with the water injection at 4.9 hours, the core temperatures also increased over more of the core initially and then reduced as water moved up into the core. Figure 35 shows the core temperature distribution at 5.0 hours after scram with temperatures in the high-power and medium-to-high power assemblies exceeding 1500 K (with the destruction of the control blades and channel boxes) over much of the assemblies above the water rising in the core. Figure 36 shows the core temperature at 5.1 hours after scram. Figure 37 compares the two scenarios with and without water injection at 4.9 hours at times of 5.0 and 5.1 hours after scram. The comparison at 5.0 hours after scram clearly shows that even though the peak core temperatures in the scenario with water injection was less than in the scenario without water injection, the extent of control blade and channel box melting and relocation is much larger in the case with water injection.

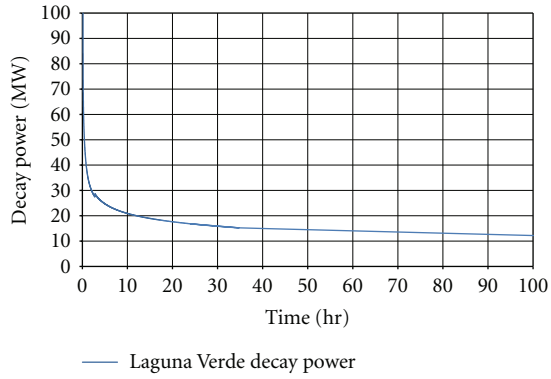

Figure 25: Variation in decay heat after reactor scram.

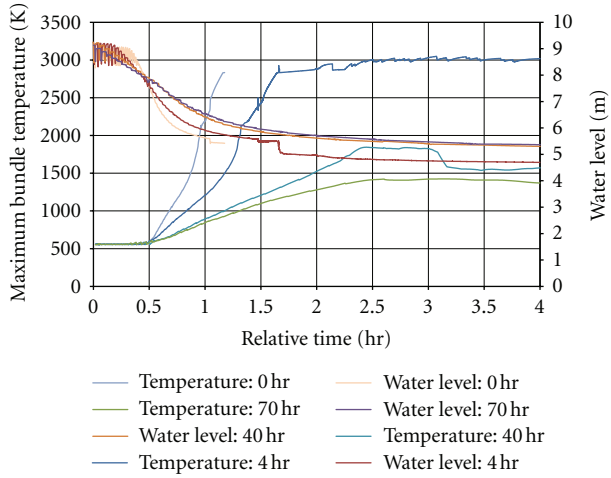

Figure 26: Maximum bundle temperature and water level for high-pressure scenarios for scenarios where all of the emergency water injection was terminated at a time varying from 0 hours to 70 hours after scram.

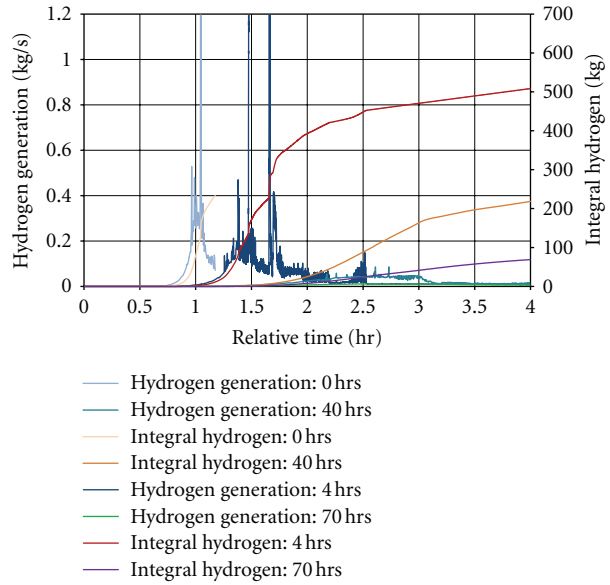

Figure 27: Hydrogen generation rate and integral hydrogen for high-pressure scenarios for scenarios where all of the emergency water injection was terminated at a time varying from 0 hours to 70 hours after scram.

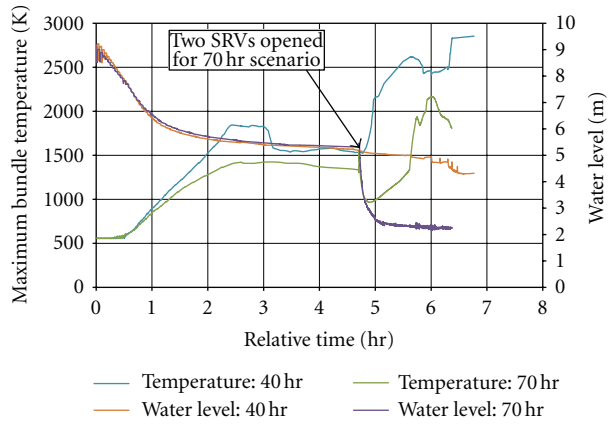

Figure 28: Maximum bundle temperature and water level for the two scenarios with initial loss of the emergency water injection at 40 hours and 70 hours.

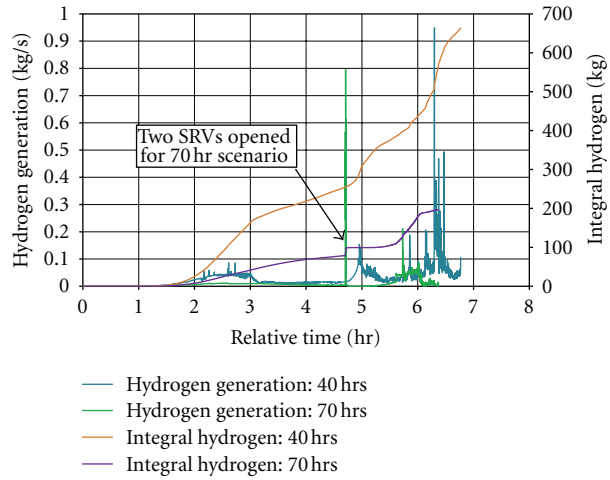

Figure 29: Hydrogen generation rate and integral hydrogen for the two scenarios with initial loss of the emergency water injection at 40 hours and 70 hours.

One of the important factors causing the greater extent of control blade/channel box destruction in the case with water injection can be seen in the results shown in Figure 38. In this figure, the hydrogen generation rate and integral hydrogen production are compared for the two scenarios with and without water injection at 4.9 hours. The comparison of the hydrogen generated in the two scenarios shows more hydrogen and associated oxidation heat generation over the period from 4.9 to 5.0 hours in the case with water injection. As discussed in Section 2, this type of behaviour was also clearly shown in the experiments with water addition like Quench 11.

8. Conclusions

The conclusions drawn from the preceding results and discussions are presented in three parts. First, what were the conclusions for the core/vessel damage expected in Units 1–3 of Fukushima Daiichi? These conclusions are based on the results and information reported for Fukushima in later March and early April, although the general information published to date appears to be consistent with the assessment presented in March to support the IAEA emergency response team and later to our Japanese colleagues. Second, what are general conclusions for a typical (Laguna Verde) BWR that may be subjected to Fukushima-Daiichi-like conditions? Third, what are the general conclusions for severe accident management strategies?

What were the conclusions for Units 1–3 of Fukushima Daiichi based on the assessment and information available in March?

(a) It was concluded within the first one or two weeks of the accident that it was likely that significant fuel melting occurred in Units 1 and 3 which lost cooling soon after loss of off-site power associated with the tsunami (Unit 1) and after approximately 40 hours (Unit 3), respectively.

(b) It was concluded that the failure of the vessel in Unit 1 was likely even given the large uncertainties in the accident conditions. Although it was considered

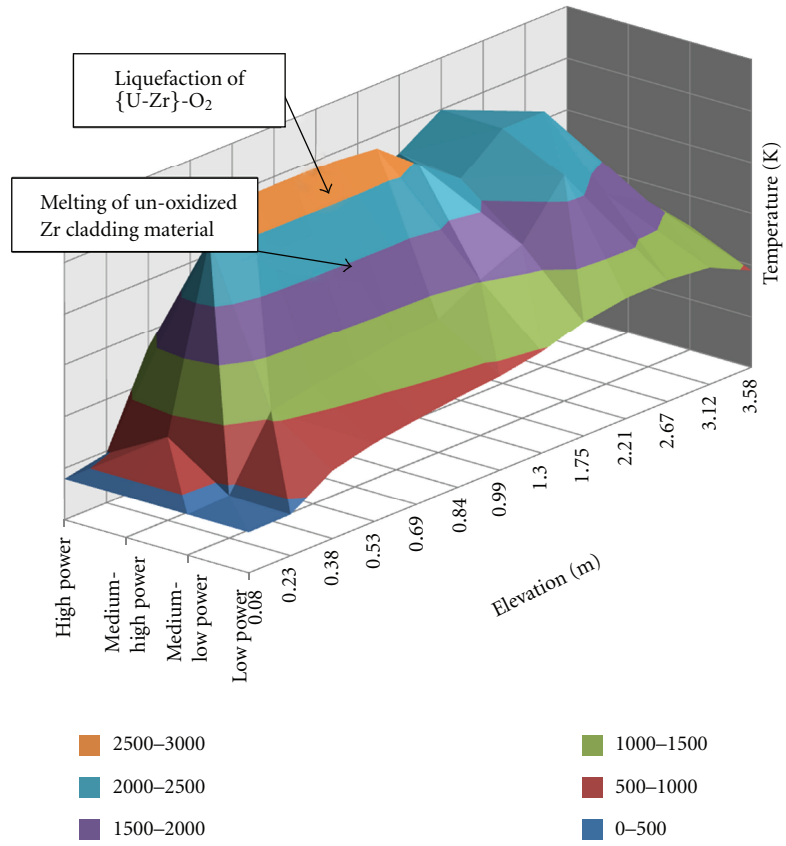

Figure 30: Core temperature at 5.1 hours for a scenario with depressurization (all emergency water injection excluding the CRDs was terminated at 4.2 hours after reactor scram).

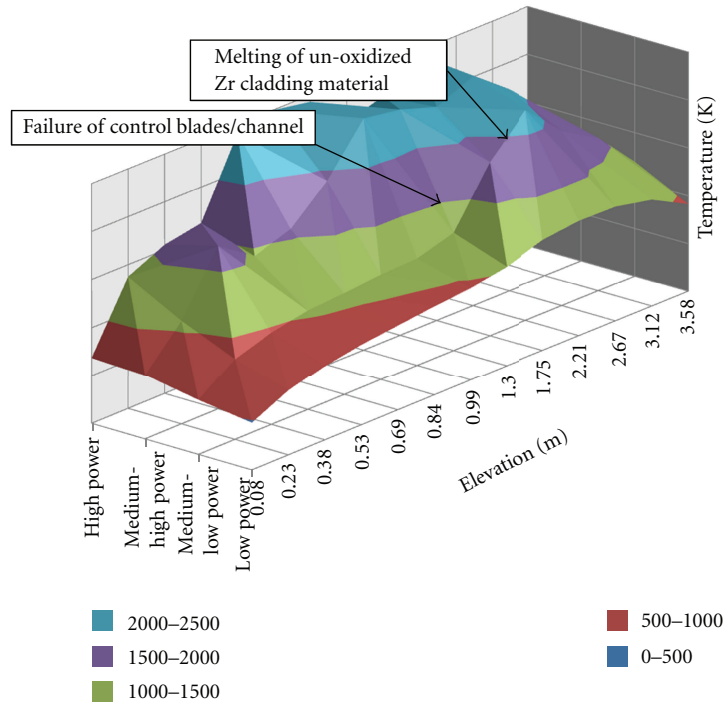

Figure 31: Core temperature at 41.7 hours for a scenario with depressurization (all emergency water injection was terminated at 40 hours after reactor scram).

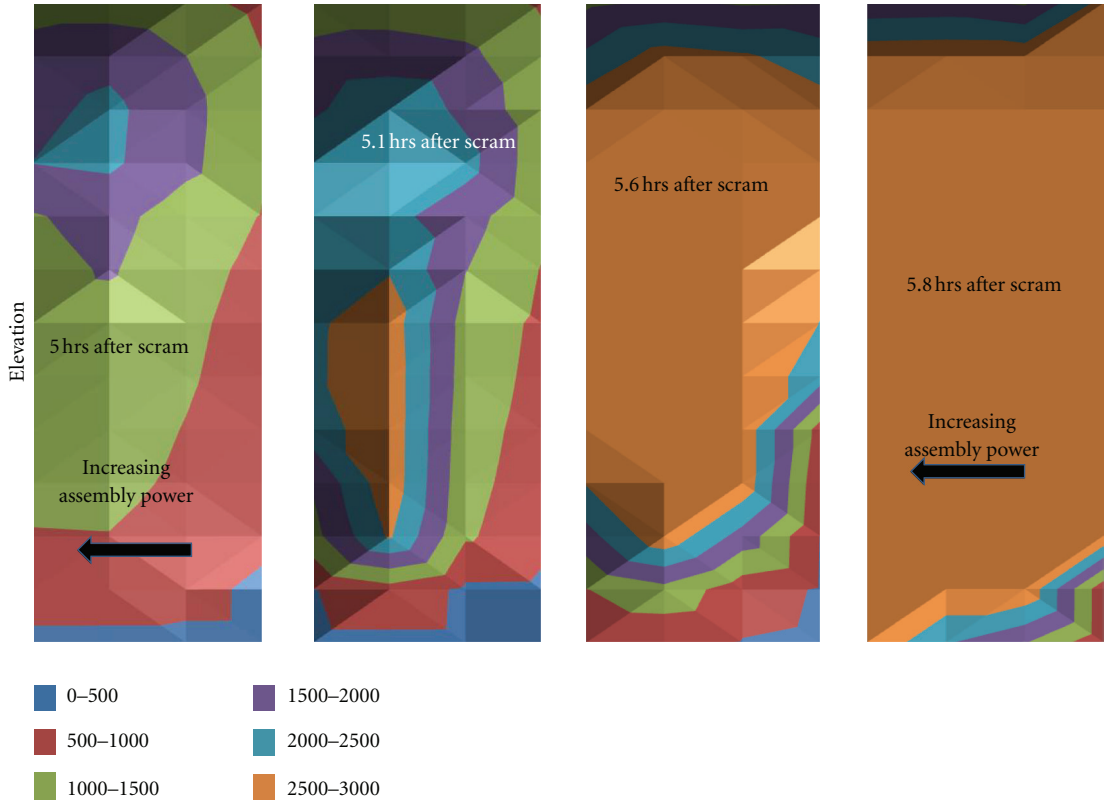

Figure 32: Core temperature distributions for a scenario with depressurization (all emergency water injection excluding the CRDs was terminated at 4.2 hours after reactor scram).

likely that the vessel in Unit 3 may have failed, the large uncertainties in the vessel pressure at the time that emergency cooling was lost precluded any definitive conclusions.

(c) It was concluded that some destruction of the core (in particular the loss of control blades and channel boxes) was likely in Unit 2, although the uncertainties associated with the attempts to depressurize the vessel at the same time salt water was being injected ruled out any definitive conclusions about fuel melting.

What are the general conclusions for a typical (Laguna Verde) BWR that may be subjected to Fukushima-Daiichi-like conditions?

(a) It only takes a few hours without emergency cooling for the core to uncover and the fuel to start melting. The time required to fuel melting temperatures will increase the longer that the emergency cooling can be maintained. In the calculations performed for Laguna Verde, the destruction of the control blades and channel boxes occurred within a few hours of loss of cooling even for scenarios with the emergency cooling maintained for three days (70 hours.) Thus, scenarios where cooling is maintained for a long period of time can result in a significant portion of the core without control blade material even though the fuel remains relatively intact.

(b) Intentional depressurization of the vessel after loss of cooling can have a very significant (negative) influence on the destruction and melting of the core. For the calculations for Laguna Verde, the depressurization of the vessel upon loss of emergency cooling accelerated the uncovery of the core and melting of the fuel to a significant degree. For the case of the loss of core cooling at 4 hours, the depressurization resulted in fuel melting within less than 1 hour, while in the high-pressure scenario under the same conditions, the fuel melting occurred more than an hour later. The fraction of the core reaching fuel melting temperatures also was increased by nearly a factor of two in the depressurization case at 4 hours. For scenarios with extended periods before emergency cooling is lost, the difference between depressurized and high-pressure scenarios becomes even more pronounced.

(c) The addition of water after the core is uncovered, and core temperatures which have exceeded 1500 K can have a mixed influence (positive and negative) on the destruction and melting of the core. The addition of water is necessary to slow or prevent the melting of the fuel but can result in the acceleration of the damage in the core initially, particularly the destruction of the control blades and channel boxes.

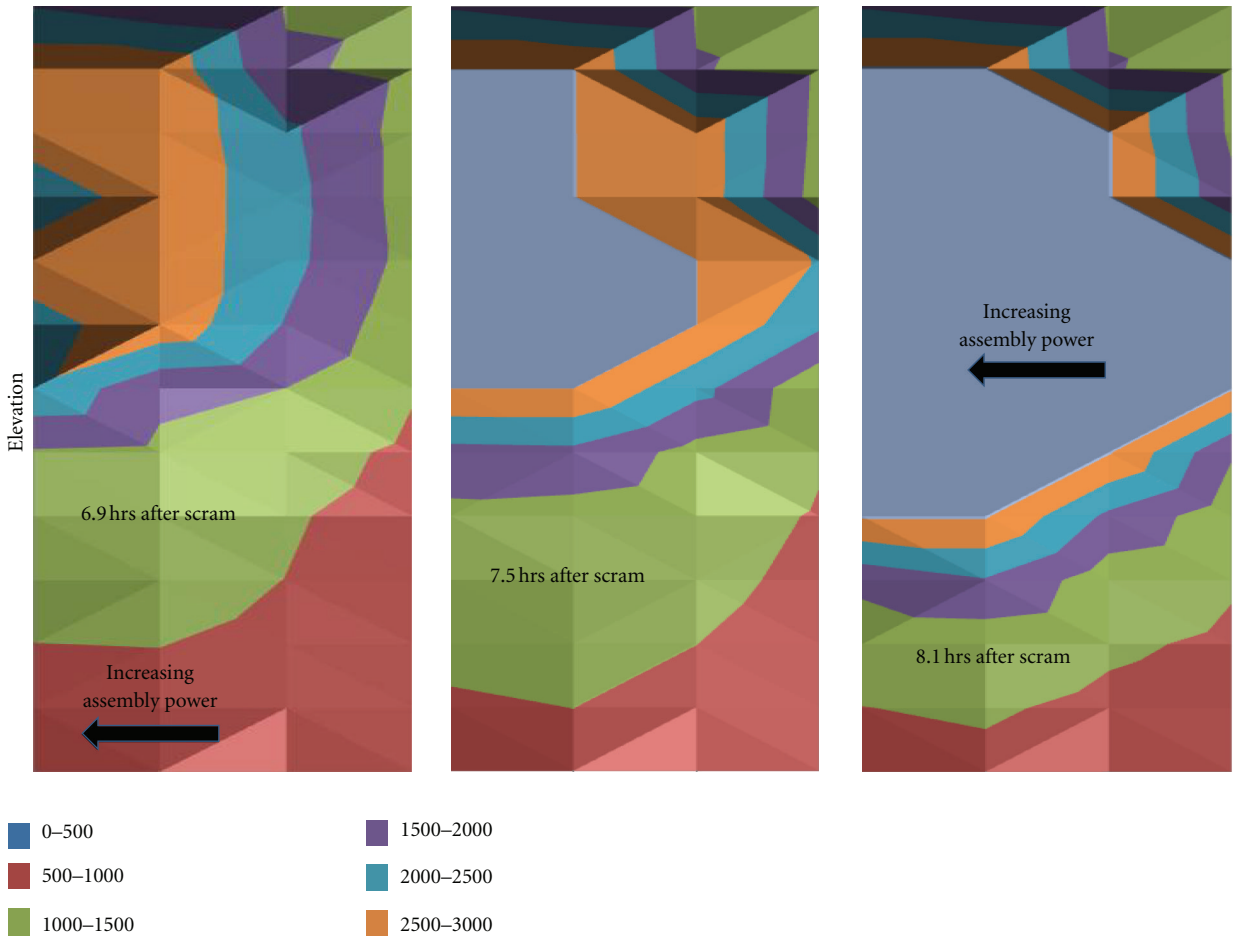

Figure 33: Core temperature distributions for a scenario without depressurization (all emergency water injection was terminated at 4.2 hours after reactor scram).

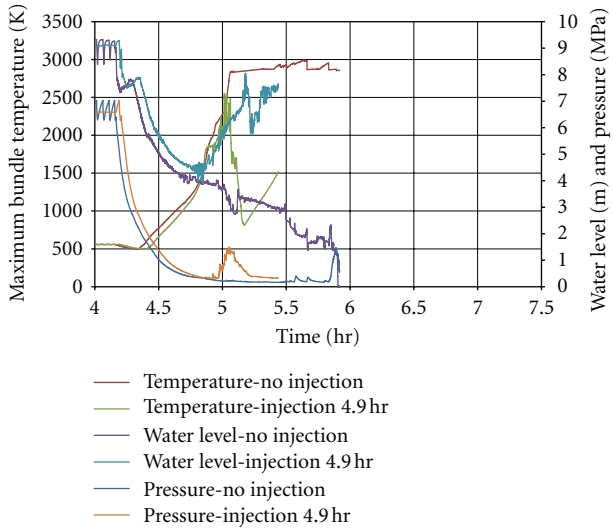

Figure 34: Maximum bundle temperature, water level, and reactor vessel pressure for scenarios without water injection and with water injection at 4.9 hours after scram (all emergency water injection was terminated at 4.2 hours after reactor scram).

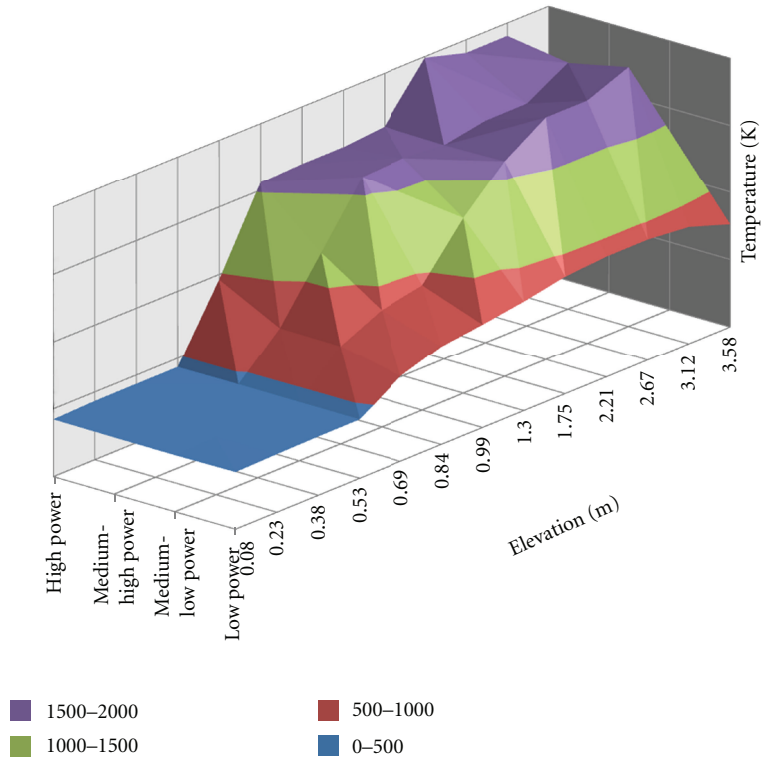

Figure 35: Core temperature distribution at 5.0 hours for scenario with water injection at 4.9 hours after scram (all emergency water injection was terminated at 4.2 hours after reactor scram).

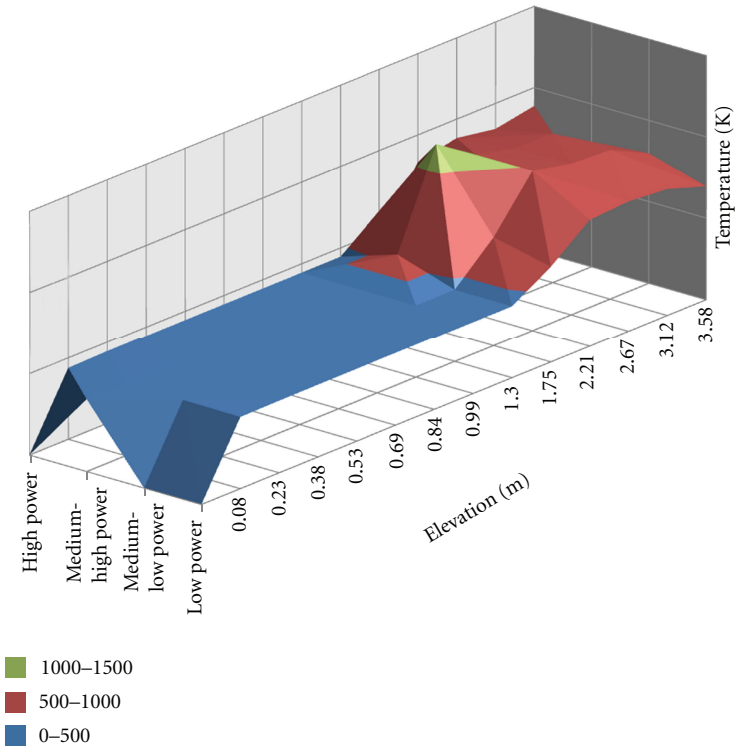

Figure 36: Core temperature distribution at 5.1 hours for scenario with water injection at 4.9 hours after scram (all emergency water injection was terminated at 4.2 hours after reactor scram).

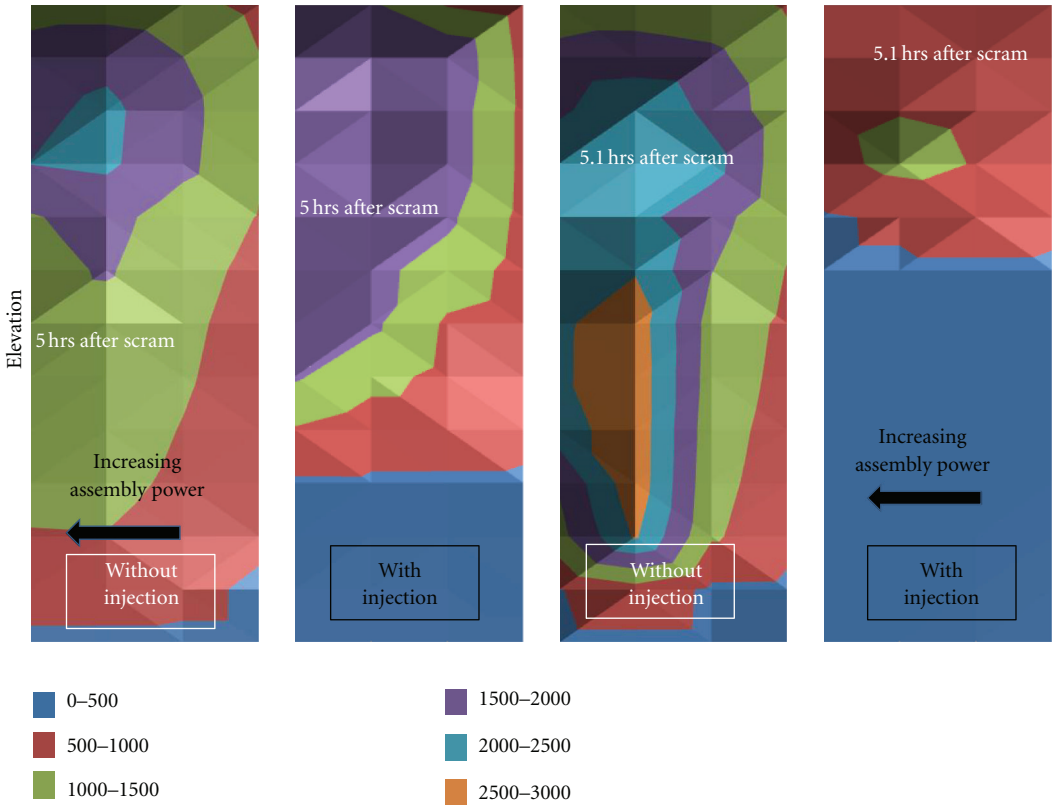

Figure 37: Core temperature distributions for scenarios with depressurization with and without water injection after core uncovery (all emergency water injection was terminated at 4.2 hours after reactor scram).

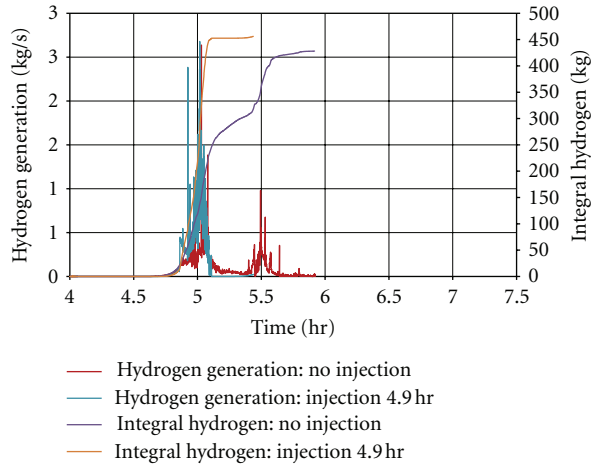

Figure 38: Hydrogen generation rate and integral hydrogen for scenarios without water injection and with water injection at 4.9 hours after scram (all emergency water injection was terminated at 4.2 hours after reactor scram).

What are the general conclusions for severe accident management strategies?

(a) Detailed analysis for realistic bounding scenarios like the station blackout scenario can provide general guidance of timing of important events like core uncovery, loss of control blades, fuel melting, and slumping of molten material into the lower plenum as well as likely consequences such as hydrogen and radionuclide release to the containment.

(1) The likely response of the measureable system parameters including core exit temperatures, pressures, water levels for different accident strategies such as, depressurization, and water addition can be determined on a plant-specific

basis including the influence of uncertainties in models, measurements, and timing of operator actions.

(2) Detailed desktop severe accident simulations for representative plant designs and bounding conditions can be performed in real time to provide guidance to regulatory and other advisory emergency response teams (the RELAP/SCDAPSIM calculations presented in Sections 5 and 6 were performed at 2–5 times faster than real time on a standard Windows laptop computer).

(b) The responses to the accident once the accident is underway can make a significant difference in the consequences of the accident.

(1) Normal emergency procedures that result in termination or limiting of emergency core cooling, that is, the termination of core cooling via the isolation condenser in the case of Fukushima Daiichi Unit 1 and termination of emergency core cooling in the case of TMI-2, need to be reevaluated in light of the potential consequences if instrument readings are faulty or external circumstances change.

(2) Accident management strategies that do not consider, under bounding accident scenarios, the realistic times required for the core (a) to be uncovered and (b) to be damaged (including the failure of control blades and fuel melting) may unnecessarily greatly increase the amount of core/vessel damage without clear benefits in reducing the consequences of the accident. For example, the timing for reactor vessel depressurization once core cooling has been lost or impeded can make a very significant difference in the timing and extent of core damage. Specifically, in a station blackout scenario, premature or early depressurization of the reactor vessel can accelerate the initiation and extent of fuel melting. Delayed depressurization may increase the likelihood of high-pressure vessel ejection and, as demonstrated in the Fukushima Daiichi scenario, can delay or prevent the injection of water into the vessel.

(3) Strategies to inject water into the core should also consider the negative impact of water injection including (a) the accelerated destruction of control blades and other damage to the core (b) and significant increases in the rate, and possibly amount, of hydrogen production.

Acronyms

ISS: Innovative Systems Software
CNSNS: Comision Nacional de Seguridad Nuclear y Salvaguardias
IAEA: International Atomic Energy Agency
SDTP: SCDAP Development and Training Program
KIT: Karlsruhe Institute of Technology
BWR: Boiling water reactor
PWR: Pressurized water reactor
PBF: Power Burst Facility
SDT: Severe Damage Test
ST: Scoping Test
CORA: KIT test facility
Quench: KIT test facility
PHEBUS: Test reactor at Cadarache, France
LOFT: Facility at Idaho National Laboratory
RCS: Reactor coolant system
RPV: Reactor Pressure Vessel
RCIC: Reactor core isolation cooling
CRD: Control rod drive
SRV: Safety relief valve
FP: Fission product
TMI-2: Three Mile Island Unit 2
OECD: Organisation for Economic Co-operation and Development.

References

[1] C. M. Allison and J. K. Hohorst, "SDTP—developing technology for the nuclear industry," in *Proceedings of the 13th International Conference on Nuclear Engineering (ICONE13-50979)*, Beijing, China, May 2005.

[2] http://www.relap.com/.

[3] C. M. Allison and J. K. Hohorst, "Role of RELAP/SCDAPSIM in nuclear safety," *Science and Technology of Nuclear Installations*, vol. 2010, Article ID 425658, 2010.

[4] C. M. Allison, R. J. Wagner, L. J Siefken, and J. K. Hohorst, "The development of RELAP5/SCDAPSIM/MOD4.0 for reactor system analysis and simulation," in *Proceedings of the 7th International Conference on Nuclear Option in Countries with Small and Medium Electricity Grids*, Dubrovnik, Croatia, May 2008.

[5] http://quench.forschung.kit.edu/82.php/.

[6] S. Hagen, P. Hofmann, V. Noack, G. Schanz, G. Schumacher, and L. Sepold, "The CORA-program: out-of-pile experiments on severe fuel damage," in *Proceedings of the 5th International Topic Meeting on Nuclear Thermal Hydraulics, Operations, and Safety*, Beijing, China, April 1997.

[7] D. J. Osetek, "Results of the four PBF severe fuel damage tests," in *Proceedings of the 15th Water Reactor Safety Information Meeting (NUREG/CP-0090)*, Gaithersburg, Md, USA, October 1987.

[8] E. W. Coryell, "Summary of Important Results and SCDAP/RELAP5 Analysis for OECD LOFT Experiment LP-FP-2," Tech. Rep. NUREG/CR/6160, EGG-2721, Nuclear Energy Agency-Committee on the Safety of Nuclear Installations-R, 1994.

[9] RELAP5 Code Development Team, "RELAP5/MOD 3.3 code manual, Vol. 1–8," NUREG/CR-5535/Rev1, December 2001.

[10] SCDAP/RELAP5 Development Team, "SCDAP/RELAP5/MOD3.2 code manual, Vol. 1–5," NUREG/CR-6150, INEL-96/0422, July 1998.

[11] B. Tóth, A. Bieliauskas, G. Bandini et al., "Benchmark study on fuel bundle degradation in the phebus FPT2 test using state-of-the-art severe accident analysis codes," *Nuclear Technology*, vol. 169, no. 2, pp. 81–96, 2010.

[12] C. M. Allison and J. K. Hohorst, "An assessment of RELAP/SCDAPSIM/MOD3.4 using the phebus FPT-2 bundle heating and melting experiment," in *Proceedings of the International Congress on Advances in Nuclear Power Plants (ICAPP '05)*, pp. 3284–3293, American Nuclear Society, Seoul, Republic of Korea, May 2005.

[13] J. H. Spencer et al., "Assessment of new modeling in RELAP/SCDAPSIM using experimental results from the Quench program," in *Proceedings of the International Congress on Advances in Nuclear Power Plants (ICAPP '11)*, Nice, France, May 2011.

[14] C. M. Allison, "Recent improvements in RELAP/SCDAPSIM/MOD3.4 resulting from QUENCH and PARAMETER bundle heating and quenching experiments," in *Proceedings of the 8th International Conference of Nuclear Options in Countries with Small and Medium Electricity Grids*, Dubrovnik, Croatia, 2010.

[15] S. Hagen, P. Hofmann, V. Noack, L. Sepold, G. Schanz, and G. Schumacher, *Large Bundle PWR Test CORA-18: Test Results*, Forschungszentrum Karlsruhe—FZKA-6031, 1998, http://www.cfn.kit.edu/.

[16] P. Hofmann, "Metallographic examination of the severe fuel damage scoping test (SFD-ST) fuel rod bundle cross sections," NUREG/CR-5119, EGG-2537, 1988.

[17] A. Stefanova et al., "SARNET benchmark on QUENCH-11—final report," Forschungszentrum Karlsruhe—FZKA 7368, 2008, http://quench.forschung.kit.edu/82.php.

Hindawi Publishing Corporation
Science and Technology of Nuclear Installations
Volume 2012, Article ID 305405, 8 pages
doi:10.1155/2012/305405

Research Article

Simulation of the Lower Head Boiling Water Reactor Vessel in a Severe Accident

Alejandro Nuñez-Carrera,[1] Raúl Camargo-Camargo,[1] Gilberto Espinosa-Paredes,[2] and Adrián López-García[1]

[1] *Comisión Nacional de Seguridad Nuclear y Salvaguardias, Dirección General Adjunta de Seguridad Nuclear, Doctor Barragán 779, Col. Narvarte, 03020 México DF, Mexico*
[2] *Área de Ingeniería en Recursos Energéticos, Universidad Autónoma Metropolitana-Iztapalapa, Avenida San Rafael Atlixco 186, Col. Vicentina, 09340 México DF, Mexico*

Correspondence should be addressed to Raúl Camargo-Camargo, rcamargoc@cnsns.gob.mx

Received 30 December 2011; Revised 14 April 2012; Accepted 25 May 2012

Academic Editor: Lluís Batet Miracle

The objective of this paper is the simulation and analysis of the BoilingWater Reactor (BWR) lower head during a severe accident. The COUPLE computer code was used in this work to model the heatup of the reactor core material that slumps in the lower head of the reactor pressure vessel. The prediction of the lower head failure is an important issue in the severe accidents field, due to the accident progression and the radiological consequences that are completely different with or without the failure of the Reactor Pressure Vessel (RPV). The release of molten material to the primary containment and the possibility of steam explosion may produce the failure of the primary containment with high radiological consequences. Then, it is important to have a detailed model in order to predict the behavior of the reactor vessel lower head in a severe accident. In this paper, a hypothetical simulation of a Loss of Coolant Accident (LOCA) with simultaneous loss of off-site power and without injection of cooling water is presented with the proposal to evaluate the temperature distribution and heatup of the lower part of the RPV. The SCDAPSIM/RELAP5 3.2 code was used to build the BWR model and conduct the numerical simulation.

1. Introduction

The loss of coolant in nuclear reactors during scenarios such as operation at full or low power, shutdown, and refueling can cause excessive heatup of the nuclear fuel; this is a beyond design basis accident where the core meltdown is the main focus. The slump of the molten core into the lower head of the Reactor Pressure Vessel (RPV) may produce the failure of it. The accident in Unit 2 of Three Mile Island (TMI-2) in 1979 was an accident with core melt but without failure of the RPV and with intact containment; therefore, the radiological consequences were negligible. The studies of severe accident are oriented into two branches: In-vessel and Ex-vessel where the failure of the RPV or ruptures in some pipes, such as the main steam lines, recirculation pipes, or feed water among others, is the interface parameter. The In-vessel phenomena include the thermal-hydraulics with natural circulation, reflooding, and refilling of the core at high temperature, oxidation of the cladding, hydrogen production, relocation of the molten core into the lower plenum of the RPV, liquefaction of control rods, recriticality, and failure of the reactor vessel. The Ex-vessel phenomena involve steam explosion, melt dispersion, fission products transport and deposition on structures and components, direct containment heating (DCH) among others [1]; evolution and management of severe accident dependent of the RPV failure, but the uncertainty in the modeling of the phenomenon in bottom of the RPV is very high.

Dupleac et al. [2] developed a detailed model of the bottom of the calandria for the CANDU 6 plant with COUPLE computer code. The objective of the work was the study of In-vessel corium retention by external vessel cooling as a series of strategies adopted in severe accident management guidelines (SAMGs) for CANDU reactor. In the work of Bishnoi and Gupta [1], the containment importance

during a severe accident, in particular for Pressurized Water Reactor (PWR), is analyzed.

Spengler et al. [3] assess with ASTEC V1 computer code the molten corium-concrete interaction (MCCI) in the pressurized water reactor (PWR). This phenomenon occurs after the failure of the reactor vessel with large amount of molten corium into the reactor cavity. The heat transfer model between melt and concrete is analyzed taking experiments as a reference.

The accident occurred in Fukushima Daiichi Nuclear Power Station on March 11, after an earthquake and tsunami, caused that all of the operating units (units 1, 2, and 3) have fuel damage due to the loss of cooling. Conservative calculations indicate that most of the cores of those units are damaged, and some of the fuel is relocated in the bottom head of the RPVs, although this has not been confirmed. Core cooling was eventually established when reactors pressure lowered enough and a fire engine was used to inject fresh water, followed by seawater [4]. The lack of core cooling to compensate for decay heat resulted in excessive fuel temperatures and oxidation of the zirconium cladding. The oxidation of zirconium in a steam environment will create significant additional heat from the exothermic reaction and large quantities of hydrogen. This hydrogen contributed to the increases in containment pressure and to the subsequent hydrogen explosions on units 1, 3, and 4. There is no real indication of the failure of the bottom of the RPVs, but some of the nozzles of the reactor vessels probably have some leakage.

Recently Ahn and Kim [5] made a comparison between three computer codes with the capability to simulate the reactor vessel lower head. The codes analyzed by these authors are MELCOR, SCDAP/RELAP5, and MAAP4. The capabilities of these codes in predicting core melt accident progression and lower head response differ substantially at each phase of the lower plenum accident progression, due to the different modeling assumptions involved in various initial and boundary conditions, different debris bed configurations and heat transfer correlations, different model parameters, and numerical schemes. Among the main conclusion of their work is that the lower head models employed in the representative US computer codes are rather simple, parametric, and depend greatly on user-specified inputs with a wide range of possibilities, especially for core material relocation (e.g., MELCOR, SCDAP/RELAP5) and debris bed thermal behavior (e.g., MAAP4, SCDAP/RELAP5) in the presence of water coolant in the lower plenum.

A large Loss of Coolant Accident (LOCA) without injection of cooling water due to the failure of the Emergency of Core Cooling Systems (ECCS) is considered. This is a hypothetical scenario in order to cause the core melt rapidly and observe the heating up of the bottom of the RPV and the slump of the core. The primary containment is simulated with boundary conditions, and external cooling of the reactor vessel is not considered. In this work, we present a model of a BWR RPV and its lower head with COUPLE and RELAP5 computer codes. SCDAPSIM/RELAP5 [6, 7] code links COUPLE and RELAP5 to simulate the heat and mass between the model of the RPV and the model of the bottom of the RPV. We found that the SCDAPSIM/RELAP5 fails to converge when an important amount of molten material slumps into the lower head of the RPV due to the abrupt change in the temperature in the lower cavity of the reactor.

2. Reactor Model

The model of RPV used to simulate the large LOCA is a typical BWR-5 with Mark II containment and is shown in Figure 1 [8]. The SCDAPSIM/RELAP5 computer code was used to simulate the severe accident [6]. In this model, the feedwater (FW), turbine, suppression pool, Control Rod Drive system (CRD), and Emergency Cooling systems (ECCS) such as Low Pressure Core Spray system (LPCS), High Pressure Core Spray system (HPCS), Low Pressure Injection system (LPCI) are represented by boundary conditions along with the Reactor Core Isolation Cooling system (RCIC). Four fuel rods channels (320, 321, 322, and 323) represent the reactor core; each fuel rod is nodalized with twelve axial nodes to model heat transfer and mass distribution in the core. Boundary conditions that represent the primary containment at constant pressure are fixed to simulate the break in the recirculation loop with the time-dependent volumes TDV-998 and TDV-999 that are connected to the valves V-487 and V-484, respectively. These valves are used to simulate breaks in the recirculation lines and they open instantly.

2.1. Features of COUPLE Computer Code. COUPLE [7] is a two-dimensional, finite element, steady-state, and transient heat conduction computer code. This code is used to calculate the heating of the reactor core material that slumps into the lower head of the reactor vessel and is subsequently represented as debris. The computer code takes into account the decay heat and initial internal energy of slumped debris and then calculates the transport by conduction of this heat in the radial and axial directions to the wall structures and the water surrounding the debris. The most important application of the code is the calculation of the heatup of the vessel wall so that the time at which the vessel may rupture can be determined. COUPLE includes the modeling of the following phenomena and conditions: (a) spatially varying porosity, (b) thermal conductivity of porous material, (c) a debris bed whose height grows sporadically with time, (d) radiation heat transfer in a porous material, and (e) natural circulation of melted debris. The limitations of this model are (a) molten material does not flow into an adjacent porous region (this is an important limitation because the calculations of the degradation of the fuel and structure elements can change significantly); (b) oxidation does not occur in the debris bed; therefore, the contribution to the total heat balances is lower and the time of the failure of the reactor vessel could be delayed; (c) fission products release does not occur in the debris bed; therefore, the contribution to the source term is lower than the real. The external cooling of the reactor vessel by flooding of the primary containment is a scenario that is possible to simulate with COUPLE.

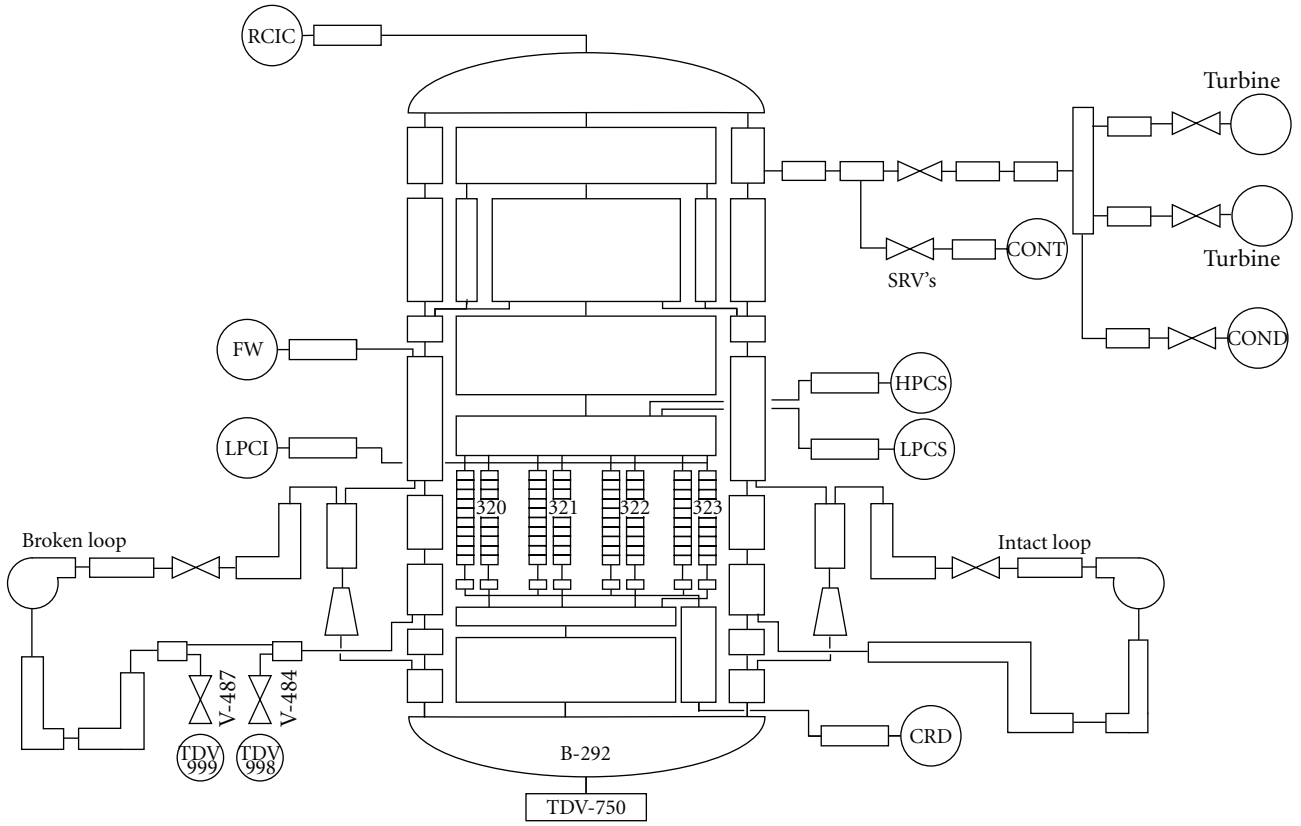

Figure 1: SCDAPSIM model of a BWR.

2.2. Model of the Lower Head of the BWR. To simulate the heatup of lower head of the BWR due to the slump of the molten material, a two-dimensional model using COUPLE [6] was developed. The lower head of the vessel is divided in 150 volumes, and each volume is surrounded by 4 nodes of the mesh (Figure 2). The control volumes and the nodes are monitored during the progression of the accident with three parameters, temperature, amount of molten material, and heat transfer. The model developed for BWR consists of 11 nodes in the axial direction by 16 in the radial direction; this nodalization is enough to conduct a detailed study of the lower head of the vessel during a severe accident.

The first 10 volumes represent the outer surface of the reactor vessel insulator, while the volumes 11 to 30 represent the wall thickness carbon steel of the vessel. The volumes 31 to 40 correspond to the 0.0032 m thick liner of stainless steel. The remaining nodes correspond to the internal volume of the lower head of the RPV. The volume B-292 of the BWR model (Figure 1) is connected to the COUPLE model to calculate the heat and mass transfer from the vessel. An additional time-dependent volume TDV-750 is used to simulate the heat transfer from the lower head of the vessel to the dry well of the primary containment.

The test problems used for the validation of the COUPLE model show that the heat transfer from the molten pool to the lower head is adequate using a relative coarse nodalization in the lower head; a mesh width about one-third of the thickness of the wall of the lower head is accurate enough [9]. This criterion is used in the nodalization of the lower head of the BWR that is presented in this work.

3. Accident Sequence

In this work, a simulation of a postulated LOCA at 100% of full power with simultaneous loss of off-site power and without injection of cooling water from the ECCS is presented (the main events occurred are presented in Table 1). This hypothetical scenario has the objective of a fast degradation of the core in order to observe the slump of molten material in the bottom of the reactor vessel. The external cooling of the reactor vessel by flooding of the primary containment is not considered so as to accelerate the heatup of the bottom of the reactor vessel. Due to the loss of off-site power, the control valves of the turbine close very fast and the recirculation pumps trips in order to avoid the increase of power due to the void fraction collapse.

The lack of cooling in the reactor core causes a high temperature due to decay heat and zircaloy oxidation; therefore, the control rods and the fuel bundles loss their geometry. The molten corium is relocalized in a cooler region of the core forming a thin crust that fails due to gravity forces and high temperature; therefore, the molten pool falls in the bottom of the reactor vessel increasing the temperature of the lower head. In this accident sequence, the fuel rods experience melting and slumping of the cladding, the bed of debris is formed when some drops of corium fall and are

Table 1: Main events of the accident sequence during the simulation of a large LOCA with simultaneous loss off-site power and failure of the ECCS.

Time (s)	Event
0	Reactor is operating at steady state condition at 100% of power
20	Guillotine rupture in the recirculation line and loss of AC Power Scram of the reactor Trip of all feedwater pumps No injection of the ECCS is assumed
21	Vessel water level reaches level 4 (low level)
30	Feedwater flow decreases to zero
22	Vessel water level reaches level 3 (low level)
24	Vessel water level reaches low-low water level (level 2). Main steam isolation valves (MSIV) close
27	Vessel water level reaches low-low-low water level (level 1). Second signal to start LPCI and LPCS due to low water level, but all the ECCSs are considered out of order
510	The meltdown begins when the region of the core exceeds the temperature for eutectic melting of stainless steel clad control rods with B_4C (boron carbide) absorber material. This temperature is about 1,500 K
682	Some drops of corium fall in the lower region of the core and are quenched
1570	An important amount of molten corium starts to form the molten pool
2300	The reactor core reaches the highest temperature (3000 K, fuel bundle 323, axial node 1). The radius of the molten pool is 1.22 m. Volume of molten pool is 3.81 m^3
2320	The most important amount of melt material slump in the lower head of the vessel when the crust fails, this is observed in the highness of the bed debris that increases 0.40 m in about 100 s. The radius of the molten pool is 0.82 m, and its volume is one third lower.
2590	Volume of molten pool is 1.16 m^3 with a temperature of 2873 K (fuel bundle 322, axial node 10). The total mass of UO_2 in the pool is 8770 kg. The code crashed before RPV failure

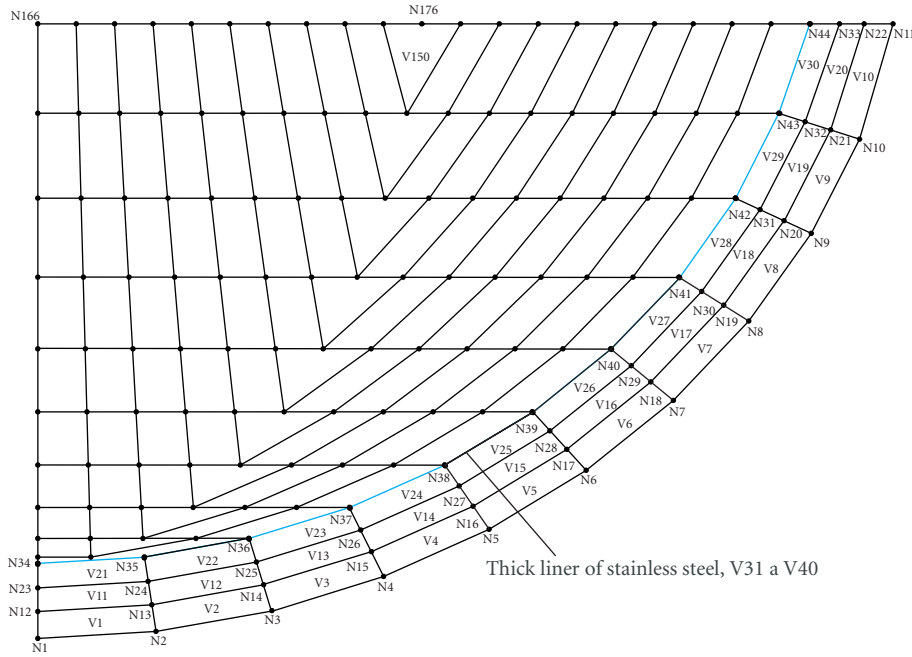

Figure 2: Model of the bottom of the reactor vessel for COUPLE computer code.

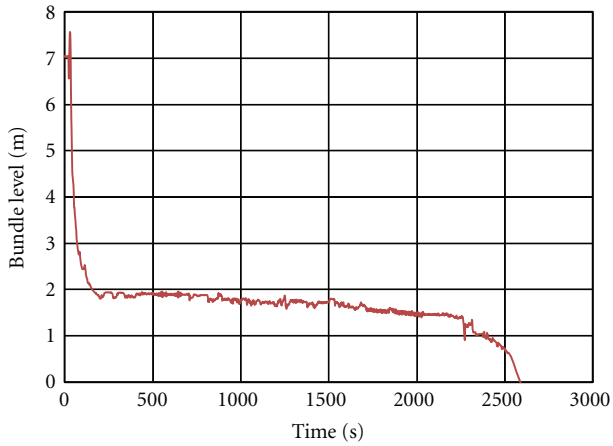

Figure 3: Level of coolant water in the fuel bundles.

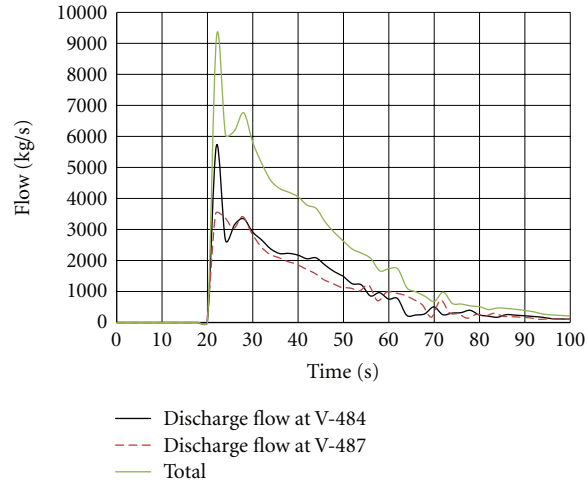

Figure 4: Discharge of coolant flow into the containment from the recirculation broken loop.

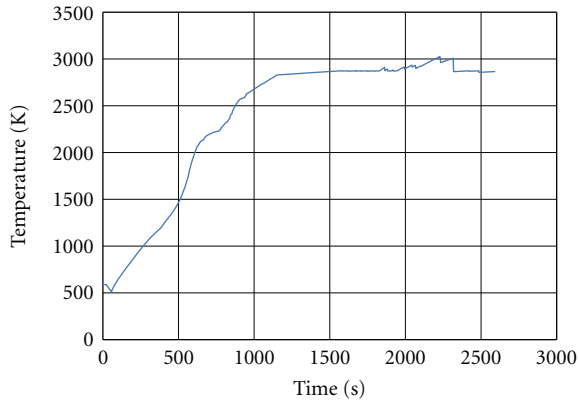

Figure 5: Maximum cladding temperature.

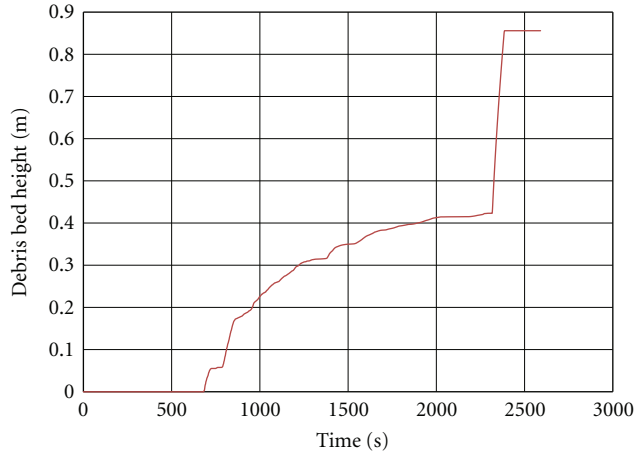

Figure 6: Debris bed height (in COUPLE mesh).

quenched by the water that remains in the lower part of the vessel; therefore, the height of the bed debris is increasing during the simulation of the accident.

The failure of the reactor vessel is not observed in this simulation due to the fact that the code crashes because of large amount of corium slumped in the lower plenum. These sudden changes in temperature produce a failure in the computer code to converge.

4. Results and Discussion

The numerical results of the simulation of a LOCA at 100% of full power with simultaneous loss of off-site power and without injection of cooling water from the ECCS are presented in this section. The large LOCA occurs at 20 s with simultaneous loss of off-site power and without injection of cooling water. Figure 3 shows the fall of water level in the fuel bundles; this quick decrease of cooling water inventory produces the increase of the temperature of the fuel bundles. The bottom of active fuel (BAF) water level is reached at 40.3 s, and it is evaporated after the slump of the molten material into the lower head at 2,590 s. Figure 4 shows the discharge of liquid to the primary containment after the break of the recirculation pipe through valves V-484 and V-487 and the total discharge flow.

The failure of the ECCS and the oxidation of the Zircaloy increase rapidly the temperature of the core. Figure 5 shows the maximum temperature in the core as a function of time. The meltdown begins when the region of the core exceeds the temperature for eutectic melting of stainless steel clad control rods with B4C absorber material; this temperature is about 1,500 K and is reached in 510 s.

In this accident sequence, the fuel rods experience cladding melting and slumping; on the other hand, the debris bed is formed due to the failure of the crust of the molten pool, and when some drops of corium fall and are quenched by the water that remains in the lower part of the vessel or are relocated in cooler regions, forming solid particles (debris) that start to deposit in the lower head of the vessel. Figure 6 shows the formation of the debris bed at 688 s.

The molten material does not slump immediately from the core region to the lower head of the vessel. The molten material moves into a colder region and freezes forming a crust that surrounds a pool of molten material known as the "molten pool." The molten pool material freezes because the solidification temperature is much higher than

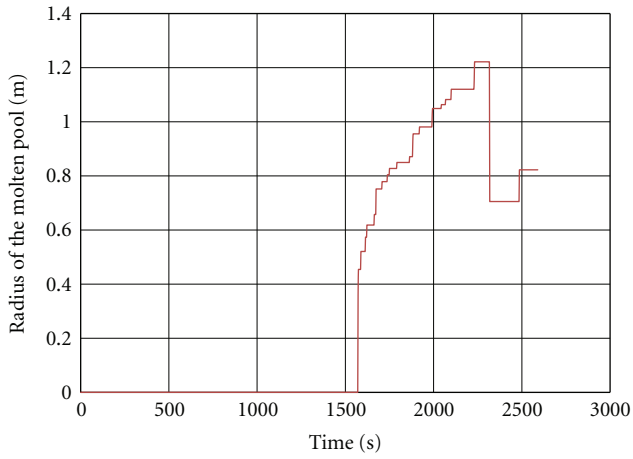

Figure 7: Radius of the molten pool. The failure of the crust is observed at 2320 s.

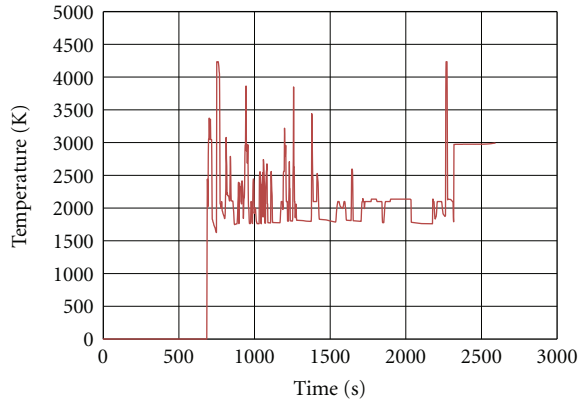

Figure 8: Maximum debris bed temperature in COUPLE mesh.

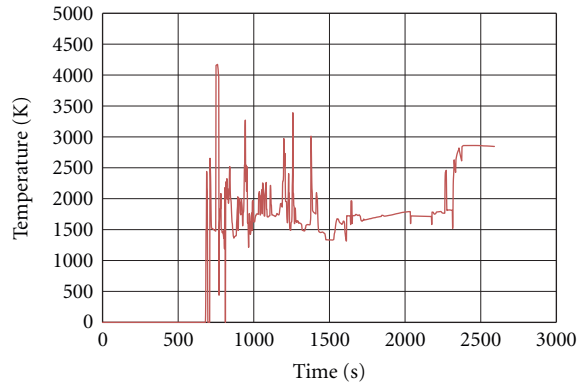

Figure 9: Average debris bed temperature (in COUPLE mesh).

the liquefaction temperature of the structure, but as the liquefaction continues, the pool may melt the material that provides support and a large amount of molten material may suddenly slump into the reactor vessel lower head.

The feature of the COUPLE assumes a homogeneous temperature distribution over the entire region of the molten pool, taking into account the effect of thermal mixing and turbulent natural convection in the molten pool [5, 10]. The crust of solidified material is unstable due to contact with the molten pool on one side and liquefied structural material on the other side. After the thickness of the region of liquefied structural material has increased to a certain value, the crust may break up, releasing the molten corium into the lower head of the RPV. The user of the code defines the thickness of the liquefied structural material at which the crust breaks up, in this case a default value of 0.001 m was chosen.

The molten pool starts to form at 1570 s (see Figure 7). Table 2 summarizes the in-core molten pool conditions at the final stages of the simulation (2,590 s). At 1,800 s, the radius of the molten pool deposited in the lower core region is 0.84 m, with a volume of 1.28 m^3 and a temperature of 2,870 K. The temperature in the core is increasing and the molten pool still growing due to the slump of molten material. At 2,300 s, the molten pool reaches the higher radius of 1.22 m (Figure 7) with a volume of 3.81 m^3 and a temperature of 3,000 K. At 2300 s, the core reaches the highest temperature, 3000 K in the fuel bundle 323 (bottom axial node).

The total oxidation heat generation in this time is 4.14×10^5 W (1.8% of residual heat), and the total mass of the UO_2 in the molten pool is 2.7×10^4 kg (66.4% of the total UO_2 in the core). At 2,320 s, the most important amount of molten material slumps into the lower head of the vessel; this is observed in the height of the debris bed that increases 0.40 m in about 100 s (Figure 6) due to the failure of the crust at the bottom of the molten pool. The rupture of the crust reduces the radius of molten pool from 1.12 m to 0.82 m, and its volume drops by one-third. At the end of simulation, the height of the bed of molten material in the lower head reaches 0.85 m (after 2,590 sec) as can be seen in Figure 6, with an average temperature of 2850 K (Figure 8).

The maximum temperature of the debris is reached at 750 s with a temperature of 4,230 K, and another important peak is observed at 2300 s with a temperature of 4,230 K as can be observed in Figure 8. The first peak corresponds to the slump of debris into the lower head, and the second one is caused by "molten pool" crust breakup, when the most important amount of molten material and debris slumps into the lower head of the vessel. The average temperature (Figure 9) and maximum temperature of the debris show important oscillations that correspond to the moment of the slump of molten material and debris that are deposited in the lower head during the degradation of the core and then freezes. Successive chunks of molten material and debris fall into the lower head. Some additional large oscillations are caused by numerical instabilities of the code: this is clearly observed in Figure 9, where the average debris bed temperature reaches a temperature of 0 K at 772 s, this is an important handicap of SCDAPSIM/RELAP5.

A picture of the lower head of the RPV obtained with COUPLE at 2,300 s is shown in Figure 10, just before of the failure of the crust that supports the molten pool. It is observed that the liner of stainless steel and the inner face of the vessel of carbon steel reach a temperature about 1078 K; this temperature is not high enough to provoke a failure of

Table 2: Conditions of in-core molten pool during the accident sequence.

Parameter	Time (s)							
	1,800	1,900	2,000	2,100	2,200	2,300	2,500	2,590
Effective radius of molten pool (m)	0.84	0.95	1.04	1.12	1.12	1.22	0.82	0.82
Temperature of molten pool (K)	2,870	2,872	2,897	2,919	3,003	2,999	2852	2858
Volume of molten pool (m^3)	1.28	1.82	2.41	2.94	2.94	3.81	1.16	1.16
Total mass of UO_2 in pool (kg)	9,220	1.29×10^4	1.70×10^4	2.09×10^4	2.09×10^4	2.67×10^4	8,770	8,770
Total mass of metallic Zr (kg)	0	131.0	378.0	378.0	378.0	989.0	334.0	335.0
Mass of liquefied material in partial liquefied porous debris (kg)	6,080	5,780	6,460	7,310	1.06×10^4	1.0×10^4	8,750	1.19×10^4
Total hydrogen production rate (kg/s)	0.083	0.0256	0.015	0.00736	0.0191	0.00279	0.00484	0.0650

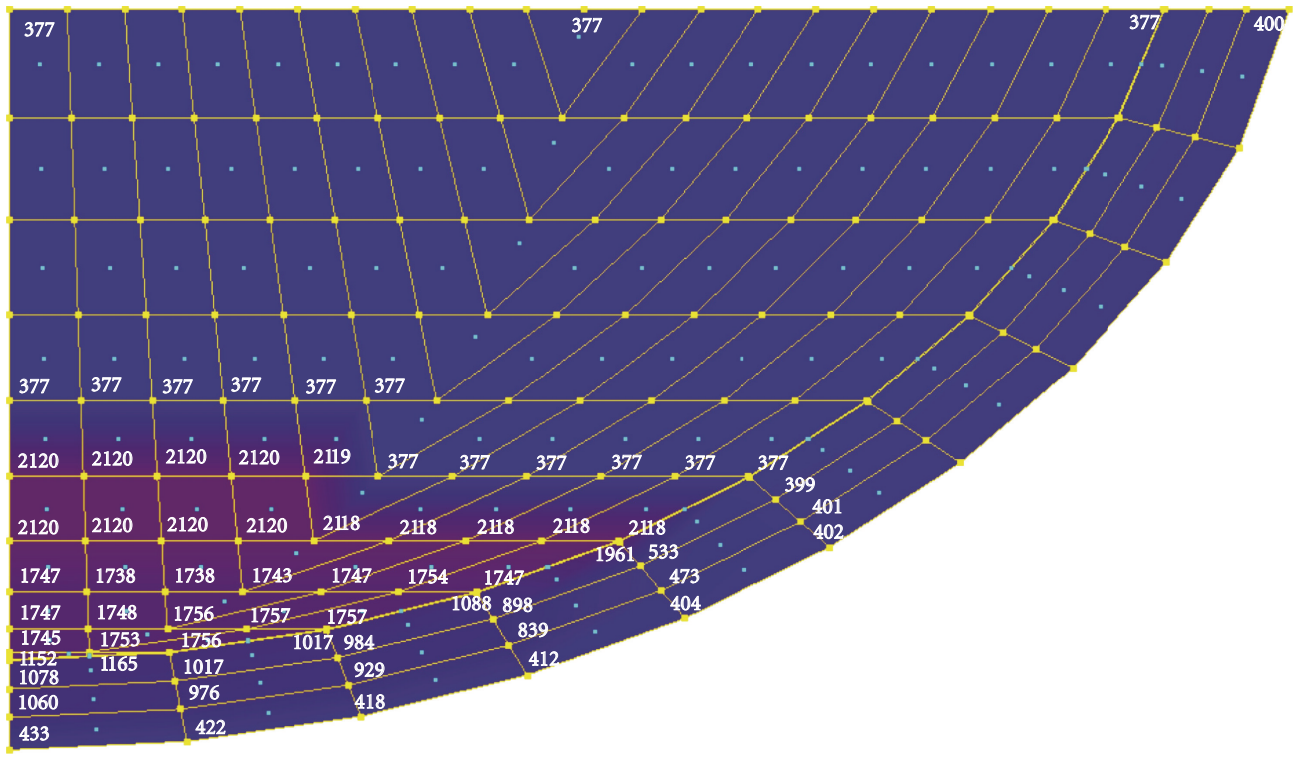

Figure 10: Temperature distribution in lower head of the RPV just before the failure of the crust at 2,300 s.

the wall of the reactor vessel. In this time step, the total mass of metallic UO_2 in the molten pool is 2.67×10^4 kg and the total mass of metallic Zr is 989 kg (see Table 2); on the other hand, the combination of UO_2 and Zr form an alloy that may produce a high thermal load in the crust until its failure. In this picture, the temperature of the debris in the lower head has a temperature of 2120 K.

The molten pool falls into the lower head after the rupture of the crust, which increases the debris temperature to 3000 K and provokes sudden changes in the mass inventory and temperature producing a failure in the computer code to converge due to the fast change in the thermodynamics properties of the steam and water. The temperature of the wall of the reactor vessel is 1756 K, which is beyond the melting point of the stainless steel and carbon steel (1723 K); therefore, the failure of the wall of the lower head is probable but not observed.

The same scenario was simulated using COUPLE with user-defined slumping (simplified option model of SCDAPSIM/RELAP5) for 6,000 s. This simulation did not present problems when the molten material slumps into the lower head of the vessel (2,300 s) and the simulation ended successfully. Figure 11 shows the debris temperature (maximum and average) using SCDAPSIM/RELAP5 with user-defined slumping option, where the failure of the crust and the increment of the temperature in the debris are observed at 2,320 s; the shape of the curve is smooth without the large numerical oscillations that can be observed in Figures 8 and 9.

The same behavior is observed in Figure 12, where temperature in the wall of the lower head of the vessel (nodes 16 and 17 of COUPLE mesh) is without the large numerical oscillations. The temperature of the wall of the vessel can be obtained by monitoring nodes of the COUPLE

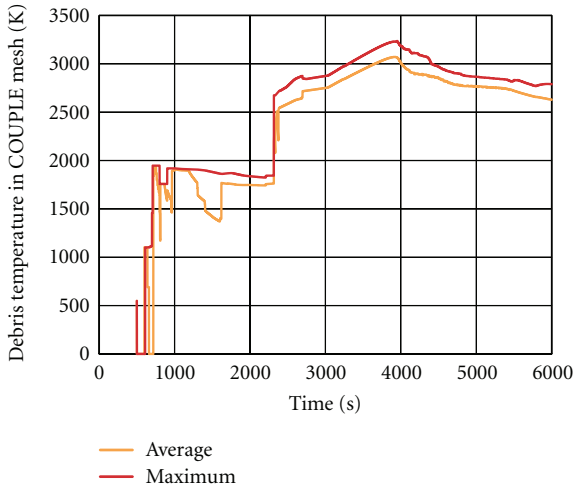

Figure 11: Debris temperature obtained with COUPLE with user-defined slumping.

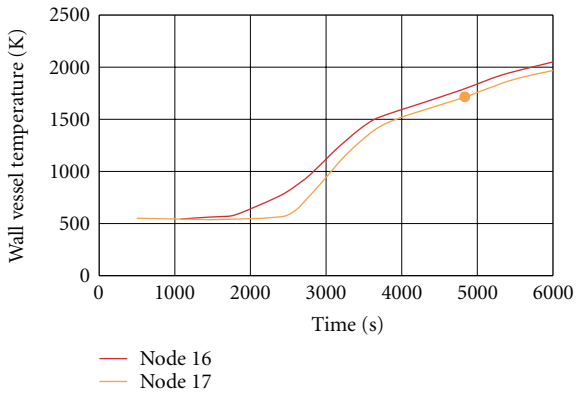

Figure 12: Wall vessel temperature with COUPLE with user-defined slumping. The red dot represents the failure temperature of the lower head of the reactor vessel.

mesh from nodes 12 to 44. The melting temperature of the carbon steel, 1723 K, is reached from 4460 to 4837 s in the outer surface of the wall, according with the simulation of COUPLE without coupling RELAP5 and SCDAP, this is represented in Figure 12 by a red dot.

5. Conclusions

A model of the reactor vessel lower head with SCDAP-SIM/RELAP5 computer code for a BWR is presented. This model was tested with an accident sequence that contemplates a LOCA with failure of the ECCS in order to cause a fast degradation of the core due to lack of cooling water. The SCDAPSIM/RELAP5 has the capability to predict the melting of the core, control rod, and some structures, with an estimation of the main parameter of the molten pool until the failure of the crust. However, SCDAPSIM/RELAP5 computer code presented a problem with the sudden changes in the mass inventory and temperature after the breakup of the crust due to the rapid change in the thermodynamics properties in the steam and water that remains in the vessel lower head. Figures 10 and 11 show that SCDAP-SIM/RELAP5 with user-defined slumping option does not report any problems in the simulation of a LOCA for long-term; therefore, the main conclusion is that for long-term simulation where the degradation of the vessel lower head should be observed, the use of COUPLE under this option is highly recommended.

References

[1] L. R. Bishnoi and S. K. Gupta, "Issues on containment integrity during severe accidents," in *Proceedings of the 2nd International Conference on Reliability, Safety & Hazard (ICRESH '10)*, pp. 300–305, IEEE, December 2010.

[2] D. Dupleac, M. Mladin, H. Prisecaru, and G. Negut, "SCDAP-SIM/RELAP5 investigation on in-vessel corium retention for CANDU 6 plant," in *Proceedings of the International Congress on Advances in Nuclear Power Plants (ICAPP '10)*, pp. 1105–1111, San Diego, Calif, USA, June 2010.

[3] C. Spengler, H.-J. Allelein, M. Cranga, F. Duval, and J.-P. Van Dorsselaere, "Assessment and Development of Molten Corium Concrete Interaction Models for the Integral Code ASTEC," Forum Eurosafe, Bruxelles (BELGIQUE), 2005.

[4] INPO 11-005, "Special report on the nuclear accident at Fukushima Daiichi Nuclear Power Station," Rev. 0. 2011.

[5] K. I. Ahn and D. H. Kim, "A state-of-the-art review of the reactor lower head models employed in three representative U.S. severe accident codes," *Progress in Nuclear Energy*, vol. 42, no. 3, pp. 361–382, 2003.

[6] C. M. Allison, G. M. Berna et al., "SCDAP/RELAP5 Users Guide and Input Manual," En, NUREG/CR-6150 EGG-2720. USA, Idaho National Engineering Laboratory, Vol. 3, 1998.

[7] C. M. Allison et al., "SCDAP/RELAP5/MOD 3.2 code manual volume II: damage progression model theory," Tech. Rep. NUREG/CR-6150 INEL-96/0422, Idaho National Engineering and Enviromental Laboratory, New York, NY, USA, 1997.

[8] G. Espinosa-Paredes and A. Nuñez-Carrera, "SBWR model for steady-state and transient analysis," *Science and Technology of Nuclear Installation*, vol. 2008, Article ID 428168, 18 pages, 2008.

[9] C. M. Allison et al., "SCAP/RELAP5/MOD3.1 code manual, volume 5a: appendix A-SCDAP/RELAP5/Mod 3.2 assessment," Tech. Rep. NUREG/CR-6150, EGG-2720, INEL, New York, NY, USA, 1993.

[10] "RELAP5/MOD3 code manual, models and correlations," Tech. Rep. NUREG/CR-5535, vol. 4, USNRC, 1995.

Hindawi Publishing Corporation
Science and Technology of Nuclear Installations
Volume 2012, Article ID 487371, 10 pages
doi:10.1155/2012/487371

Research Article

Failure Assessment Methodologies for Pressure-Retaining Components under Severe Accident Loading

J. Arndt, H. Grebner, and J. Sievers

Reactor Safety Research–Barrier Effectiveness, Gesellschaft für Anlagen- und Reaktorsicherheit (GRS) mbH, Schwertnergasse 1, 50667 Cologne, Germany

Correspondence should be addressed to J. Arndt, jens.arndt@grs.de

Received 16 December 2011; Accepted 27 March 2012

Academic Editor: Lluís Batet Miracle

During postulated high-pressure core melt accident scenarios, temperature values of more than 800°C can be reached in the reactor coolant line and the surge line of a pressurised water reactor (PWR), before the bottom of the reactor pressure vessel experiences a significant temperature increase due to core melting. For the assessment of components of the primary cooling circuit, two methods are used by GRS. One is the simplified method ASTOR (approximated structural time of rupture). This method employs the hypothesis of linear damage accumulation for modeling damage progression. A failure time surface which is generated by structural finite element (FE) analysis of varying pressure and temperature loads serves as a basis for estimations of failure times. The second method is to perform thermohydraulic and structure mechanic calculations for the accident scenario under consideration using complex calculation models. The paper shortly describes both assessment procedures. Validation of the ASTOR method concerning a large-scale test on a pipe section with geometric properties similar to a reactor coolant line is presented as well as severe accident scenarios investigated with both methods.

1. Introduction

In face of severe accident scenarios with melted core material which occurred recently at Fukushima Daiichi and in 1979 at Three Mile Island-2 the integrity assessment of primary circuit components requires a special concern. A best estimate simulation of components under severe accident loading scenarios may be complex and time consuming (see second part of the paper). For the accomplishment of a simplified analysis concerning integrity of the components during a severe accident and especially the question which component fails first in framework of thermohydraulic analysis with system codes, an efficient method has been developed which will be described in the following chapters.

2. Method ASTOR

The method ASTOR is an easy applicable tool for fast estimation of failure times. Furthermore the reduced complexity enables the integration into thermohydraulic codes and may help to find results of structure mechanical properties which are required for coupled calculation of mechanical and thermohydraulic structure characteristics of primary circuit devices. Moreover the method ASTOR helps to determine the degree of structural damage after a history of load at the actual point of time. Therefore it is possible to determine the remaining durability of components under the assumption that the actual loads will continue at a constant level. The method ASTOR can be employed for failure time calculation without time intensive nonlinear structure-mechanical analysis. The analysis requires a suitable failure time surface. The method ASTOR published already in [1] has been developed further to have more accurate results. In the following the method and the further development will be displayed. During a high-pressure core melt accident a transient temperature and pressure load will occur on the inner surface of a pipe (see Figure 1). The load can be characterized by a range of temperature and pressure.

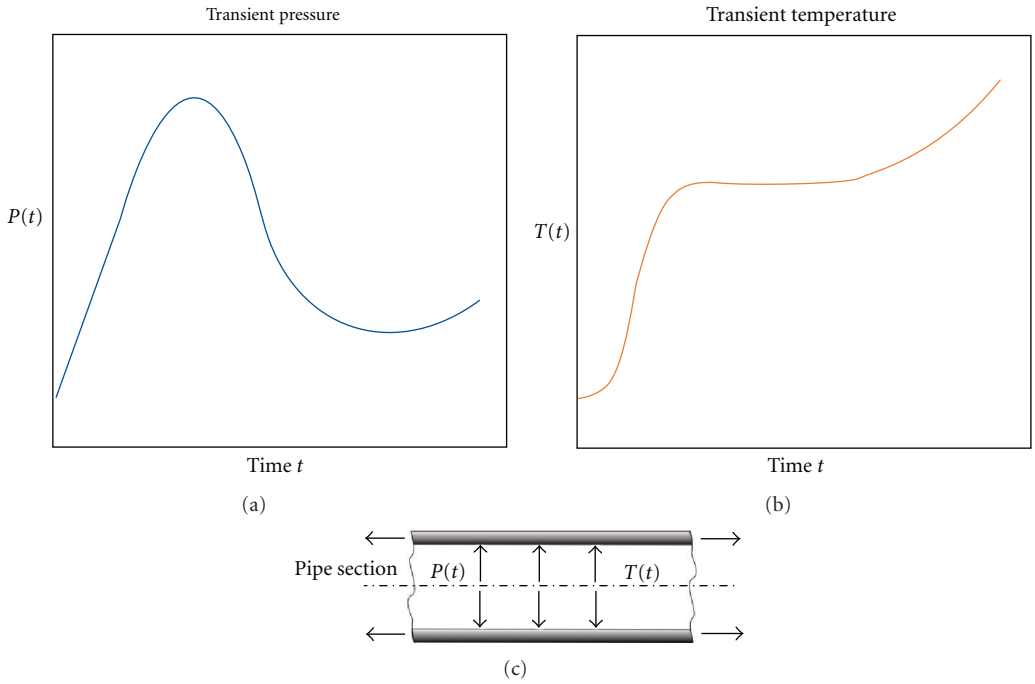

Figure 1: Transient loads on pipe.

Within the defined ranges, cascaded pressure steps and temperature steps are defined. Failure times of the pipe structure under combinations of pressure steps and temperature steps are determined by finite element analysis with the FE-program ADINA [2].

Performing several numerical analyses of this kind to cover the ranges of temperatures and pressures to be expected in an accident yields a series of structural failure times which can be regarded as discrete pivots of a continuous failure time surface in the failure time-temperature-pressure space (see Figure 2). In the next step of the procedure, the failure time surface is used in connection with some damage accumulation hypothesis to predict the time to failure of the structure when subjected to loads which are varying in time. In these cases the characterizing parameters, that is, inner surface temperature and internal pressure, do change in the course of time. For each point of time which is characterized by a temperature and a pressure value, a damage increment can be calculated. The result of the summation of damage increments is a damage value $D(t)$. The failure can be assumed when the damage value $D(t)$ reaches a value of 1 or a smaller value if safety factors are included.

In the framework of further development, a time-consuming method for the determination of failure surfaces has been developed. The chain of software modules consists of three modules. The first module provides a file structure and builds up the framework for forthcoming FE analysis and failure assessment. The module requires input data about FE geometry, material data, data about failure assessment, and information about the number of nodes of the failure surface. After each simulation run, a failure assessment is accomplished by a software module. Failure

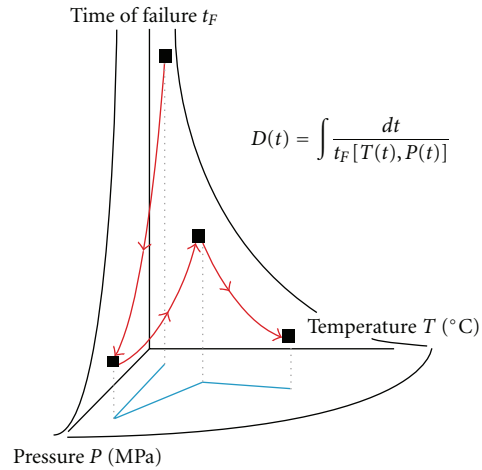

Figure 2: Linear damage accumulation hypothesis in ASTOR.

criteria for plastification and creep failure are used for failure assessment. After all simulation runs and failure assessments are accomplished, a final software module collects all available output and failure data for compilation of the input file for analysis by ASTOR.

3. Material Data and Approximation of Creep Curves

Bases for the temperature-dependent stress-strain-relations of the piping material steel 20 MnMoNi 55 used in German NPPs are data measured by the testing facility "Materialprüfungsanstalt (MPA)" of the University of Stuttgart

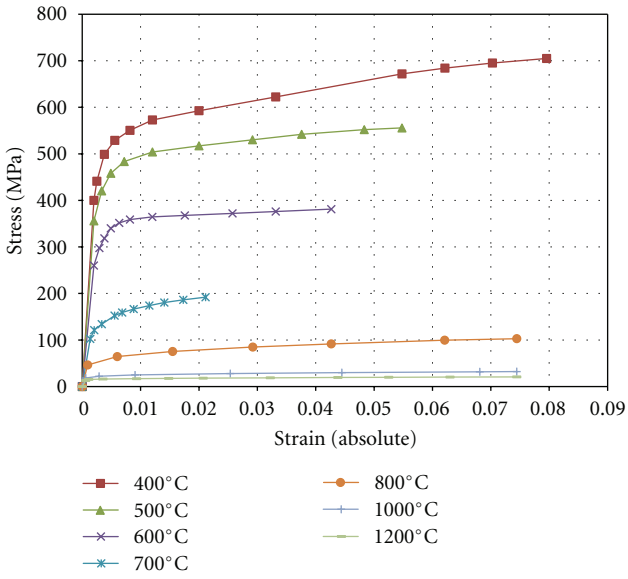

Figure 3: Steel 20 MnMoNi 55: true stress-strain curves up to uniform elongation (400°C–1200°C) derived from measured data.

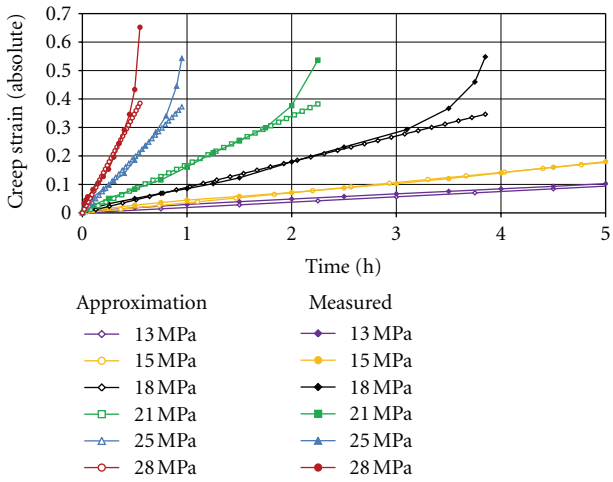

Figure 4: Linear approximation of measured creep curves (load controlled) of steel 20 MnMoNi 55 at 1000°C.

[3, 4]. Temperature-dependent stress-strain curves were derived for the temperatures up to 1200°C (Figure 3) to build up the basis for the material model of the FE-Program ADINA [2].

For the simulation of creep behaviour of components, the FE-codes usually include material models which describe the time dependence of creep strain with parameters stress and temperature. On the other hand the material characterisation is usually determined by load-controlled creep curves. Exemplary in Figure 4, the approximation of load-controlled creep curves for a temperature level of 1000°C is displayed.

For modeling of creep properties of the steel 20 MnMoNi 55, a "Creep Law" of the FE program ADINA [2] was employed:

$$e_c = a_0 \sigma^{a_1} t^{a_2}, \tag{1}$$

with temperature- and stress-dependent parameters a_0, a_1, and a_2.

The steel 20 MnMoNi 55 does not show a pronounced primary creep phase. Therefore, the secondary phase, which is important for the progress of creep, can be approximated by a straight line determined by the stress- and temperature-dependent parameter a_0 for the slope, $a_1 = 0$, and $a_2 = 1$. The tertiary creep phases of the load-controlled creep curves are not considered because in that phase the stress level increases. According to this method, the approximated creep curves of the steel 20 MnMoNi 55 were computed based on a spreadsheet analysis with MS Excel.

4. Failure Criteria

Both failures due to plastification and due to creep are employed as failure criteria for an integrity assessment based on FE analysis. Due to the higher level of stresses and strains, failure at the inside of the pipe structure is considered. To predict the time to failure of a piping based on a FE analysis it is necessary to define criteria for failure. The analysis results are assessed concerning failure on basis of a strain criterion. An ADINA material model is employed which considers plastic strains as well as creep strains. The value of strain is determined by the temperature-dependent strength and the temperature/stress-dependent creep characteristic of the relevant material. As the uniaxial strain limit for plastification, the uniform elongation is considered. Based on calculations of large-scale creep experiments, the limit of uniaxial creep strain is determined by 60% of the creep failure strain of the uniaxial creep tests for a safety-related assessment [5]. Especially for the question which component of a primary circuit fails first, additionally an assessment concerning failure as a matter of fact is necessary. This kind of assessment employs a limit of uniaxial creep strain determined by 100% of the creep failure strain of the uniaxial creep tests. Figure 5 shows the temperature dependency of the uniaxial limit of creep strain for the 60% and the 100%, criterion.

For consideration of multiaxial stress and strain states it is common practice to reduce the strain limits by division with a triaxial-factor TF which appears in the following form [6]:

$$\mathrm{TF} = \frac{|\sigma_1 + \sigma_2 + \sigma_3|}{\sigma_{\text{effective}}}. \tag{2}$$

The stresses σ_1, σ_2 and σ_3 represent the principal stresses and $\sigma_{\text{effective}}$ the von Mises effective stress. The triaxial factor may reduce the strain limits for safety-related assessments significantly.

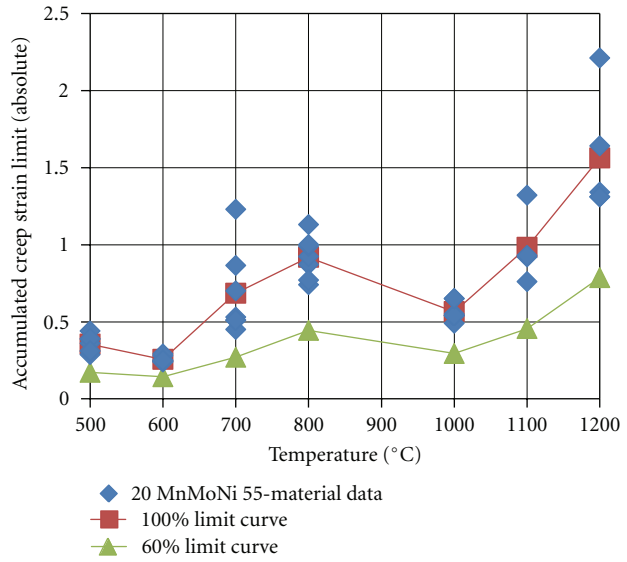

Figure 5: Steel 20 MnMoNi 55. Approach for definition of uniaxial creep limit.

5. Simplified Finite Element Model of a Pipe Structure

The abstraction from the pipe structure to the analysis model is displayed in Figure 6. The rotational symmetry of the pipe can be used for a reduction of the model into a 2D representation of the geometry. This helps to reduce computation times significantly which is obligatory in case of a high number of required computations.

Loads (forces and temperature) as well as boundary conditions are defined. Because of the rotational symmetry, it is possible to define loads and boundaries on lines. The temperature is defined as a homogenous temperature load on all elements.

6. Failure Surface

In the following a failure surface of a PWR reactor coolant line (RCL) with the geometry inner diameter 750 mm and wall thickness 62 mm is considered. In Figure 7 the calculated times of failure due to different constant temperature/pressure loads are summarized. A total of 740 FE computations and failure assessments of a pipe structure were performed. There are 10 pressure steps from 0.5 MPa up to 18 MPa. The temperature progression covers temperatures from 100°C up to 1300°C. The correlation between increase of failure time by decrease of pressure and temperature is obvious. Failure times above a time limit of 40000 s are not considered. Exemplary the load steps of 0.5, 2, 6, 10, 14, and 18 MPa are displayed. The failure time surface is considered as the surface which is spanned by the peaks of the columns.

7. Component Test and Simulation

For validation of the employed FE simulation and the failure assessment, procedure test data of a component test [7] are employed. The question of the short-term creep behavior at high temperatures was in the focus of this experimental investigation. The endurance and the fracture opening behavior of the reactor coolant piping were determined. For verification of the results from small specimen tests, a component test on a section of piping was carried out. The reactor steel 20 MnMoNi 55 was used as the test material. The conduct of this test was to simulate specific accident conditions; under a constant internal pressure of about 16.6 MPa using air as the pressurizing medium, the vessel was heated from outside to about 730°C to determine the time to failure (see Figure 8). The component test was conducted on a pipe of about 8 m total length closed at its ends by dished heads. The actual test pipe section which was welded into the center had a length of 2700 mm, an internal diameter of 700 mm, and a wall thickness of 47 mm. The whole test assembly was freely suspended by means of welded-on lugs. Pronounced plastic deformation commenced about 780 s before failure, that is, about 320 s after begin of the holding phase at a temperature of about 720°C. Failure occurred by the appearance of a longitudinal crack which after reaching the circumferential weld seam of one of the two extension pipes was deflected into the circumferential direction. A thermal FE analysis by ADINA [2] is accomplished to obtain the temperature distribution of the structure. The output of thermal FE analysis is used as temperature input data for the following implicit FE analysis. A simulation model with the geometrical properties of the test pipe was employed for a FE simulation with ADINA. The reduced 2D model revealed in Figure 6 was employed with modified dimensions. The test pipe has an inner diameter of $D_i = 700$ mm and a thickness $t = 47$ mm. A failure criterion which employs the 60% of the creep failure strain of the uniaxial creep tests reduced by the calculated stress triaxiality factor was used for a safety-related assessment (see Figure 9). The used criterion predicts a failure at 12470 s which is very close to the failure time of the test (12469 s). The results of the component test simulation have been presented on SMiRT 21 [8].

8. Simulation of Severe Accident Scenario

In the following section the results of an FE-based failure assessment and an ASTOR failure analysis for an RCL loaded during a severe accident scenario are compared. Due to an assumed station blackout scenario of a PWR, molten core material in the reactor pressure vessel-lower head (RPV-LH) may cause catastrophic consequences. The time of failure of the RCL is of special concern because a failure before the RPV-LH's failure may enable a significant pressure decrease. In the following a reactor coolant line, as considered in Section 6 is assessed under high-pressure and temperature conditions. Table 1 gives an overview of the relevant simulation runs and the employed failure assessment criteria.

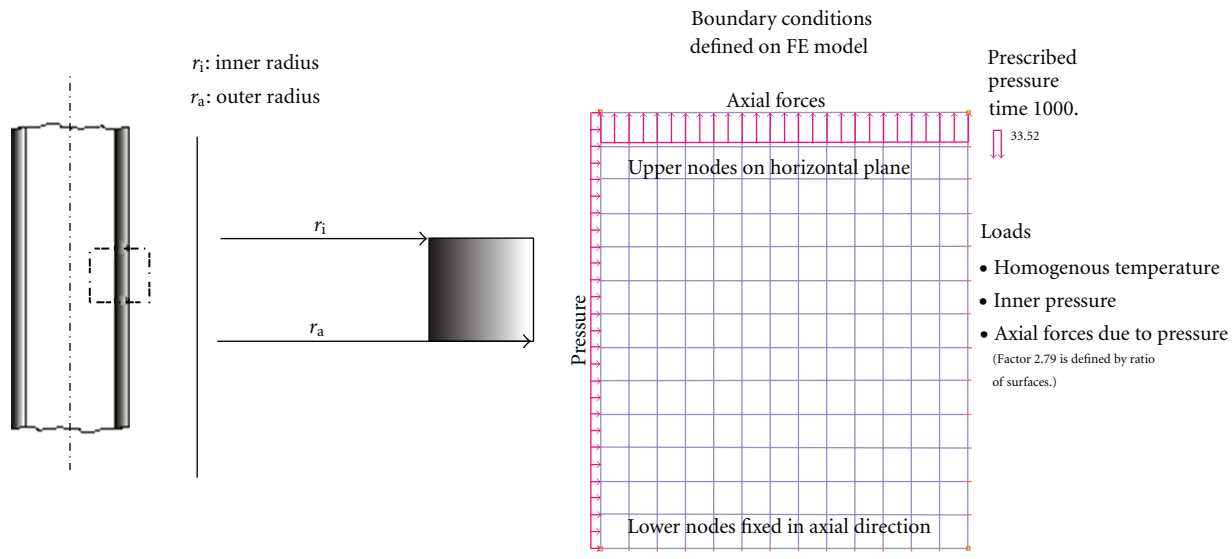

Figure 6: 2D representation of pipe structure, dimensions, loads, and boundary conditions.

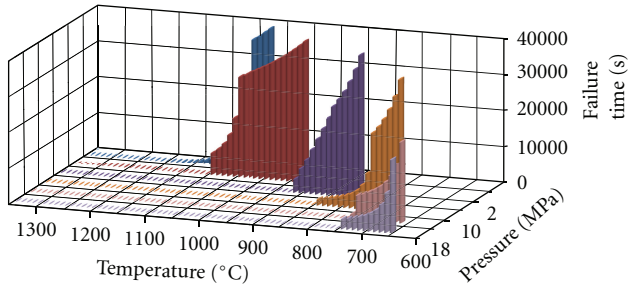

Figure 7: Failure time diagram for a RCL of 20 MnMoNi 55.

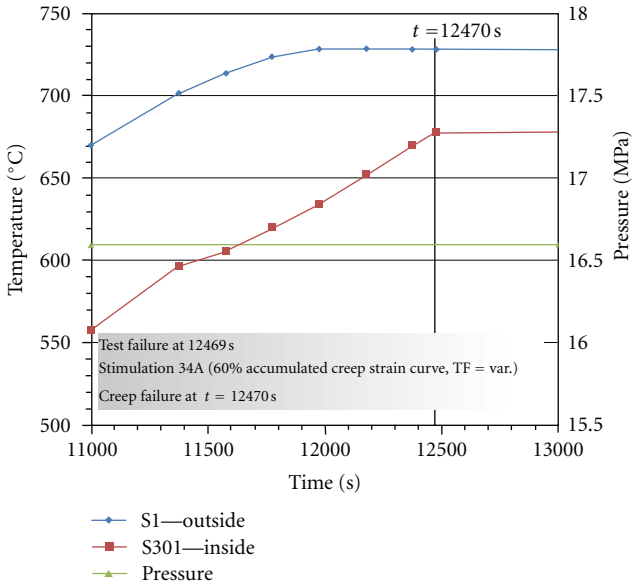

Figure 8: Loading conditions in the test pipe.

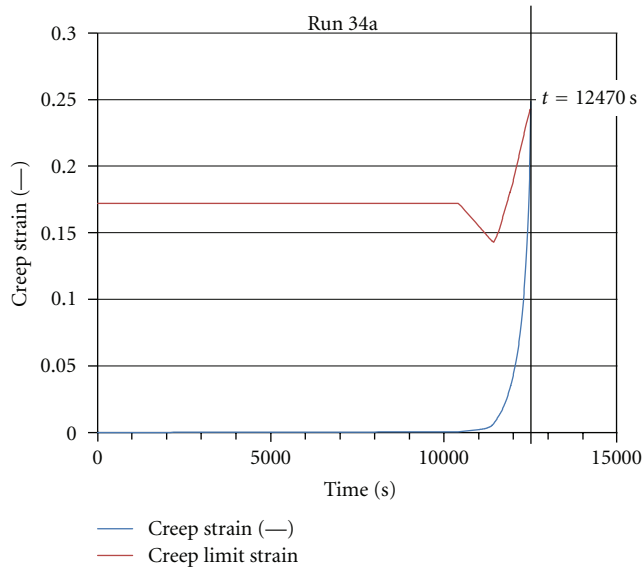

Figure 9: Accumulated creep strain and strain limit curve (failure at 12470 s).

Figure 10 reveals the temperature and pressure progression of the RCL calculated with MELCOR [9]. The temperatures reach a maximum of 969°C at 66280 s. The pressure oscillates at 12 MPa with an amplitude of 0.8 MPa. For simplification purposes up to a time of 40,000 s, the maximum value of the amplitude is assumed as input data for ADINA. This simplification is only applied at low temperature levels (<500°C), where no significant failure progression is expected.

In Run A the creep strains meet the limit strain prior to the plastic strains based on the safety-related failure criterion with consideration of the triaxial stress factor after about

Table 1: Failure assessment criteria.

Run #	Creep failure assessment	Plastic failure assessment
A	60% limit curve (see Figure 5) with variable TF	Uniform elongation/variable TF
B	100% limit curve (see Figure 5) with constant TF = 1	Uniform elongation/constant TF

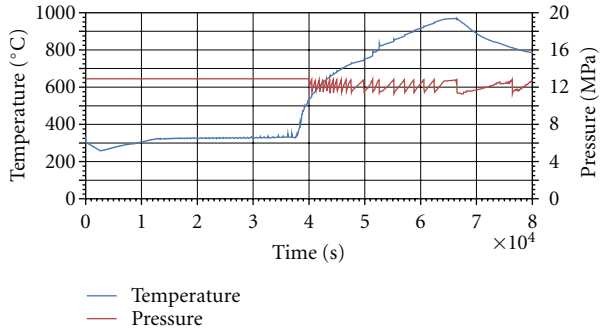

Figure 10: Temperature and pressure progression.

47471 s (see Figure 11). From safety-related point of view failure due to creep cannot be excluded after that time.

In Run B after about 47500 s, a strong increase of the plastic strains can be observed. The calculated plastic strains meet the criterion for failure as a matter of fact after about 47656 s.

Figure 12 displays the summation of damage increments within a calculation with ASTOR. For failure assessment, different damage values are considered. An accumulated damage $D = 1.0$ is fulfilled at a time of 49118 s, $D = 0.5$ is reached at 47750 s and $D = 0.4$ at 46760 s.

Figure 13 summarizes the failure times of all failure assessments. As one can see, the time gap between the safety-related assessment and the failure; as a matter of fact based on FE analysis can be estimated by about 185 s. The failure times determined by ASTOR vary from 46760 s ($D = 0.4$) to 49118 s ($D = 1.0$). The investigation shows that ASTOR results for damage values of about 0.4-0.5 are close to the FE results. Further work with different loading scenarios should be performed to confirm this conclusion. The results of the severe accident simulation have been presented on SMiRT 21 [8].

9. Detailed Thermohydraulic and Structure Mechanic Calculation of a Severe Accident Scenario

As a further example, the integrity of components in the primary circuit of a PWR loaded by a core-melt scenario with remaining high-pressure in the primary cooling circuit has been investigated with a complex analysis model. Thermohydraulic evaluations for this case show that the reactor pressure vessel (RPV) bottom, the main coolant lines (MCL),

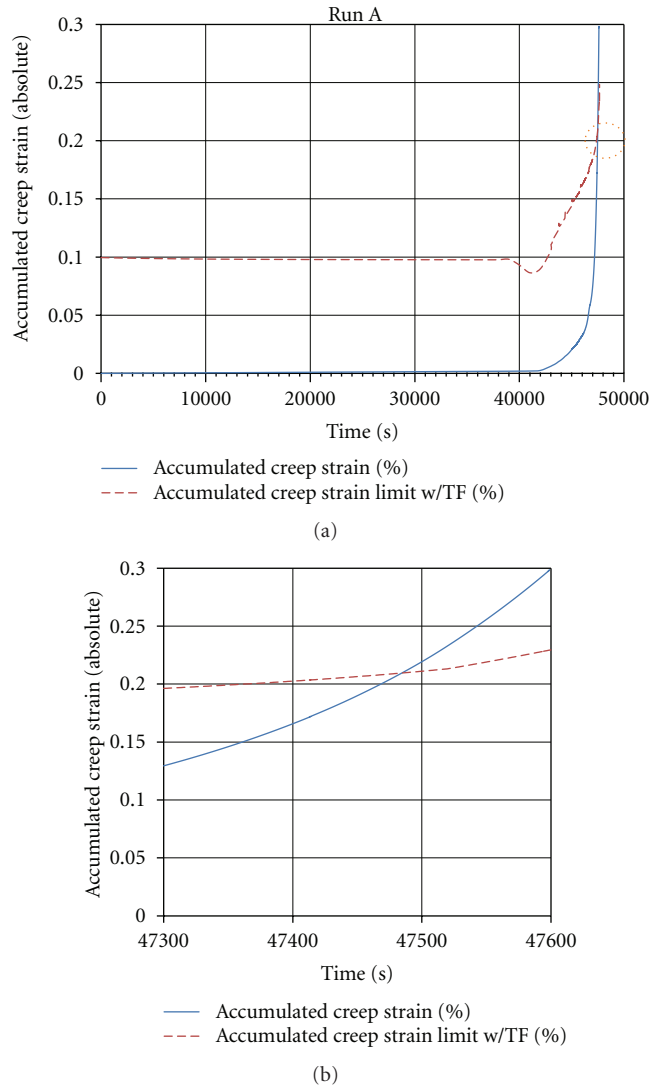

Figure 11: Accumulated creep strain and strain limit curve (failure at 47471 s): overview and detailed view.

and the surge line can reach temperatures above 800°C. A main aim of the study was to clarify whether the pipe lines will fail earlier than the RPV bottom or vice versa.

To estimate the failure temperatures and times, structure mechanic calculations with the FE code ADINA [2] were performed with load assumptions concerning internal pressure and component temperatures which are gained by Thermohydraulic calculations.

9.1. Essential Results of Thermohydraulic Calculations . For the Thermohydraulic calculation of the assumed accident scenario, the program MELCOR [9] was used. The complete primary circuit of a PWR was simulated. Some essential results of temperature and pressure distributions are presented in Figures 14 and 15.

9.2. FE Model for Structure Mechanic Calculations. For the FE calculations with ADINA [2], a model of the surge-line loop

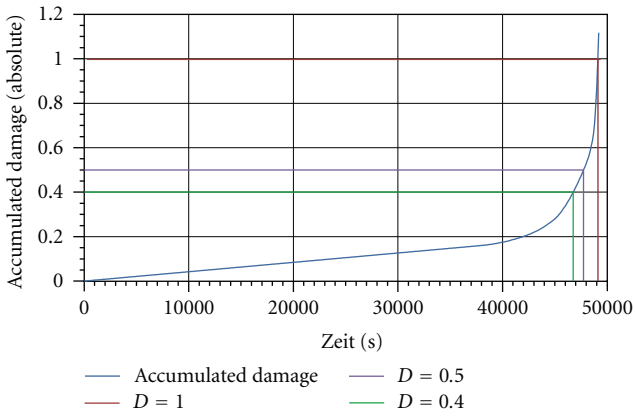

Figure 12: Summation of damage increments (ASTOR).

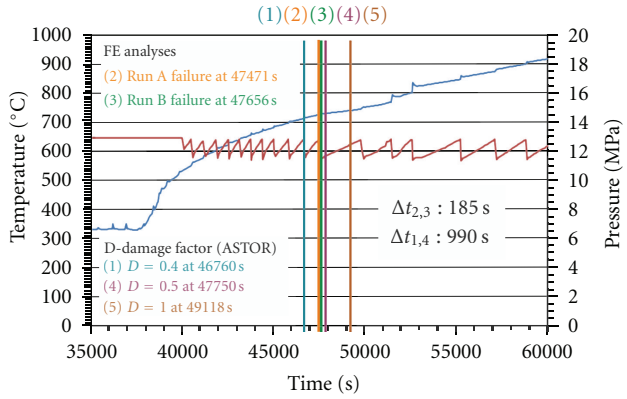

Figure 13: Failure times and load progression.

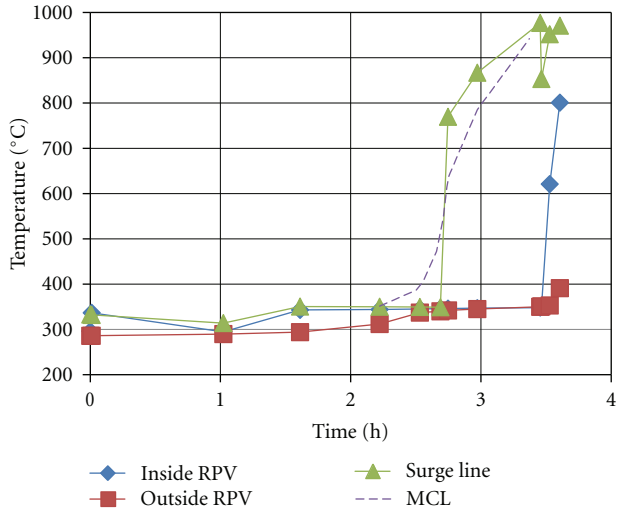

Figure 14: Temperatures versus transient time for different positions.

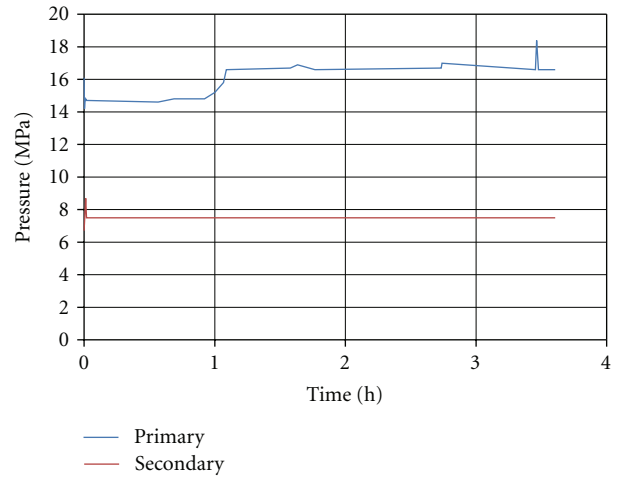

Figure 15: Pressures versus transient time for primary and secondary circuit positions.

of a PWR was used. The model shown in Figure 16 was built up during research projects at GRS; see for example, [10]. It also contains feedwater and steam line from steam generator to the containment penetration.

As the model is loaded by temperatures up to nearly 1000°C, corresponding high-temperature material data have to be used. For the ferritic parts, the stress-strain curves shown in Figure 3 are used. Similar data are provided for the austenitic part of the model (surge line).

As mentioned already, the load functions for the FE model concerning the wall temperatures of the components and the internal pressure are delivered by results of MELCOR calculations (accident scenario "total station blackout"). At 35 positions of the FE loop model, the temperature inside and outside the wall was evaluated. The temperature values between these positions are gained by interpolation. Also the temperature values in the middle of the wall were found by interpolation.

9.3. Estimation of Time of Failure. As described before a strain-based approach is used for the failure assessment. From the material side, the temperature-dependent strain value at uniform elongation is considered. To take constraint effects into account, this value is divided by the stress triaxiality factor TF as defined before. If the calculated accumulated effective plastic strain exceeds the strain limit at some integration point, the failure of the component is assumed in the sense of a safety-related assessment. Furthermore an assessment concerning failure as a matter of fact is performed with TF = 1.

9.4. Selected Results of the Structure Mechanic Calculation. To show how the estimation of failure time is carried out, two selected evaluations are shown in Figures 17 and 18. The first one is for a typical integration point in the main coolant line (hot leg) between RPV and steam generator; the second one is an integration point in the surge line.

The intersection points of eg/TF and ep deliver the failure times of a safety-related assessment. For the MCL this gives a failure time of about 3.1 h of the transient time. An assessment of the MCL with TF = 1, that is, failure as a matter

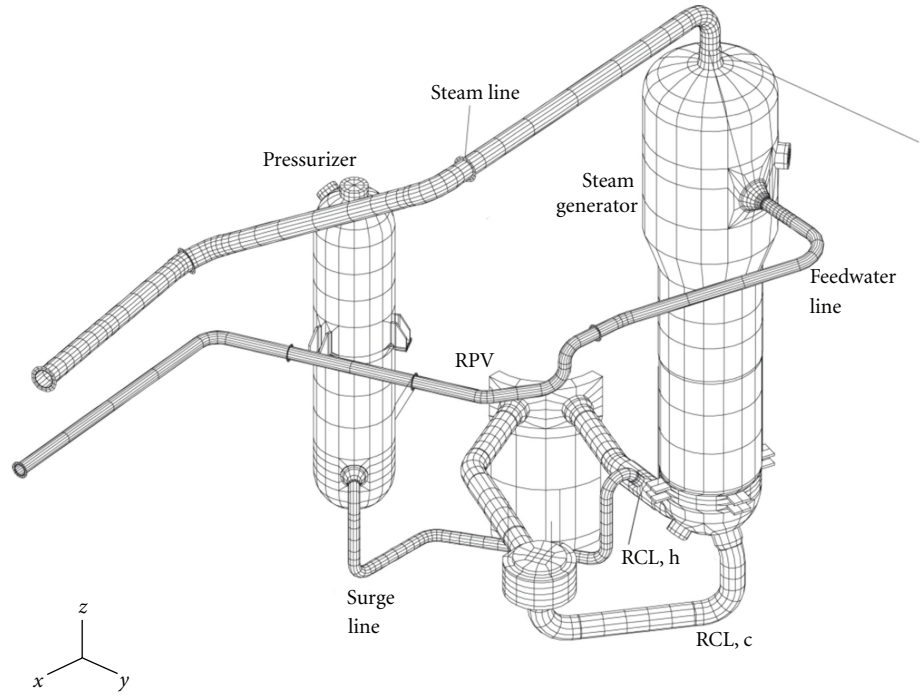

Figure 16: FE model of the coolant loop including surge line and pressurizer.

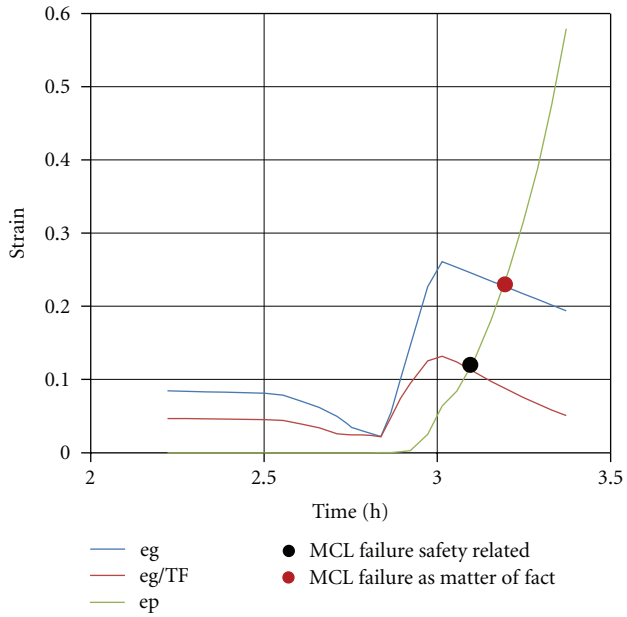

Figure 17: Structure mechanic assessment for a typical integration point in the MCL (eg: strain at uniform elongation concerning the respective temperature, eg/TF: strain at uniform elongation divided by stress triaxiality factor, ep: accumulated plastic strain).

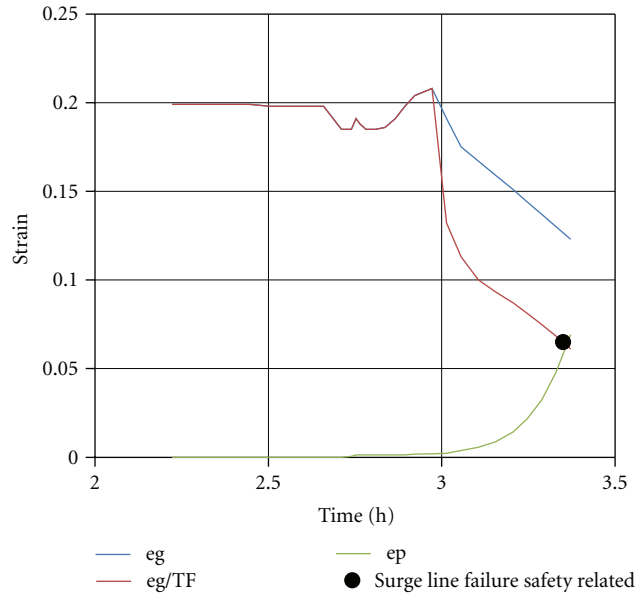

Figure 18: Structure mechanic assessment for a typical integration point in the surge line (eg: strain at uniform elongation concerning the respective temperature, eg/TF: strain at uniform elongation divided by stress triaxiality factor, ep: calculated accumulated plastic strain).

of fact, gives a failure time of about 3.2 h. For the surge line a failure time of about 3.35 h is found based on a safety related assessment.

Additionally Figure 19 presents times and temperature values at failure for MCL and surge line together with the transient temperatures calculated by MELCOR.

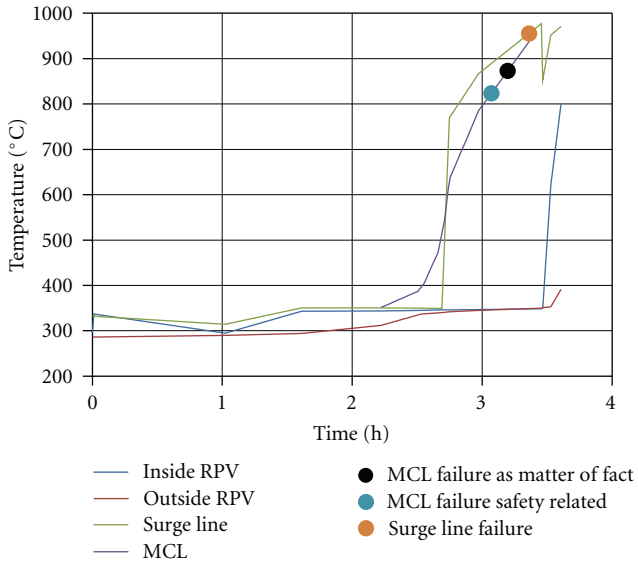

Figure 19: Temperatures versus transient time for different positions together with times and temperatures of failure for MCL and surge line.

The steep increase of the RPV temperature starts at about 3.5 h transient time. It may be concluded that failure of the MCL is expected about 0.3 h before the temperature increase of the RPV starts. Creep effects have not been considered in this analysis, but they would contribute to an increase of the time difference mentioned before.

10. Conclusions

The comparison of failure times of a large-scale creep test and FE analysis confirms that the FE analysis method including the used failure criterion is a best estimate method.

The method ASTOR enables a fast estimation of failure times and can be integrated into the framework of thermohydraulic system analysis programs. The application of ASTOR is limited to the boundary conditions concerning pipe geometry, material data, and type of loading used for generation of the failure surface. An uncertainty of the calculated failure times exists but can be constrained by a decrease of the assumed damage limit value. The comparison of ASTOR results with more rigorous FE analysis results requires verifications to quantify error bands. The results of the investigation show that the time of failure is strongly dependent on the changing stress level during the transient loading and the temperature-dependent material properties characterizing plastification as well as the temperature/stress-dependent material properties characterizing creep of the piping material. Also the uncertainty of the employed material data has to be mentioned. The required creep data are derived from load-controlled creep curves by use of a simplification method. Because the material creep data are only available for a limited range of stresses and temperatures, the FE code may use extrapolated data by trend analysis outside the range.

An accident with a core melt scenario under high-pressure loading caused by a station blackout is used as an example for an estimation of failure times by complex thermohydraulic and structure mechanic calculations. The thermohydraulic calculations with MELCOR show that in the course of the transient temperature values of above 800°C are reached at several positions of the cooling circuit. Using the temperatures and pressures evaluated by MELCOR as input for the structure mechanic calculation with ADINA, results in terms of stresses and strains were gained for the primary coolant loop under the accident scenario is considered. Using a strain-based failure assessment, failure times were estimated for the relevant positions of the loop model. While the temperatures in the RPV bottom are still relatively low, plastic strains in the main coolant and surge line reach limit values. Therefore it might be concluded that the MCL fails earlier than the RPV bottom. Since the failure times of the different positions do not differ very much, more studies might be necessary for the quantification of uncertainties. Especially the influence of creep could be considered more precisely. Finally it has to be pointed out that here only a special accident has been treated. Other accidents with different temperature and pressure transients might give other failure sequences.

Dependent on the required accuracy of the time of failure of a pipe, three failure assessment methods are accomplishable:

(i) ASTOR (useful for implementation in system codes, limited applicability, limited accuracy, extensive concerning generation of failure surfaces),

(ii) FE analysis with simplified FE model (flexible concerning application, limited applicability concerning complexity, high accuracy),

(iii) Complex FE analysis model with consideration of interaction between components [10] (extensive concerning generation of analysis model, flexible concerning application, high accuracy).

Abbreviations

ADINA:	Automatic dynamic incremental nonlinear analysis
ASTOR:	Approximated structural time of rupture
FE:	Finite element
MCL:	Main coolant line
MELCOR:	Thermohydraulic system code
NPP:	Nuclear power plant
PWR:	Pressurized water reactor
RCL:	Reactor coolant line
RPV-LH:	Reactor pressure vessel-lower head
TF:	Triaxiality factor.

Acknowledgments

The work has been predominantly performed in the framework of the Reactor Safety Research Program of the German Federal Ministry of Economics and Technology. The support of parts of the work by the German Federal Ministry for

the Environment, Nature Conversation and Nuclear Safety is also acknowledged.

References

[1] P. Eisert, P. Gruner, and W. Kuntze, "Estimation of PWR lower head failure times using the method ASTOR".

[2] ADINA (Automatic Dynamic Incremental Nonlinear Analysis), "Version 8.7, Theory and Modeling Guide," ADINA R&D, 2010.

[3] "Determination and modeling of material behavior of reactor steels under multiaxial loading in the temperature range from 400°C up to 1000°C," Reactor Safety Research Project 1501 010, MPA-Stuttgart, 1999.

[4] "Description of the short-time rupture behavior at temperatures up to 1200°C exceeding usual design on the basis of damage mechanism," Reactor Safety Research Project 1501 257, MPA-Stuttgart, 2005.

[5] P. Eisert, P. Bachmann, and J. Sievers, "Further development of the structure mechanic analysis methods for the determination of the creep behaviour of components," Final Report on Research project RS 1115, GRS-A- 3104, 2003.

[6] F. Ju and T. Buttler, "Review of proposed failure criteria for ductile materials," NUREG/CR 3644, 1984.

[7] K. Maile, A. Klenk, V. Obst, and D. Sturm, "Load carrying behaviour of the primary system of PWRs for loads beyond the design limits. Part 2: creep and failure behaviour of a piping section under internal pressure and high temperature," *Nuclear Engineering and Design*, vol. 119, no. 2-3, pp. 131–137, 1990.

[8] J. Arndt and J. Sievers, "Failure assessment methodology for piping under high temperature and pressure due to creep and plastification," in *Proceedings of the 21st International Conference on Structure Mechanics in Reactor Technology (SMiRT '21)*, New Delhi, India, November 2011.

[9] K. B. Cady, V. K. Dhir, and R. J. Witt, "Peer review of models for lower vessel head heat transfer and larson-miller failure criterion proposed for implementation into MELCOR," ERI/NRC 94-202, 1994, MELCOR 1.86 Reference Manual (NUREG/CR-6119, Vol. 2, Rev. 3).

[10] H. Grebner and J. Sievers, "Limit load of a PWR coolant loop for a hypothetical core melt scenario with high temperature and high pressure," 27. MPA-Seminar, Stuttgart, Germany, October 2001.

Hindawi Publishing Corporation
Science and Technology of Nuclear Installations
Volume 2012, Article ID 656590, 15 pages
doi:10.1155/2012/656590

Research Article

Response Analysis on Electrical Pulses under Severe Nuclear Accident Temperature Conditions Using an Abnormal Signal Simulation Analysis Module

Kil-Mo Koo,[1] Jin-Ho Song,[1] Sang-Baik Kim,[1] Kwang-Il Ahn,[2] Won-Pil Baek,[3] Kil-Nam Oh,[4] and Gyu-Tae Kim[5]

[1] *Severe Accident and PHWR Safety Research Division, Korea Atomic Energy Research Institute, 150 Dukjin-dong, Yusong-gu, Daejeon 305-353, Republic of Korea*
[2] *Integrated Safety Assessment Division, KAERI, 150 Dukjin-dong, Yuseong-gu, Daejeon 305-353, Republic of Korea*
[3] *Nuclear Safety Research Headquarter, KAERI, 150 Dukjin-dong, Yuseong-gu, Daejeon 305-353, Republic of Korea*
[4] *Department of Optical Communications Engineering, Gwangju University, 52 Hyuodeok-ro, Nam-gu, Gwangju 503-703, Republic of Korea*
[5] *Department of Electrical Engineering, Korea University, 5ka, Anam-dong, Sungbuk-ku, Seoul 136-701, Republic of Korea*

Correspondence should be addressed to Kil-Mo Koo, kmkoo@kaeri.re.kr

Received 7 December 2011; Revised 19 March 2012; Accepted 19 March 2012

Academic Editor: Gilberto Espinosa-Paredes

Unlike design basis accidents, some inherent uncertainties of the reliability of instrumentations are expected while subjected to harsh environments (e.g., high temperature and pressure, high humidity, and high radioactivity) occurring in severe nuclear accident conditions. Even under such conditions, an electrical signal should be within its expected range so that some mitigating actions can be taken based on the signal in the control room. For example, an industrial process control standard requires that the normal signal level for pressure, flow, and resistance temperature detector sensors be in the range of 4~20 mA for most instruments. Whereas, in the case that an abnormal signal is expected from an instrument, such a signal should be refined through a signal validation process so that the refined signal could be available in the control room. For some abnormal signals expected under severe accident conditions, to date, diagnostics and response analysis have been evaluated with an equivalent circuit model of real instruments, which is regarded as the best method. The main objective of this paper is to introduce a program designed to implement a diagnostic and response analysis for equivalent circuit modeling. The program links signal analysis tool code to abnormal signal simulation engine code not only as a one body order system, but also as a part of functions of a PC-based ASSA (abnormal signal simulation analysis) module developed to obtain a varying range of the *R-C* circuit elements in high temperature conditions. As a result, a special function for abnormal pulse signal patterns can be obtained through the program, which in turn makes it possible to analyze the abnormal output pulse signals through a response characteristic of a 4~20 mA circuit model and a range of the elements changing with temperature under an accident condition.

1. Introduction

To diagnose a severe nuclear accident, it is essential to determine a plant's status and to continuously monitor a plant's responses, expected from the actions taken by operators to mitigate a given accident [1]. In addition, a correct interpretation of a plant's conditions during such an accident is of significant importance for a successful accident management [2]. According to SECY 89-012, the United State Nuclear Regulatory Commission (U.S. NRC) requires that in a reasonable way instrumentation is identified as one of the key elements in utility accident management plants [3]. Moreover, a review of a plant's accident management capabilities is regarded as a crucial element in achieving a regulatory closure for severe accident issues. During accidents, information and data from a plant's instruments are essential in assessing the status and response of that plant. There are some inherent uncertainties of the

reliability of instrumentations expected while subjected to harsh environments occurring in severe nuclear accident conditions. Even for a severe accident condition, however, there are a few ways to obtain the relevant information and data. According to [4, 5], for example, circuit simulation analysis and diagnosis methods are available to assess these instruments in detail even when they provide apparently abnormal readings. Then, some abnormal signal diagnostics and analysis could be made through modeling of an important circuit that is composed of passive elements (*R-L-C*), an input multifunction generator, and an output pulse measurement system. These simulations would be useful for investigating what the signal and circuit response characteristics would be, similar to the relevant symptoms that can be obtained under severe environmental conditions as a quality analysis method [5].

In this paper, a newly enhanced simulation module has been designed through the realization of a one body order system [6] via one program that links an abnormal signal simulation engine program (PSpice and Multi-SIM code) to a signal analysis tool program (LabVIEW code), which includes signal analysis functions from an important circuit model applicable under the conditions [7]. In that case, the aforementioned abnormal signal simulation engine is used as a one order command which means a nonstop processing command to import the simulation data from an output of the engine code to an input of the main analysis tool program. The design of the above simulation module can be broken up into three main steps [8]. The first step is a section of a comparative assessment of the instruments between the instrument specifications or EQ (environment qualification) requirement parameters and the environment parameters that can be obtained through a severe accident simulation code such as MAAP4 whose mean circumstance data is obtained through a simulation of various accident scenarios [9]. From the results, if its comparative result is not satisfied, the second step is a section of the design of a circuit simulation to apply an abnormal signal simulation processing technique with an equivalent circuit, the third step is a section of a signal analysis of functions that have an additional 5 substeps. Consequently, three main functions exist and are characterized as an abnormal signal processing, an accident management, and an additional guide that are displayed on the initial screen of a simulation system ASSA module. Using the ASSA module, we could obtain the response characteristics from the output voltage levels of a pulse parameter according to a change of the resistance for each of R_2, and R_3, and the response characteristic from the output voltage level and time constants of the pulse parameter according to a change of the capacitance for each of C_1, and C_2.

As a result, when we can analyze the cause from an equivalent circuit, which consists of an *R-C* distribution parameter, from a response characteristic for a 4~20 mA instrument during high temperature conditions of the severe accident conditions (SACs), it is also possible to detect and diagnose the abnormal signal patterns of a malfunctioning instrument. In addition, the pulse parameter estimation is operable to estimate a pulse parameter for a signal based on an analysis of the detected pulses and information pertaining to there being abnormal pulses in the signal as a quantitative analysis method.

When this simulation module is set up in a laboratory, we can obtain a variety of abnormal signals simulated under degraded conditions like higher temperature conditions of the SACs. A large variety of built-in models and a simulator adds flexibility to a simulation and includes the effect of harsh environments by using a special function to identify the components exceeding a manufactures' limits from a circuit modeling including the *R-C* passive elements.

We present the design steps with the diagnosis methods and the circuit simulation using a specific signal processing in Section 2, followed by a detailed description of work carried out during the past five years of our diagnostics and analysis work in Sections 3–5. Some concluding remarks are presented in Section 6 and a reference of papers resulting from the project is included.

2. Design Steps of Diagnosis Methods and the Circuit Simulation with Specific Signal Processing

2.1. Design Steps of Diagnosis Methods for the Malfunctioning Instruments. When an instrument which is providing information and data for severe accident management is apparently malfunctioning, a series of steps can be taken which include an indirect diagnosis of the instrument and a direct method of determining the value of the parameter. These methods are identified by five steps which are called operational aids. They are combinations of diagnostic actions and other means of measurement. These combinations can be applied when instrument readouts are suspect or faulty. The five types of aids are a diverse indication, parameter inference, a portable instrument, circuit diagnosis, and a portable circuit readout [4] (Figure 1). In this case, a circuit diagnosis from among the diagnostic evaluations belongs to action items for a malfunctioning instrument where a circuit diagnosis using a simulation tool code is possible.

2.2. Design Steps of the Circuit Simulator. Figure 2 shows an initial screen consisting of functions for the ASSA module. It has three main functions which have not only an abnormal signal processing function, but also a severe accident management function based on EPRI TR-103412 and EPRI TR-102371 technical reports including a comparative assessment procedure for instruments [4, 5], and an additional guide on the initial screen of an ASSA module.

Figure 3 shows a flowchart of the overall design steps for the simulator as an ASSA module system. The comparative assessment procedure for the instruments has the main information and data including the information needs for the instrument specifications, position information according to five areas in the containment building, and the circumstance parameters from the accident scenarios using the MAAP4 code. Figure 4(a) shows the three EQ conditions which include a normal condition, an abnormal condition, and an out of range condition. Figure 4(b) shows five phases of

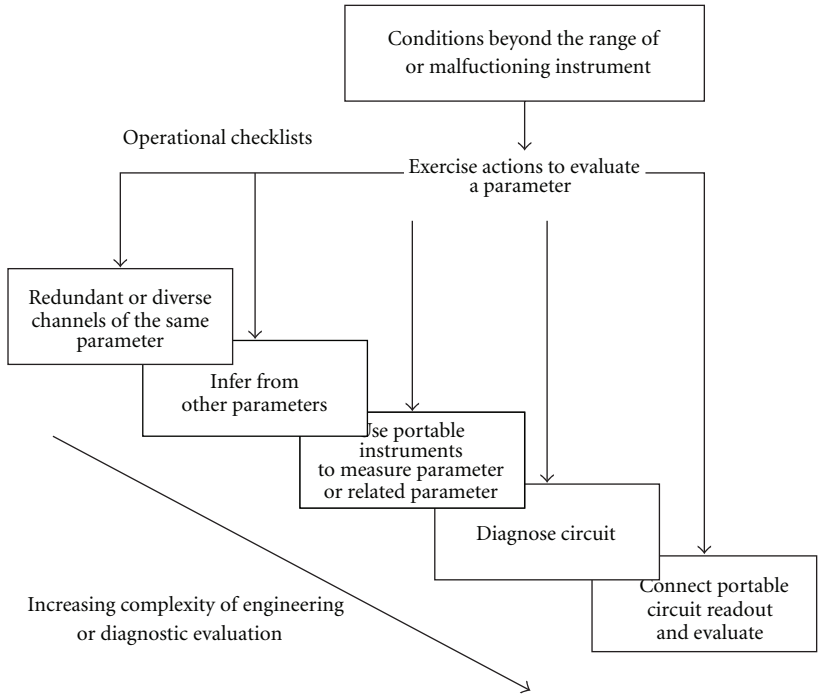

Figure 1: Flowchart for the circuit diagnosis methods among the five types of aids.

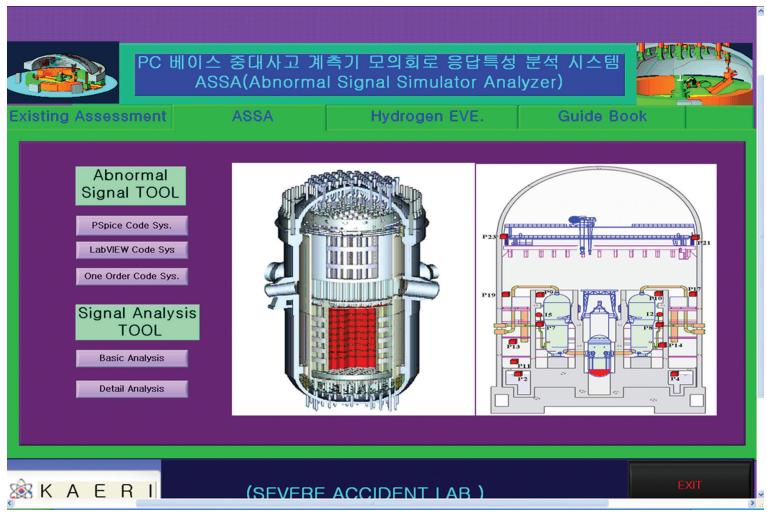

Figure 2: Initial screen consisting of functions for ASSA module.

a scenario taken by MAAP4 code. Figure 5 shows a screen for a comparative assessment procedure as the first step for the ASSA module system. As a result, if the proper conditions are not satisfied by using the comparative assessment method, then proceed to a next step as the section of LabVIEW Tool code. As the next step, we need decision making for signal conditions which means three kinds of signal conditions, of which the first is normal condition signals, the second is abnormal condition signals, and the third is out of control condition signals.

In the case of abnormal condition signals, we are interested in the information on the patterns of the abnormal signals and the database for the signal patterns that also could be obtained by the engine code, which then need to be processed by any other five substeps from the analysis tool code, and finally we are able to obtain corrective signals as a final step, but not yet here. There are two codes to be used for the simulation, the designed simulator which is composed of the LabVIEW code as a main analysis tool code, and the PSpice and MultiSIM code as a simulation engine code. For these abnormal signals simulations, a new simulator through an analysis of a typical equivalent circuit modeling has been designed, which is composed of an analysis tool code as a main body and a simulation engine code whose

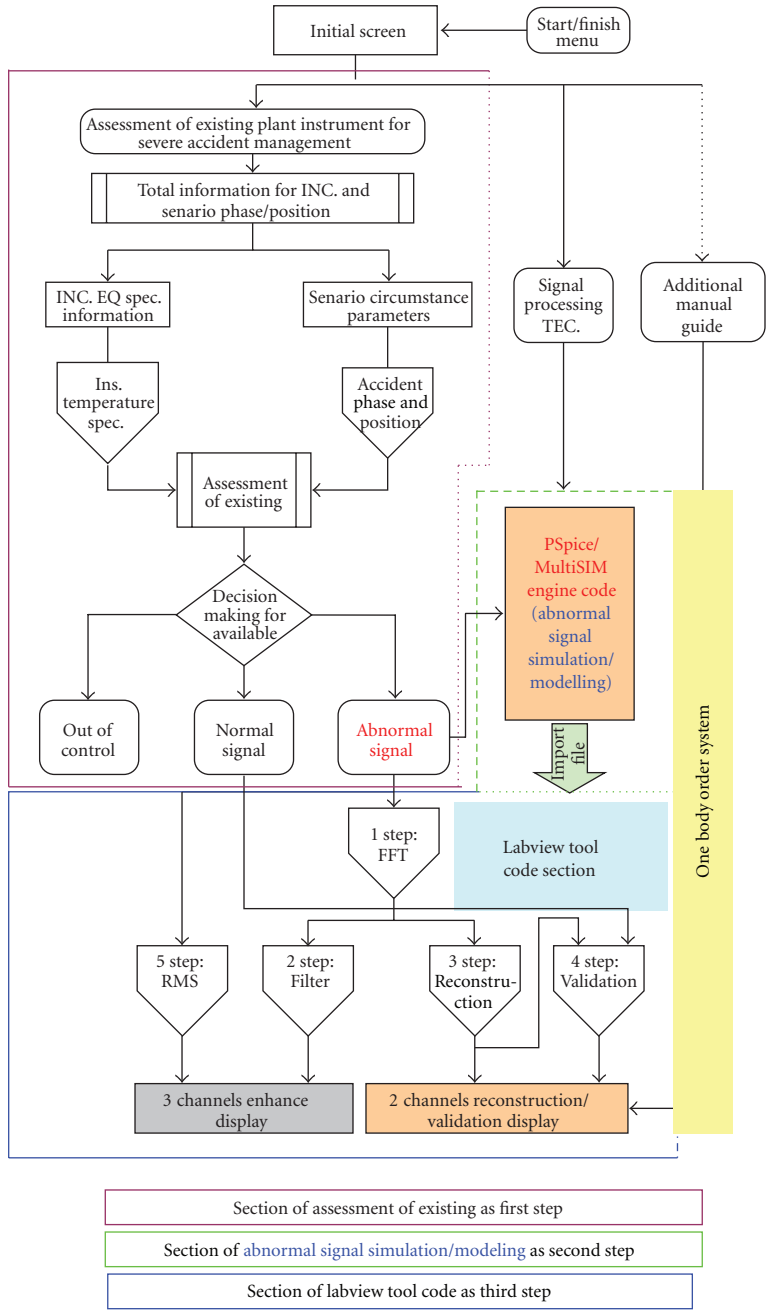

Figure 3: Flowchart of the overall design steps for the simulator as ASSA module.

systems are imported to link an output file to an input file.

3. Detailed Design and Functions of the ASSA Module

3.1. Functions and Equivalent Circuit of the Engine Code. The engine code for the circuit simulation program was used to simulate the effects of an instrument loop degradation on a measurement condition. This engine code is useful for obtaining a correlation between the simulation circuit conditions and the actual circuit conditions. Although the goal was to develop a real model, the intricacies of developing the appropriate waveforms and incorporating the effects of the induced noise into the circuit turned a degraded circuit loop into lines and lines of netlists. A 4~20 mA loop was used to measure the reactor coolant pressure the same as for most instruments. The overall circuit loop consists of a section of a control room, a section of a twisted pair shield cable, and a section of a transmitter. A transmitter circuit was treated as a loop for an important circuit for the passive elements *R-L-C* which could be affected by the severe accident conditions. In this case, the imported passive elements of the transmitter circuit were R_2, R_3, C_1, and C_2, as distributed parameters

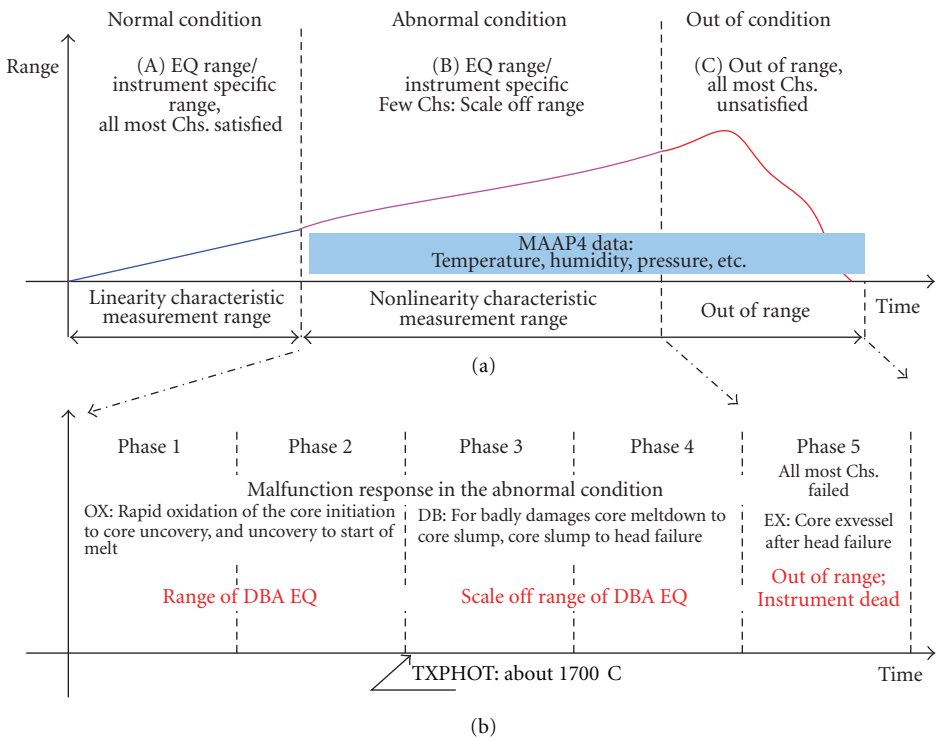

Figure 4: Three EQ conditions and five phases of a scenario taken by MAAP4 code.

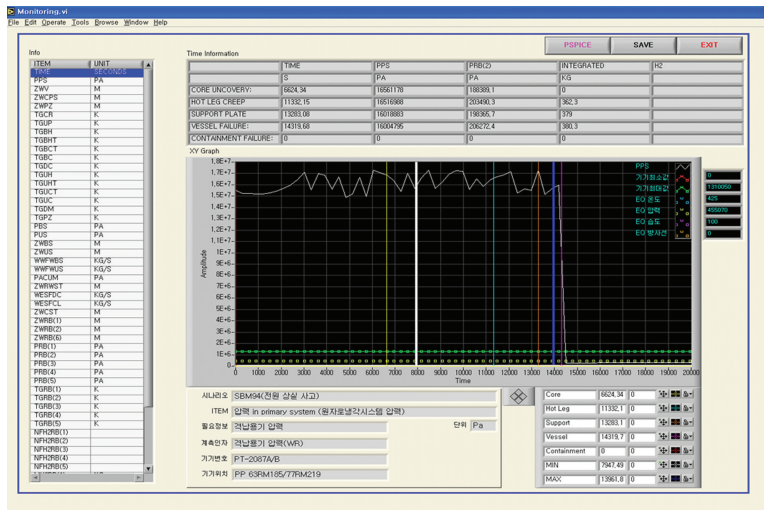

Figure 5: Screen of comparative assessment procedure as the first step for the ASSA module.

of the circuit. Figure 6 represents an overall circuit model modified to run in the MultiSIM code.

3.2. Procedure for a One Body Order Simulation and Digital Signal Processing. For the first step, during the operating procedure, the establishment of a simulation circuit modeling by the PSpice/MultiSIM code is attempted, where the PSpice/MultiSIM simulation output file is used for all the files; *.cir, *.sim, and *.net files. The next step needs the information on the circuit elements from the *.net file, and then the *.net file can be controlled by an element in the circuit, for using the Labview *.net file condition, and then we take the csd file out of the *.net file in the Labview and execute the system exec.vi file of the PSpice/MultiSIM condition. As the last step, we extract the output results from the csd file, and then the file can be displayed as some of the output abnormal signals. Finally, these signals can be processed by an analyzing tool. Thus, this system will be used for circumstance diagnostic for the abnormal signals, and this code will also allow us to use the enhanced signals from the abnormal signals for some malfunctioning instruments. There are two types of programs which consist

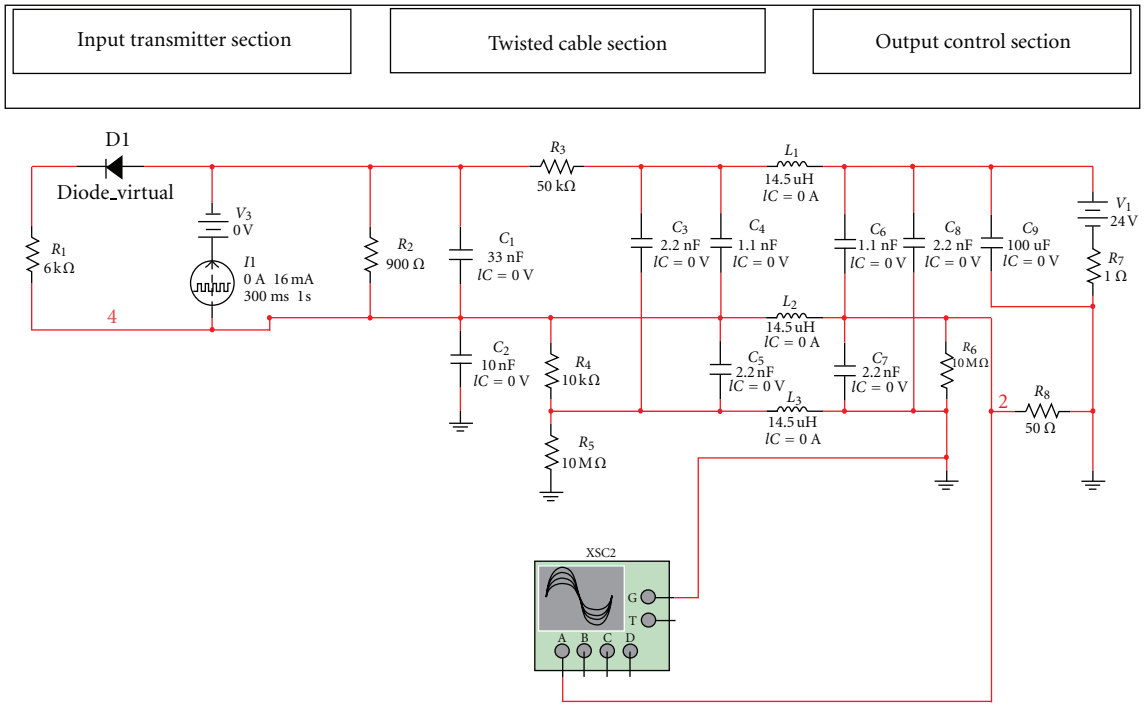

Figure 6: Overall circuit model modified to run in the MultiSIM code.

of the PSpice/MultiSIM engine code and the LabVIEW tool code, which can work as a one body order system for this simulation. The overall simulation result data can be used by one operation system as a one order command. So that the programs could be operated quickly and conveniently as an onsite instrument, in this simulation, we changed the element values in the circuit which is possible by directly changing the *R-C* element value according to the temperature condition in the initial screen menu of the tool code, so we do not need to use the functions of the engine code.

As a result, it is also possible to change the output signal patterns according to the changing element values in the tool code menu functions under SACs. It is also easy and convenient for a signal analysis for some types of noise patterns. The output results can be extended and analyzed for their response characteristics by the tool code, because the LabVIEW code has powerful analyzing functions and good interface while being onsite. Figure 7 shows the block diagram for a one body order simulation system. The loop circuit was composed of three sections which include the pressure transmitter section, the twisted shielded pair connection cable section, and the receiver section. The pressure transmitter has been simplified to obtain an equivalent representation of the resisters, capacitors, and inductors as distributive parameters of the circuit. It also includes voltage or current sources that can be varied through the circuit simulation code to obtain realistic circuit response characteristics from environmental changes in the containment. A specific parameter includes: an input leakage (shunt) resistance that is affected by damage to an interconnecting cable and; input series resistance to represent the

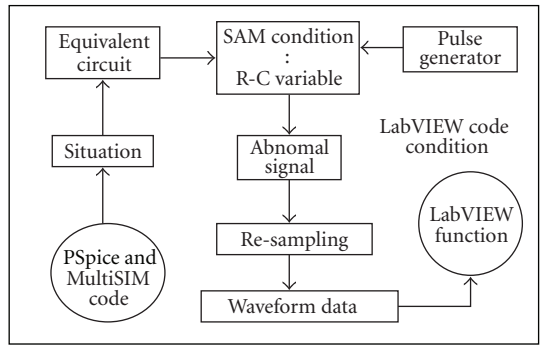

Figure 7: Block diagram for one body order simulation system.

spliced connections that might be affected by corrosion and whiskers phenomenon. Input capacitance is increased easily by a water intrusion into the cable or the transmitter housing. Capacitance for the ground is easily increased by the presence of water. A diode and load resistors represent the power supply current. A current generator represents the actual transmitter output signal. A typical cable is represented to describe the wire inductance and resistance, and the dielectric capacitance. The shield is represented as a third conductor. It is simplified to eliminate all the resistances, and to only model the inductance and capacitance. The voltage source drives a current to a voltage sensing resistor in series with the transmitter. Negative sides of the voltage source and the shields are attempted for the ground source in this analysis. Figure 8 shows a detail block diagram for the signal processing and analysis from the ASSA module system. Figure 9 is a screen of the ASSA for one body order simulation system.

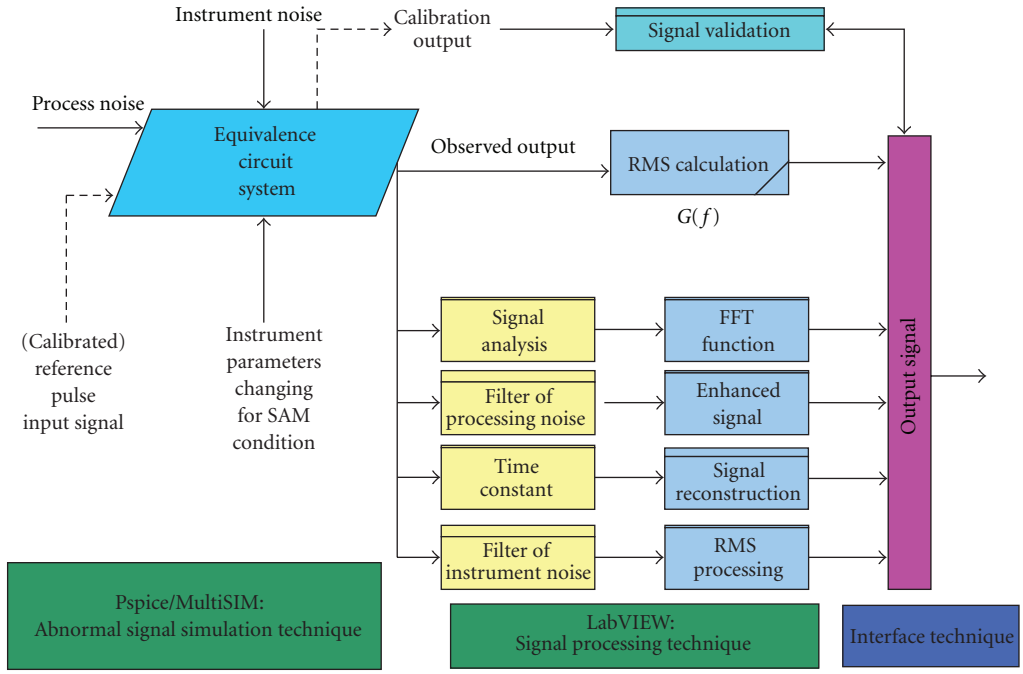

Figure 8: Block diagram for the signal processing and analysis from ASSA module system.

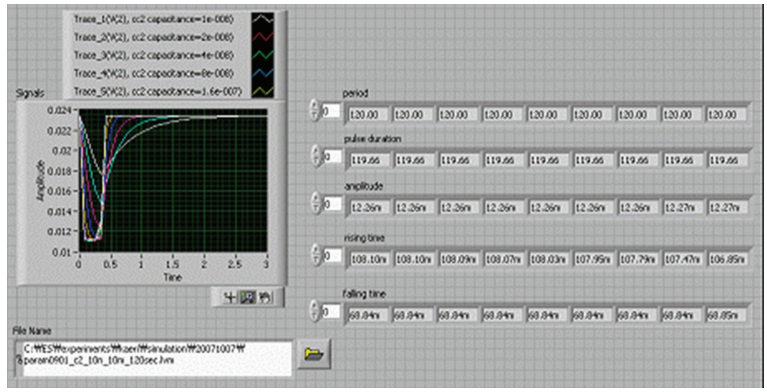

Figure 9: A screen of the ASSA for a one body order simulation system.

4. Simulation and Response Characteristic Analysis from the Obtained Data

There are two types regarding information of pulse parameters which means changing a value for the output pulse signal with certain information to diagnosis a circuit condition such as a voltage level, a time constant including information of a rising time, falling time, and bandwidth compare to information for pulse parameters of the reference input signal. As a result, when we can analyze the cause of an equivalent circuit, which consists of an *R-L-C* distribution parameter, for a 4~20 mA instrument of a severe accident condition from response characteristics, it is also the same meaning that is also possible to detect and diagnose the abnormal signal of a malfunctioning instrument from a simulation and response characteristic analysis. Figure 10 is patterns of output pulse signal of ASSA for a one body order simulation system.

Method for the pulse parameter estimation: for pulse parameter, estimation for ASSA module has designed as the basic concept for circuit analysis procedure. In addition to this method, there is pulse detection logic, an abnormal pulse filter, and a pulse parameter estimation for pulse parameter estimation was already said and it is redundant. The pulse detection logic is operable to detect pulses and to estimate a pulse parameter of each detected pulse [10]. The abnormal pulse filter is operable to analyze a pulse parameter of the detected pulses and to determine whether there are any abnormal pulses based on the analysis. The pulse parameter estimation is operable to estimate a pulse parameter for

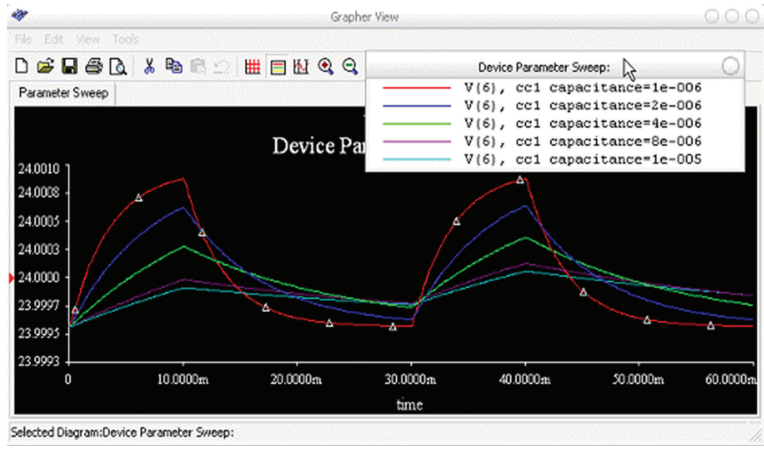

Figure 10: Patterns of output pulse signal of ASSA for a one body order simulation system.

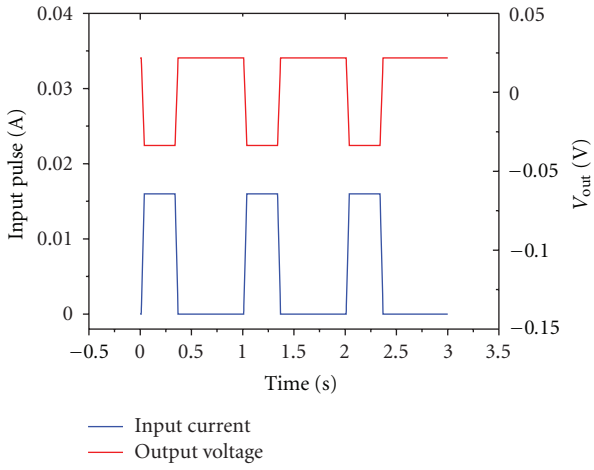

Figure 11: Reference input current (A) and output voltage (V) data for the pulse parameter as an initial value.

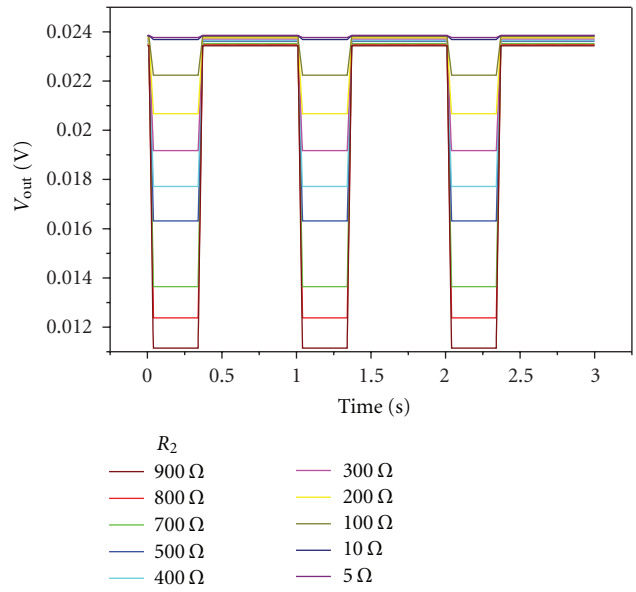

Figure 12: Output voltage levels for the pulse parameter for a change of the resistance of R_2 (5 (Ω)~900 (Ω)).

the signal based on an analysis of the detected pulses and information pertaining to there being any abnormal pulses in the signal.

4.1. Defining the Reference Signal from the Equivalent Circuit. Figure 11 is reference input current (A) and output voltage (V) data for the pulse parameter as an initial value. This reference pulse signal was defined in the engine code as a linear approximation, with a 0–16 mA pulse with a 0 ms delay, 30 ms rising time, 30 ms falling time, and a 1 PPS repetition rate. The reference pulse also describes an output current pulse as measured across the current to voltage converter at the receiver. This is a reference input current I (A) and output voltage V (V) data of the pulse parameter as an initial value. In this figure, it appears as about 0.1 to 1.0 (V) pulse at a temperature of 27 (°C).

4.2. Results with Change of Resistances. Figures 12 and 13 show the output voltage level of the pulse parameter according to a change of the resistance R_2 which range has 5 (Ω)~900 (Ω) and 1 (kΩ)~10 (kΩ), respectively. Figure 14 shows the variations of output voltage according to the R_2. In the case of the R_2 simulation using the tool code, it can be seen that the resistor value changes for the high-voltage level data which means a good linearity (sensitivity) response characteristic over 1 (kΩ) to 10 (kΩ). In this resistance R_2, the impulse response of an equivalent circuit for the 4–20 mA is its output when presented with an input standard signal called an impulse. The impulse response refers to the reaction of the circuit system which was consisted with that resistance R_2 to be obtain the response characteristic for the maximum resistance changing value facing each external temperature as the changing parameter, the response characteristic has an increasing characteristic in the circuit according to basic circuit theory, because the resistor (R_2) was consisted of the parallel component.

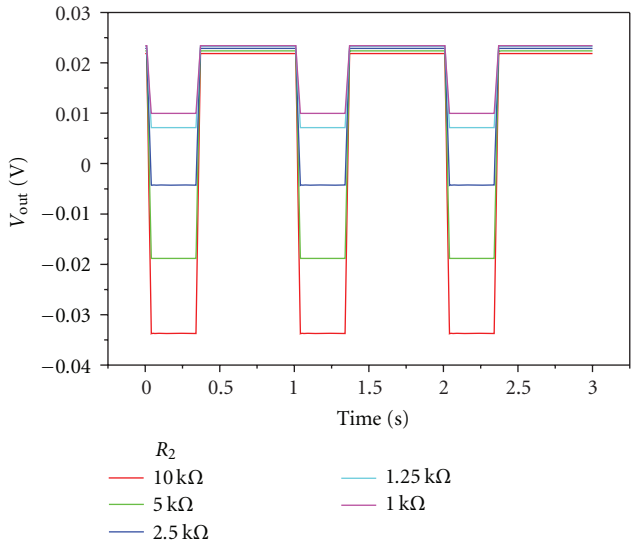

Figure 13: Output voltage levels for the pulse parameter for a change of the resistance of R_2 (1 (kΩ)~10 (kΩ)).

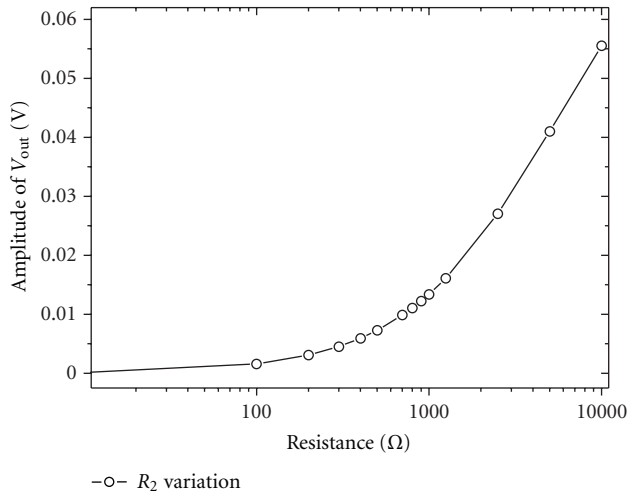

Figure 14: Response characteristic of the output voltage for the pulse parameter for a change of the resistance of R_2 (5 (Ω)~10 (kΩ)).

Figures 15 and 16 show the output voltage level of the pulse parameter according to a change of the resistance R_3 which has a range of 5 (Ω)~4 (kΩ) and 5 (kΩ)~50 (kΩ), respectively. In the case of the R_3 simulation using the tool code, it can be seen that the resistor value changes for the high voltage level data which means a good linearity (sensitivity) response characteristic over 5 (Ω) to 50 (kΩ), in the case of an overall response characteristic with a decreasing response characteristic for an increasing resistance because the resistor (R_3) was consisted of the serial component in Figure 17 according to the basic circuit theory. Figure 17 shows a response characteristic of the output voltage for the pulse parameter for a change of the resistance of R_3 (5 (Ω)~50 (kΩ)).

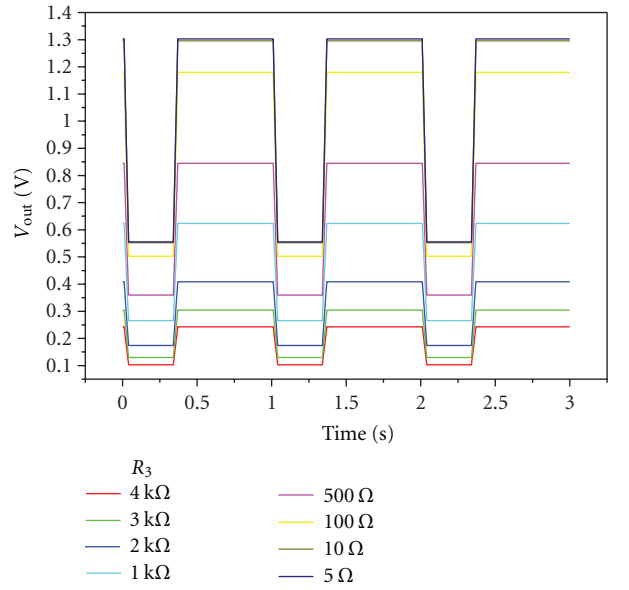

Figure 15: Output voltage levels for the pulse parameter for a change of the resistance of R_3 (5 (Ω)~4 (kΩ)).

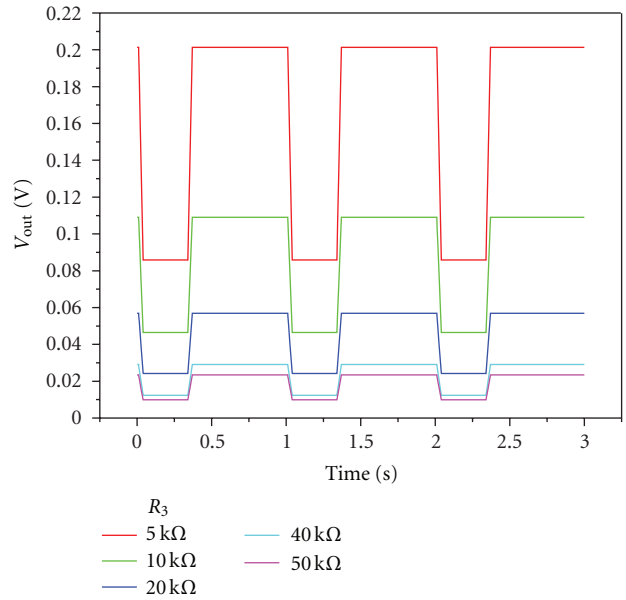

Figure 16: Output voltage levels for the pulse parameter for a change of the resistance of R_3 (5 (KΩ)~50 (KΩ)).

4.3. Results with Change of Capacitances. Figure 18 shows the output voltage level data and the time constant for the pulse parameter according to a change of the capacitance of C_1 which has a range of 33 (nF)~33 (mF). Figure 19 shows the response characteristics of the output voltage curve for the pulse parameter according to a change of the capacitance of C_1. Figure 20 shows the response characteristics of the rising time (Tr) for the pulse parameter according to a change of the capacitance of C_1. In the case of the C_1 simulation by using the tool code, it can be seen that the capacitance

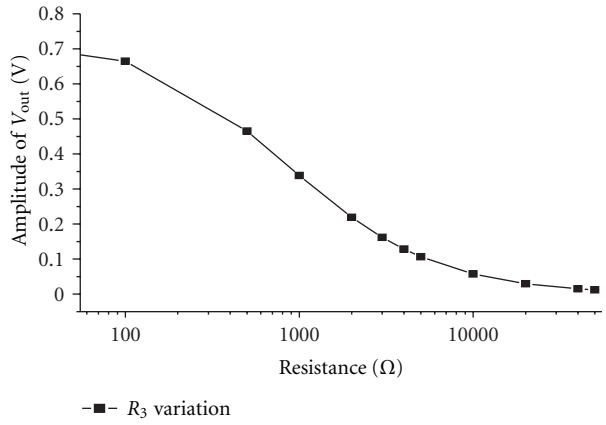

Figure 17: Response characteristic of the output voltage for the pulse parameter for a change of the resistance of R_3 (5 (Ω)~50 (kΩ)).

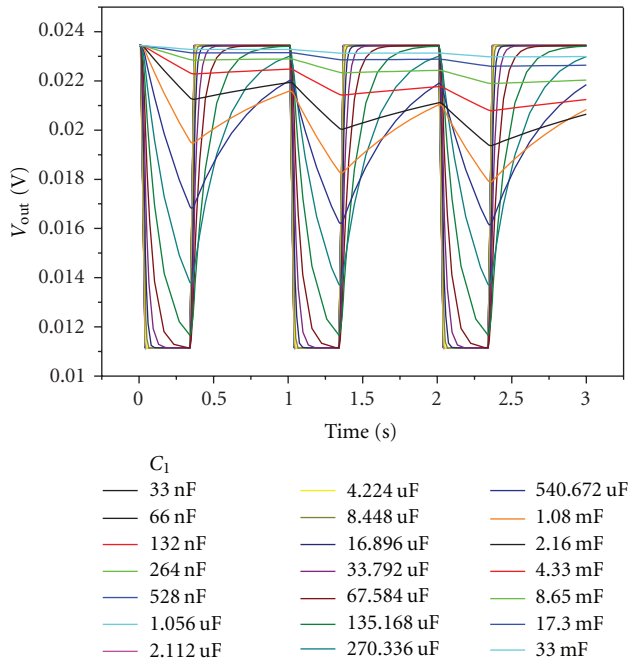

Figure 18: Output data for the pulse parameter for a change of the capacitance of C_1 (33 (nF)~33 (mF)).

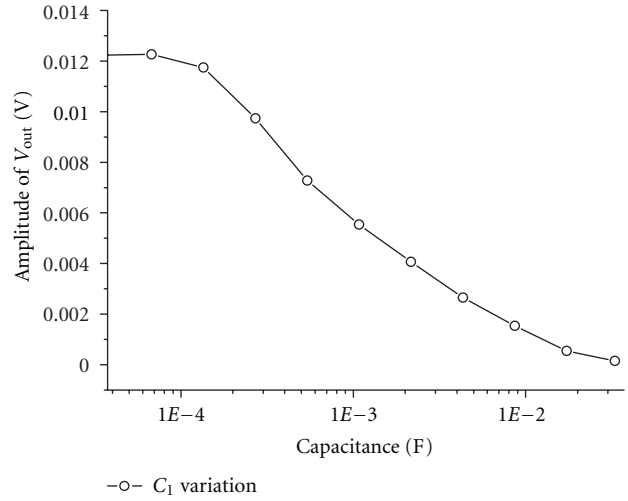

Figure 19: Response characteristic of the output voltage curve for the pulse parameter for a change of the capacitance C_1 (33 (nF)~33 (mF)).

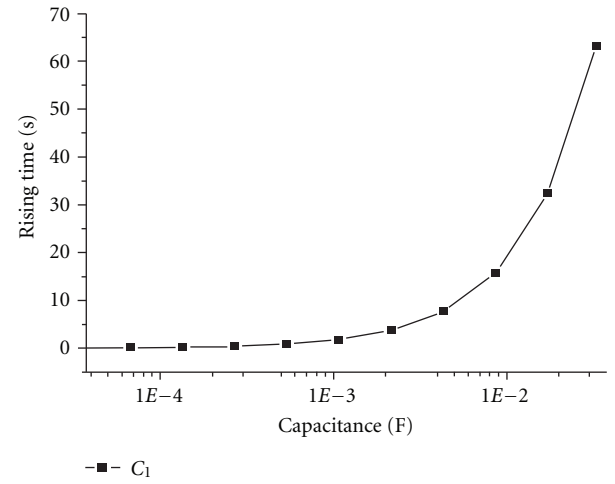

Figure 20: Response characteristic of the rising time (Tr) for the pulse parameter for a change of the capacitance of C_1 (33 (nF)~33 (mF)).

value changes for the high voltage level data which means a good linearity (sensitivity) response characteristic over the same range, in the case of an overall response characteristic with a decreasing response characteristic for an increasing capacitance. The response characteristic of the rising time (Tr) for the pulse parameter which also means a good linearity (sensitivity) for the response characteristics over the same range, in the case of an overall response characteristic, reveals an increasing response characteristic for an increasing capacitance of C_1. In this capacitance C_1, the impulse response of an equivalent circuit for the 4–20 mA is its output when presented with an input standard signal called an impulse. The impulse response refers to the reaction of the circuit system which was consisted with that capacitance C_1 to obtain the response characteristic for the maximum capacitance changing value facing each external temperature as the changing parameter, the response characteristic of the output voltage curve is a decreasing characteristic, the response characteristic of the rising time (Tr) is an increasing characteristic in the circuit according to basic circuit theory, because the capacitance (C_1) was consisted of the parallel component.

Figure 21 shows the output voltage level data for the pulse parameter according to a change of the capacitance of C_2 which has a range of 10 (nF)~10 (mF). Figure 22 shows the response characteristics of the output voltage level data for the pulse parameter according to a change of the capacitance of C_2. Figure 23 shows the response characteristics of the rising time (Tr) for the pulse parameter according to a change

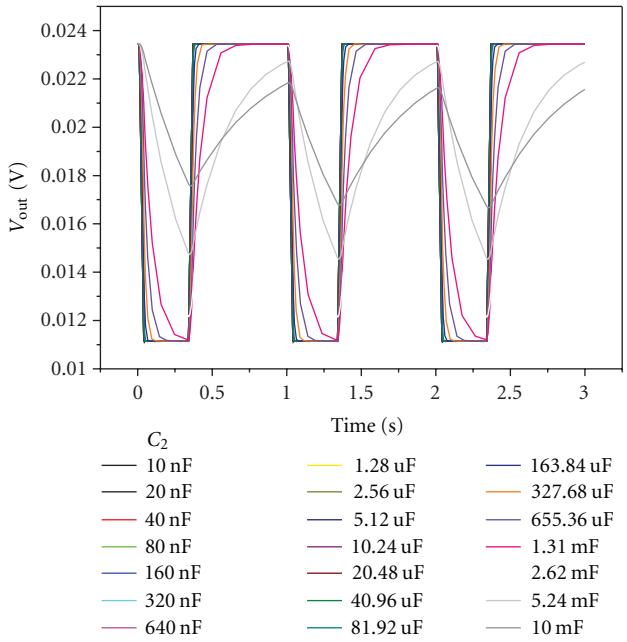

Figure 21: Output data for the pulse parameter for a change of the capacitance of C_2 (10 (nF)~10 (mF)).

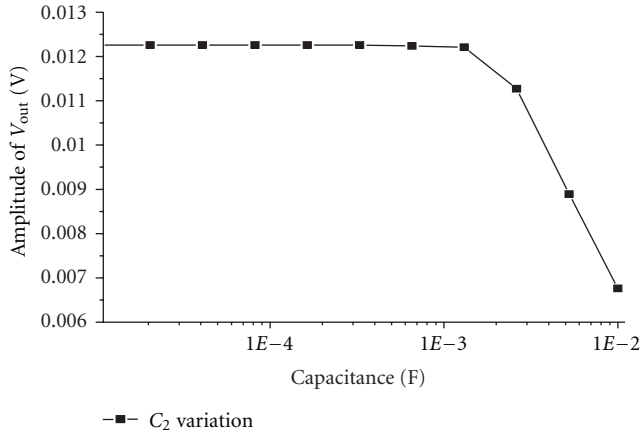

Figure 22: Response characteristic of the output voltage for the pulse parameter for a change of the capacitance of C_2 (10 (nF)~10 (mF)).

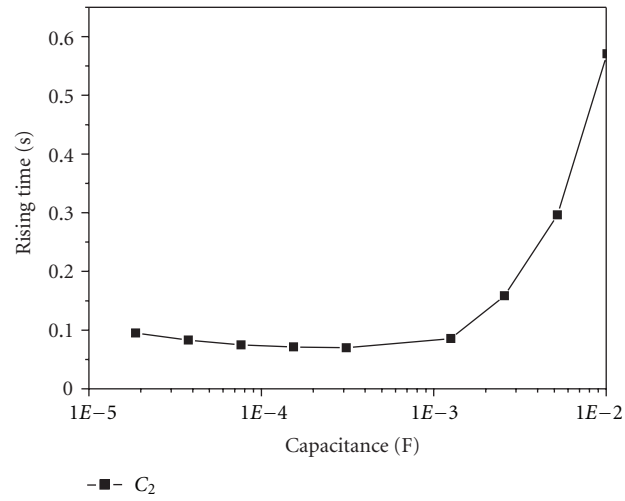

Figure 23: Response characteristic of the rising time for the pulse parameter for a change of the capacitance of C_2 (10 (nF)~10 (mF)).

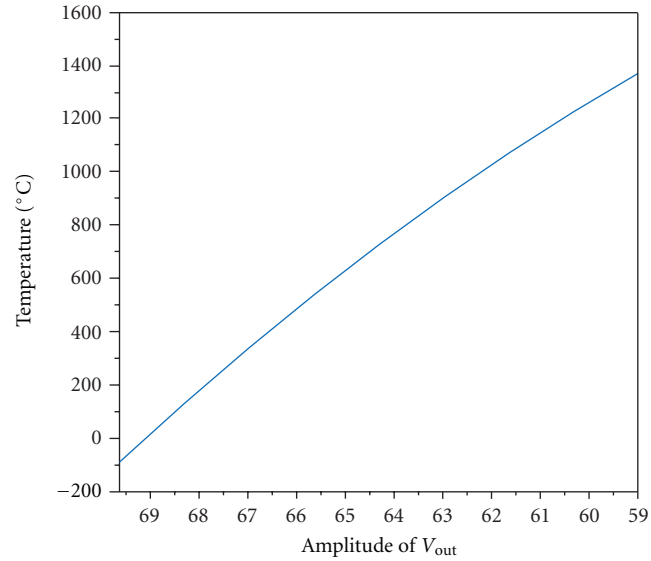

Figure 24: Relation curve between the T temperature and the Amplitude of V_{out} according to (1).

of the capacitance of C_2. In the case of the C_2 simulation using the tool code, it can be seen that the capacitance value changes for the high voltage level data which means a good linearity (sensitivity) response characteristic over the same range, in the case of an overall response characteristic with a decreasing response characteristic for an increasing capacitance at 1.31 (mF), until about 1.31 (mF) it was a steady state.

But the response characteristic of the rising time (Tr) for the pulse parameter which means a good linearity (sensitivity) for the response characteristics over the same range, in the case of an overall response characteristic reveals an increasing response characteristic for an increasing capacitance of C_2 in the circuit according to basic circuit theory.

5. Correlation Equation

5.1. Correlative Equation between R_2 and Temperature. There is a correlative equation between the temperature and the amplitude of an output voltage in the equivalent circuit, which means that R_2 has been changing in the resistance range as a distributed parameter when the T temperature has been changing in the temperature range due to the accident conditions. Equation (1) is a correlative equation between the temperature and the amplitude of an output voltage. Figure 24 shows a relation curve between the T temperature and the amplitude of the V_{out} according to (1). From this

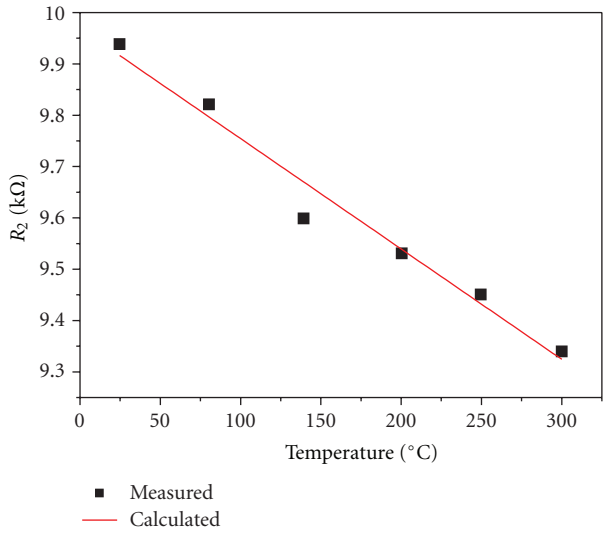

Figure 25: Relation curve between R_2 and the T temperature according to (2).

equation, for an inverse operation, it could also be said that T temperature has been changing in the temperature range when R_2 has been changing in the resistance as a distributed parameter in the equivalent circuit due to the accident conditions. In this case of the changing R_2 resistance value according to the changing temperature, experimental data is obtained by using in an electric oven as a real test. Equation (2) is also a correlative equation between the temperature and the amplitude of an output voltage, in the case of the changing R_2 resistance according to the T temperature. Figure 25 shows the relation curve between the R_2 and the T temperature according to (2). Table 1 shows the changing R_2 resistance range according to the temperature changing range in a real test using in an electric oven:

$$T = \frac{((1/(R_3 + R_7 + R_8))(i_m R_8/v_0 - 1) - 1/R_1)^{-1} - R_0}{c_1} + T_0, \quad (1)$$

$$R_2(T) = c_1(T - T_0) + R_0, \quad (2)$$

where T: changing temperature, T_0: normal/initial temperature, R_0: normal/initial resistance, $R_2(T)$: changing resistance at T temperature, c_1 : 1st-order temperature coefficient, i_m: maximum input pulse current, v_0: the normal/initial voltage, and R_3, R_7, R_8: the circuit elements.

5.2. Relation between the C_1 and the Time Constant. The changing range for the time constant of the output voltage in the equivalent circuit when the C_1 has a maximum changing range from 33 nF to 33 mF, to be placed in extreme simulation conditions should be investigated. From the simulation result, it is also possible to explain an approximate equation for the relation between the C_1 and the time constant. In the case of above 33 uF, the time constant of the output voltage has a response characteristic as a steep

Table 1: R_2 Resistance changing range according to the temperature changing range in a real test.

T (°C)	R_2 (kΩ)
25	9.94
80	9.82
140	9.60
200	9.53
250	9.45
300	9.34

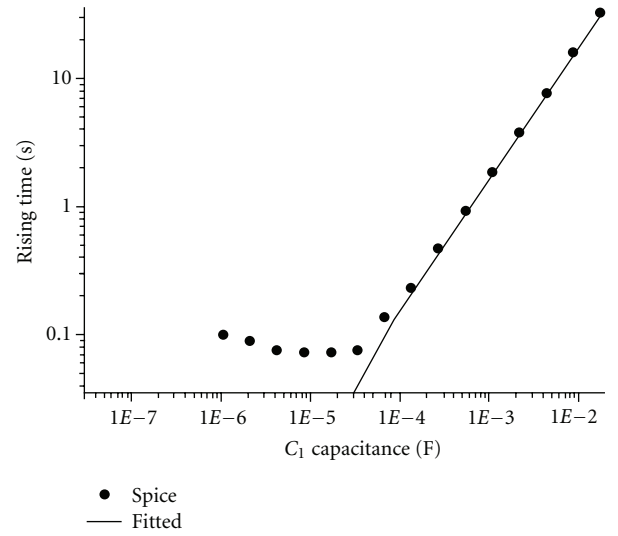

Figure 26: A linear response characteristic between the rising time and C_1.

slope but it has response characteristic of almost no change when the C_1 has a changing range from 33 nF to 33 uF. Therefore, the time constant of the output voltage has a linear response characteristic when the C_1 has a changing range from 33 uF to 33 mF. Figure 26 shows a linear response characteristic between the rising time parameter and when C_1 has a changing range from 33 uF to 33 mF. Equation (3) defines a relation between the C_1 and the time constant as a rising time parameter from an output voltage shape. When the t is a time constant as a rising time parameter, c is the 1st-order temperature coefficient for the C_1 changing range. To obtain a rising time for R-C elements, Figure 27 shows changing output data for the pulse parameter for a changing range of the temperature of C_2 (27 (°C) ~ 87 (°C)) according to correlation equation temperature coefficient to the time constant as a rising time parameter for R-C elements. Table 2 is output parameters of the pulse parameter according to a change of the capacitance of C_1:

$$t = 1682c - 0.0155417, \quad (3)$$

where t: time constant as a rising time parameter, c: 1st-order temperature coefficient.

Table 2: Output data of the pulse parameter according to a change of the capacitance of C_1.

C_1 (Parameter)	Amplitude	Rising time	Falling time
33 n	$1.2240E-02$	$1.08E-01$	$6.88E-02$
66 n	$1.2240E-02$	$1.08E-01$	$6.88E-02$
132 n	$1.2240E-02$	$1.07E-01$	$6.88E-02$
264 n	$1.2240E-02$	$1.06E-01$	$6.88E-02$
528 n	$1.2250E-02$	$1.04E-01$	$6.88E-02$
1.056 u	$1.2250E-02$	$9.95E-02$	$6.88E-02$
2.112 u	$1.2240E-02$	$8.95E-02$	$6.88E-02$
4.224 u	$1.2250E-02$	$7.58E-02$	$6.88E-02$
8.448 u	$1.2250E-02$	$7.27E-02$	$6.88E-02$
16.896 u	$1.2240E-02$	$7.20E-02$	$6.88E-02$
33.792 u	$1.2240E-02$	$7.48E-02$	$8.35E-02$
67.584 u	$1.2260E-02$	$1.37E-01$	$1.41E-01$
135.168 u	$1.1740E-02$	$2.33E-01$	$2.15E-01$
270.336 u	$9.7300E-03$	$4.67E-01$	$2.57E-01$
540.672 u	$7.2800E-03$	$9.28E-01$	$2.67E-01$
1.08 m	$5.5400E-03$	1.86	$2.68E-01$
2.16 m	$4.0600E-03$	3.77	$2.68E-01$
4.33 m	$2.6500E-03$	7.71	$2.70E-01$
8.65 m	$1.5400E-03$	15.82	$2.73E-01$
17.3 m	$5.4459E-04$	32.39	$2.74E-01$
33 m	$1.4995E-04$	63.16	$2.79E-01$

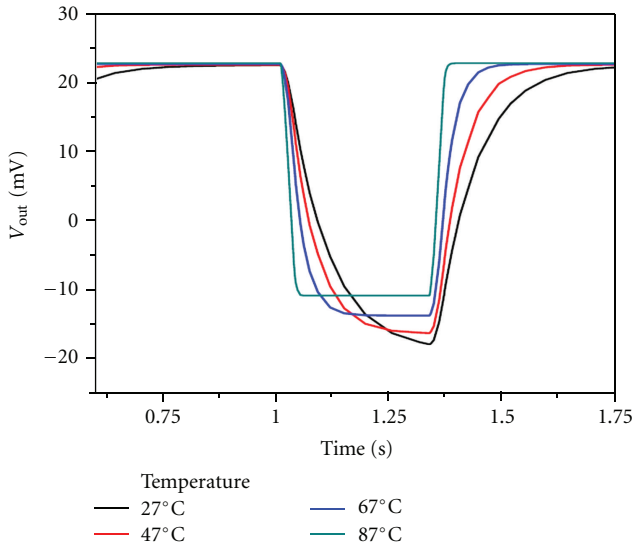

Figure 27: Output data for the pulse parameter for a change of the temperature of C_2 (27 (°C) ~ 87 (°C)).

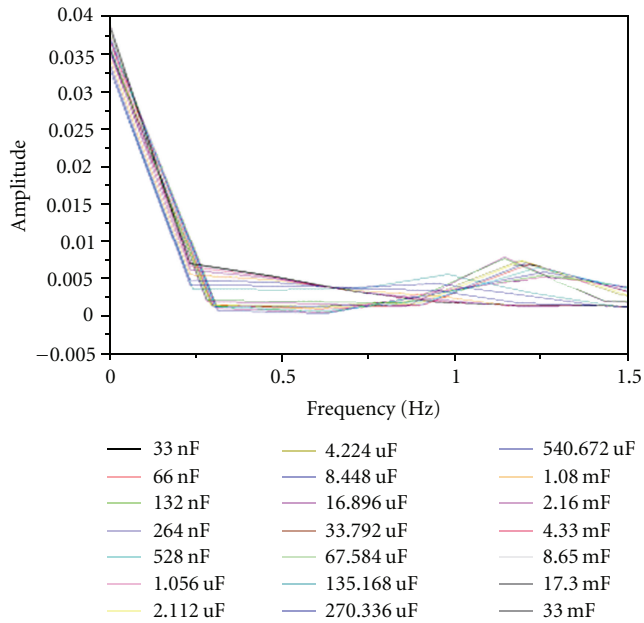

Figure 28: Frequency response characteristic of two dimensions of the pulse parameter for a change of the capacitance C_1.

5.3. Data Analysis. We could obtain frequency response characteristics of the multidimensions from the pulse parameter for a changing range of the capacitance C_1. From this Fourier fast transform (FFT) analysis of the 3 dimensions plot, it will find the activity of distorting shape and it become loosing for a direct current (DC) property for a changing range. Therefore, it also will be able to provide correct fault detection and diagnosis of the faulted components through the monitoring system for error signal detection and diagnosis. Figures 28 and 29 show frequency response characteristic each of two dimensions and three dimensions

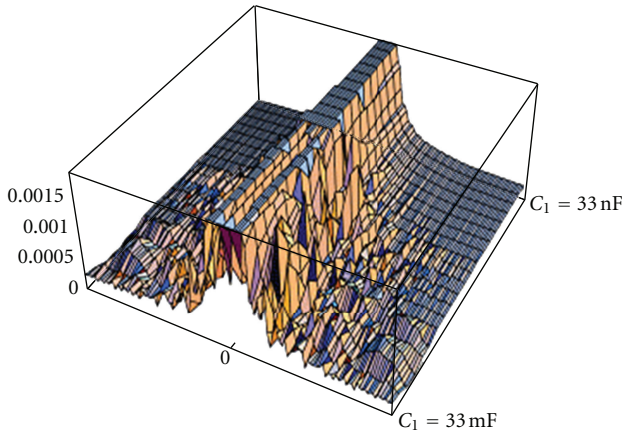

Figure 29: Frequency response characteristic of three dimensions of the pulse parameter for a change of the capacitance C_1.

of the pulse parameter for a change of the capacitance C_1, respectively.

6. Conclusions

In this paper, we provided a new simulator (called ASSA) developed through a circuit simulation with instrument diagnosis methods. Its underlying design requirements are fundamentally based on both EPRI TR-103412 and EPRI TR-102371 covering a variety of information for the performance assessment of plant instrumentation under severe accident conditions. As an alternative device to real systems, the simulator makes it possible for operators to take a correct action through a reasonable assessment of the performance of the plant instrumentation, even for severe accidents. The ASSA module system has been designed through a realization of a one body order system of one program linked to signal analysis tool programs and to an abnormal signal simulation engine as a one order command. As a result, the program will be able to analyze data quickly and conveniently, onsite.

Using the ASSA module system, we could obtain the response characteristics from the output voltage levels of a pulse parameter according to a change of the resistance for each of R_2, and R_3, and the response characteristic from the output voltage level data and time constant of the pulse parameter according to a change of the capacitance for each of C_1, and C_2. For the case of the pulse parameter following a change of the resistance, we obtained good response characteristics for the output voltage level data. For the case of the pulse parameter following a change of the capacitance, we could obtain much better response characteristics for the output voltage level data including the time constant patterns. With the ASSA module system, we additionally obtained a type of the varying signal patterns by a simple change of another element's *R-C* values. The forgoing function of the ASSA module makes it possible to change the abnormal signal patterns by changing the element *R-C* value and by using specific signal processing. In this paper, we can also obtain a correlative equation between the temperature and the amplitude of an output voltage in the equivalent circuit, which means that an R_2 has been changing in the resistance range as a distributed parameter when the T temperature has been changing in the temperature range by accident conditions. While the system module makes a signal analysis of noise patterns easy and convenient, it has not been built as a full simulation system as of yet. To make the ASSA module fully available for harsh environments, further research must be focused on developing an *R-L-C* (including active elements: a diode, N-P-N, P-N-P transistors) correlation equation for reflecting the effects of the circumstance parameters such as a high temperature, high pressure, high humidity, and high radiation. Since a variety of simulations to check on malfunctions or abnormal indications from instruments are possible through the ASSA module, it is possible to develop an alternative method to check on a degradation of the instruments with diagnosis logics for severe conditions and a database from the ASSA module analysis results.

Acknowledgment

This study has been carried out under the Nuclear R&D Program by the Korean Ministry of Education, Science and Technology.

References

[1] Fauske & Associates, "Severe accident management guidance," Tech. Rep. EPRI TR-101869, Fauske & Associates, Burr Ridge, Ill, USA, 1992.

[2] NUREG/CR-5444, "Instrumentation availability during sever accidents for a boiling water reactor with a MARK 1 containment," Tech. Rep. EGG-2661, 1992.

[3] M. E. Yancey and R. C. Strahm, 1985, Examination and Evaluation of TMI-2 Transmitters CF-1-PT4 and CF-2-LT, GEND-INF-029, Vol. III.

[4] J. Horn, R. W. James, and D. E. True, "Assessment of existing plant instrumentation for severe accident management," Tech. Rep. EPRI TR-103412, 1993.

[5] C. A. Negin et al., "Instrument performance under severe accident conditions," Tech. Rep. EPRI TR-102371, 1993.

[6] K. M. Koo, S. B. Kim, H. D. Kim, and H. Y. Kang, "Design for a new signal analyzer through a circuit modeling simulation as a one body system for SAC's," in *Proceedings of the International Congress on Advances in Nuclear Power Plants (ICAPP '06)*, pp. 1028–1032, Reno, Nev, USA, June 2006.

[7] K. M. Koo, S. B. Kim, H. D. Kim, and H. Y. Kang, "Design for a new signals analyzer through the circuit modeling simulation under severe accident conditions," in *Proceedings of the IEEK Fall Conference*, vol. 28, pp. 171–174, Seoul, Korea, November 2005.

[8] K. M. Koo, S. B. Kim, H. D. Kim, and H. Y. Kang, "Frequency analysis and new diagnosis by the important circuit modeling simulation including active elements under severe accident conditions," in *Proceedings of the Korean Standard Nuclear Power Plant (KSNP '03)*, pp. 184–186, October 2003.

[9] K. M. Koo, S. B. Kim, H. D. Kim, and H. Y. Kang, "Assessment of existing Ul-Jin 3~4 plants instrumentation for severe

accident management," in *Proceedings of the Korean Standard Nuclear Power Plant (KSNP '04)*, pp. 144–146, June 2004.

[10] B. Jones, 2008, Method and Apparatus for Real-time Pulse Parameter Estimator, Pub. No.: US 2008/0298514 A1.

Hindawi Publishing Corporation
Science and Technology of Nuclear Installations
Volume 2012, Article ID 209420, 11 pages
doi:10.1155/2012/209420

Research Article

Severe Accident Simulation of the Laguna Verde Nuclear Power Plant

Gilberto Espinosa-Paredes,[1] Raúl Camargo-Camargo,[2] and Alejandro Nuñez-Carrera[1]

[1] *Área de Ingeniería en Recursos Energéticos, Universidad Autónoma Metropolitana-Iztapalapa, Avenida San Rafael Atlixco 186 Col. Vicentina, 09340 Mèxico City, DF, Mexico*
[2] *Nuclear Safety Division, Comisión Nacional de Seguridad Nuclear y Salvaguardias, Doctor Barragán 779, Col. Narvarte, 03020 Mèxico City, DF, Mexico*

Correspondence should be addressed to Alejandro Nuñez-Carrera, anunezc@cnsns.gob.mx

Received 30 December 2011; Revised 13 March 2012; Accepted 30 March 2012

Academic Editor: Jun Sugimoto

The loss-of-coolant accident (LOCA) simulation in the boiling water reactor (BWR) of Laguna Verde Nuclear Power Plant (LVNPP) at 105% of rated power is analyzed in this work. The LVNPP model was developed using RELAP/SCDAPSIM code. The lack of cooling water after the LOCA gets to the LVNPP to melting of the core that exceeds the design basis of the nuclear power plant (NPP) sufficiently to cause failure of structures, materials, and systems that are needed to ensure proper cooling of the reactor core by normal means. Faced with a severe accident, the first response is to maintain the reactor core cooling by any means available, but in order to carry out such an attempt is necessary to understand fully the progression of core damage, since such action has effects that may be decisive in accident progression. The simulation considers a LOCA in the recirculation loop of the reactor with and without cooling water injection. During the progression of core damage, we analyze the cooling water injection at different times and the results show that there are significant differences in the level of core damage and hydrogen production, among other variables analyzed such as maximum surface temperature, fission products released, and debris bed height.

1. Introduction

Currently Laguna Verde Nuclear Power Plant (LVNPP) uses, for decision-making in emergency case, the Emergency Operating Procedures Guides (EOPG) in order to ensure safe operation and prevent serious consequence in case of possible accident. However, the EOPG does not include the stage of core damage and currently, for the specific case of the LVNPP, there is not a clear definition about the develop of specific guidelines for the management of the severe accident.

LVNPP has two units and is located on the coast of the Gulf of Mexico in the municipality of Alto Lucero in the state of Veracruz. Both units of this plant have a boiling water reactor nuclear steam supply system as designed and supplied by the General Electric Company and designated as BWR 5.

The primary containment is part of the overall containment system, which provides the capability to reliably limit the release of radioactive materials to the environs subsequent to the occurrence of the postulated Loss-of-coolant accident (LOCA) so that offsite doses are below the *reference values* stated in Title 10 of the United States Code of Federal Regulations, Part 50 [1]. The design employs the drywell/pressure-suppression features of the BWR/Mark II containment concept [2].

The Unit 1 started operation in 1990 and the Unit 2 in 1995 with rated power levels of 1931 MWt each. The Unit 1 has been operated with a capacity factor of 80.73% and the Unit 2 with 85.34%, and this NPP contributes with the 4% of the national electricity production. This NPP utilizes a single-cycle forced circulation BWR provided by General Electric (GE). LVNPP was originally designed to operate at a gross electrical power output of approximately 695 MWe and a net electrical power output of approximately 674 MWe.

The thermal power was uprated by 5% (from 1931 MWt to 2027 MWt) during cycle 7 for unit 1 and cycle 4 for unit 2. In December of 1999, both units were authorized to operate

to power uprate conditions. In July of 2008, the Comisión Federal de Electricidad (CFE, Mexican Electric Power Company) submitted the applications to the Mexican Regulatory Authority (CNSNS) for an operating license at power level of 2317 MWt. This corresponds to 120% of the original licensed thermal power (OLTP). This approach is referred as constant pressure power uprate (CPPU) because there are no changes in reactor dome pressure for this extended power uprate (EPU).

The BWR are designed with structures, systems, and components (SSCs) to accommodate steam flow rate at least 5% above the original rating. Safety analysis using better computer codes, methodologies, and operation experience allow the increase the thermal power by 5% without any hardware modification in the nuclear steam supply system (NSSS). However, the power increases up to 20% involve major changes in the SSC. Changes in the main condenser, turbine blades, main generator, steam reheater, and booster pump with more capacity are some of the most important changes performed in LVNPP.

In nuclear safety, defense in depth concept should consider accident conditions beyond design basis (severe accidents), although these are highly unlikely, and such conditions have not been explicitly addressed in the original design current nuclear power plants.

An important part of mitigating the damage to the core is the cooling of the debris produced during the melting of the core, but so far not known with certainty at what point should be the cooling by any of the emergency systems and whether it is appropriate to do so. Then, the aim of this work is to present numerical experiments in transient conditions to analyze the behavior of progression of core damage, and consequences such as hydrogen generation and fission products released: (1) without coolant injection in the core region and (2) three different times of the coolant injection with the high-pressure core spray (HPCS) during scenario of a LOCA. The LVNPP model was developed using RELAP/SCDAPSIM code [3–5].

At least until 2003, RELAP/SCDAPSIM [3–5], MELCOR [6], and MAAP4 [7] have been considered as three representative U.S. computer codes that are being widely used for the integral analysis of the core melt accident progression [8]. In this work, we used the RELAP/SCDAPSIM computer code for the analysis of the core and lower plenum phenomena in the simulation of the postulated accident LOCA with and without cooling in LVNPP. RELAP/SCDAPSIM considers the core and vessel with two-dimensional model both axial and radial directions.

2. System Description

In order to understand the phenomena of the thermohydraulics process during a hypothetical LOCA with core damage, we presented a brief description of a BWR, where Figure 1 shows the schematic diagram [9].

The reactor water recirculation system (circulates the required coolant flow through the reactor core) consists of two external loops to the reactor vessel. The jet pumps located within the reactor vessel provide a continuous internal circulation path for a major portion of the core coolant flow. The recirculation pumps take the coolant suction from the downward flow in the annulus between the core shroud and the vessel wall. This flow is discharged into the lower core plenum from jet pumps. The coolant water passes along the individual fuel rods inside the fuel channel where it boils and becomes a two-phase steam/water mixture. In the core, the two-phase fluid generates upward flows through the axial steam separators while the steam continues through the dryers and flows directly out through the steam lines into the turbine generator.

The LOCA is postulated as rupture in the suction of the recirculation pipe as is illustrated in Figure 1, in this figure can be observed that the emergency cooling systems: high-pressure core spray system (HPCS), low pressure spray system (LPCS), and low-pressure coolant injection system (LPCI) that inject in the upper plenum.

3. Preliminaries

A severe accident is one that exceeds the design basis of the plant sufficiently to cause failure of structures, materials, systems, and so forth, without which it can ensure proper cooling of the reactor core by normal means [10]. Faced with a severe accident the first response is to try to maintain the core cooling by any means available, but in order to carry out such an effort, the response is understand necessary the progression of core damage, because such action has effects that may be determinants in the progression of the accident.

Due to that the severe accident phenomenology is very broad and not all aspects can be studied with a computer code of analysis of the core damage [8]. Then, the information presented in this paper is focused on the study of the progression of core damage phenomena called "In-Vessel". These phenomena are dominated primarily by the temperature, which increases significantly in the absence of coolant flow. Figure 2 shows the progression of core damage for a BWR reactor as a function of temperature [11].

The overheating in the fuel due to lack of cooling, the decay heat, and the chemical reaction between the zirconium and steam, in about an hour, start to discover the fuel, causing the temperature in the center of the core can reach high values, such as 2000 at 2600°C, so the core begins to melt. With the LOCA scenario, these processes are observed and analyzed in this work.

The molten material will flow slowly down by gravity effects into the lower regions, and colder of the core region, where it resolidifies and blocks the channels between the fuel rods. By this mechanism, a block of solidified material (basin-shaped) of the core (corium) is formed, which collects the molten material. When a sufficient amount of molten material is collected, it will flow to the bottom of the reactor vessel. After a certain time (greater than 30 minutes), the amount of molten corium has flowed to the bottom of the vessel which may correspond to about two thirds of the fuel material from the core region. The rest of the combustible material overheats more slowly and may take several hours to melt. Finally, if the molten material of the core cannot cool due to the loss of geometric and failure of the cooling

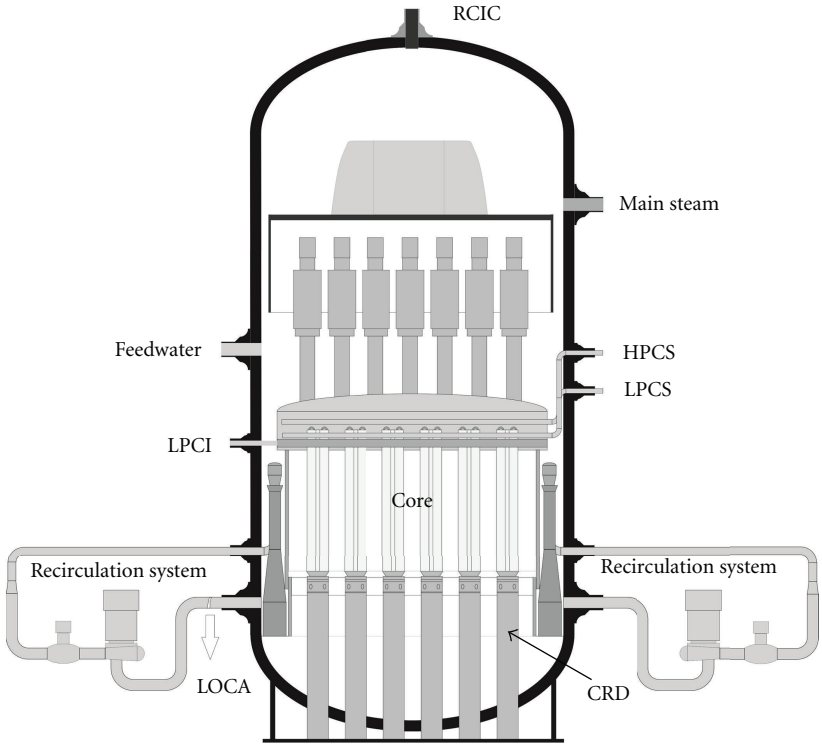

Figure 1: Schematic diagram of the boiling water reactor (BWR) [9].

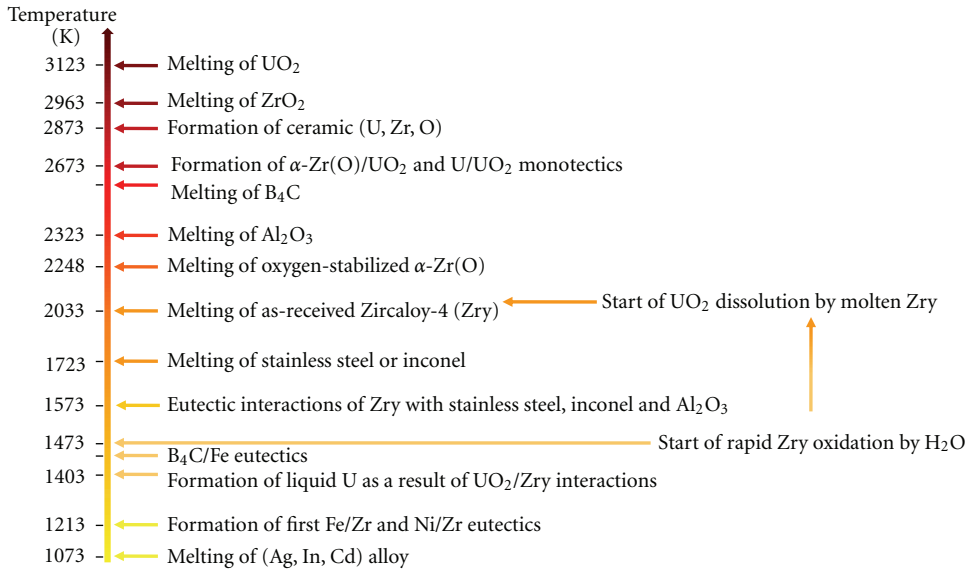

Figure 2: Progression of core damage.

systems, the wall of the reactor vessel will fail. If at that time the pressure in the reactor coolant system is low, the corium will flow down the cavity of the container. If the pressure is high, the corium is violently eject and dispersed. The impacts on the containment due to these two scenarios are completely different, but in both cases, the containment can fail early or late or even may remain intact.

3.1. Core Damage Progression. As a result of heat produced by radioactive decay of the active elements, known as the decay energy, the fuel temperature begins to rise, even when the reactor is off after a scram, if the core cooling is inadequate [12].

In the case of severe accidents, where it is anticipated that the safety engineering systems (IS) functions incorrectly, to the extent that the core loses its cooling, the core will be damaged by overheating and release radioactive elements, mainly the primary system reactor.

At temperatures of 1073 K, molten occurs of the alloy Ag-In-Cd of the control rod for pressurized water reactors

(PWRs, Figure 2), the molten alloy is thermodynamically stable within the fuel element due to pressure vapor of the alloy, especially due to cadmium. For BWR, the molten of the control rods occurs around 1,500 K, and according with CORA 17 experiment, the release of energy and hydrogen production is higher than a PWR as the steam reaction with the remnant B_4C, absorber of the BWR control rods, is more exothermic per gram of material than Zircaloy during the quench phenomenon [13].

The guide tube failure will cause the attack of the alloy Zircaloy of the fuel element. The liquid mixture may fall down by gravity effects and move into the core regions, causing localized damage in the fuel cladding. Eventually is resolidified and may produce blockage in cold areas of the lower region of the core region.

At temperatures around 1173 K, the zirconium of the fuel cladding begins to react chemically with steam, which produces hydrogen and reaction heat.

At temperatures above 1500 K, the reaction becomes very large, accelerating overheating of the fuel, the oxidation of zircaloy (Zr) of the fuel cladding by steam effects, it becomes important. This reaction is exothermic and the temperature increases the rate of oxidation increases, the energy release is large as well as the generation of hydrogen (H_2).

The hydrogen production rate depends on the temperature of zirconium in the core and the amount of steam available. When the temperature rises about 1500 K, the following reaction can be carried out:

$$Zr + 2H_2O \longrightarrow ZrO_2 + 2H_2 + 586\,\text{kJ/mol}. \quad (1)$$

On the other hand, the heating of the fuel elements results in loss of mechanical properties with consequent ballooning that can lead to breakage. The deformation occurs due to the difference in pressure between the inside of the fuel element and reactor pressure. The internal pressure of the fuel element is a function of fuel temperature on the thermodynamic process of heating at constant volume. Regarding the reactor pressure will depend on the type of accident. Large breaks in the primary cooling system have much higher risk of ballooning when the pressure of the system mentioned above is almost atmospheric.

The effects of ballooning in the fuel elements are mainly to (1) reduce the passage section of coolant flow in the core and (2) hinder the cooling of localized areas of the fuel. Both phenomena lead a further increase in temperature and higher deformation. In addition to the deformation by pressure difference, it also can occurs due to thermal expansion. Another possible mechanism is the breaking strain differential expansion between the oxide layer and the inner layer of metal. This latter mechanism may induce breakage of oxidized fuel element even without differential pressure. The break of the fuel rods produces that the reaction between steam and cladding increases twice.

Experiments have shown that the rupture of the fuel does not block the flow of steam but whether it deviates by reducing the natural flow in the core. The fuel temperature increases and most of the hydrogen generated in the accident occur during this early stage.

At intermediate temperatures (2033 and 2273 K), if the thickness of the oxide layer is sufficiently large, the oxide will retain the Zr molten metal, preventing the fall down by gravity and staying in touch with the pellets of dioxide uranium (UO_2), which will remain until the outer layer of oxide loses their resistance due to its dissolution by molten Zr or due to mechanical failure or because it reaches the melting temperature (2963 K) of ZrO_2.

If the fuel element has ballooned previously, the ability to contact the pellets will be reduced, thereby reducing the ability of UO_2 dissolution. In the analysis of severe accidents, the phenomenology is very important because it is capable of producing nuclear fuel liquefaction temperatures (1000 K) below the melting point of the UO_2 (3123 K), where the interaction process is complex.

At temperatures above 2873 K will occur the melting of ceramic materials UO_2, ZrO_2 and mixed oxide (U, Zr) O_2, and total loss of the geometry of the affected zone.

4. Severe Accident Scenarios for the LVNPP

The severe accidents simulations consider the occurrence of the postulated LOCA in the recirculation loop of the reactor (Figure 1), with water coolant injection with HPCS at different times. Also, another scenario considered the postulated LOCA without water coolant injection. For this study, we used as a reference the data presented in Figure 2, which is information that Innovative Systems Software (ISS) has published [11] and that is generally similar the reference [14].

5. Numerical Model of the LVNPP

The nuclear steam supply system (NSSS) whose function is to carry the steam from the reactor vessel to the main turbine, and then drive the feed-water flow from the condenser to the vessel, holding constant all parameters in the reactor. The NSSS model representing the LVNPP using SCADAP/RELAP5 is illustrated in Figure 3. The operating conditions correspond to power uprate (PU) LVNPP, that is, 2027 MWt of the thermal power rate. This model includes the following main elements: (1) feed-water system, (2) reactor vessel and internals, (3) recirculation loops, (4) the reactor core, (5) main steam line, (6) bottom of the reactor vessel. The bottom model of the vessel is a fundamental element for the analysis in accident scenarios, for which it is included as a separate element that interacts with the other models.

6. Numerical Experiments

In order to evaluate the effect of time on the core cooling, we considered various cases, starting from a steady-state reactor of the LVNPP at to power uprate conditions (2027 MWt). In particular, we present the results and discussions of three conditions at different times of injection of HPCS, for reference conditions Which were determined without the performance of security systems, subsequently with damage in the core region was injected coolant flow with the HPCS

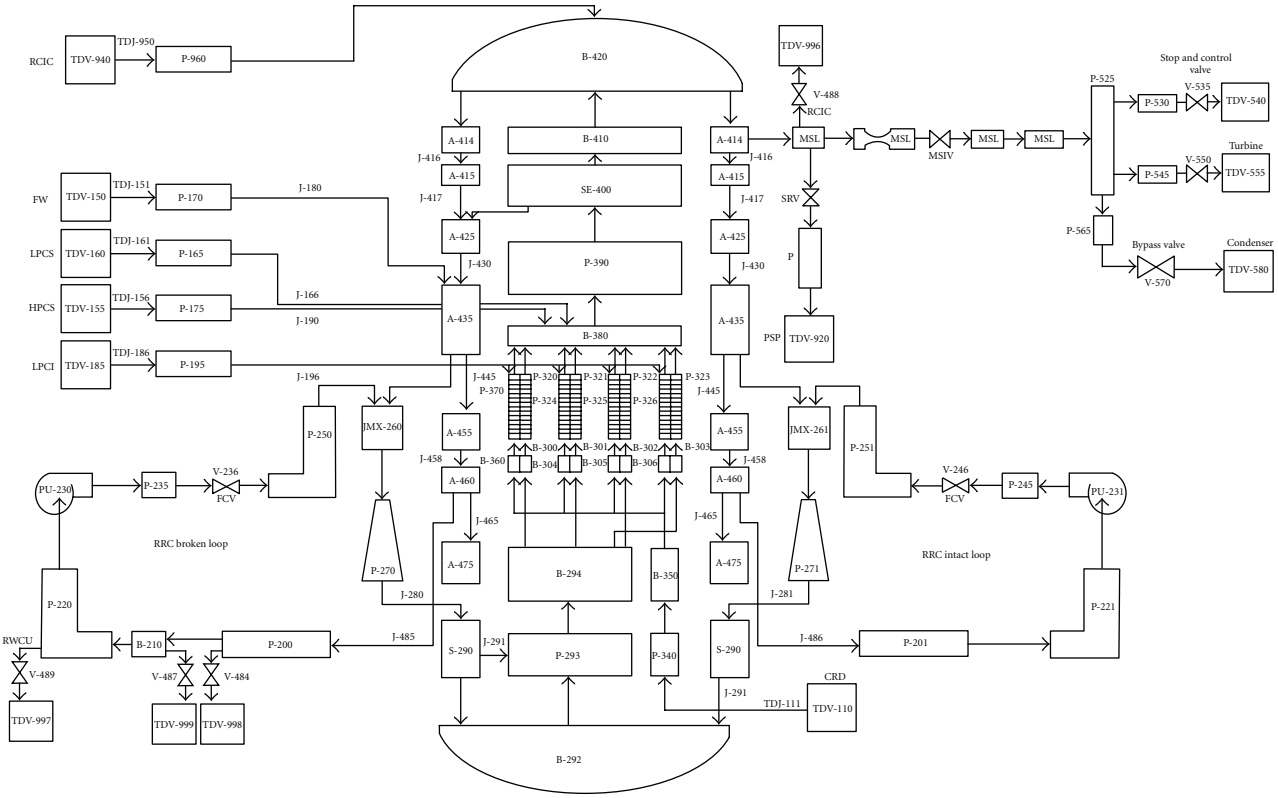

Figure 3: SCADAP/RELAP5 Laguna Verde Nuclear Power Plant model [22].

at 700, 900, 1200 s; therefore, four numerical experiments are analyzed in this work.

For each numerical experiment the following parameters were analyzed:

(i) collapsed level,

(ii) pressure in the dome of the vessel,

(iii) maximum surface temperature in the core region,

(iv) noncondensable fission products released,

(v) soluble fission products released.

(vi) hydrogen generation,

(vii) core damage,

(viii) control rod damage,

(ix) debris bed height in lower plenum.

7. Simulations and Discussions

A comprehensive analysis of the nuclear reactor during the transient evolution for the LOCA event with and without cooling is presented in this section.

The studied scenario (base case) is a loss of coolant accident (LOCA) due to rupture of a pipe in a recirculation circuit, imposing no coolant flow injection in the core region. This causes the signal to activate isolation of main steam (MS) and activates the coolant injection systems. Due to this, recirculation pumps trips and reactor scram occure. Subsequently, we expected decrease of the thermal power, level, pressure in the dome, steam flow, feed-water flow, and mass flow rate in the core, the close of the main steam insolation valves (MISVs) and trips the feed-water turbine pumps. The reactor collapsed level drops dramatically activating the emergency core cooling systems but these do not provide coolant flow, which causes damage in the core region.

The sequence of events is presented in summary form in Table 1, for the case without cooling effects. In this table, it is observed that the hypothetical accident due to LOCA and no available emergency systems to cooling core, where at 324 s the hydrogen generation starts. Oxidation of the cladding, rods, and other components in the core constructed in zirconium base alloy, by steam, is a critical issue in LWR accident producing severe core damage. During a severe accident in a nuclear reactor, several works are focusing on core degradation by metal core components oxidation by air or steam (e.g., [15–18]), on the other hand, Royl et al. [19] have made a hydrogen risk analysis during severe accident using computational fluid dynamics (CFD) codes, to obtain localized detailed information and supplement the results of lumped parameter codes, which focus on global or average effect.

In this table, the maximum surface temperature in the core at different times match the event which is related with the progression of the core damage as is illustrated in the schematic diagram of the Figure 2.

The numerical results of nuclear reactor during the transient evolution for the LOCA event with and without cooling are presented in Figures 4–10.

Table 1: Main sequence of events in a LOCA without cooling effects.

Time (seconds)	Event
0.0	The reactor operates to power uprate conditions (2027 MWt).
30.0	Loss of external power, loss of coolant in a recirculation loop, closing of the turbine control valves, and trip of the reactor and recirculation pumps.
34.3	Low level in the reactor vessel (L2), before high pressure occurs in the drywell. The emergency core cooling systems (HPCS* and RCIC*) are active without injecting. Starts closing insolation valves (MSIV*).
37.4	Low-low level (L1) is reached.
40.0	Level in the BAF*.
200.0	Level below the core support plate.
324.0	Hydrogen generation starts.
370.0	Maximum temperature at the core surface of 1073 K.
458.0	Core damage stage starts with release of fission products. Maximum Temperature at the core surface of 1185 K.
936.0	Control rod damage starts Maximum temperature at control rod of 2136 K.
1800.0	Core damage de 19%.
3600.0	Core damage of 78%.

*HPCS: high pressure core spray system; RCIC: reactor core isolation cooling; MISV: main steam insolation valves; BAF: bottom of active fuel.

The core melt accident progression can be divided into two stages.

(1) An early phase up to the partial melting of core material, where involves core uncover, heat up, and partial melting in the reactor core region.

(2) A late phase results in the significant melting of the core material with relocation, and redistribution in the lower plenum. The governing phenomena involves porous debris bed, molten pool, and formation cavity, where the process heat, momentum, and mass are complex due to very high temperatures, multicomponent and multiphase materials, melting and freezing process, and geometrical configurations.

In general terms, if not cooled in the core region, the molten core materials (known as corium that is a conglomerated mixture of various core materials; mainly but not exclusively as oxide component-UO_2, and ZrO_2-, metallic components-U, Zr, Fe, and stainless steel), accumulated on the core support plate, would be eventually relocated into de lower plenum region and the thermal attack on the lower plenum could occur. In the presence of water in the lower plenum, some portions of the relocating molten core material could be fragmented into small solid particles in the lower head, and the remain material will maintain its original

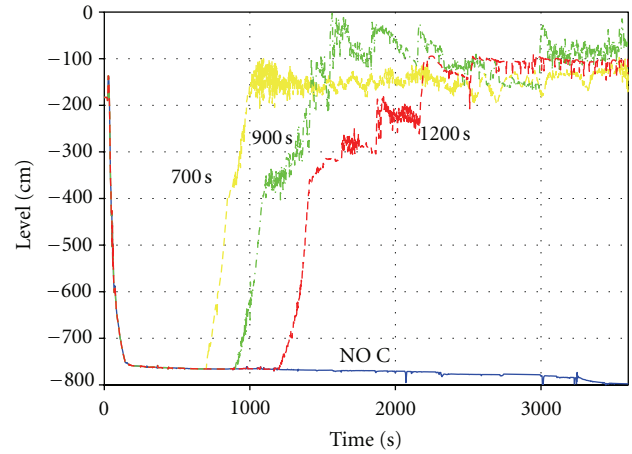

Figure 4: Level respect to top of active fuel (TAF) or fuel zone. HPCS injection to 700 s, 900 s, and 1200 s; NO C indicates without HPCS injection.

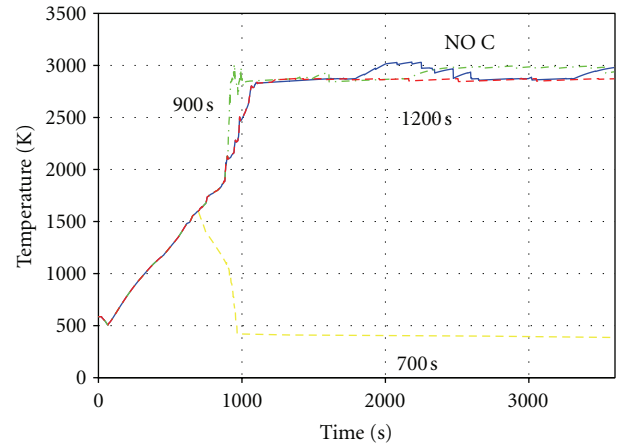

Figure 5: Maximum surface temperature in the core. HPCS injection to 700 s, 900 s, and 1200 s; NO C indicates without HPCS injection.

liquid phase [8]. The main mechanism of fragmentation (debris jet) is a hydrodynamics process, where rapid heat transfer from the debris jet to the lower plenum water accompanies the hydrodynamic fragmentation process and debris oxidation, results in steam and hydrogen production and an abrupt increase of the pressure. The heat removal from the lower head debris bed is determined by amount of the heat generated in the corium accumulated in the lower plenum, heat transfer inside the core material, heat transfer from the corium to the reactor vessel, and heat transfer to outer vessel.

7.1. Level Behavior. The transient behavior comparison of the level in the vessel respect to TAF (Top of Active Fuel) with and without cooling is shown in Figure 4. This figure shows that core is discovered for all cases analyzed in this work. The core discovers that time is crucial for the progression of the core damage, due to the temperature of the core region increase, even be lost cooling capacity. In all cases

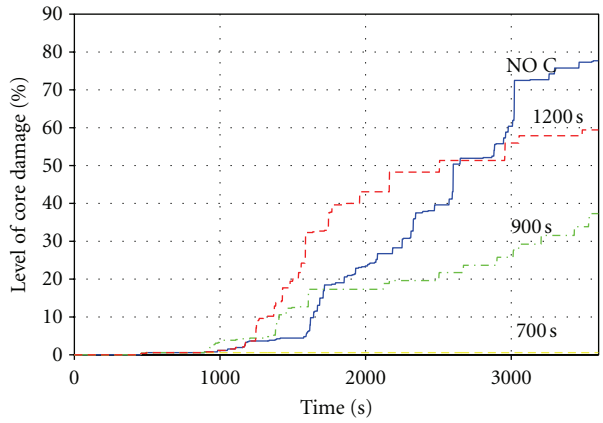

Figure 6: Level of core damage. HPCS injection to 700 s, 900 s, and 1200 s; NO C indicates without HPCS injection.

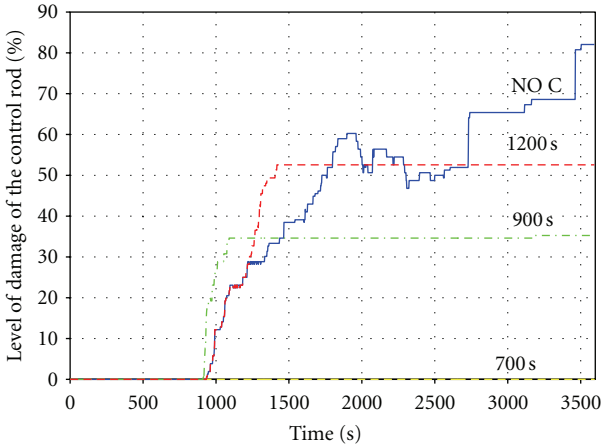

Figure 7: Level of damage of the control rod. HPCS injection to 700 s, 900 s, and 1200 s; NO C indicates without HPCS injection.

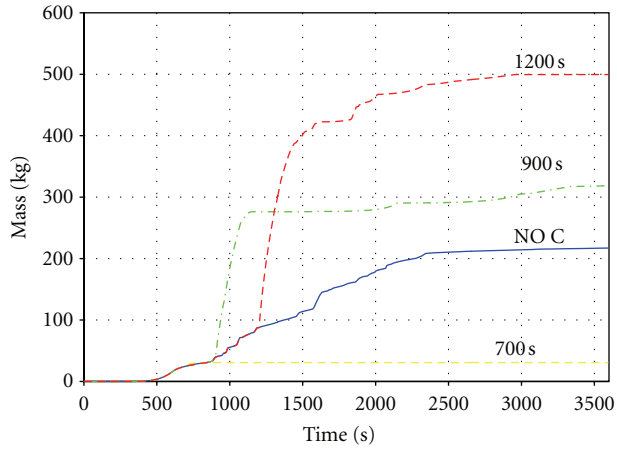

Figure 8: Core total hydrogen generation (kg). HPCS injection to 700 s, 900 s, and 1200 s; NO C indicates without HPCS injection.

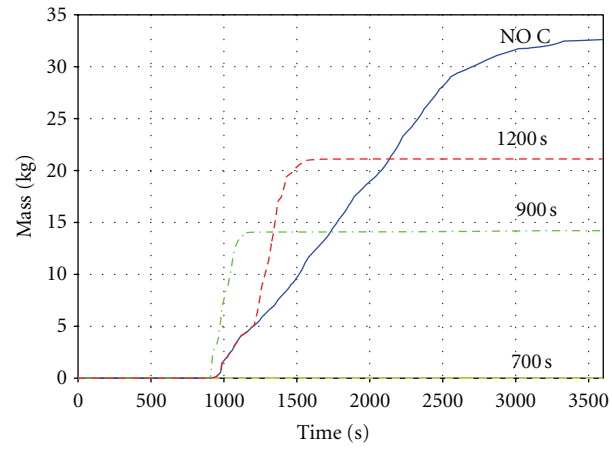

Figure 9: Noncondensable fission product released. HPCS injection to 700 s, 900 s, and 1200 s; NO C indicates without HPCS injection.

in which the coolant injected, recovering refrigerant level in the reactor vessel is according to the time of action of HPCS (Figure 4).

According with these results when the HPCS started, the water level in the vessel is partially recovered to ensure the reactor core cooling. Approximately in −400 cm, the increased level presents a change in trend accompanied (or mounted) by oscillations apparently of high frequencies, and these are very strong when the core is practically covered (−150 cm of the level) especially for the case of 700 s of HPCS injection, which is presented between 1000 to 1500 s of elapsed time in the simulation. These effects are produced due to convective heat transfer process between core region and the cooling where the rapid change of liquid phase to gas phase occurs, which causes variations of the pressure in the reactor vessel, these being the main phenomena. Regarding the 900 s of HPCS injection, it can be seen that these effects occur immediately after the coolant interacts with the core region which occurs at −400 cm of water level, while that for the case to 700 s occurs at −150 cm of water level. These differences between two cases (700 and 900 s HPCS injection) are the energy accumulated in the core region being higher for 900 s. Then, removing energy (900 s) with the same water flow of the HPCS is more complex respect to 700 s, which can be inferred due to the greater instabilities (respect to 700 s) along the simulation time (see 900 s in the Figure 4).

In the case of the 1200 s of HPCS injection, the water level in the reactor vessel is recovered but with significant lower stability, that is, apparently the steam by convective effects and heat transfer mechanism by radiation remove heat generated and accumulated in the core region at this time (1200 s) before the injection of HPCS; also can be observed some agglutinated oscillations of the level in approximately −300 cm and −200 cm characteristics the thermodynamics effects due to phase changes or due to pressure changes. For the case without HPCS injection, the progression of the core damage is expected and the consequences were widely discussed previously.

7.2. Maximum Surface Temperature in the Core. The behavior of the maximum surface temperature in the core is

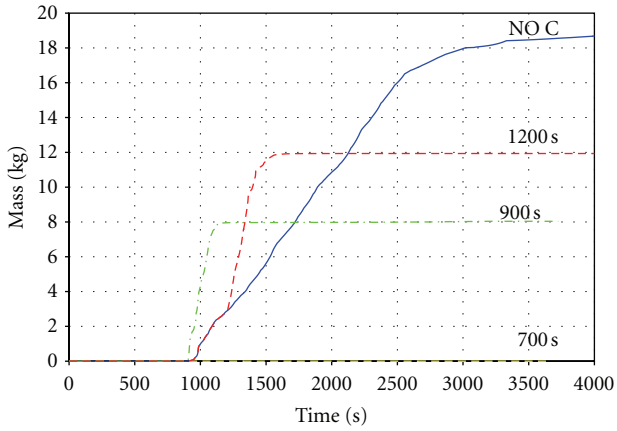

Figure 10: Soluble fission products released. HPCS injection to 700 s, 900 s, and 1200 s; NO C indicates without HPCS injection.

presented in Figure 5. For the case of 700 s of HPCS injection, the temperature increases linearly to a temperature of 1600 K at 700 s the elapsed time, under this conditions some fuel elements fail. When acts the HPCS at 700 s; the temperature decreases to 401 K at 900 s of elapsed time, due to presence of coolant removing the heat in the core region primarily by convective mechanism.

For the rest of the numerical experiments, that is, with cooling (HPCS injection to 900 s, 1200 s), and without cooling, it does not cool the core region, as can be observed in Figure 5. However, there are some peculiarities that it should be noted.

(1) At 900 s of HPCS injection, the temperature is approximately of 2126 K that represents conditions of significant core damage, in this case the presence of the coolant flow apparently increases the core damage due to presence the two temperature peaks of approximately of 3000 K. The interpretation physical of this peaks is that the chemicals reactions with materials of the core region (control rod, uranium oxide, Zr, etc.) in average are exothermic, this occurs in time lapse of 900 s to 1000 s the elapsed time, after this time, the temperature decreases to approximately to 2750 K, which is maintained until 2200 s of elapsed time, and after of this time, the temperature increases again to 3000 K, indicating the presence of complex phenomena such as loss geometry in the core region, therefore, some loss of cooling capacity due to coolant flow blockage.

(2) For the case of 1200 s of the HPCS injection and without cooling (NO C in Figure 5), the temperature behavior follows the same trends until 1800 s the elapse time, that is, the behavior is practically the same with and without cooling. It is important to note for cooling case at 1200 s, that the temperature is increased until of 2750 K and remains around this value from the 1150 s to complete simulation, that is, the presence of coolant flow is not responsible that for the temperature does not increase further, due to that the inflexion point occurs 150 s before injection of HPCS.

(3) For the case without cooling of the core region as was previously mentioned, the temperature behavior follows the same trends of the HPCS injection until 1800 s, in this time, a temperature increase can be observed slightly more than 3000 K, and at 2600 s of the elapse time, the temperature decreases to 2750 K, then afterward, therecan be observed some increases.

The preliminary conclusions according with the behavior of maximum surface temperature in the core, with and without cooling in the core region are as follows: (1) The injection of the HPCS at 700 s, cooling is achieved properly of the core region and the consequence of core damage can be stopped. (2) The injection of the HPCS at 900 s can be not recommendable due to exothermal process that cause large increase of the temperature (temperatures peaks) in the core region. (3) The injection of the HPCS at 1200 s has not significant effect and the behavior is similar to without cooling, apparently due to the loss of cooling capacity due to loss of geometry of the core region.

The energy accumulated and generated by different process such as chemical reactions is a indicative that the time the injection is crucial as after the core region, it is not possible to cool (with HPCS), at least at short times, the order of the hours. Also as is showed by results, the injection at 900 s generates higher thermal shock, which may make it harder to mitigate core damage.

Figure 5 is obtained using the variable BGMCT of RELAP/SCDAPSIM that represent the maximum temperature in the surface of the core, this case is observed that the maximum temperature in the surface of one axial node remains high even after the injection of the HPCS, this is because of the loss of configuration of the core, the hottest axial node is not cooled.

7.3. Level of the Core Damage. The behavior of the level of the core damage is presented in Figure 6. This result provides sufficient information to establish the effect of time of injection of cooling water to the core region. In this figure, it can be see that the simulation start with little core damage before of 500 s for four analyzed cases, that is, with injection (HPCS to 700, 900, and 1200 s) and without cooling the core region. The core damage that is represented in the Y axis (Figure 7) refers to 0% when all the axial nodes of the core fuel bundles are intact, and 100% refers when the whole axial nodes of the fuel bundles are in an intermediate stage as ballooning, rubble, and cohesive debris or molten. This core damage is a consequence of the deficiency or lack of cooling the reactor for a prolonged period of time; in this case, the core damage is presented at approximately 750 s. According to Figure 6, the level of core damage is about 1% for the case where the HPCS injection acts at 700 s.

Now, in the following analysis, we take as a reference the behavior without HPCS injection (NO C) to emphasize the importance of time of injection of cooling water in the core region. In Figure 6, it can be seen that without HPCS injection the core damage remains unchanged at a minimum

value (1%) until about 1000 s, and after this time the core damage increases. When the injection is at 900 s, the level of the core damage is greater than without cooling until 1750 s where the core damage rate increases slightly. For the case HPCS injection at 1200, this behavior is observed, that is, the level the core damage with and without cooling is practically the same until the 1250 s, after the presence of the cooling water accelerates the core damage whose increase is greater than without cooling case, after 1700 s, this behavior is reversed as can be observed in Figure 6.

In summary form, these results indicate that possible negative effect of cooling can be observed in cases of HPCS injecting at 900 to 1200 s, where a sudden increase (at early times of the injection) to the core damage is fully associated with the entry of coolant into the reactor, being greater the core damage than without coolant injection. However, in Figure 6, it can be observed that the rates of core damage decrease due to the phenomena associated with the heat removal.

7.4. Average Level of Control Rod Damage. The behavior of the level of the core damage is presented in Figure 7. According to these results in general terms, the negative effect of cooling can be observed in cases of HPCS injected at 900 to 1200 s, where a sudden increase to the control rod damage is fully associated with the entry of coolant flow into the core region, being greater than without injection for time elapse of 1400 s and 1800 s, respectively. We must notice that the level of damage in the control rods is a function of the cooling rate; therefore, the damage is greater when the cooling starts late or is missing. The control rods damage that is represented in the Y axis (Figure 7) refers to 0% when all the axial nodes of the control rods are intact, and 100% refers when the whole axial nodes of the control rods are not intact. In Figure 6, it is observed that the level of damage of the control rod decreased between 2250 s and 2600 s is an abnormal behavior and is attributable to a mistake in the version 3.2 of RELAP/SCDAPSIM.

7.5. Hydrogen Generation. The behavior of the hydrogen generation in the core region is presented in Figure 8. The hydrogen generation is coming mainly from the Zircaloy cladding oxidation and partly from the boron carbide oxidation of the control rod. In this figure, it can be observed that the level more low of hydrogen generation is when the HPCS injection acts at 700 s, and, therefore, the heat of reaction is less about the other cases studied. Now, when the HPCS injection acts at 900 s and 1200 s, the masses of the hydrogen generation are practically 11 (which is generated in 150 s) and 17 (is generated in 250 s) times greater than the case of the HPCS injection at 700 s (31 kg of hydrogen generated), respectively. Finally, in 3500 s of the elapsed time, the mass generated for the case of 900 s (HPCS injection) is 320 kg and for the case of 1200 s (HPCS injection) is 500 kg. In both cases, the rate of the heat due to oxidation reaction is very high with respect to the case of 700 s of HPCS injection. For the case without cooling with the HPCS, the mass of the generation hydrogen was 220 kg, being 7 times higher than the case of 700 s (HPCS injection).

From the point of view of hydrogen generation, it can be observed of the simulations results in Figure 8, that the following hold:

(1) Hydrogen production is maintained at a low level if the coolant flow is appropriate at the right time (in this work correspond to 700 s of the HPCS injection).

(2) If the coolant flow is not appropriate at the right time (cases 900 and 1200 s of HPCS injection), the hydrogen generation increases to more than one order of magnitude, due to coolant flow entering the core region, including the lower the hydrogen generation is smaller than without cooling as is shows in Figure 8.

(3) The consequences are the following: for the cases of the 900 s and 1200 s, the HPCS injection produces high rates of hydrogen generation due to oxidation and therefore high rates of heat of reaction because it is an exothermic reaction (clearly predominates in this numerical experiment this mechanism), which produces high temperatures at the core surface near 3000 K as is observed in Figure 5. Then, the reaction heat is crucial in the cooling of the core region, and the HPCS injection under these conditions is insufficient to cool the core region.

(4) The core and control rod damage (Figures 6 and 7, resp.) has two components that predominate; the first is the time without cooling flow, and reaction heat due to hydrogen generation.

7.6. Fission Products Released from Core Region. The prediction of the behavior of the released fission products from the core are presented in Figure 9 for noncondensable fission products and in Figure 10 for soluble fission products. The released fission products are a function of the level of the core and control rod damage (as was discussed previously in Figures 6 and 7), which is affected by the injection time of the HPCS. According to the progression of the core damage, the mass of fission products (noncondensable and soluble) is higher for the case without cooling (NO C in Figures 9 and 10), which presents higher level of core and control rod damage, with respect to the others cases, that is, 900 s and 1200 s (of HPCS injection).

For the case of 700 s of the HPCS injection, apparently no fission products are released. However, the core damage for this case is less than 1% (Figure 5) and the control rod damage is null (Figure 7). Obviously, one should expect the minimum amount of fission products released if there is failure the reactor core as shown if Figure 7 (see behavior at 700 s).

It is important to note that the release of the fission products contributes to the energy generated and accumulated in the core region; therefore, this fission heat (to call it in some way) the decay heat, reaction heat due to generation of the hydrogen, in other phenomena as melting process causes that the temperature at core region is too high (3000 K) as can be observed in Figure 5 for the case of the 900 s and 1200 s (of

Table 2: Severe accident (LOCA) with and without cooling.

Parameter	Without cooling	HPCS injection at 700 s	HPCS injection at 900 s	HPCS injection at 1200 s
Level	Below the core support plate	Below the core support plate. After is recovers	Below the core support plate. After is recovers	Below the core support plate. After is recovers
Pressure	Low by decompression	Low by decompression	Low by decompression	Low by decompression
Maximum surface temperature in the core (K)	3028.00	1640.00 (proper cooling with HPCS)	2960.00 (cooling is not insured with HPCS)	3000.00 (cooling is not insured with HPCS)
Non-condensable fission product (kg)	33.00	0.00	19.00	21.00
Soluble fission product (kg)	18.70	0.00	8.00	11.90
Hydrogen generation (kg)	218.70	30.70	319.50	499.50
Debris bed height (m)	0.36	0.00	0.23	0.21
Core damage (%)	77.70	0.60	37.30	59.40
Control rod damage (%)	82.10	0.00	35.30	52.60

HPCS injection). At this point in the analysis and discussion of the results, we see that the injection of water for the cases of 900 and 1200, generating greater amounts of hydrogen (Figure 8), but smaller amounts of fission products released, with respect to the case without cooling (Figures 9 and 10). Figure 9 refers to noncondensable fission product released (krypton, xenon and Iodine), and Figure 10 is the soluble fission products released (Cesium Iodine (CsI) and Cesium hydroxide (CsOH)) during the LOCA [20, 21].

The comparisons of the four cases studied in this work are summarized in Table 2. In this table, are presented other variables such as control rod damage, hydrogen generation, and debris bed height, which are included in this analysis. But before addressing these variables, it can be observed in this table that the exposition time without cooling is determined for the progression of core damage, for 900 s and 1200 s the cooling cannot assured with HPCS injection, at least in 4000 s of the simulation. The maximum surface temperature in the core indicates that the melting of ZrO_2 and near the melting UO_2 for the case without cooling, 900 s and 1200 s of HPCS injection. The fission products released for the case without cooling are greater than the other cases but not the hydrogen generation being higher for the cases of 900 s and 1200 s of HPCS injection (under this condition, the water accelerated the hydrogen generation, when the temperature of the core region is of the order of 1470 K). The core and control rod damage is proportional to the injection time of the HPCS, being maximum for the case without cooling and minimum for 700 s of HPCS injection.

Now, respect to the debris bed height also can be observed that is proportional to core and control rod damage, being maximum for the case without cooling and null for 700 s of HPCS injection. The core region molten core materials accumulated on the core support plate would be eventually relocated into de lower plenum region and the thermal attack on the lower head vessel could occur. From phenomenological point of the view, the physical and chemical processes of the core debris are very complex, due to configuration, temperature, and composition. The heat removal from the debris bed in the lower plenum is determined by amount of the heat generated in the molten core materials, heat transfer inside the core material, and heat transfer from the core material to the reactor vessel. In this work, the thermal attack on the lower plenum is not presented, which requires a broad and specific study.

8. Conclusions

The severe accident simulation in the BWR of the Laguna Verde Nuclear Power Plant (LVNPP) to 105% of rated power was analyzed in this work using RELAP/SCDAPSIM code. The severe accidents start with a loss-of-coolant accident (LOCA) in loop of the recirculation of the reactor with and without water cooling injection. The variables analyzed were level, pressure, maximum surface temperature in the core region, maximum temperature of the control rod, fission products released (noncondensable and soluble), hydrogen generation, core and control rod damage, and debris bed height in lower plenum. The numerical experiments consider a little damage in the core with three different times of HPCS injection at 700 s, 900 s, and 1200 s. The following results were obtained.

(i) In the case of the 1200 s of HPCS injection, the level is recovered but with significant lower stability (Figure 4), indicative of the low activity of heat transfer processes, losing the cooling capacity for severe core damage.

(ii) For the case of HPCS injection at 900 s, two temperature peaks in the surface of the core of approximately of 3000 K were observed when the water cooling was injected (Figure 5).

(iii) For the case of 1200 s of the HPCS injection and without cooling, the behavior of the surface temperature in the core is practically until 1800 s (Figure 5).

(iv) The energy accumulated and generated by different process such as reactions chemical is an indicative that the time the injection is crucial due to that after the core region is not possible to cool, at least a short time the order of the hours (Figure 5).

(v) The negative effect of cooling can be observed in cases of HPCS injecting at 900 s and 1200 s, where a sudden increase to the core damage is fully associated with the entry of coolant into the core region, being greater than the core damage than without injection (Figure 6).

(vi) The hydrogen generation is higher with coolant injection for the cases of 900 s and 1200 s (of HPCS injection) that without coolant injection (Figure 8).

(vii) The fission products released for the case without coolant injection are greater than with coolant injection (Figures 9 and 10).

These results are crucial and can be applied to establishing strategies for LVNPP and development of severe accident guide.

References

[1] NRC, "Nuclear Regulatory Commission: 10 CRF 100 "Reactor Site Criteria" and 10 CFR 50 Appendix A, Criterion 19 "Control Room"," 1999.

[2] CFE, Comisión Federal de Electricidad (CFE): Final Safety Analysis Report (FSAR), México, 1979.

[3] Innovative Systems Software, LLC (ISS), "Software, System thermal hydraulics", 2012, http://www.relap.com/sdtp/software.php/.

[4] C. M. Allison and J. K. Hohorst, "Role of RELAP/SCDAPSIM in nuclear safety," *Science and Technology of Nuclear Installations*, vol. 2010, Article ID 425658, 2010.

[5] RELAP5/MOD3.3 Code Manual Volume I: Code Structure, System Models, and Solution Methods, Nuclear Safety Analysis Division, NUREG/CR-5535/Rev 1-Vol I.

[6] R. Gaunt, R. Cole, C. Erickson et al., "MELCOR Computer code manuals," NUREG/CR-6119, Rev. 1, National Laboratory, USA, 1998.

[7] MAAP4, "MAAP4: Modular accident analysis program for LWR plants, code manual vols. 1–4," Fauske & Associates Inc., Burr Ridge, Ill, USA, 1994.

[8] K. I. Ahn and D. H. Kim, "A state-of-the-art review of the reactor lower head models employed in three representative U.S. severe accident codes," *Progress in Nuclear Energy*, vol. 42, no. 3, pp. 361–382, 2003.

[9] BWR/6, *BWR/6 General Description of a Boiling Water Reactor*, Nuclear Energy Division, General Electric Company, 1975.

[10] Guía de Seguridad No. 1.10, Consejo de Seguridad Nuclear, Madrid, España, 1995.

[11] C. Allison, "Phenomenology of Severe Accident," IAEA sponsored training workshops on Analysis of Severe Accident.

[12] B. De Boeck and D. Gryffroy, "Introduction to severe accidents especially the containment behaviour," AVN-97/013, AIB VINÇOTTE, NUCLEAR, 1997.

[13] S. Hagen, P. Hofmann, V. Noack, L. Sepold, G. Schanz, and G. Schumacher, *Comparison of the Quench Experiments CORA-12, CORA-13, CORA-17*, Forschungszentrum Karlsruhe, 1996.

[14] NUREG/CR-6042, *Rev. 2, Perspectives on Reactor Safety*, U. S. Nuclear Regulatory Commission, Washington, DC, USA, 2002.

[15] G. Schanz, B. Adroguer, and A. Volchek, "Advanced treatment of zircaloy cladding high-temperature oxidation in severe accident code calculations Part I. Experimental database and basic modeling," *Nuclear Engineering and Design*, vol. 232, no. 1, pp. 75–84, 2004.

[16] C. Duriez, M. Steinbrück, D. Ohai, T. Meleg, J. Birchley, and T. Haste, "Separate-effect tests on zirconium cladding degradation in air ingress situations," *Nuclear Engineering and Design*, vol. 239, no. 2, pp. 244–253, 2009.

[17] M. Steinbrück, "Prototypical experiments relating to air oxidation of Zircaloy-4 at high temperatures," *Journal of Nuclear Materials*, vol. 392, no. 3, pp. 531–544, 2009.

[18] E. Beuzet, J. S. Lamy, A. Bretault, and E. Simoni, "Modelling of Zry-4 cladding oxidation by air, under severe accident conditions using the MAAP4 code," *Nuclear Engineering and Design*, vol. 241, no. 4, pp. 1217–1224, 2011.

[19] P. Royl, H. Rochholz, W. Breitung, J. R. Travis, and G. Necker, "Analysis of steam and hydrogen distributions with PAR mitigation in NPP containments," *Nuclear Engineering and Design*, vol. 202, no. 2-3, pp. 231–248, 2000.

[20] SCDAP/RELAP5/MOD3.2 Code Manual, Volume II: Damage Progression Model Theory, NUREG/CR-6150, INEL-96/0422, Revision 1, October 1997.

[21] SCDAP/RELAP5/MOD3.2 Code Manual Volume IIII: User's Guide and Input Manual, NUREG/CR-6150, INEL-96/0422, Revision 1, November 1997.

[22] G. Espinosa-Paredes and A. Nuñez-Carrera, "SBWR model for steady state and transient analysis," *Science and Technology of Nuclear Installations*, vol. 2008, Article ID 428168, 18 pages, 2008.

Hindawi Publishing Corporation
Science and Technology of Nuclear Installations
Volume 2012, Article ID 620298, 17 pages
doi:10.1155/2012/620298

Review Article

Station Black-Out Analysis with MELCOR 1.8.6 Code for Atucha 2 Nuclear Power Plant

Analia Bonelli,[1] Oscar Mazzantini,[1] Martin Sonnenkalb,[2] Marcelo Caputo,[3] Juan Matias García,[3] Pablo Zanocco,[3] and Marcelo Gimenez[3]

[1] *Licensing, Nuclear Safety and Core Design, UG-CNAII-IVCN-Nucleoeléctrica Argentina S.A, Lima, B2806AEL Buenos Aires, Argentina*
[2] *Barrier Effectiveness Department, Gesellschaft für Anlagen und Reaktorsicherheit (GRS) mbH, Schwertnergasse 1, 50667 Cologne, Germany, Germany*
[3] *Nuclear Safety Department, Centro Atómico Bariloche (CAB)-Comisión Nacional de Energía Atómica (CNEA), Bustillo Avenue Km. 9.5, Bariloche, Río Negro 8400, Argentina*

Correspondence should be addressed to Analia Bonelli, abonelli@na-sa.com.ar

Received 30 November 2011; Accepted 13 February 2012

Academic Editor: Alejandro Nuñez-Carrera

A description of the results for a Station Black-Out analysis for Atucha 2 Nuclear Power Plant is presented here. Calculations were performed with MELCOR 1.8.6 YV3165 Code. Atucha 2 is a pressurized heavy water reactor, cooled and moderated with heavy water, by two separate systems, presently under final construction in Argentina. The initiating event is loss of power, accompanied by the failure of four out of four diesel generators. All remaining plant safety systems are supposed to be available. It is assumed that during the Station Black-Out sequence the first pressurizer safety valve fails stuck open after 3 cycles of water release, respectively, 17 cycles in total. During the transient, the water in the fuel channels evaporates first while the moderator tank is still partially full. The moderator tank inventory acts as a temporary heat sink for the decay heat, which is evacuated through conduction and radiation heat transfer, delaying core degradation. This feature, together with the large volume of the steel filler pieces in the lower plenum and a high primary system volume to thermal power ratio, derives in a very slow transient in which RPV failure time is four to five times larger than that of other German PWRs.

1. Introduction

The Central Nuclear Atucha 2 (CNA-2) is a nuclear power plant (NPP) with a two-loop, 745 MWe, Pressurized Heavy Water Reactor (PHWR), designed by Siemens-KWU and being under final construction in Lima, Argentina. The NPP is cooled and moderated by heavy water like a similar unit of smaller power (CNA-I) in operation at the same site since 1974.

The reactor pressure vessel is very large and has a diameter of ~7.4 m. In difference to other PWRs the upper and lower plenum is to a large content occupied by filler pieces made of steel to reduce the necessary heavy water inventory (Figure 1). The *reactor core* consists of 451 vertical natural Uranium fuel assemblies located in the same number of coolant channels, connected each to the lower and upper reactor plenum. Each assembly consists of 37 fuel rods. The thermohydraulic design of the core divides the channels into five zones. For the external zones, specially designed flow limiters (drossels) are installed, so that the coolant flow in each channel zone is proportional to the average generated power in it, achieving almost the same channel outlet temperature for all the zones (Figure 2). The coolant channels are within the large moderator (MOD) tank. For reactivity reasons the moderator in it is maintained at a lower temperature than the reactor coolant. This is accomplished by the MOD system (Figure 4), which extracts the moderator from the MOD tank, cools it in the MOD coolers, and feeds it back to the MOD tank.

During full-load operation, 95% of the total thermal power is generated in the fuel, and the remaining 5% in the MOD tank, because of the neutron moderation.

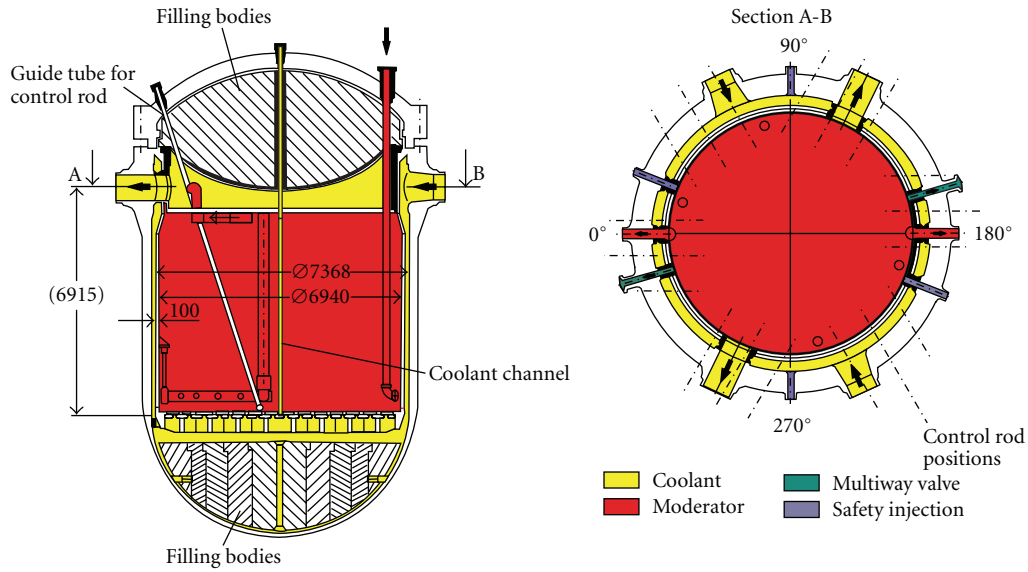

Figure 1: CNA-2 reactor pressure vessel (1 fuel channel and 1 control rod shown only).

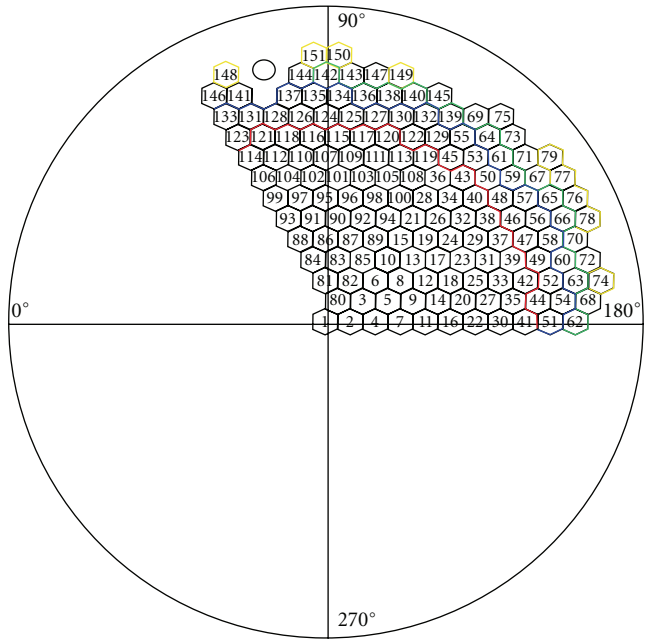

Throttle zone	Number of coolant channels	Intel throttle type
1	30	1b
2	36	2b
3	42	3b
4	90	5c
5	253	Unthrottled

Figure 2: CNA-2 thermohydraulic zones.

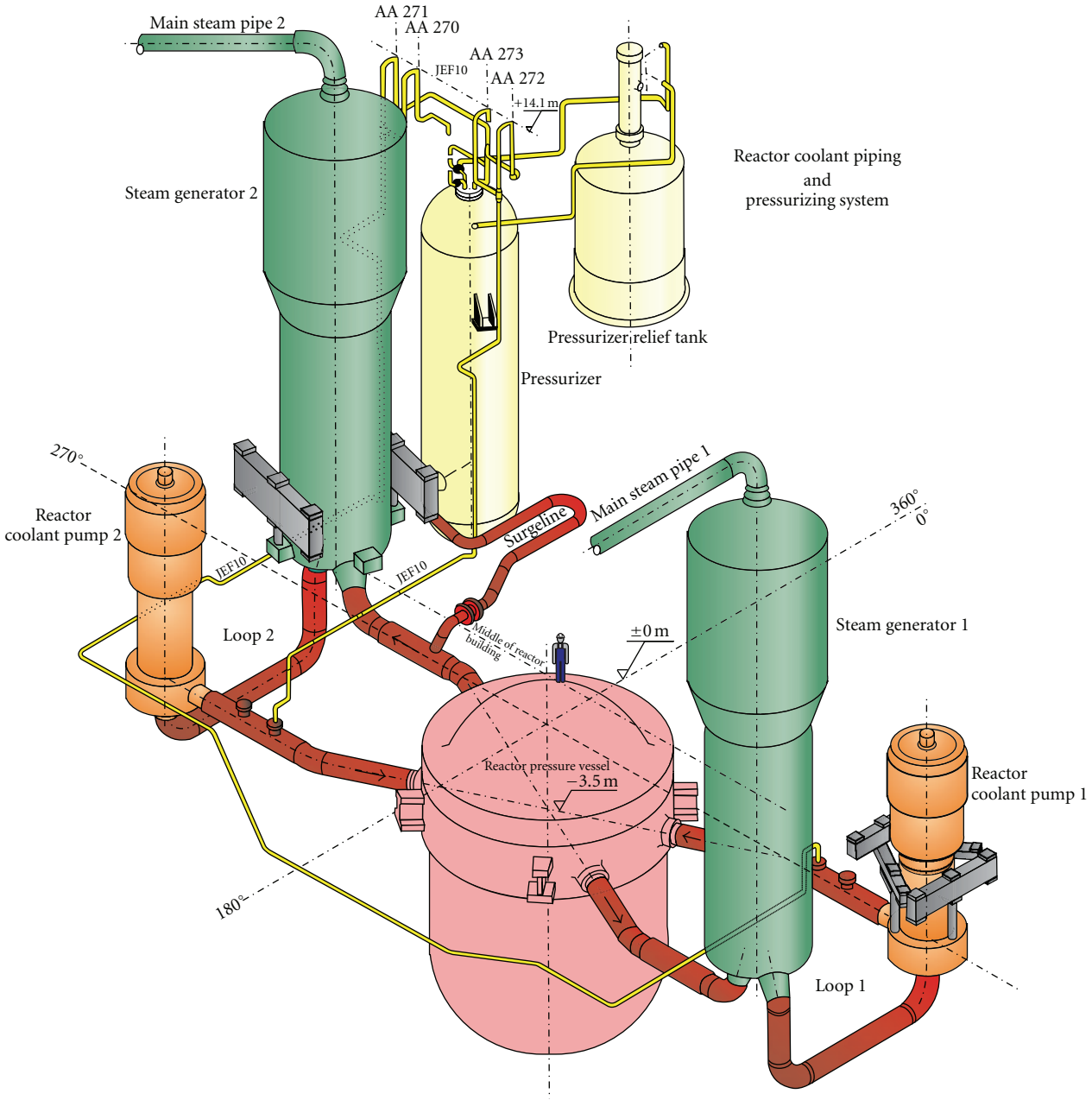

Figure 3: CNA-2 primary system layout.

Additionally, approximately 5% of the thermal power is transferred from the coolant channels to the MOD tank by heat transfer due to the temperature difference between the systems. The heat removed from the MOD system is used for preheating the feed water of the two Steam Generators (SGs), (Figure 3). The reactor coolant system and the MOD system are connected by pressure equalization openings of the moderator tank closure head. Therefore, the pressure differences in the core between the primary coolant and MOD systems are comparatively small, which results in thin walls for the coolant channels. Furthermore, the connection between the reactor coolant system and the MOD system permits the use of common auxiliary systems to maintain the necessary water quality.

Various methods are applied to control reactivity and thus the power output of the reactor. The reactor contains "black" (Hafnium absorbers) and "gray" (steel absorbers) control elements (Figure 1). These control elements are used to control the reactivity and the power distribution, to compensate the buildup of Xenon poisoning following a reactor power reduction and to shut down the reactor. Additionally, a fast boron injection system, as a second independent shutdown system, is provided, which injects boric acid into the MOD tank. The reactivity can be also

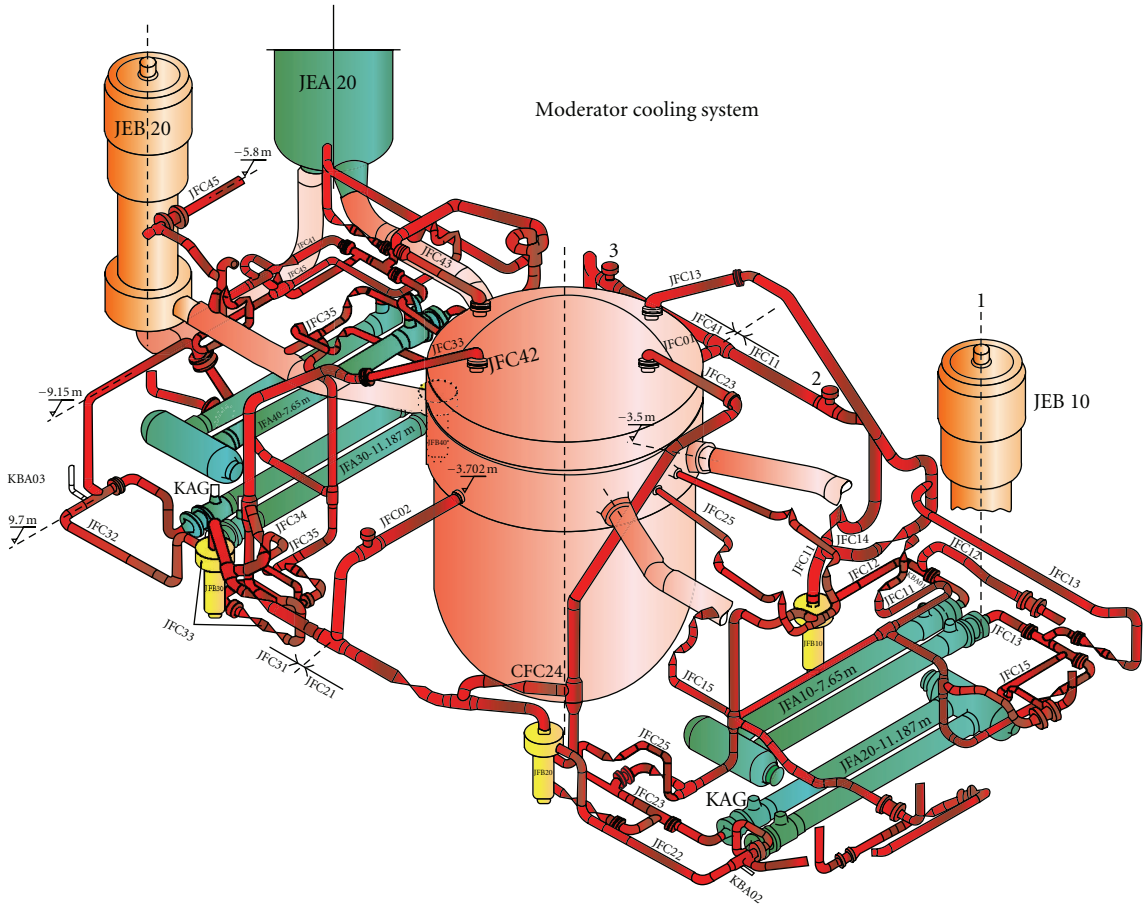

Figure 4: CNA-2 moderator system layout.

controlled by varying the MOD temperature within a certain range, which is advantageous for some operating modes. Table 1 shows the main overall data of the plant, while Figures 3 and Figure 4 show a schematic view of the reactor and moderator system.

The *reactor coolant system* (RCS) (Figure 3) removes the heat generated in the reactor core and transfers it via the steam generators to the turbine and the generator of the plant. The system is structured similar to that of a pressurized light water reactor but consists only of two identical loops, each comprising a steam generator, a reactor coolant pump, and the interconnecting piping, as well as one pressurizer linked to one loop.

The *moderator system* (Figure 4) consists of four identical loops operating in parallel. Each loop comprises a moderator cooler, a moderator pump, and the interconnecting lines and valves. The moderator system performs various functions depending on the reactor operating mode.

During *normal operation* the moderator system maintains the moderator at a lower temperature than that of the reactor coolant. The moderator leaves the top of the moderator tank, flows to the moderator pumps, is pumped through the moderator coolers, and flows back to the bottom of the moderator tank through special pipes coming down from the top of the RPV. The heat transferred in the moderator coolers is used to preheat the steam generator feed water.

For *residual heat removal,* the moderator system is switched over to the residual heat removal position by means of the moderator valves. Under this operation mode, the moderator is extracted from the bottom of the moderator tank (reverse flow to nominal operation) by the moderator pumps. Passing the moderator coolers, the moderator is injected through the hot or cold reactor coolant lines into the core. The moderator system forms the first link of the residual heat removal chain. The residual heat is transferred from the moderator system to the residual heat removal system and then to the service cooling water system.

During *emergency core cooling* the moderator serves as a high-pressure core cooling system. Determinant for the design of the moderator system is the demand for a high reliability during emergency core cooling condition. Therefore, the system consists of four separated loops from which the injection capacity of two moderator circuits (334 kg/s) is sufficient for emergency core cooling operation. For emergency core cooling operation, the moderator system is switched over in the so-called residual heat removal mode. The moderator pumps take the water again from the bottom of the moderator tank and feed through the moderator coolers into the cold and hot reactor coolant

Table 1: CNA-2 PHWR NPP overall data.

CNA-2 overall plant data	
Reactor type	PHWR
Net power station output	~745 MWe
Reactor coolant system and moderator system	
Total thermal power	2160 MW
Number of coolant channels or fuel assemblies	451
Active core length	5300 mm
Shape of fuel assembly	37-rod cluster
Reactor coolant system and moderator system	
Coolant and moderator	D_2O
Total thermal power transferred to the feed water/main steam cycle	2174 MW
Total thermal power transferred to steam generators	1954.5 MW
Total thermal power transferred to moderator coolers	220 MW
Number of coolant circuits	2
Number of moderator circuits	4
Total coolant circulation flow	10300 kg/s
Total moderator circulation flow	890 kg/s
Pressure at reactor vessel outlet	115 bar
Coolant temperature at reactor pressure vessel	278°C
Average moderator temperature normal/maximum	170°C/220°C
Steam pressure at steam generator outlet	54.9 bar
Total steam flow	956 kg/s

lines, respectively, the upper and lower plenum of the RPV. The residual heat removal chain connected to the moderator coolers during emergency core cooling is the same as during residual heat removal.

The primary flow rate through the moderator coolers and the moderator pumps is 222 kg/s for each pump, the net injection flow into the reactor coolant system is 167 kg/s for each pump, taking into account a bypass flow to the suction line of the moderator pumps. This is designed to reduce the temperature of the water on the suction side of the pumps.

Additionally to the moderator pumps, the ECCS includes 4 low pressure safety injection pumps, 4 water storage tanks, and 4 accumulators. After the emergency core cooling signal is triggered, the water storage tanks inject the inventory directly into the containment sump. The safety injection pumps, with a flow rate of 167 kg/s each, charge the coolant collected in the containment sump through the moderator coolers into the primary system. Accumulators also inject into the moderator lines downstream the moderator coolers.

Atucha 2 NPP has developed Probabilistic Safety Analyses (PSAs) of Levels 1 to 3. While PSA Levels 1 and 3 have been made by NA-SA Atucha-2, Argentina, with support from CNEA Instituto Balseiro, Bariloche, Argentina, PSA Level 2 was developed by GRS Cologne, Germany, with support from CNEA Instituto Balseiro, Bariloche, Argentina, in regard to the MELCOR modeling of the reactor coolant and the moderator coolant system, and NA-SA Atucha-2, Argentina, who provided all necessary information on request and supported especially the determination of containment and reactor building relevant data. A detailed MELCOR input deck [1] is the basis for the deterministic analyses in the PSA Level 2, and models all systems, components and buildings of the plant relevant for severe accidents, as well as the reactor and moderator circuit, the feed water and steam circuit, the heat removal system KAG connected to the moderator coolers, the reactor building with the containment and the relevant part of the auxiliary building and the stack. The selection of the buildings to be modeled in the MELCOR deck has been made based on a determination of possible radionuclide release paths from the containment into the environment assuming severe (core melt) accidents starting from full power operation. The universal modeling of systems and components and reactor protection signals allows the usage of the input deck for a large spectrum of LOCAs and transients starting from normal plant operation.

This nodalisation has been extensively discussed with NA-SA and reviewed by ARN and its subcontractor SNL before final application for PSA Level 2 analyses. It was also validated against a very detailed RELAP5 (version MOD 3.3) model developed by NA-SA and used within the PSA Level 1, to match results for the steady state calculations, and some selected accidents until core heatup in order to gain confidence on obtained results [2].

As a result of the plant specific PSA Level 1, a number of relevant Core Damage States have been identified. In the PSA Level 2, MELCOR calculations have been done for each of the relevant CDS in order to assess the severe accident progression and the possible radionuclide releases into the environment. The results have been used directly by PSA Level 3 study.

One of the most extensively studied transients has been the Station Black-Out, for which a low pressure scenario, a high pressure scenario, and several sensitivity cases have been assessed, as this was the dominating sequence according to PSA Level 1 analysis. In particular, a review of the Low Pressure Station Black-Out (SBO) scenario will be presented here, in order to highlight specifics of CNA-2 NPP regarding timing of the accident scenario, in comparison to other PWR reactors.

2. Brief Description of CNA-2 SBO Sequence

The postulated Station Black-Out event without accumulator injection causes reactor scram and the running-off of both reactor cooling pumps as well as the moderator pumps at the time the initiating event was defined, time = 0.0 s. By an automatic action of the reactor protection system, a 100 K/h cooldown by the steam generators steam dump stations, which is electrically supported by batteries, is initiated. After termination of the cooldown, the primary pressure increases again. The safety valve of the pressurizer opens several times to limit the primary pressure. After 17 cycles of the first pressurizer safety valve, respectively, 3 cycles of pure water

release, it is assumed that it fails stuck open. Under leak condition, a permanent flow into the containment occurs through the pressurizer relief tank with a depressurization of the primary systems. The condition for the initiation of the accumulator injection is reached more than 2 hours after the initiating event, when the batteries are already empty. Thus, an accumulator injection is not considered for that case, as an active action is needed to open valves to load the accumulator tanks by nitrogen from the tanks nearby.

If no accident management measure is considered, the above transient is to be expected, which results in a severe core damage. This is thus the transient that will be presented here.

On the other hand, a second base case has been analyzed: the Station Black-Out event with accumulator injection. The accumulator injection can only be pursued if the valves of the accumulator system are opened by a manual accident management measure during the first two hours of the sequence (batteries still available) so that the accumulators get pressurized. The results of this calculation show that due to the accumulator injection, core degradation and RPV failure are delayed by at least 5 hours. The increase in the hydrogen generation is small and does not imply a disadvantage of the accumulator injection because it does not mean an additional endangering. Thus, the accumulator injection seems to be a reasonable measure and it will be probably made available for the Station Black-Out event as an accident management measure in order to gain more time for the handling of the accident.

3. Outline of MELCOR Code

MELCOR [3] is a fully integrated, engineering-level computer code whose primary purpose is to model the progression of accidents in light water reactor nuclear power plants. A broad spectrum of severe accident phenomena in both boiling and pressurized water reactors is treated in MELCOR in a unified framework; current uses of MELCOR include estimation of fission product source terms and their sensitivities and uncertainties in a variety of applications.

The MELCOR code is composed of an executive driver and a number of major modules, or packages, that together model the major systems of a reactor plant and their generally coupled interactions. Reactor plant systems and their response to off-normal or accident conditions include the following:

(i) thermal-hydraulic response of the primary reactor coolant system, the reactor cavity, the containment, and the confinement buildings,

(ii) core uncovering (loss of coolant), fuel heatup, cladding oxidation, fuel degradation (loss of rod geometry), and core material melting and relocation,

(iii) heatup of reactor vessel lower head from relocated fuel materials and the thermal and mechanical loading and failure of the vessel lower head, and transfer of core materials to the reactor vessel cavity,

(iv) core-concrete attack and ensuing aerosol generation,

(v) in-vessel and ex-vessel hydrogen production, transport, and combustion,

(vi) fission product release (aerosol and vapor), transport, and deposition,

(vii) behavior of radioactive aerosols in the reactor containment building, including scrubbing in water pools, and aerosol mechanics in the containment atmosphere such as particle agglomeration and gravitational settling, and,

(viii) impact of engineered safety features on thermal-hydraulic and radionuclide behavior.

Initially, the MELCOR code was envisioned as being predominantly parametric with respect to modeling complicated physical processes (in the interest of quick code execution time and a general lack of understanding of reactor accident physics). However, over the years as phenomenological uncertainties have been reduced and user expectations and demands from MELCOR have increased, the models implemented into MELCOR have become increasingly best estimate in nature. The increased speed (and decreased cost) of modern computers (including PCs) has eased many of the perceived constraints on MELCOR code development. Today, most MELCOR models are mechanistic, with capabilities approaching those of the most detailed codes of a few years ago. The use of models that are strictly parametric is limited, in general, to areas of high phenomenological uncertainty where there is no consensus concerning an acceptable mechanistic approach.

4. MELCOR Model for CNA-2 NPP

Atucha 2 NPP MELCOR nodalisation was made on the basis of knowledge gained by GRS in previous PSA Level 2 studies for PWR and BWR, and state of the art knowledge on the field. The RPV nodalisation can be seen in Figure 5. The reactor model consists, like in a German PWR model [4], of one volume each for downcomer (CV100), lower plenum (CV110), upper plenum (CV140), and RPV head (CV150) plus one for the upper ends of the coolant channels (CV145).

The 451 coolant channels are subdivided in 6 parallel hydraulic groups, different as typically done in other PWR decks. The reason for this is the PHWR core design which is more similar to a BWR core with canisters. The inner part of the core has no flow limiters, while in the core periphery different regions with different flow limiters exist (Figure 2). The number of coolant channels differs in each of the 6 groups. Each channel and the moderator tank are further subdivided into 3 axial levels. In total 21 CVs are used. This modeling takes into account that the water level in the channels and in the moderator tank may be significantly different in case of an accident and that the channels will fail sequentially in different axial levels. If the channel fails, in each axial level a horizontal flow path opens towards the moderator tank. These flow paths are not shown in Figure 5.

The MELCOR core model uses a BWR model because only this option allows the melting of the zircaloy coolant channels, which are modeled by the BWR fuel assembly

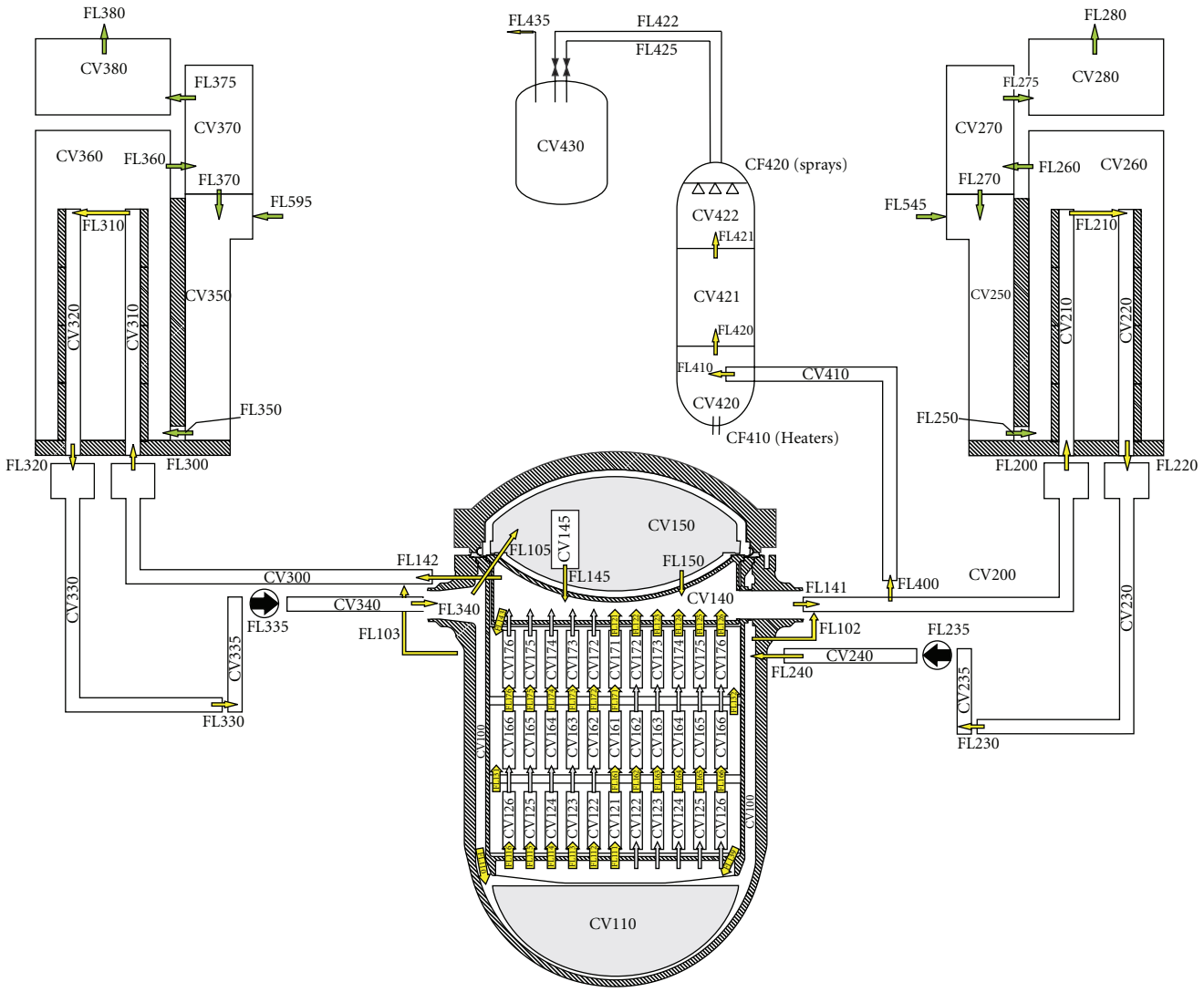

Figure 5: MELCOR nodalisation scheme of reactor, coolant circuits, and SGs (cross connection inside the core not shown).

canister components. The model consists in total of 7 radial rings and 28 axial levels for the core and the lower plenum. The selection of the radial rings was made taking into account different aspects like the location of flow limiters, the axial and radial power distribution and the burn-up zones. The MELCOR core nodalisation consists of 20 levels. The active part of the fuel consists of 18 levels; 16 of them have an identical length of 30 cm while the other two (axial levels of upper and lower end of active fuel) are only 25 cm long each. The lengths of the inactive core levels at the upper end (level 28) and lower end (level 9) of the fuel assembly are 35 cm and 46.5 cm, respectively. The nodalisation consists of additional 8 levels for the lower plenum, 5 of them are used for the filler pieces and one for the moderator tank bottom (the lower core support plate in MELCOR). The remaining two axial levels model the free space above the filler pieces and the area of the heavy support grid to the moderator tank bottom (Figure 6). The RPV wall is subdivided in 11 segments as shown in Figure 6. The RPV segments 9 to 11 will get in contact with molten material first, after its relocation into the lower plenum.

Each of the two loops of the reactor circuit of CNA-2 is modeled separately (Figure 5). The loop 10 is connected via the surge line (CV410) to the pressurizer (CV420-422) and the relief tank (CV430). The two safety valves of the pressurizer are modeled, and the pressurizer heaters and spray systems as well (normal operation spray system and KBA spray). If the pressure rises in the relief tank, a burst membrane will fail and open towards the containment. In addition, a failure of a safety valve stuck open can be simulated, as described here. Each reactor circuit consists of 6 control volumes, one is used for the hot leg, two are used for the SG piping, and three for modeling the cold leg. This is identical to the PWR model used at GRS before. In case of an accident, the injection of heavy water by the volume control system (KBA) into both cold legs is started. In total 70 m^3 can be injected.

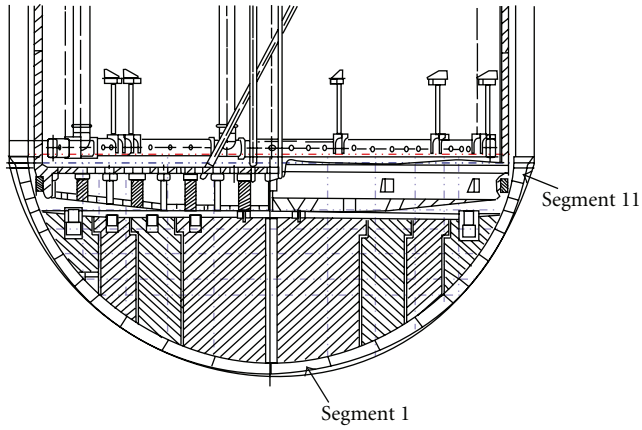

Figure 6: MELCOR model of RPV lower head.

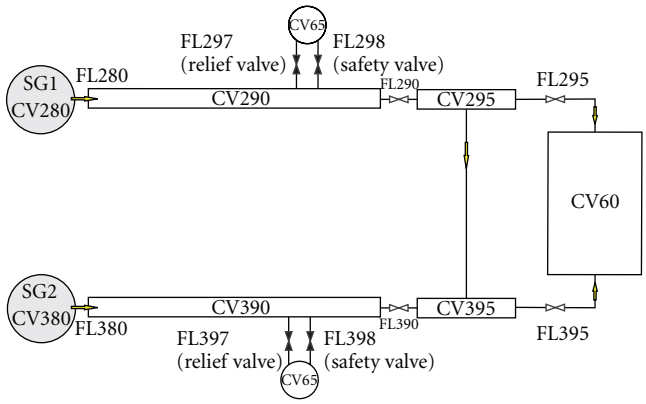

Figure 7: MELCOR nodalisation scheme of steam system.

The SG secondary side is modeled by 4 volumes, the downcomer, the riser, the steam separator region, and the steam dome (Figure 5). The connections between the SG secondary sides volumes by flow paths are shown as well. The steam system is simplified as shown in Figure 7. This scheme has already been used for German PWRs because such a SG model has proved to be best applicable for this plant design type [4].

The moderator system of the plant consists of four loops, as schematically shown in Figure 8. A moderator pump (MCP) and a heat exchanger (MHEx) are located in each loop. Under normal operation, the hot water (D_2O) is taken out at the upper end of the moderator tank through a collector and two pipes, leaving the RPV at the same elevation as the reactor loops. The cold water flows back through four pipes connected to the top of the RPV, ending inside in a special collector at the lower end of the moderator tank. The collector was not modeled in the MELCOR deck. The moderator pumps are also used during accident sequences as emergency core cooling pumps. A failure of a MCP due to cavitation is assumed, if the steam temperature in a suction pipe of an MCP equals to the saturation temperature for more than 2 minutes. This simple model takes into account a high steam concentration at the pump entrance. It is a pessimistic assumption related to the possible continued MCP operation under two-phase flow conditions, but such conditions cannot be simulated well with MELCOR.

The moderator heat exchangers are used to preheat the feed water during normal operation and to cool down the primary system by the KAG system during plant shut down. The secondary side (feed water system) flow of two moderator loops provides the feed water to one SG. The heat exchangers of these two loops are located at two different levels in the containment. The nodalisation of the moderator system is shown in Figure 8 and that of the feed water system in Figure 9. Because of the design specifics, a separate modeling of all 4 loops of the moderator circuit was needed. Moderator loops 10 and 20 are connected to RCS loop 10 (with pressurizer) while loops 30 and 40 are connected to the other RCS loop 20. Moderator loops 10 and 40 are the ones having their Heat Exchanger located at a higher position inside the containment, at floor level −8 m. The other two are located at −11.5 m level.

The MELCOR nodalisation follows the same rules as those applied for the reactor circuit. Vertical and horizontal parts of the piping are modeled separately by CVs. The volume of each individual CV should not be too small to avoid numerical instabilities, which was not possible for instance for the heat exchanger volumes. The pipes of each loop are modeled by 3 CVs plus some CVs for the pipes/collectors inside the moderator tank and as well near the RPV. The heat exchanger itself consists of 3 CVs on the primary as well as on the secondary side. In addition, a heat sink/source of 5 MW in each heat exchanger "node pair" is modeled, to enhance the heat transfer from the primary to the secondary side during normal plant operation. This is necessary to obtain realistic heat transfer rates, similar to those to be found in the real plant, as MELCOR has no model for "cross flow heat exchangers."

The moderator system is connected through separate pipes with the RCS loops (hot and cold leg) and the RPV (upper plenum and downcomer) for emergency core cooling operation. The injection pipes in each loop are lumped together into one CV with two separate connections (FL) to the injection points. During ECC operation, the system is switched into the so-called "reverse or commutation mode" (reverse flow with extraction of water from moderator tank bottom and injection into RCS and RPV). The pipe, which will be opened for injection, is modeled only by a flow path in each loop (FL521, FL571, FL621, FL671 in Figure 8). There is a bypass flow of about 50 kg/s per loop downstream the heat exchanger back to the suction side of the MCP, which is as well taken into account through flow paths FL515, FL565, FL615, and FL665. The existence of this bypass significantly extends the MCP operation before cavitation occurs.

The feed water system consists of several CVs in each loop. The feed water system upstream the MHEx is modeled by a time independent volume (CV50 in Figure 9) only. As mentioned the heat exchanger secondary side is modeled by 3 CVs in each loop. Downstream, an individual pipe section is modeled and the common feed water pipeline connected to each SG. The bypass of the MHEx is modeled

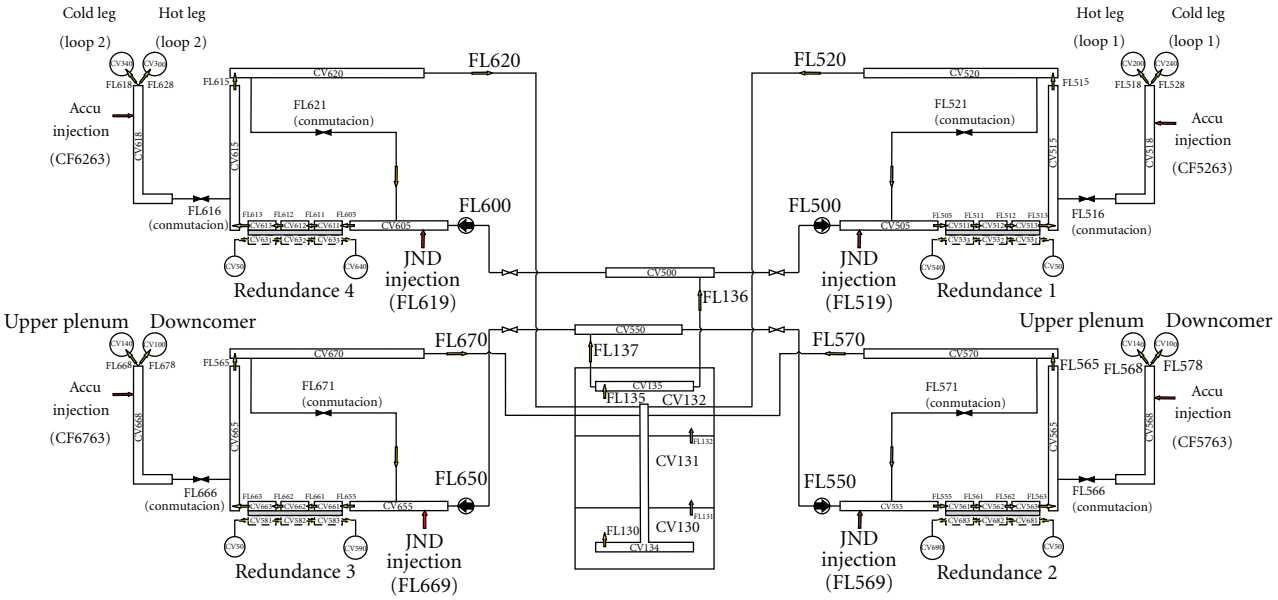

Figure 8: MELCOR nodalisation scheme of moderator systems 10 to 40.

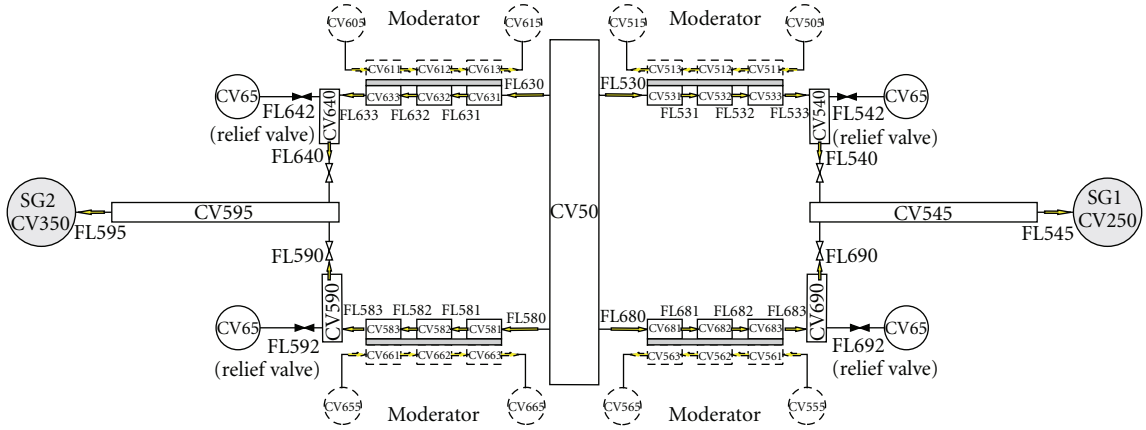

Figure 9: MELCOR nodalisation scheme of feed water systems 10 to 40.

only by one FL in each loop. For emergency feed water injection, the startup and shutdown pumps (LAJ) are used and simulated by mass sources directly into the feed water line at the SGs. In each feed water loop a relief valve is modeled, which limits the maximum pressure, if the system is switched off.

The containment nodalisation scheme is similar in principle to the modeling of the main rooms of the German PWR [4], but much more detailed related to the smaller rooms inside the containment. A general view of the CNA II nodalisation scheme developed for the containment and reactor building is shown in Figure 10. Each colored zone is an individual CV.

Inside the containment and the annulus of the reactor building different floors are located. The developed containment nodalisation consists of 33 control volumes (CVs) and about 90 flow paths (FLs). Several small rooms have been lumped together. Larger rooms are modeled separately. The dome area was subdivided to allow the calculation of convection loops (as described in [4]). The main reasons for this large level of detail are phenomena related to the hydrogen issue and the need for a detailed modeling of a larger number of small compartments located nearby the tilting machine (an automatic machine in charge of transporting new and burned fuel elements from the spent fuel pool to the refueling machine). The open flow paths have been determined based on containment drawings. About 480 heat structures have been defined to simulate the walls, floors, and ceilings and some of the equipment not modeled by the primary and the moderator circuit.

The detail of the annulus model and that of parts of the auxiliary model are similar to the containment. In addition, all relevant air ventilation systems are modeled. More details are given in [1].

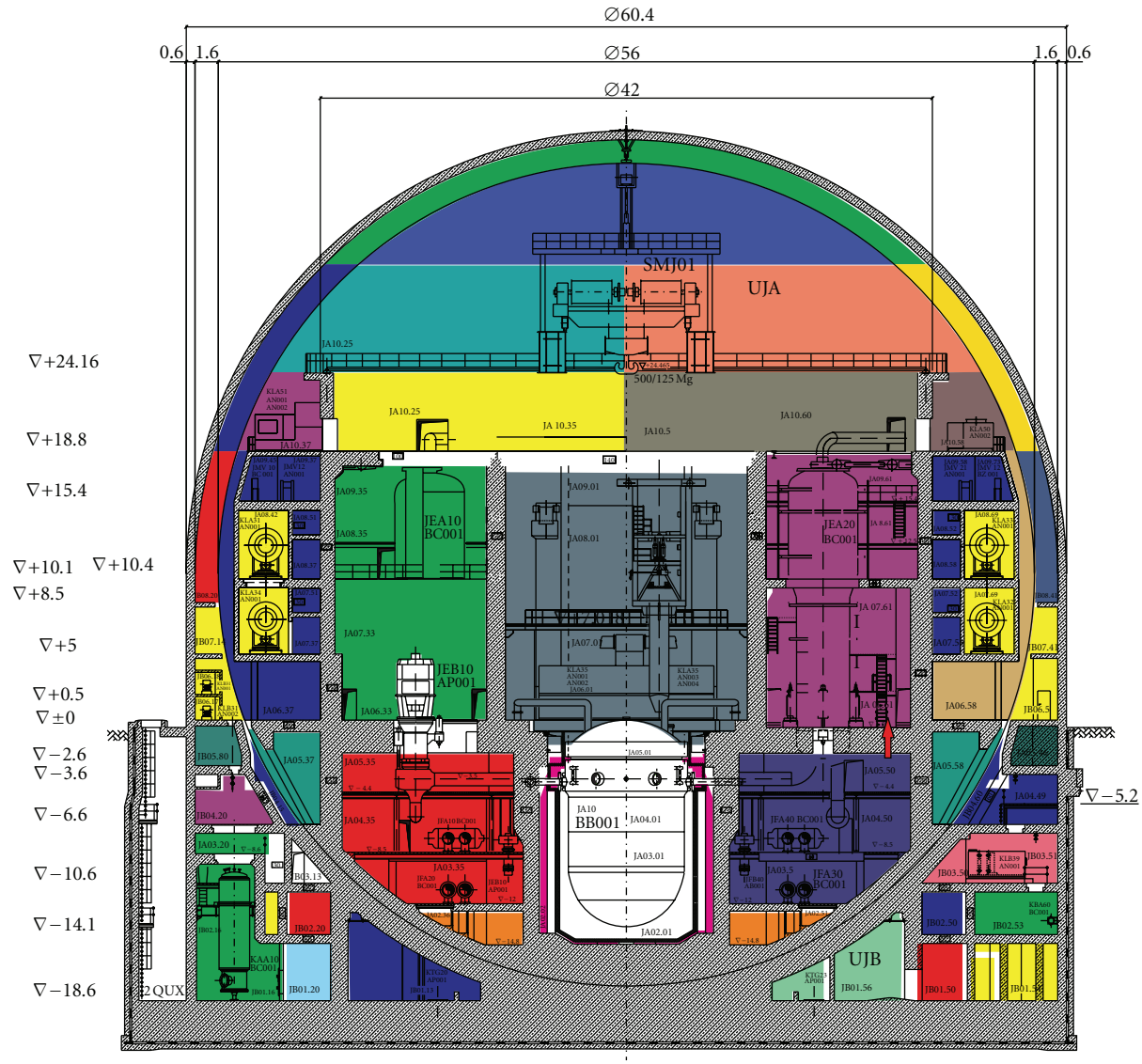

Figure 10: MELCOR nodalisation scheme of containment and reactor building annulus (principle scheme).

5. Initial Data and Boundary Conditions

The boundary conditions and assumptions concerning the failure of systems are briefly summarized in this section. The initiating event is loss of power, accompanied by the failure of four out of four diesel generators. All remaining plant safety systems are supposed to be available; only boron shutdown system is not considered, because it has not been accounted for in the MELCOR model for CNA-2. For the depressurization, it is assumed that during the Station Black-Out sequence the pressurizer safety valve fails stuck open after 3 cycles of water discharge, respectively, 17 cycles in total.

Due to the lack of electrical power supply, the so-called commutation of the moderator loop to ECC mode does not occur.

During that base case, an accumulator injection does not occur because the automatic initiation of the accumulators does not take place before the capacity of the batteries is lost. An accident management measure in order to open the valves of the accumulator system before the batteries get empty is not considered for this base case.

6. MELCOR Input Deck Qualification by Comparison to RELAP5

The qualification of the MELCOR input deck was performed by a comparison with the detailed RELAP5 (version MOD 3.3) input deck developed by NA-SA. This model was used in the early phases of the project, to match the steady state calculations between the two codes, and thus validate the MELCOR model. Furthermore, RELAP5 version uses D_2O thermal properties while MELCOR uses H_2O. This has a minor effect on the general excellent results, which is shown by the following figures from [2] for the SBO transient. Shown are the first ~4 h of the same scenario, described more

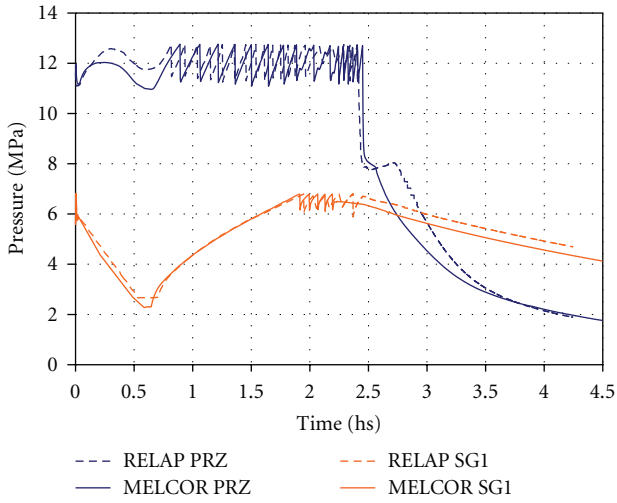

Figure 11: Pressures in primary and secondary systems.

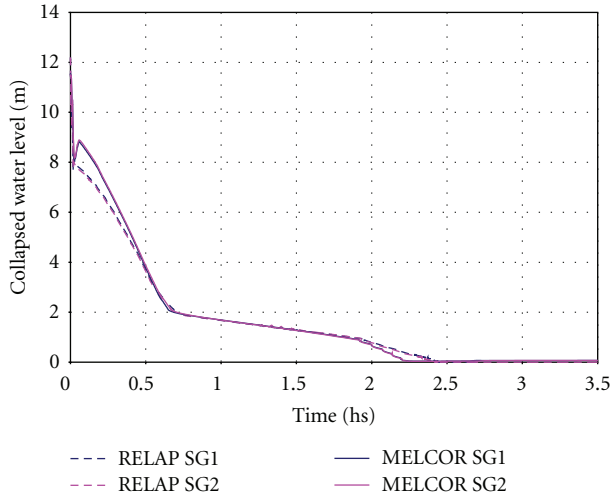

Figure 12: Steam generator 10 and 20 water levels.

in detail in Section 7. For these analyses the containment input deck in MELCOR was not used, as such does not exist in RELAP5 nodalisation either.

Figure 11 shows the primary and secondary pressure. After ~40 min the SG steam valves are closed automatically to limit the further level decrease. Therefore, the secondary pressure rises again. After nearly 2.5 h the pressurizer safety valve was assumed to fail stuck open so that the pressure decreases rapidly. Figure 12 shows the SG water level. Besides some minor differences in the first minutes of the accident, caused by the simpler nodalisation of the SG secondary side with influence on the water level determination, the dry-out of the SG is calculated to be the same. 2 m water level in the SGs is reached almost at the same point in time. This is important for the calculation of the natural circulation in the reactor circuit, shown in Figure 13. The circulation stops at about 2.5 h when the SGs are empty. Nearly identical behaviour was calculated by both codes. Figure 14 shows a comparison between the Cladding Temperatures calculated by MELCOR and by RELAP5. The core heatup phase shows a very good agreement between the two models as well. For more details of the event progression please refer to next chapter.

As a conclusion, not only the light versus heavy water issue is excluded as a possible cause of discrepancies in results, but also the differences between a coarser MELCOR nodalisation, and a much more detailed RELAP5 nodalisation.

7. Results of MELCOR Simulation

Starting from normal plant operation a Station Black-Out (SBO) was assumed at time 0:00 h:min. The main cooling pumps and moderator pumps run down due to the loss of electrical power supply. Injection of water into the reactor cooling circuits is not available because of the loss of all pumps. The containment is successfully isolated due to the SBO condition (fail-safe principle of isolation valves).

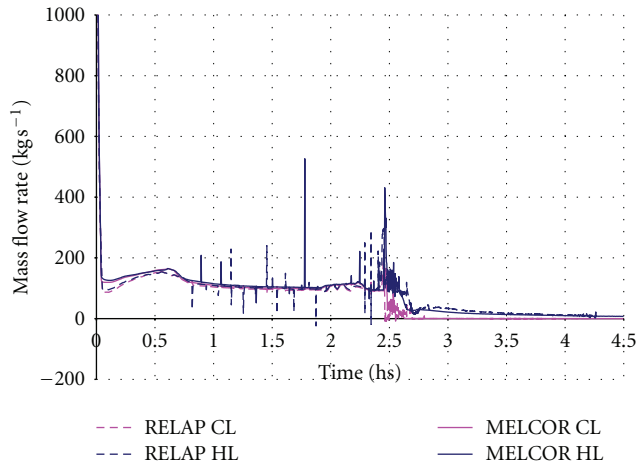

Figure 13: Primary loops mass flow rates.

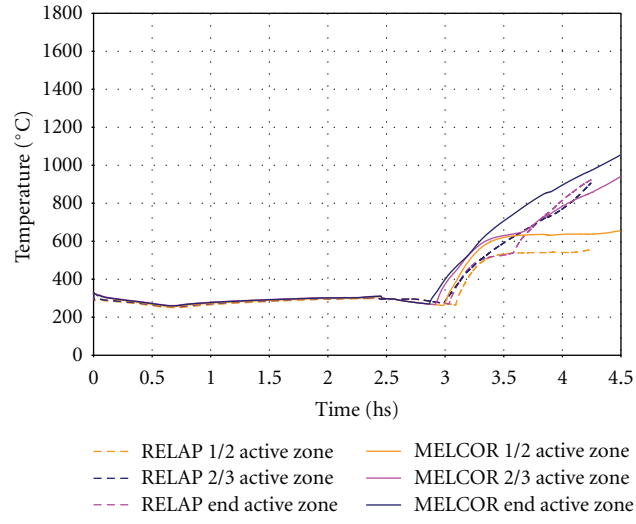

Figure 14: Cladding temperatures at different axial positions.

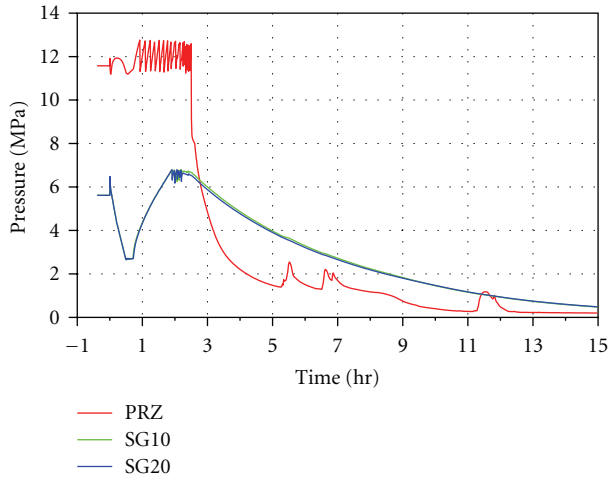

Figure 15: Pressure in pressurizer and SG10 and SG20.

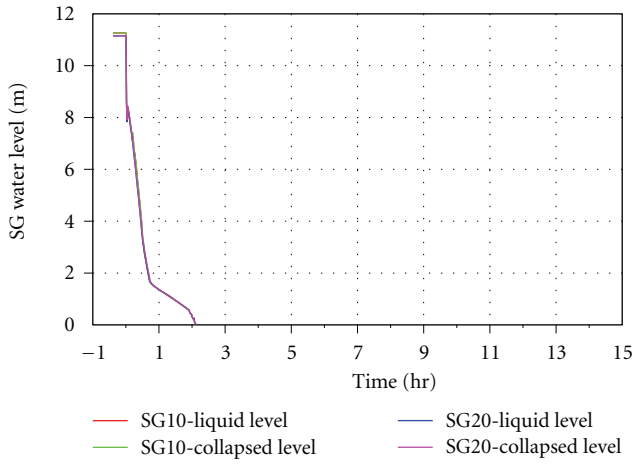

Figure 16: SG10 and SG20 water levels.

Due to the loss of heat sinks, both the primary and secondary side pressures start to increase. On the secondary side, the cooldown by a rate of 100 K/h is initiated. This cooldown is available because the relief valves of the secondary side steam dump stations are supported electrically by batteries. The secondary side pressure decreases, while pressure increase on the primary side is bounded (Figure 15). The water level of the steam generators is continuously decreasing due to the cooldown process and falls below 2 m at 0:43 h and 0:43 h, respectively (Figure 16). Thus, the isolation of both steam valves and steam dump stations occurs (reactor protection signals JR65 and JR66). After steam isolation, small steam leakages of the pilot valves are considered.

Due to the lack of heat release from the primary circuit, the water level inside the pressurizer rises. After completion of the 100 K/h cooldown, the primary pressure starts to increase again. At 0:52 h the primary pressure reaches 12.45 MPa for the first time (Figure 15). The first opening of the pressurizer safety valve occurs at 0:55 h. Subsequently, the valve opens intermittently in order to limit the primary pressure. During the first cycles of the valve only steam is

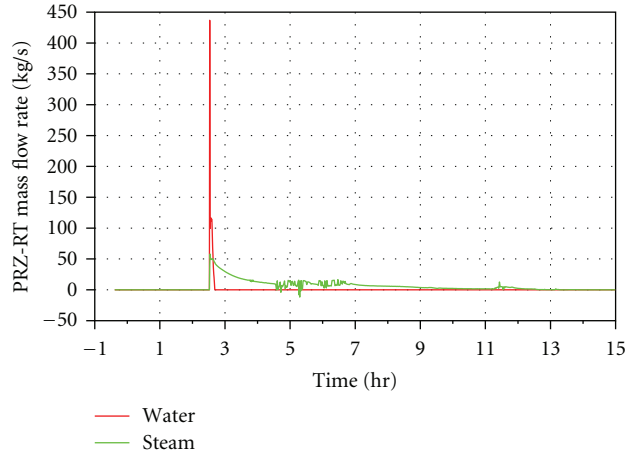

Figure 17: Flow rate through pressurizer relief tank—water and steam.

blown into the relief tank. Following, a water steam mixture is released into the relief tank. The burst disk of the relief tank fails at 2:31 h because a pressure gradient over the disk of 1.4 MPa is reached. Altogether, the safety valve makes 17 cycles before it fails stuck open. For the last three cycles only water is discharged into the relief tank. After the safety valve fails stuck open, a continuous leak flow through the relief tank occurs. Due to the leak flow through the relief tank (Figure 17) the primary pressure starts to decrease (Figure 15).

Up to about 2:40 h a free convection flow can be observed at the two upper loops of the moderator system. For each of the lower moderator loops the flow disappears with initiation of the Station Black-Out event, as the moderator heat exchangers are located below the core height.

The JR31 ECCS signal is triggered at 2:31 h. The containment pressure rises due to the leak flow. Thus, several burst membranes located at the steam generator boxes and pressurizer box fail. The flooding signal JR36 occurs at 2:43 h because the primary pressure has fallen below 6.6 MPa. However, the water of the flooding tanks cannot be discharged into the sump due to the lack of electrical power supply.

Owing to the permanent loss of coolant, the water level inside the cooling channels of the core decreases. At about 3:30 h the cooling channels are nearly empty. At that time the water level inside the moderator tank is still located at two thirds of the total height of the tank (Figure 18). From this time on, the decay heat is evacuated from the fuel elements to the coolant channel walls by convection and radiation, as far as they are cooled from the outside by the moderator tank water. The temperature increase shows, specially in the lower parts of the core, a plateau at about 3 h to 4:30 h of the transient (Figures 21 and 22) which evidences the decay heat evacuation by radiation as already stated. As a consequence, the water level inside the moderator tank continues decreasing (Figure 18).

Simultaneously, the water level of the pressurizer slowly decreases (Figure 19). Because of the exposure of the cooling

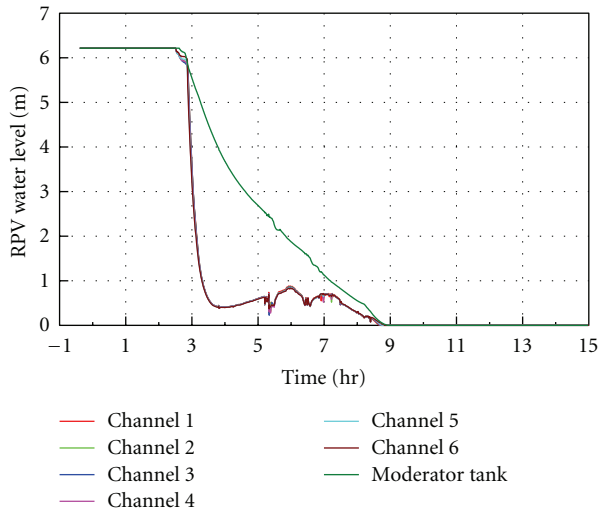

Figure 18: Water level in coolant channel rings 1 to 6 and moderator tank.

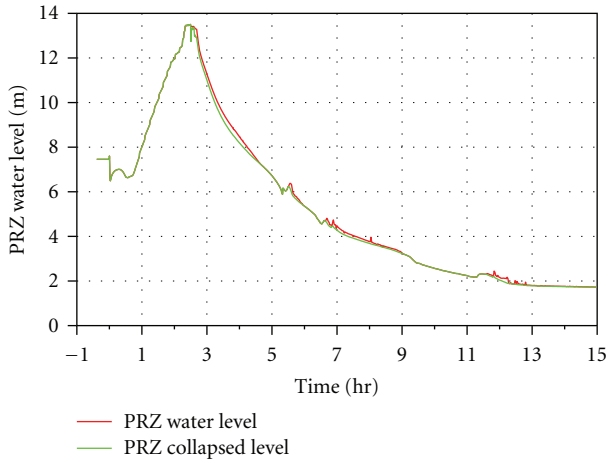

Figure 19: Pressurizer water level.

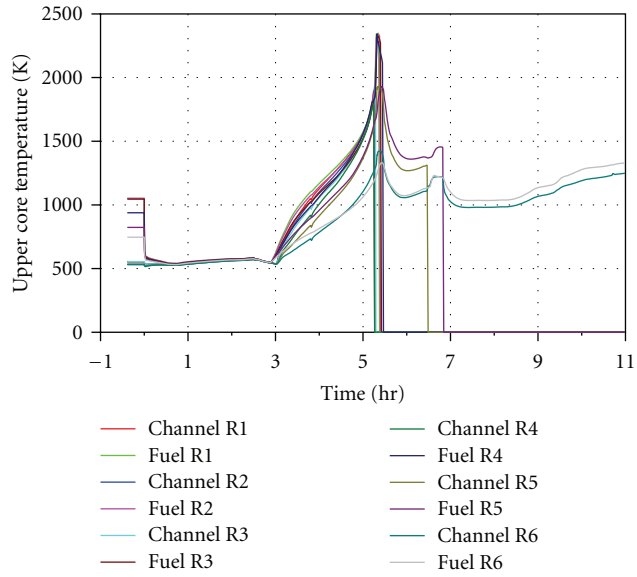

Figure 20: Temperature of fuel and coolant channels in R1 to R6 of upper core.

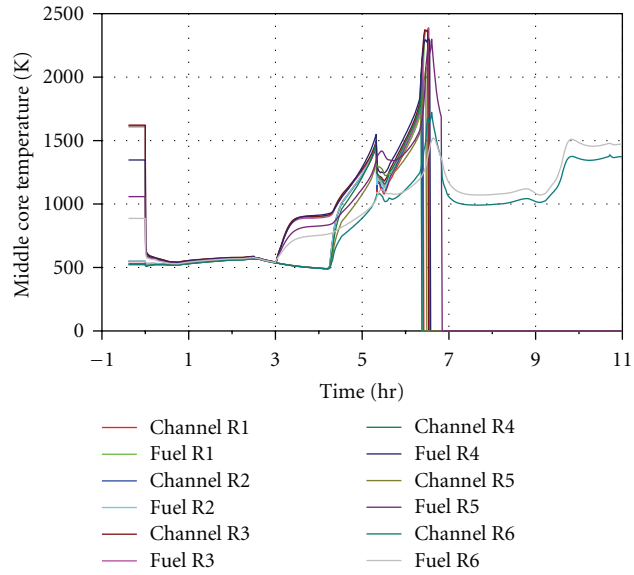

Figure 21: Temperature of fuel and coolant channels in R1 to R6 of mid core.

channel, the core starts to heat up in the upper part (Figure 20). The heatup of the lower parts of the core follows with a delay (Figures 21 and 22). The water discharged through the relief tank flows into the containment sump and is lost for core cooling, because safety injection pumps are not available due to the total loss of electrical power supply.

The first radionuclides—noble gases and volatile radionuclides—are released from the fuel elements gap after bursting of the cladding starting at ~3:56 h. The gap release starts in the central part of the core and migrates to the outer radial core rings. After 5:10 h, all radial core regions have got a gap release. The radionuclides form aerosols which are released together with steam through the open relief tank into the containment. Some of the aerosols may deposit as well inside the RCS.

The core heatup accelerates when the oxidation process of the zircaloy cladding and coolant channels starts at about 3:30 h (Figure 20). The hydrogen formed by the oxidation is mainly released through the relief tank into the upper containment compartment where the relief tank is located. After 10 h some of the hydrogen generated inside the pressure vessel is stored inside the Reactor Cooling System (Figure 23). In this analysis no combustion was calculated neither in the rooms near the relief tank nor in other rooms. Hydrogen fractions during the first 10 hours are small because of the presence of Passive Autocatalytic Recombiners (PARs). The amount of hydrogen removed by the PARs installed in the containment compared to the generated amount is shown in Figure 23.

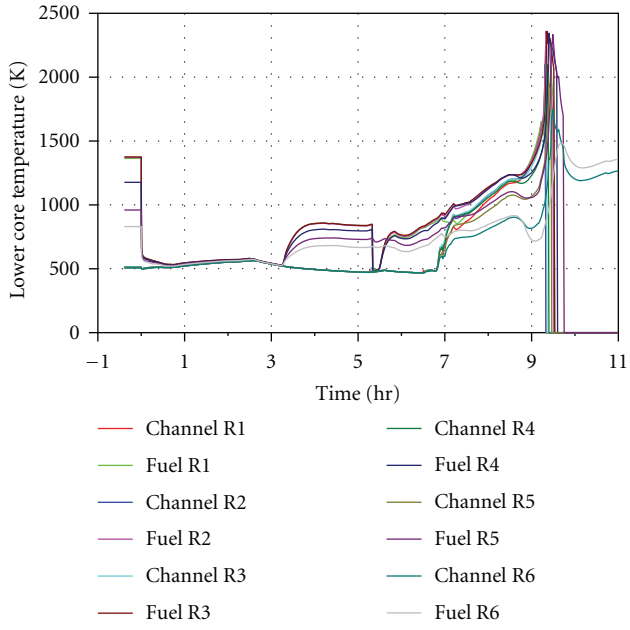

Figure 22: Temperature of fuel and coolant channels in R1 to R6 of lower core.

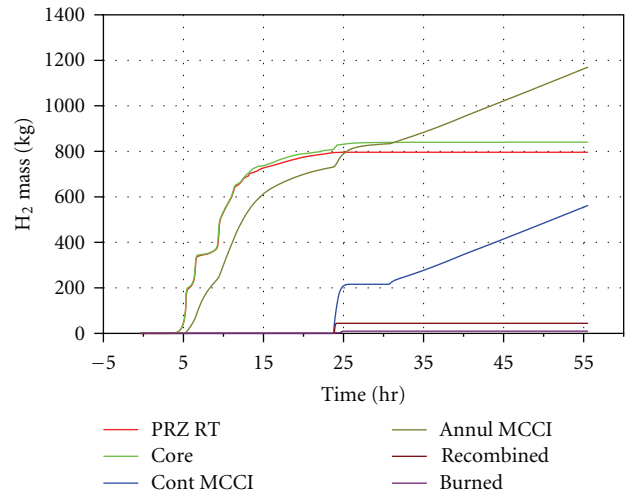

Figure 23: Hydrogen mass generated in core and from MCCI in containment, released from leak and recombined by PARs.

The failure of the coolant channels starts in the upper part of the four inner core rings at 5:16 h. At 5:20 h the damage of the middle part of the inner rings already starts. This process opens additional flow connections between the damaged parts of the coolant channels and the moderator tank. Thus, some water flows from the moderator tank into the lower intact parts of the cooling channels where the water level is increased (Figure 18). Up to 8:20 h the lower plenum of RPV is still full of water. Then, its evaporation starts due to first small relocation of core materials. Inside the moderator tank and cooling channels the water is fully evacuated at about 9 hours after event initiation (Figure 18).

The ongoing core heatup causes a failure of the fuel assemblies and the core failure process spreads radially to the core periphery and axially downwards. This is shown by an abrupt decrease in temperatures in Figures 20 to 22. Failure temperature for fuel rods is around 2300 K. The reason for this is the following: in CNA-2, fuel elements are hanging from a special construction located in the upper part of the channels above the core, which allows the so-called on-line refuelling. As the "fall-down" process of a fuel assembly inside the coolant channel after support failure cannot be modelled by MELCOR, some assumptions have to be made about the failure of the fuel assembly. The mechanical failure of fuel rods is assumed to result from a combination of loss of intact, unoxidized cladding material; thermal stress; molten zircaloy, which "breaks out" from ZrO_2 shell at 2400 K; and the collapse of standing fuel rods (that will form particulate debris) based on a cumulative damage function. Due to swelling and thermal expansion, the mechanical stresses inside the pellets increase with temperature. Therefore, a function was build-modelling the fuel integrity with time at temperature taking into account that a long free standing largely damaged fuel column is nonrealistic. As a conclusion failure is shown at a lower temperature than the one usually found in experiments, because a loss of integrity concept for fuel elements is being applied.

Together with the core degradation, significant amounts of noble gases and volatile radionuclides are released from the fuel. The failure of the control rods before the coolant channel failure is of less importance for the core melting process of CNA-2 compared to LWR because of the small masses of control rod material. Recriticality is not a topic as reflooding of a partly destroyed core is not calculated.

The upper (Figure 20) and middle (Figure 21) parts of the fuel in the inner rings fail in two phases at ~5:30 h and ~6:30 h. The failure of the whole five inner core rings is completed at about 9:30 which is shown in Figure 22 as an abrupt decrease in temperature. At that time the outer sixth core ring is still intact, because of the low decay power level. Then, the core debris of the five inner rings accumulates on the moderator tank bottom. The first significant material relocation into the lower plenum after local failure of the moderator tank bottom of radial ring 3 happens at 11:17 h. Thereafter, the particulate debris and melt, respectively, are released into the lower plenum, start evaporating the remaining water and heat up/melt the lower core/moderator tank support grid and the filler pieces in the lower plenum from the top. The water of the lower plenum has been fully evaporated at 12:14 h. As the melt spreads radially on the filler pieces, it gets into contact with the RPV bottom head side wall as well, which heats up (Figures 24 and 25). In the next almost 12.5 hours besides the core debris/melt, additional several tons of metallic melt are formed from the filler pieces and an additional significant amount of radionuclides are released into the RCS. After 19:44 h the outer radial core ring (6th Ring) totally collapses instantaneously due to the loss of support from below and relocates into lower plenum. At this point, the mechanical loading to the RPV wall is very limited, determined by the mass of melt, filler pieces, and the RPV bottom itself.

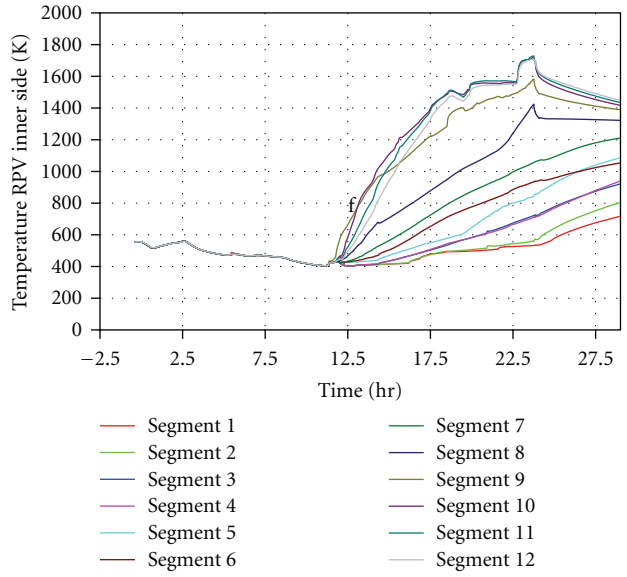

Figure 24: Temperature of RPV bottom wall at inner side.

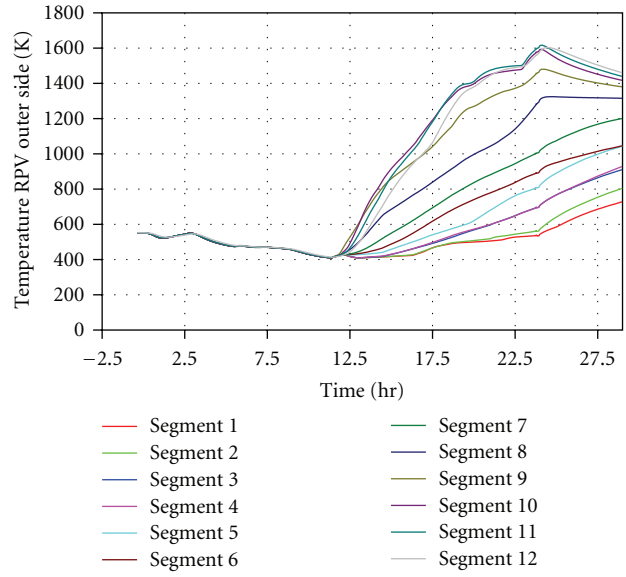

Figure 25: Temperature of RPV bottom wall at outer side.

This means that creeping effects are probably proceeding slowly, as the pressure difference across the wall is almost zero. Therefore, RPV failure is assumed in the MELCOR calculation if the outer RPV wall temperature in a segment reaches 1573 K (1300°C). This consideration is also done because no pressure difference exists across the wall in the late phase of the analyzed transient, which otherwise drives the 1D creep rupture model in MELCOR. The RPV failure is calculated to take place at 23:45 h after event initiation (temperature peak for segments 10 to 12 in Figure 25).

8. Discussion of Results

Several publications on SBO transients for PWR reactors can be found in the open literature. In particular, information on the expected timing of core uncovery and beginning of core heatup for a German PWR reactor of type KONVOI has been selected from PSA level 2 results of GRS [5] to be compared with the very specific characteristics of CNA-2 PHWR.

Table 2 shows some selected data comparing results of the Low Pressure SBO transient for CNA-2, with a German PWR type KONVOI SBO transient considering depressurization as a result of creep rupture failure of the surge line after core melting has started. In difference to CNA-2, in the German PWR the hot leg accumulators will inject after depressurization and stop the core degradation for some time. This will happen even if the batteries are already depleted. If the accumulator injection was neglected, the RPV would probably fail up to one hour earlier.

As it can be seen, time of start core uncovery is almost one hour later for CNA-2 NPP than for the Reference PWR and mainly caused by the failure of the pressurizer SV stuck open and the nonfunctional accumulators. This can be explained by two means. Firstly, the Primary System volume-to-core power ratio for CNA-2 doubles that of the reference PWR, which means that there is a larger mass of water to be evaporated to reach complete emptiness of the primary system. This, combined with the very low values of CNA-2 decay heat, results in a great advantage.

On the other hand, the existence of two separated systems, namely, the coolant and the moderator systems, has as a consequence a very specific means of heat evacuation of the decay heat produced in the fuel elements. As it has been seen in a previous section, fuel channels are nearly empty at about 3:30 h, but water level in the moderator tank is still at two-thirds of the total height of the tank at that time. Although upper parts of core channels start to heat up (and eventually fail), the bottom of the fuel channels is in contact with water from the outside, which cools them mostly due to radiation heat transfer. The existence of such a heat sink derives in an increase of channel failure timing, which in the end derives into a later relocation to LP, and a larger time to implement Severe Accident Management Procedures prior to RPV breach. It should be mentioned that in the German PWRs, Accident Management Measures are implemented to depressurize the secondary side and the reactor circuit before the core heats up to use all water resources, but at least the accumulators, to gain time for other measures. More details are given in [5].

It is important to highlight that the correct modeling of radiation heat transfer from the empty fuel channels to the partially full moderator tank is of particular importance for the PHWR and strongly influences the time at which the moderator tank empties. The comparison between RELAP5 and MELCOR shows that the applied MELCOR model is able to predict this process very well.

This behavior has also been observed on all other transients calculated by MELCOR for the PSA Level 2 analysis

Table 2: CNA-2 PHWR NPP versus German PWR—timing of events in an SBO.

Plant characteristic	CNA-2 PHWR low pressure SBO MELCOR	Ref. German PWR KONVOI low pressure SBO MELCOR
Core thermal power (MW) (total)	2160	3765
Core decay power (MW) at reactor scram	129.6	241.9
Total volume of primary system (m^3)	520	415
Primary system volume to core power ratio (m^3/MW)	0.241	0.110
Event listed for CNA-2 PHWR/Event listed for PWR	Time (h:m)	Time (h:m)
SG dryout	~2:00	0:57
PRZ SV failure stuck open	2:31	—
Start of uncovery of core/moderator tank	3:00/3:00	~2:10/—
Total uncovery of core/moderator tank	3:30/9:00	~4:30/—
Gap release from fuel	3:56	2:22
Beginning of core channel failure (PHWR), respectively Core failure and debris formation (PWR)	5:16	2:35
Failure of surge line due to creep rupture followed by accumulator injection	—	2:55
Fuel relocation to moderator tank bottom (PHWR) Molten pool formation in core (PWR)	>5:30	>4 h
Failure of moderator tank bottom (PHWR)/core support plate (PWR) and debris relocation to lower head	11:17	5:02
RPV failure	23:45	6:22

of CNA-2, and as well for LOCAs in the reactor circuit. An exception is LOCAs in the piping of the moderator system, in which the moderator tank gets empty relatively fast, being this CNA-2 specific heat sink lost.

9. Conclusions

In the paper, a description of the results of a Station Black-Out sequence for Atucha 2 Nuclear Power Plant calculated with MELCOR 1.8.6 YV3165 code has been presented. For the described transient, loss of power was assumed as an initiating event, accompanied by the failure of four out of four diesel generators. All remaining plant safety systems were considered to be available. For the depressurization of the system, it was assumed that during the Station Black-Out sequence the pressurizer safety valve failed stuck open after 17 cycles, respectively, 3 cycles of a blowdown of water.

An overview of CNA-2 NPP design characteristics was presented, together with the description of MELCOR nodalisation of the plant performed by GRS in the frame of PSA Level 2 Analysis. This input deck was set according to previous works performed by GRS for other German NPPs as well as state of the art recommendations. The qualification was done together with CNEA through a comparison of results obtained with a RELAP5 input deck used at NA-SA for PSA Level 1.

A very detailed description of the accident sequence was then presented, highlighting CNA-2 specific thermal-hydraulic plant behaviour as well as specific phenomena. Special attention was given to the fact that, at about 3:30 h after the start of the transient, fuel channels get empty while the moderator tank is still partially full. The moderator tank acts then as a heat sink to decay heat, which is evacuated by radiation heat transfer. The moderator is further evaporated lowering its level. This feature derived from the fact that cooling and moderator systems are separated, together with a high primary system volume to thermal power ratio, results in a very slow transient. As a consequence, calculated RPV breach time for CNA-2 Low Pressure SBO transient is almost four to five times larger than that of other German PWRs.

Nomenclature

CNA-2: Central Nuclear Atucha-2 (Atucha 2 Nuclear Power Plant)
CNEA: Comisión Nacional de Energía Atómica
GRS: Gesellschaft für Anlagen-und Reaktorsicherheit (GRS) mbH
KBA: Volume control system of CNA-2
LOCA: Loss of coolant accident
LP: Lower plenum
LWR: Light water reactor
MCP: Moderator pumps
NA-SA: Nucleoeléctrica Argentina Sociedad Anónima
NPP: Nuclear power plant
PARs: Passive autocatalytic recombiners
PHWR: Pressurized heavy water reactor
PSA-L2: Probabilistic Safety Analysis—Level 2
PWR: Pressurized water reactor
RCS: Reactor cooling system
RPV: Reactor pressure vessel
SNL: Sandia National Laboratories

SBO: Station Black-Out
SG: Steam generator.

References

[1] M. Sonnenkalb and T. H. Steinrötter, "Probabilistic Safety Analysis (PSA) Level 2 for CNA II, CNA II—MELCOR Input Deck Description," Tech. Rep., GRS 01/2010, 2011.
[2] J. M. Garcia et al., "CNAII MELCOR and RELAP models comparison," CNEA number 41-033-10, Rev.1, 2011.
[3] R. O. Gauntt et al., "MELCOR Computer Code Manuals, Vol. 1: Primer and Users' Guide, Version 1.8.6 September 2005," Sandia National Laboratories Albuquerque, NM 87185-0739, NUREG/CR-6119, Rev. 3, SAND 2005-5713.
[4] M. Sonnenkalb, "Summary of MELCOR Applications to German NPPs," in *Proceedings of the Cooperative Severe Accident Research Program/MELCOR Code Assessment Program Meeting*, Albuquerque, NM, USA, 2005.
[5] "GRS mbH, Bewertung des Unfallrisikos fortschrittlicher Druckwasserreaktoren in Deutschland," GRS-175, 2001.

Hindawi Publishing Corporation
Science and Technology of Nuclear Installations
Volume 2012, Article ID 735719, 13 pages
doi:10.1155/2012/735719

Research Article

An Evaluation Methodology Development and Application Process for Severe Accident Safety Issue Resolution

Robert P. Martin

Safety Analysis & Methods Development, Babcock and Wilcox Nuclear Energy, 109 Ramsey Place, Lynchburg, VA 24501, USA

Correspondence should be addressed to Robert P. Martin, rpmartin@babcock.com

Received 2 November 2011; Accepted 8 February 2012

Academic Editor: Gilberto Espinosa-Paredes

A general evaluation methodology development and application process (EMDAP) paradigm is described for the resolution of severe accident safety issues. For the broader objective of complete and comprehensive design validation, severe accident safety issues are resolved by demonstrating comprehensive severe-accident-related engineering through applicable testing programs, process studies demonstrating certain deterministic elements, probabilistic risk assessment, and severe accident management guidelines. The basic framework described in this paper extends the top-down, bottom-up strategy described in the U.S Nuclear Regulatory Commission Regulatory Guide 1.203 to severe accident evaluations addressing U.S. NRC expectation for plant design certification applications.

1. Introduction

Associated with rare, hazardous events, such as nuclear power plant (NPP) severe accidents, is a degree of uncertainty that provides a significant challenge to the evaluation and resolution of related design and analysis methods issues. For events occurring at some sufficiently observable frequency, design improvements can evolve through the understanding gained from such events and applicable test programs, leading to long-term acceptance. The broad uncertainties associated with severe accident initiators and event progression impose inherent limits on the benefits of this approach for severe accident design. As such, there is greater reliance on analysis and emphasis on the better understood severe accident phenomena. The engineering design process for an NPP's severe accident response strategy has evolved to a process that relies on the

(i) establishment of safety goals,

(ii) identification of processes and phenomena,

(iii) iterative design processes focused on risk reduction,

(iv) test programs,

(v) expert elicitation on important severe accident safety issues,

(vi) analysis methods development,

(vii) process studies.

Consistent with current US regulatory requirements and guidance, final acceptance and resolution of relevant beyond-design-basis events is demonstrated through detailed deterministic studies and probabilistic risk assessment (PRA).

The unique characteristic of this process for severe accidents is the consideration of risk in the resolution of severe accident safety issues. Generation III and IV advanced reactors designs incorporate features that significantly reduced risk relative to current-generation light water reactors (LWRs). Practical consideration of this reduced risk requires that this information be incorporated into measures not only of acceptable performance, but also of relevance.

The key objectives of any severe accident safety issue resolution methodology are to

(i) define the technical basis for the engineered event prevention and mitigation features,

(ii) develop/identify analysis tools,

(iii) identify key uncertainties and uncertainty treatments impacting acceptance criteria figures of merit,

(iv) determine the calculation matrix to demonstrate containment performance during severe accidents,

(v) calculate safety margins against regulatory expectation.

While the major components of severe accident engineering are the credited test programs and corresponding analytical methods, the identification of the necessary analyses involves engineering insights that combine regulation, industry experience, fundamental understanding of thermal hydraulic and severe accident phenomena, and risk/consequence factors. The principal severe accident design goal for all cases is the demonstration that the containment is preserved as a leak-tight barrier for at least 24 hours. By virtue of the inherent low probability of severe accidents, there is broad diversity in postulated mechanisms that can lead to containment failure. In light of this unique challenge, priority must be established so that meaningful conclusions can be drawn from analysis.

This paper presents a general paradigm for the resolution of severe accident safety issues related to the more likely severe accidents. It is a natural extension of the top-down, bottom-up analysis framework described in the U.S. Nuclear Regulatory Commission Regulatory Guide 1.203 on the Evaluation Methodology Development and Application Process (EMDAP) [1]. The top-down, that is, requirements, element begins with the identification of safety goals, documentation of severe accident engineering activities related to addressing these goals, and the identification of important phenomena that relate to acceptance criterion. The bottom-up, or methodology adequacy element addresses the many facets of uncertainty management, including test data applicability, code and model development, code verification and validation, uncertainty quantification, human reliability, and the consequence of failure.

This methodology complements PRA activities that address the broader event trees describing all possible scenarios leading to core damage and radiological releases. It addresses the elements stated above and has been applied to AREVAs U.S. EPR design [2].

2. Methodology Description

The objective of an evaluation methodology is to confirm the adequacy of a particular system, structure, or component to reliably and safely perform under phenomenological challenges associated with normal operation, anticipated operational occurrences, postulated accidents, and severe accidents. For an NPP design, the EMDAP addresses the regulatory expectation related to the content of the safety analysis reports that are reviewed and approved by the safety authority. In the US the industry is guided by US NRC's Standard Review Plan and Regulatory Guide 1.206 [3, 4] for preparing safety analysis report content.

In 2005, the US NRC published RG 1.203, describing the structured evaluation model development and assessment process. With its introduction, greater responsibility has been placed on applicants for defining the technical basis of design-basis evaluation methodologies, rather than procedural compliance with the elements of 10 CFR 50 (e.g., Appendix K) or the SRP. The EMDAP is considered to be generally applicable to the development of analysis methods for the purpose of evaluating safety issues related to NPP unanticipated transients and accidents. EMDAP starts from the definition of the objectives, the functional requirements, and the identification of important phenomena. Guided by these top-level priorities, code development and assessment follow, ultimately leading to the evaluation model adequacy decision.

With regard to severe accident analysis, the U.S. NRC's SECY-93-087 [5] provides further clarification of the regulatory expectation by stating that "containment integrity be maintained for approximately 24 hours following the onset of core damage for the more likely severe accident challenges." The application of an evaluation methodology is not simply analysis, but a suite of activities that guide an acceptability determination. They encompass the breadth of understanding on the subject, beginning with the characterization of perceived risks. This includes the statement of safety goals and identification of the corresponding safety issues. Safety issue resolution begins with a review of the severe accident engineering accomplishments that demonstrate proof of principle, such as the identification of relevant phenomena, the credited test programs, the evolution of analytical techniques, and related ranges of applicability of the conclusions drawn from these activities.

With this foundation, the development of an evaluation methodology can begin in earnest. Safety goals are translated into analysis measures (i.e., figures of merit), process and phenomenological uncertainties are characterized, and calculations are designed to demonstrate the completeness of the design in terms of the expected domain of possibilities. Calculations are performed and conclusions drawn. These activities are illustrated in Figure 1 within four elements for this severe accident safety issue resolution methodology. The nomenclature deviates from that appearing in RG 1.203 by emphasizing the role of an evaluation methodology to address specific regulatory compliance issues and the unique role of risk assessment to inform severe accident analysis. By emphasizing compliance in a separate process element, activities related to managing preexisting knowledge and experience are naturally combined in the second element. Elements 3 and 4 are analogous to elements 3 and 4 of RG 1.203 while uniquely addressing severe accident issues and the role of PRA and severe accident management guidelines.

2.1. Managing Compliance. Managing compliance begins with the identification of the regulatory goals, which emphasize safety. The ultimate NPP safety goal is the protection of the public from uncontrolled release of fission products through a breach in containment following a severe accident. As outlined in WASH-1400 [6], the commonly recognized modes of containment failure following a postulated severe accident are steam explosion, containment bypass, hydrogen explosion, containment overpressurization, and basemat ablation.

These containment failure mechanisms are expected to be resolved through design features providing both

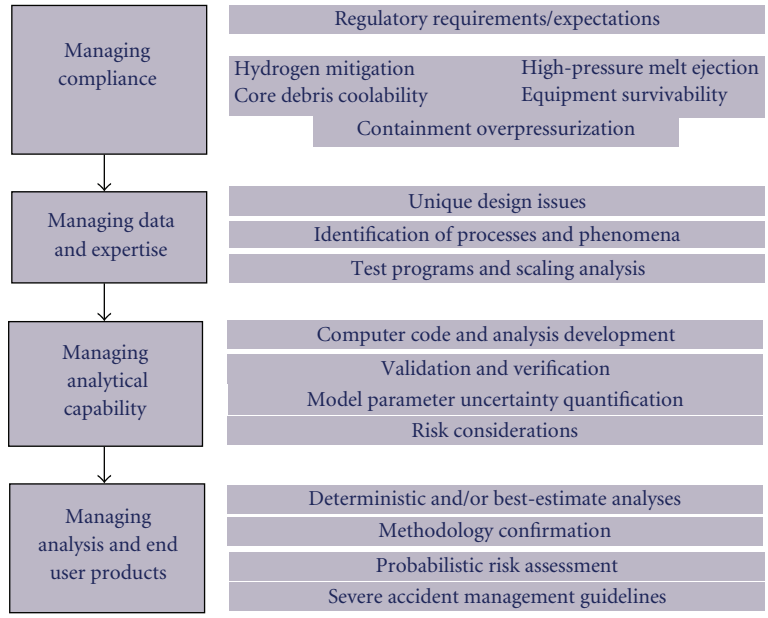

Figure 1: Process for severe accident safety issue resolution.

preventive and consequence mitigation protection. To benchmark plant safety for new light water reactor designs, the NRC has outlined in SECY-93-087 and SRP Section 19.2 the following acceptance criteria for a plant's response to severe accidents.

2.1.1. Hydrogen Mitigation

(i) Accommodate hydrogen generation equivalent to a 100% metal-water reaction of the fuel cladding.

(ii) Limit containment hydrogen concentration under 10%.

(iii) Provide containment-wide hydrogen control.

2.1.2. Core Debris Coolability

(i) Provide reactor cavity floor space to enhance debris spreading.

(ii) Provide a means to flood the reactor cavity to assist in the cooling process.

(iii) Protect the containment liner and other structural members with concrete, if necessary.

(iv) Ensure that the best-estimate environmental conditions (pressure and temperature) resulting from core-concrete interactions do not exceed service level C for steel containments or factored load category for concrete containments, for approximately 24 hours. Also ensure that the containment capability has margin to accommodate uncertainties in the environmental conditions from core-concrete interactions.

2.1.3. High-Pressure Melt Ejection (HPME)

(i) Provide a reliable depressurization system.

(ii) Provide cavity design that limits the amount of ejected core debris that reaches the upper containment.

2.1.4. Containment Performance

(i) Preserve the containment's role as a reliable, leak-tight barrier for approximately 24 hours following the onset of core damage under the more likely severe accident challenges.

(ii) Beyond 24 hours, ensure that the containment continues to serve as a barrier against the uncontrolled release of fission products.

2.1.5. Equipment Survivability

(i) Maintain reliability of functions during relevant severe accident scenarios.

2.2. Managing Data and Expertise. While there is still much to learn about the nature of severe accident causes and progression, a rich database of international research and development exists to support the technical basis of an evaluation methodology (see, e.g., [7–64]). In general, these references provide a good compilation and discussion of the experience gained and conclusions drawn from those tests. This information gets fed back into the engineering process to

(1) refine design features,

(2) provide technical bases for resolving safety issues,

(3) validate computational tools for production analysis,

(4) define applicability and uncertainty ranges to be considered in performance analyses.

Generation III and IV NPP designs incorporate design features to specifically address the severe accident safety issues identified in Section 2.1. Associated with each of these issues are processes and phenomena expected during a severe accident. Drawing on the general understanding of severe accident initiators and their progression, as developed from research and development, and considering analysis objectives, expert opinion is captured into phenomena identification and ranking tables (PIRTs) [65], many of which appear in the public domain (see, for example, [66, 67]). With severe accidents, there is often the temptation to include sequences having low frequency with potentially high consequence. Such events are best examined individually (see discussion in Section 2.4.3), as the uncertainties associated with these more remote events are, by definition, much more difficult to quantify. Table 1 provides a general list of phenomenological categories that theoretically could appear during a severe accident. The related processes and phenomena must be characterized and understood to make an informed judgment on the merits of a particular design.

Table 1: Identification of severe accident processes and phenomena for generic ALWR.

Phenomena	Safety Issue
(1) Thermal-hydraulic and fuel rod degradation	Hydrogen control/core debris Coolability
(2) Core melt progression (degradation of core structure)	Hydrogen control/core debris Coolability
(3) Core melt relocation to lower head	Hydrogen control/core debris coolability
(4) Oxide/metal separation	Hydrogen control/core debris coolability
(5) Crust formation and failure	Core debris coolability
(6) In-vessel debris formation	Core debris coolability
(7) External reactor vessel cooling (in-vessel retention only)	Core debris coolability
(8) RPV failure modes	Containment performance/hpme
(9) In-vessel fuel-coolant interaction	Containment performance
(10) High-pressure melt ejection	HPME
(11) Steam/hydrogen transport	Hydrogen Control/Containment Performance
(12) Hydrogen recombination	Containment Performance
(13) Hydrogen combustion	Containment Performance
(14) Ex-vessel steam explosion	Containment Performance
(15) Molten core-concrete interactions and melt spreading	Hydrogen control/core debris coolability/containment performance
(16) Ex-vessel core debris stabilization	Core debris coolability/containment performance
(17) Long-term containment heat removal	Containment performance
(18) Fission product transport	Containment performance

2.3. Managing Analytical Capability. Analytical capability relies on a calculation procedure or instruction, the basis of which builds from the complete evaluation methodology. Addressing the completeness and range of applicability of individual analytical models and correlations represents a necessary, but not unique code/model challenge to demonstrating the adequacy of an analysis tool. Code/model development challenges may begin with the form of the governing equations, but, for complex events like a severe accident, certainly will appear with any empiricism introduced for analytical closure.

Beyond code structure, flexible user-defined input presents a near endless opportunity for improper nodalization and/or useroptions. The so-called user effect reflects the consequence of a robust and flexible modeling interface popular within the modeling and simulation community [68]. The most common strategy used to address the user effect is to define a priori restrictions on nodalization and the application of user options that are codified into automation.

Several computer codes have been developed to specifically address severe accident phenomena. Among those developed to support the US industry and address most of the phenomenological categories appearing in Table 1 are MELCOR and SCDAP/RELAP5, sponsored by the U.S. NRC [69, 70], and MAAP, sponsored by the Electric Power Research Institute (EPRI) [71].

While these codes have been developed to address a broad range of severe accident phenomena and the integral relationship of the core, reactor coolant system, and containment, specialty codes are often required to assess unique phenomena, such as corium spreading and stabilization and fission product transport.

The credibility of an evaluation methodology relies on the associated verification and validation through code assessments. Verification is the confirmation that documented statements accurately reflect the coding and evaluation methodology procedure mechanics, while validation is the act of demonstrating or testing. Verification typically takes the form of a line-by-line review of coding and supporting evaluation documentation, and confirmation of compliance with an approved quality assurance plan. Standard problems, benchmarks with other codes, or analytical exercises with known solutions (e.g., method of manufactured solutions) are also useful complements to explicit code-to-data comparisons.

Computational tools are validated using an appropriate developmental assessment matrix consisting of both separate and integral effects test program data that address the more important phenomena influencing the figures of merit. The assessment matrix supports the evaluation methodology development in defining nodalization, quantifying code accuracy, and demonstrating any code or model scaling effects. The principal objectives are to demonstrate sufficient accuracy in modeling dominant physical processes

Table 2: Mapping of key severe accident phenomena to test programs.

Key phenomena	Test program
(1) Thermal-hydraulic and fuel rod degradation (i) Stored energy (ii) Decay heat (iii) Oxidation	CORA (FZK) [7] PBF SFD tests (INL) [8]
(2) Core melt progression (i) Zr melt breakout temperature (ii) Fuel rod collapse temperature (iii) Core material melt temperatures	PHEBUS (CEA) [9, 10] QUENCH (FZK) [12] LOFT (OECD) [13]
(3) Core melt relocation to lower head (i) Melt relocation heat transfer coefficient	Lower head failure program (NRC) [14]
(4) In-vessel oxide/metal separation	RASPLAV/MASCA (OECD) [15]
(5) Crust formation and failure (i) Gap heat transfer	Super-critical water reactor material property evaluations (INL) [16]
(6) In-vessel debris formation (i) Heat transfer within fuel debris beds	TMI-2 vessel investigation project (OECD) [17, 18]
(7) External reactor vessel cooling	SNL LHF program (SNL) [19]
(8) RPV failure modes (i) Local and global lower head/vessel failure (ii) Material properties (iii) Thermal radiation exchange	
(9) In-vessel steam (research overlaps with (14) below) (i) Premixing (ii) Quenching (iii) Propagation	FARO (JRC, Ispra) [20] KROTOS (JRC, Ispra) [21] TROI (KAERI) [22]
(10) High pressure melt ejection (i) Particle size (ii) Obstructions	DCH/TDS/LFP/WC (SNL) [23–27] IET-Zion/IET-surry/U (SNL/ANL) [28, 29] CWTI (ANL) [31] DCH (FAI) [32]
(11) Steam/hydrogen transport (i) Containment transition to single convective volume	HDR (Germany) [33] NUPEC large scale test facility (MITI, Japan) [34] Battelle model containment (USA) [35]
(12) Hydrogen recombination (i) PAR efficiency	Large scale vented containment test facility (Canada/AECL) [36] Battelle model containment (Germany/Battelle) [37] KALI (CEA) [38] H2PAR (CEA) [39]
(13) Hydrogen combustion (i) Autoignition temperaturez	Large view (University of Pisa) [40] AECL interconnected vessels (Canada/AECL) [40] Large-scale vented containment test facility(Canada/AECL) [40] Battelle model containment (BMC) (Germany/Battelle) [40] PHDR (Germany/FZK) [40] NUPEC large-scale test facility (Japan) [36, 40] RUT (Russian Research Centre "Kurchatov Institute") [40]
(14) ex-vessel steam (research overlaps with (9) above) (i) Premixing (ii) Quenching (iii) Propagation	FARO (JRC, Ispra) [20]KROTOS (JRC, Ispra) [21] TROI (KAERI) [22]

Table 2: Continued.

Key phenomena	Test program
(15) Molten core-concrete interactions and melt spreading	BETA (FZK) [41] ACE (ANL) MACE (ANL) OECD-MCCI [42–48] BALI (CEA Grenoble) [49] BALISE (CEA Grenoble) [50] CORESA (SNT, FANP) [51, 52] CIT (EU-FW5) [53] KAPOOL (FZK) [54] MET-1 (ANL) [55] CORINE (CEA) [56] KATS (FZK) [57] COMAS (SNU) COMAS-EU (SNU) [58] VULCANO (CEA) [59] FARO (JRC-Ispra) [60] RIT-spreading (RIT, Stockholm) [61]
(16) Ex-vessel core debris stabilization (flooding and basemat cooling)	OECD-MCCI (ANL) [62] ECOKATS-2 (FZK) [63] BENSON CHF-tests (AREVA NP) [64]

(determined from a PIRT), appropriate nodalization, independence of scale effects, and the relative insensitivity of compensating error. Table 2 relates many of the severe accident phenomena appearing in Table 1 to major test programs conducted internationally.

Analysis uncertainty in modeling and simulation has many sources. These include those associated with approximated models that describe the underlying physics; those associated with the settings of parameters used in physical models, those associated with performing a simulation at a given spatial resolution; those associated with approximations in the numerical algorithms. Uncertainty quantification is the process of characterizing, estimating, propagating, and analyzing all kinds of uncertainty to support decision making.

Because of the investment involved in quantifying uncertainty, the set of uncertainty parameters must be manageable and consider the task outcomes from the previous evaluation methodology development tasks, in particular, expertise documented in a PIRT. Data from separate-effects tests are separated into control and validation sets. The control set is used to derive the uncertainty and, as the name implies, the validation set is used to validate the integrity of the uncertainty model. A general uncertainty model is characterized by a bias and a probability density function; however, the uncertainty model does not necessarily reflect a task unique to performing a probabilistic analysis. A deterministic analysis can be viewed as one built from uncertainty models consisting of parameter biases. While the bias may simply reflect a static error in a model parameter, it can also be used to define a conservative or bounding treatment based on a limited set of test data.

A broad definition of uncertainty quantification includes risk quantification, which is particularly applicable when examining severe accident phenomena. Risk quantification requires a model that takes system response metrics and their uncertainties as an input and produces risk metrics and their uncertainties as the output. For severe accident analysis, an applicable system response metric could be core damage frequency (CDF). Defining CDF threshold to use to manage the scope of analysis must have a reasonable technical basis. For Generation III and IV NPP designs, new safety features have driven the CDF very low. As such, a poorly identified threshold might exclude so many events that the completeness of a severe accident analysis comes into question. Herein lies the concept of "relevant" or "more likely" events, a term that comes from SECY 93-087 and is interpreted to mean that there exists a threshold of relevance for which certain events or combination of events becomes so unlikely that detailed analytical consideration is unnecessary. Just as PIRT provides guidance of important phenomena, the risk metric CDF provides guidance of the risk-relevant scenarios.

2.4. Managing Analysis and End-User Products. Considering the high degree of uncertainty often associated with severe accident progression, the assignment of event studies can be speculative. Accordingly, a 3-fold strategy for the development of a sufficient calculation matrix is employed incorporating

(i) best-estimate calculations of relevant events,

(ii) uncertainty analysis calculations,

(iii) supplemental sensitivity calculations.

An overview of activities involved in preparing these calculations is described in the following subsections.

2.4.1. Best-Estimate Analysis. Best-estimate calculations of the risk-relevant scenarios are included to reveal performance target insights appropriate for a relevant discussion. Such calculations are best-estimate considering both risk factors leading to a particular event and the subsequent phenomenological progression. These risk-relevant scenarios are identified by incorporating risk information from PRA to select those most probable events that lead to core damage and challenge containment integrity. Regarding the former, deterministic analysis is performed to identify particular initiating events and subsequent failures that lead to the onset of core damage. For licensing purposes, the criteria delineating a severe accident are simply taken as a core state that exceeds the design-basis LOCA regulatory limit on clad temperature, which per US code is 2200°F (1204 C). The fidelity of the analytical tool being used in this exercise must be considered. As such, adjustments on that criterion may be necessary (see [72]). Analysis and conclusion from the PRA are expected to provide (1) the demarcation of specific core damage end states (CDESs) and (2) the probability of a particular "risk-relevant" event type leading to a particular CDES.

Table 3 presents common initiating event families considered in typical PWR level 1 PRA. In practice, not all of these event families can be considered relevant. U.S. NRC's Regulatory Guide 1.216 on containment structural integrity evaluations describes an acceptable way to identify the more likely severe accident initiators as a suite of sequences or plant damage states that, when ordered by percentage contribution, represent 90 percent or more of the CDF. A CDF threshold is identified associated with that criterion, which becomes the filter for identifying the suite of relevant events or event families.

CDESs are used by PRA to link the level 1 core damage event trees to the level 2 containment event trees by bringing together core damage sequences with similar characteristics and using those sequences as the initiating event for examining severe accident mitigation and containment failure probability. A selection of CDES for a typical PWR includes

(i) a high RCS pressure at core damage such as transient sequences where the bleed valves have not been opened prior to core damage;

(ii) a low RCS pressure at core damage sequence such as with a stuck open pressurizer safety/relief valve;

(iii) a loss-of-offsite power concurrent with a small LOCA (e.g., pump seal);

(iv) sequences initiated by Small LOCAs with bleed failure.

PRA considers an expanded list of CDES and plant damage ends states; however, for the purpose of identifying relevant scenarios, the CDESs of interest are those representing a unique RCS condition at the onset of core damage. Specifically, this is system pressure and the nature of ongoing feed and bleed. Concern about the RCS condition ends when the reactor pressure vessel fails. For these reasons, the four categories of CDESs were viewed as sufficient to cover (1) the situation of no RCS boundary failure (high pressure) as would result from the loss of secondary cooling to (2) a TMI-2-like scenario with a stuck pressurizer relief valve to (3) a LOOP with RCP-seal LOCAs and (4) small (and larger) LOCAs. It should be noted that RCS breaches are addressed at both low system locations with the RCP-seal and small breaks and high system locations with the stuck pressurizer relief valve high in the system.

Table 3: Postulated initiating events.

Initiating event (IE) description
Interfacing system loss of coolant accident
Loss of balance of plant (LBOP)
Loss of coolant accident (LOCA)
Loss of condenser heat sink
Loss of component cooling water
Loss of main feedwater flow (LOMFW)
Loss of offsite power (LOOP)
Inadvertent opening of a main steam safety valve
Loss of one emergency bus
Steam generator tube rupture
Steam line break
Turbine trip

Table 4: Relevant core damage events and frequency.

Description	% Total CDF
LOOP with seal LOCA (LOOP SS)	F_A
LOOP with a low-pressure end state (LOOP PL)	F_B
LOOP with a high-pressure end state (LOOP TR)	F_C
LBOP/LOMFW (LBOP TR)	F_D
All LOCAs	F_E

By considering only the relevant event families and binning event families based on similar CDES, the relevant events and the corresponding event frequency, presented as percent total CDF, may be compiled as shown in Table 4. The event frequency data provides the probability of a particular event type given a random relevant severe accident.

2.4.2. Uncertainty Analysis. An objective of the uncertainty analysis is to consider the range of conditions over which severe accidents are most likely to occur. Performance metrics associated with the identified severe accident safety issues (e.g., hydrogen concentrations, containment pressure, corium temperature, RCS pressure at RPV failure, etc.) and sensitive to the many processes and phenomena appearing in Table 1 can be evaluated using this uncertainty analysis. A large number of different code model parameters can be associated with those 18 phenomenological categories. Table 5 presents a mapping from phenomena to code input.

Table 5: Sample mapping of identified phenomena to code model parameters.

Phenomena Class	Associated phenomena	Model implementation description
Thermal-hydraulic and fuel rod degradation	Stored energy	Total power
	Decay Heat	
	Zr-steam oxidation parameters	Zr-H_2O oxidation multiplier
Core melt progression	Zr melt breakout temperature	Cladding integrity with oxidation
		Cladding creep Rupture temperature
	Fuel rod collapse temperature	Material creep (Larson-Miller) limit
	Fractional local dissolution of UO2 in molten Zr	Contact area multiplier
	Core material melt temperatures	Fuel melt temperature
		Control rod melt temperature
Melt relocation to lower head	Melt relocation heat transfer coefficient	Flow blockage based on porosity
Fuel coolant interaction	Large uncertainties, addressed in separate supplementary analysis	
Oxide/metal separation	(No unique model parameter, a function of oxidation process and relocation)	
Crust formation and failure	Gap heat transfer	Conservatively neglected
In-vessel debris formation	Heat transfer within fuel debris beds	Particulate debris size and debris porosity in lower plenum
Ex-reactor vessel cooling	Heat transfer rate	Heat transfer coefficient multiplier
		Material properties
		CHF on lower plenum surface
RPV failure modes	Local and global lower head/vessel failure	Initial radius of the local vessel failure
		Lower head damage fraction for failure
		Corium friction coefficient (in contact with vessel following failure)
	Thermal radiation exchange	Emissivities
MCCI	MCCI integrity of ex-vessel protective structure	Downward heat transfer coefficient
		Side wall heat transfer coefficient
		Flat plate CHF Kutateladze number (multiplier)
Melt spreading	Design dependent	
Steam/hydrogen transport	Containment transition to single convective volume	Flow area between containment compartments
Hydrogen recombination	PAR efficiency	Rate of recombination
		Operation cutoff based on H_2 concentration
Hydrogen combustion	Autoignition temperature	Local/global
Long-term containment heat removal	Design dependent	
Fission product transport	Flow area between containment compartments	

The specific model parameters appear in the MAAP4 code; however, analogous model parameters appear in other severe accidents like MELCOR. As a practical matter, MAAP4 was not viewed as being the preferred code to address all severe accident phenomena. As such, Table 5 only present the set of phenomena (and corresponding code input) well represented by the MAAP4 code. MAAP4 is particularly convenient for this exercise because uncertainty ranges for most of these parameters have been identified by Fauske and Associates, Inc., EPRI's contractor responsible for code development.

The common method for convolving this uncertainty domain relies on a "Monte-Carlo"-like nonparametric statistical approach. For each analysis code execution, each of the important uncertainty parameters being treated statistically is randomly sampled based on a previously determined probability distribution. Among the model parameters sample, are model parameters that describe the event initiator, which is sampled according to the predicted frequency (i.e., Table 4). Each sample code calculation can be viewed as the performance of an experiment with the experimental parameters being the important phenomena and plant

process parameters and the result being any appropriately represented performance metric (i.e., based on correlation with uncertainty parameters).

Based on the results of a suite of 59 sample calculations, the uncertainty domain of any particular performance metric of interest is quantified. The selection of 59 samples is based on the work of Wilks for defining tolerance regions [73, 74]. Following this nonparametric statistical approach, when 59 observations are drawn from an arbitrary, random distribution of outcomes, it can be shown that the largest value is such that with 95 percent confidence, at least 95 percent of all possible observations from that distribution will be less than the resulting largest value; that is, this result is the 95/95 tolerance limit. For severe accident evaluation applications, this 95/95 benchmark is assumed to be a sufficient estimation of the total tolerance limit of any particular performance metric used to demonstrate the US EPR severe accident response features.

2.4.3. Supplemental Analysis. Supplemental analyses should be performed to complete or complement the best-estimate analysis of the relevant scenarios and the uncertainty analysis. Of particular note are analyses for containment failure probability from HPME and fuel-coolant interactions (both in- and ex-vessel) using parametric models applying methodologies similar to [75]; combustion loads; source term; selected low-frequency, high-consequence events. Inputs required for these studies can usually benefit from extracting bounding values presented in the uncertainty analysis results.

2.4.4. Methodology Confirmation. The methodology confirmation step serves to confirm methodology assumptions introduced through the PIRT and through the reliance on data derived from scaled experiments. The principal objective is to assure that the important processes of interest are well scaled and, in situations in which scale distortion is evident, quantify analytical biases that relate to the safety analysis tool's ability to scale up the important phenomena. In practice, this exercise involves quantifying the degree to which a model input parameter affects a model output variable. Several approaches have been proposed [76–80]; however, variance-based methods are well suited for accompanying nonparametric best-estimate-plus-uncertainty analysis. Variance-based "importance" analysis is performed by first building a mathematical model and, through a stepwise multiple regression exercise, identifying the set of inputs subject to large variability or uncertainty.

The relevance of this understanding is that improved resolution of importance serves to enhance the credibility of this new best-estimate evaluation methodology through the validation of the engineering judgments and code model scaleup that guide methodology development. In addition, it provides insight into the processes and phenomena that impact key analysis measures and thus limits unnecessary characterization of uncertainty contributors of lesser importance.

2.4.5. PRA and SAMG. For severe accidents, understanding phenomenological performance of plant design features addressing the prevention and mitigation of a severe accident only partially fulfills the regulations. 10 CFR 50.34f, presenting the TMI-2 inspired regulatory changes, also introduced the trifecta of phenomenological process studies, PRA, and SAMG as tools for severe accident technical issue resolution. As previously described, phenomenological analysis and PRA have a symbiotic relationship in that result from one can be used to improve the results of an other. This is also true with SAMG, which incorporates operator actions to the inherent process and phenomenological uncertainties. PRA and SAMG are both recognized components to ultimately closing severe accident technical issues. Methods and applications for PRA and SAMG are well represented in existing literature and are not described in this paper.

3. Results

Application of this severe accident issue resolution methodology appears in Section 19.2 of the U.S. EPR FSAR [81]. Specifically, Section 19.2.4 describes the containment performance analysis for the U.S. EPR that meets the regulatory goals that are presented in Section 2.1.

The containment performance analysis shows that the containment maintains its role as a reliable, leak-tight barrier for at least 24 hours following the onset of core damage for the following listed severe accident challenges:

(i) hydrogen levels are kept sufficiently low to preclude containment failure by global deflagration and meets the 10 CFR 50.34(f)(2)(ix) requirement that uniformly distributed hydrogen concentrations in the containment do not exceed 10 percent during and following an accident that releases an equivalent amount of hydrogen as would be generated from a 100 percent fuel-clad metal water reaction;

(ii) the corium is reliably conditioned in the reactor cavity to promote spreadability in the spreading area after melt gate failure. The core melt stabilization system transfers the corium into a coolable geometry within the spreading compartment, thus providing sufficient removal of residual decay and long-term stabilization;

(iii) the U.S. EPR design, which incorporates several design features with enhanced preventive response to an HPME, precludes the potential mechanisms for HPME initiation and subsequent direct containment heating;

(iv) design characteristics of the U.S. EPR inherently impede the potential for steam explosion-induced containment failure because the necessary conditions required for steam explosions to exist are avoided;

(v) instrumentation and equipment that are relied upon to mitigate the consequences of a severe accident are qualified for use in beyond design basis accident environmental conditions.

Table 6: Dominant Severe Accident Phenomena.

Process or Phenomena
Break size
Zr-H_2O oxidation multiplier
Fuel melt temperature
Control rod melt temperature
Porosity of fuel debris beds
Opening of the PDS valves
Lower head damage fraction for failure
Flat plate CHF Kutateladze #
Steaming rate
PAR capacity scale factor
PAR threshold for operation

In addition, the results of an importance analysis identified 11 uncertainty contributors that dominate U.S. EPR severe accidents. These are summarized in Table 6. The principle phases of a severe accident are well characterized by these 11 uncertainty contributors. The dominant initiating event is the loss of offsite power with pump seal LOCA (i.e., one capturing the broadest spectrum of process and phenomenological characteristics). Corresponding to that event, the break size parameter appears as an important uncertainty contributor. During the core heatup and degradation phase, metal-water reaction and fuel and control rod melt temperature dominate. Event progression is also seen to be impacted by the timing of the primary depressurization system signal. The ex-vessel phase of the event begins with the lower head failure, sensitive to the lower head damage fraction for failure. Core debris coolability and containment response are obviously sensitive to energy input, which appears as high-temperature corium. Fuel and control rod melt temperatures play a role in setting the initial corium temperature as it enters the reactor cavity. Heat removal occurs primarily in the spreading area, where the flat-plate critical heat flux (CHF) Kutateladze number parameter defines the heat transfer rate from the corium pool. Operation of the many passive autocatalytic recombiners (PARs) mitigates the hydrogen threat and contributes to containment cooling. As such, PAR performance parameters have an observable impact on severe accident progression during this phase.

4. Conclusions

A general paradigm for severe accident safety issue resolution, adopting several principles from EMDAP, as appearing in U.S. NRC Regulatory Guide 1.203, has been described. This methodology provides a thorough report of the severe accident engineering activities for addressing the regulatory expectations for demonstrating severe accident response features. While the major components of severe accident engineering are the credited test programs and corresponding analytical methods, the identification of the necessary analyses involves engineering insights that combine regulation, industry experience, fundamental understanding of thermal-hydraulic and severe accident phenomena, and risk/consequence factors.

This safety issue resolution evaluation methodology was applied to the U.S. EPR for the development on content for its final safety analysis report. The results confirmed the designs adequacy to address the principal acceptance criteria. The conclusion is that the approach for demonstrating an NPP's performance during a severe accident is systematic, complete, and comprehensive and will provide sufficient insight for resolution of severe accident safety issues.

Nomenclature

CDES: core damage end states
CDF: Core damage frequency
CHF: Critical heat flux
EMDAP: Evaluation methodology development and application process
EPRI: Electric power research institute
FSAR: Final safety analysis report
HPME: High pressure melt ejection
LBOP: Loss of balance of plant
LOCA: Loss of coolant accident
LOMFW: Loss of main feedwater flow
LOOP: Loss of offsite power
MCCI: Molten core-concrete interaction
PIRT: Phenomena identification and ranking table
PAR: Passive autocatalytic recombiner
PDS: Primary depressurization system
PRA: Probabilistic risk assessment
SAMG: Severe accident management guidelines.

Acknowledgments

This paper reflects a similarly titled lecture delivered by the author for the attendees of the Scaling, UNcertainty, and 3D COuPled code calculations seminars (3D S.UN.COP). The 3D S.UN.COP seminars, which provided support for the preparation of this paper, is organized by the University of Pisa's San Piero a Grado Nuclear Research Group and highlights contemporary insights on topics including system codes, evaluation methodologies, uncertainty qualification, licensing.

References

[1] U.S. Nuclear Regulatory Commission and Regulatory Guide 1.203, "Transient and Accident Analysis Methods," Revision 0, December 2005.

[2] R. P. Martin, M. W. Bingham, C. A. Bonilla et al., "AREVA NP's severe accident safety issue resolution methodology for the U.S. EPR," in *Proceedings of the International Conference on Advances in Nuclear Power Plants (ICAPP'08)*, pp. 1122–1131, Anaheim, Calif, USA, June 2008.

[3] USNRC and NUREG-0800, "Standard Review Plan for the Review of Safety Analysis Reports for Nuclear Power Plants," most recent revision.

[4] USNRC and Regulatory Guide 1.206, "Combined License Applications for Nuclear Power Plants," most recent revision.

[5] US NRC and SECY-93-087, "Policy, Technical, and Licensing Issues Pertaining to Evolutionary and Advanced Light-Water (ALWR) Designs," issued April, 1993 and the corresponding SRM, issued July, 1993.

[6] US NRC, "Reactor Safety Study-An Assessment of Accident Risks in U.S. Commercial Nuclear Power Plants," WASH-1400 (NUREG-75/014), 1975.

[7] M. Firnhaber, K. Trambauer, S. Hagen et al., "CORA-13 Experiment on Severe Fuel Damage," NEA/CSNI-(93) 17, GRS-106, KfK 5287, July, 1993.

[8] Z. R. Martinson, Idaho National Engineering Laboratory et al., *PBF Severe Accident Fuel Damage Test 1–3 Test Results Report*, 1989, NUREG/CR-5354.

[9] M. Firnhaber, "ISP 28: Phebus-SFD B9+ Experiment on the Degradation of a PWR Type Core," NEA/CSNI/R(92)17, Volumes 1 and 2, 1992.

[10] B. Clément, N. Hanniet-Girault et al., "The first international PHEBUS fission product program for investigation of phenomena of severe water reactor accidents," *Nuclear Engineering and Design*, vol. 226, no. 1, pp. 5–28, 2003.

[11] W. Hering, Ch. Homann, and J. S. Lamy, "Comparison report on the blind phase of the OECD International Standard Problem no.45, exercise (QUENCH-06)," OECD Document ISP45-OECD, 2002, Report FZKA-6677.

[12] W. Hering, Ch. Homann, J. S. Lamy et al., "Comparison and interpretation report of OECD International Standard Problem no.45 exercise (QUENCH-06)," ISP45-OECD, 2002, Report FZKA-6722.

[13] E. W. Coryell, *Summary of Important Results and SCDAP/RELAP5 Analysis for OECD LOFT Experiment LP-FP-2*, 1994, NUREG/CR-6160, NEA/CSNI-(94) 3.

[14] J. L. Rempe, S. A. Chavez, G. L. Thinnes et al., *Light Water Reactor Lower Head Failure Analysis*, 1993, NUREG/CR-5642, EGG-2618.

[15] J. L. Rempe, "MASCA and RASPLAV test program—description, status, and implications," INEEL/EXT- 03-00224, 2003.

[16] J. L. Rempe, K. G. Condie, and D. L. Knudson, "Thermal properties for candidate SCWR materials," INL/EXT- 05-01030, 2005.

[17] L. A. Stickler, J. L. Rempe et al., "Calculations to estimate the margin-to-failure in the TMI-2 vessel," NUREG/CR-6196, EGG-2733, 1994.

[18] T. Y. Chu, U.S. Nuclear Regulatory Commission et al., *Lower Head Failure Experiments and Analyses*, 1999, NUREG/CR-5582 (SAND98-2047).

[19] J. R. Wolf, J. L. Rempe et al., "TMI-2 vessel investigation project integration report," NUREG/CR -6197, 1994, EGG-2734.

[20] D. Magallon and I. Huhtiniemi, "Corium melt quenching tests at low pressure and subcooled water in FARO," *Nuclear Engineering and Design*, vol. 204, no. 1–3, pp. 369–376, 2001.

[21] I. Huhtiniemi and D. Magallon, "Insight into steam explosions with corium melts in KROTOS," *Nuclear Engineering and Design*, vol. 204, no. 1–3, pp. 391–400, 2001.

[22] J. H. Kim, I. K. Park, Y. S. Shin et al., "A study on intermediate scale steam explosion experiments with zirconia and corium melts," in *Proceedings of the Transactions of the International Congress on Advanced Nuclear Power Plants (ICAPP'02)*, Hollywood, Fla, USA, June 2002.

[23] W. W. Tarbell, Sandia National Laboratories et al., *Results from the DCH-1 Experiment*, Sandia National Laboratory, 1987, SAND86-2483, NUREG/CR-4871.

[24] M. D. Allen, R. T. Nichols, J. E. Brockmann et al., *DCH-2: Results from the Second Experiment Performed in the Surtsey Direct Heating Test Facility*, Sandia National Laboratory, 1988, SAND87-0976, NUREG/CR-4917.

[25] M. D. Allen, M. M. Pilch, R. O. Griffith, and R. T. Nichols, *Experiments to Investigate the Effects of Water in the Cavity on Direct Containment Heating in Surtsey Test Facility- the WC-1 and WC-2 Tests*, Sandia National Laboratories, 1992, SAND91-1173.

[26] M. D. Allen, M. M. Pilch, T. K. Blanchat et al., *Experiments to Investigate to Direct Containment Heating Phenomena With Scaled Models of the Zion Nuclear Power Plant in the Surtsey Test Facility*, 1994, NUREG/CR-6044.

[27] T. K. Blanchat, U.S. Nuclear Regulatory Commission et al., *Experiments to Investigate Direct Containment Heating Phenomena With Scaled Models of a Surry Nuclear Power Plant*, 1994, NUREG/CR- 6152.

[28] M. Pilch, M. D. Allen, E. W. Klamerus et al., *Resolution of the Direct Containment Heating Issue for All Westinghouse Plants With Large Dry Containments or Subatmospheric Containments*, 1996, NUREG/CR-6338, SAND95-2381.

[29] M. M. Pilch and U.S. Nuclear Regulatory Commission, *The Probability of Containment Failure by Direct Containment Heating in Surry*, 1995, NUREG/CR-6109, SAND93-2078.

[30] J. L. Binder, L. M. McUmber, and B. W. Spencer, *Direct Containment Heating Integral Effects Tests at 1/40 Scale in Zion Nuclear Power Plant Geometry*, Argonne National Laboratory, 1994, NUREG/CR-6168, ANL-94/18.

[31] B. W. Spencer, J. J. Sienicki, L. M. McUmber et al., *Hydrodynamics and Heat Transfer Aspects of Corium-water Interactions*, Argonne National Laboratory, 1987, EPRI NP-5127.

[32] R. E. Henry, R. J. Hammersley, and G. T. Klopp, "Direct containment heating experiments in a zion-like geometry," *AIChE Symposium Series*, vol. 87, no. 283, pp. 86–98, 1991.

[33] H. Karwat, "SOAR on Containment Thermalhydraulics and Hydrogen Distribution," NEA/CSNI (99), 1999.

[34] J. Royen, "Final Comparison Report on ISP-35: NUPEC Hydrogen Mixing and Distribution Test (Test M-7-1)," NEA/CSNI (94), 1994.

[35] M. Firnhaber, T. F. Kanzleiter, S. Schwarz et al., "ISP37: VANAM M3—a multi compartment aerosol depletion test with hygroscopic aerosol material," NEA/CSNI (96), 1996.

[36] G. W. Koroll, W. A. Dewit, J. L. Sitar et al., "Hydrogen recombiner development at AECL," in *Proceedings of the OECD/NEA/CSNI Workshop on the Implementation of Hydrogen Mitigation Techniques, Winnipeg*, 1996, AECL-11762, NEA/CSNI/R(96)8.

[37] K. Fischer, "Qualification of a passive catalytic module for hydrogen mitigation," *Nuclear Technology*, vol. 112, no. 1, pp. 58–62, 1995.

[38] J. Hosler and G. Sliter, "PARs for combustible gas control in advanced light water reactors," in *Proceedings of the OECD/NEA/CSNI Workshop on the Implementation of Hydrogen Mitigation Techniques, Winnipeg*, 1996, AECL-11762, NEA/CSNI/R(96)8.

[39] P. Rongier and E. Studer, "H2PAR facility," in *Proceedings of the OECD/NEA/CSNI Workshop on the Implementation of Hydrogen Mitigation Techniques, Winnipeg*, 1996, AECL-11762, NEA/CSNI/R(96)8.

[40] W. Breitung, C. Chan, S. B. Dorofeev et al., "Flame acceleration and deflagration-to-detonation transition in nuclear safety," NEA/CSNI (2000), 2000.

[41] M. Firnhaber, "ISP 30: BETA V5.1 experiment on melt-concrete interaction," NEA/CSNI/R (92)9, 1992.

[42] D. G. Thompson et al., "Compilation, analysis and interpretation of ACE phase C and MACE experimental data—MCCI thermohydraulic results," ACEX TR-C 14, Argonne National Laboratory, 1997.

[43] M. T. Farmer, S. Lomperski, and S. Basu, "Mace test M3b data report volume 1," EPRI TR-108806, 1997, MACE-TR-D13.

[44] Farmer M. T. et al., "Mace test M4 data report," MACE-TR-D 16, 1999.

[45] M. T. Farmer, S. Lomperski, D. J. Kilsdonk, and R. W. Aeschlimann, "OECD MCCI project 2-D core concrete interaction (CCI) tests: CCI-1 test data report-thermalhydraulic results," OECD/MCCI 2004-TR01, 2004.

[46] M. T. Farmer, S. Lomperski, D. J. Kilsdonk, and R. W. Aeschlimann, "OECD MCCI project 2-D core concrete interaction (CCI) tests: CCI-2 test data report-thermalhydraulic results," OECD/MCCI 2004-TR05, 2004.

[47] M. T. Farmer, S. Lomperski, D. J. Kilsdonk, and R. W. Aeschlimann, "OECD MCCI project 2-D core concrete interaction (CCI) tests: CCI-3 test data report-thermalhydraulic results," OECD/MCCI 2005-TR04, 2005.

[48] B. W. Spencer, M. Fischer, M. T. Farmer et al., "MACE scoping test," MACE-TR-D 03, Argonne National Laboratory, 1999.

[49] J.-M. Bonnet, "Thermal hydraulic phenomena in corium pools for ex-vessel situations: the BALI experiment," in *Proceedings of the 8th International Conference on Nuclear Engineering (ICONE 8)*, Baltimore, Md, USA, April 2000.

[50] B. Tourniaire and J.-M. Bonnet, "Study of the mixing of immiscible liquids by sparging gas results of the BALISE experiments," in *Proceedings of the 10th International Topical Meeting on Nuclear Reactor Thermal Hydraulics (NURETH-10)*, Seoul, Korea, October 2003.

[51] M. Nie, M. Fischer, and W. Koller, "Status of interpretation of selected transient MCCI experiments conducted in the frame of the CORESA R&D project," in *Proceedings of the Jahrestagung Kerntechnik*, Stuttgart, Germany, May 2002.

[52] S. Hellmann, V. Lansmann, B. Friedrich et al., "Physico-chemical and material aspects of the core melt retention concept of the EPR," in *Proceedings of the OECD Workshop on Ex-Vessel Debris Coolability*, Karlsruhe, Germany, November 1999.

[53] B. Adroguer, P. Chatelard, J. P. van Dorsselaere et al., "Corium interactions and thermochemistry (CIT project)," INV-CIT (99)-P040, European Commission, 1999.

[54] B. Eppinger, T. Cron, G. Stern et al., "KAPOOL experiments on melt-through of a metal plate by an overlying melt pool," FZKA 7024, Forschungszentrum Karlsruhe, August 2004.

[55] M. T. Farmer, "Melt eruption test (MET-1) results," in *Proceedings of the 6th Program Review Meeting of the MCCI-OECD Project*, Madrid, Spain, April 2005.

[56] J. M. Veteau and R. Wittmaack, "CORINE experiments and theoretical modelling," FISA-95-EU Research on Severe Accidents, EUR 16896 EN, 1996.

[57] B. Eppinger, F. Fellmoser, G. Fieg et al., "Simulationsexperimente zum Ausbreitungsverhalten von Kernschmelze: KATS 8-17," Forschungszentrum, Karlsruhe, FZKA 6589, March 2001.

[58] W. Steinwarz et al., "COMAS spreading experiments with prototypic oxidic corium melts for optimization of spreading compartment designs," ICONE7, Tokyo, Japan, April 1999.

[59] R. Silverii and D. Magallon, "FARO LWR programme, test L26-S data report, technical note," EXV-CSC (98)-D007, 1998, EU 4th FWP.

[60] G. Cognet, J.-M. Seiler, I. Szabo et al., "The VULCANO spreading programme article," EU 4th FWP, EXV-CSC(98)-D018, SARJ-98, 1999.

[61] M. J. Konovalikhin, T. N. Dinh, and B. R. Sehgal, "Experimental simulation of core melt spreading in two dimensions," in *Proceedings of the The 9th International Topical Meeting on Nuclear Reactor Thermal Hydraulics (NURETH-9)*, San Francisco, Calif, USA, October 1999.

[62] B. R. Sehgal and B. W. Spencer, "Ace program phase D: melt attack and coolability experiments (MACE) program," in *Proceedings of the Second OECD (NEA) CSNI Specialist Meeting on Molten Core Debris-Concrete Interactions*, Karlsruhe, Germany, April 1992, NEA/CSNI-(92) 10, KfK 5108.

[63] H. Alsmeyer et al., "Experiment ECOKATS-2 on melt spreading and subsequent top flooding test and data report," Forschungszentrum, Karlsruhe, FZKA 7084, January 2005.

[64] M. Fischer, O. Herbst, and H. Schmidt, "Demonstration of the heat removing capabilities of the EPR spreading compartment," in *Proceedings of the 3rd International Symposium on Two-Phase flow Modelling and Experimentation*, Pisa, Italy, September 2004.

[65] G. E. Wilson and B. E. Boyack, "The role of the PIRT process in experiments, code development and code applications associated with reactor safety analysis," *Nuclear Engineering and Design*, vol. 186, no. 1-2, pp. 23–37, 1998.

[66] D. Magallon, A. Mailliat, J. M. Seiler et al., "European expert network for the reduction of uncertainties in severe accident safety issues (EURSAFE)," *Nuclear Engineering and Design*, vol. 235, no. 2–4, pp. 309–346, 2005.

[67] K. Nagashima, M. Alammar, and H. C. da Silva, "Application of uncertainty analyses with the MAAP4 code," in *Proceedings of the 5th International Conference on Simulation Methods in Nuclear Engineering*, Canadian Nuclear Society, Montreal, Quebec, month year.

[68] R. Ashley, M. El-Shanawany, F. Eltawila et al., "Good practices for user effect reduction," Status Report NEA/CSNI/R(98)22, 1998, Paris, France.

[69] R. O. Gauntt, R. K. Cole, C. M. Erickson et al., "MELCOR computer code manuals," Version 1.8.6, NUREG/CR-6119, Rev. 3, SAND-2417/2, Sandia National Laboratory, September 2005.

[70] SCDAP/RELAP5 Development Team, "SCDAP/RELAP5/MOD3.2 code manual, Vol. 1–5," NUREG/CR-6150, INEL-96/0422, July 1998.

[71] Fauske and Associates, Inc, "MAAP4—modular accident analysis program for LWR power plants, vol. 2, part 1: code structure and theory," prepared for Electric Power Research Institute, May 1994.

[72] J. S. Butler, D. Kapitz, R. K. Sundaram, and R. P. Martin, "MAAP4.0.7 analysis and justification for PRA level 1 mission success criteria," in *Proceedings of the International Congress on Advances in Nuclear Power Plants (ICAPP '08)*, Anaheim, Calif, USA, June 2008, paper 8200.

[73] S. S. Wilks, "Determination of sample sizes for setting tolerance limits," *The Annals of Mathematical Statistics*, vol. 12, pp. 91–96, 1941.

[74] R. P. Martin and W. T. Nutt, "Perspectives on the application of order-statistics in best-estimate plus uncertainty nuclear safety analysis," *Nuclear Engineering and Design*, vol. 241, no. 1, pp. 274–284, 2011.

[75] M. M. Pilch, M. D. Allen, E. W. Klamerus et al., *Resolution of the Direct Containment Heating Issue for All Westinghouse Plants With Large Dry Containments or Subatmospheric Containments*, 1996, NUREG/CR-6338, SAND95-2381.

[76] N. Zuber, G. E. Wilson, M. Ishii et al., "An integrated structure and scaling methodology for severe accident technical issue resolution: development of methodology," *Nuclear Engineering and Design*, vol. 186, no. 1-2, pp. 1–21, 1998.

[77] J. C. Helton, J. D. Johnson, C. J. Sallaberry, and C. B. Storlie, "Survey of sampling-based methods for uncertainty and sensitivity analysis," *Reliability Engineering and System Safety*, vol. 91, no. 10-11, pp. 1175–1209, 2006.

[78] K. Chan, A. Saltelli, and S. Tarantola, "Sensitivity analysis of model output: variance-based methods make the difference," in *Proceedings of the Winter Simulation Conference*, pp. 261–268, Atlanta, Ga, USA, December 1997.

[79] H. Glaeser, "Uncertainty evaluation of thermal-hydraulic code results," in *Proceedings of the International Mtg. Best-Estimate Methods in Nuclear Installation Safety Analysis (BE-2000)*, Washington, DC, USA, November 2000.

[80] R. P. Martin, "Quantifying phenomenological importance in best-estimate plus uncertainty analyses," *Nuclear Technology*, vol. 175, no. 3, pp. 652–662, 2011.

[81] "U.S. EPR final safety analysis report," Rev. 0, AREVA NP Inc., December 2007.

Hindawi Publishing Corporation
Science and Technology of Nuclear Installations
Volume 2012, Article ID 878174, 10 pages
doi:10.1155/2012/878174

Research Article

Heat and Mass Transfer during Hydrogen Generation in an Array of Fuel Bars of a BWR Using a Periodic Unit Cell

H. Romero-Paredes, F. J. Valdés-Parada, and G. Espinosa-Paredes

Área de Ingeniería en Recursos Energéticos, Universidad Autónoma Metropolitana, Unidad Iztapalapa Avenida San Rafael Atlixco 186, Col. Vicentina, 09340 México, DF, Mexico

Correspondence should be addressed to F. J. Valdés-Parada, iqfv@xanum.uam.mx

Received 18 December 2011; Accepted 1 February 2012

Academic Editor: Alejandro Nuñez-Carrera

This paper presents, the numerical analysis of heat and mass transfer during hydrogen generation in an array of fuel cylinder bars, each coated with a cladding and a steam current flowing outside the cylinders. The analysis considers the fuel element without mitigation effects. The system consists of a representative periodic unit cell where the initial and boundary-value problems for heat and mass transfer were solved. In this unit cell, we considered that a fuel element is coated by a cladding with steam surrounding it as a coolant. The numerical simulations allow describing the evolution of the temperature and concentration profiles inside the nuclear reactor and could be used as a basis for hybrid upscaling simulations.

1. Introduction

During a severe nuclear reactor accident, several works are focusing on core degradation by metal core components oxidation by air or steam [1–4]. Studies on possible consequences of core meltdown have demonstrated that hydrogen combustion is one of the contributors to the containment early failure [5]. Justly, during Fukushima accident, hydrogen explosion induced to a reduced public confidence in nuclear safety [6]. Other, hydrogen distribution, combustion, and mitigation studies have been applied in nuclear power plant models. Royl et al. [7] have made a hydrogen risk analysis during severe nuclear accident using CFD codes, to obtain localized detailed information and supplement the results of lumped parameter codes, which focus on global or average effect.

Oxidation of the cladding, rods, and other components in the core constructed in zirconium base alloy by steam is a critical issue in LWR accident producing severe core damage. The oxygen consumed by the zirconium is supplied by the upflow of steam from the water pool below the uncovered core, supplemented in the case of PWR by gas recirculation from the cooler outer regions of the core to hotter zones. In BWR, the gas recirculation process is prevented, since each fuel assembly is housed in its own channel box [8].

Fuel rod cladding oxidation is then one of the key phenomena influencing the core behaviour under high-temperature accident conditions. The chemical reaction of oxidation is very large exothermic, which determines the hydrogen rate generation and the cladding brittleness and degradation [9]. As the cladding material construction, Zircaloy-4 (Zry-4), oxidation process has been extensively studied for decades, whether in gaseous medium with air or oxygen or steam [1–4, 8–10]. Those studies showed that Zry-4 oxidation by air has similarities with oxidation in steam due to the common reaction partner oxygen, and also important differences. The exothermal heat released during air oxidation is around 1.8 times higher than steam, which causes a higher rise rate temperature [4].

Most of the works available in the literature dealing with the oxidation of Zry-4, agree that it is carried out in two temperature ranges. However experimental database at temperatures below 1800 K is very large and the oxidation kinetics in steam medium is well defined and their applicability. Variables predicted by them, as mass gain of oxygen and oxide growth, vary in the range of 20 to 30%. It is the same with

which leads to higher temperatures of 1800 K, which is much more important uncertainty [1]. Since then, there have been several works to supplement the database at elevated temperatures. Schanz et al. [1] conducted a series of experiments to reduce uncertainty in the results and, lately, Shi and Cao [10] reports their work in compiling experimental data at elevated temperatures. Thus, in these works, there is reliable information that allows us to know the rate of hydrogen can be produced in the reactor core derived from the oxidation of Zry-4. However, there is still little information regarding the hydrogen generation rate as a function of the temperature profile in the fuel rods and the steam mass fraction. These parameters are very important to foresee the magnitude of accumulated hydrogen and the risk of this accumulation during a severe accident.

In this paper, we present the numerical analysis of heat and mass transfer with hydrogen generation in an array of fuel cylinder bars, each coated with a cladding and a current of water vapor flowing outside the cylinders. This analysis considers the fuel element without mitigation effects. The method applied consists in a representative periodic unit cell where the initial and boundary-value problems for heat and mass transfer (water reduction) were solved. The unit cell consists in a fuel element and steam water which allow analyzing the problem in small scale length. In this approximation, the fuel element and steam are assumed continuous, that is, the hypothesis for the heat flux in the interphase fuel-steam: $q'' = h(T_w - T_\infty)$ where h is the heat transfer coefficient, T_w is the wall temperature and T_∞ is the steam temperature far from the well, is not applied in this work. The paper is organized as follows: In Section 2, we provide an overview of the transport and reaction phenomena taking place in the system; in Section 3, we present the mathematical model that was numerically solved; the results are discussed in Section 4; finally in Section 5, we present the corresponding conclusions of the work.

2. Overview of Transport and Reaction Phenomena

Steam reduction occurs at the solid surface of the cladding and roads. Accordingly with Beuzet et al. [4], the oxidation process of the cladding and rods is divided into two regimes called pre- and postbreakaway regimes. During the prebreakaway regime, oxide growth is controlled by oxygen diffusion inside the oxide layer. Diffusion leads to equilibrium of the chemical species concentration. Assuming that hydrogen is present as a diluted solute in the steam flow allows applying Fick's law as a constitutive equation for the diffusive mass flux. Then, the reaction can be divided in two steps:

$$\mathrm{H_2O} \longrightarrow \frac{1}{2}\mathrm{O_2} + \mathrm{H_2} \tag{1}$$

Then, the O/Zr ratio at the solid surface is a function of the steam-H_2 ratio in the adjacent gas. Oxygen at the solid surface moves through the oxide scale by solid-state diffusion. At the oxide-metal interface, oxygen from steam reacts with the Zr to produce a substoichiometric oxide $\mathrm{ZrO}_{(2-x)}$, that is,

$$\mathrm{Zr} + (2-x)\mathrm{H_2O} \longrightarrow \mathrm{ZrO}_{(2-x)} + (2-x)\mathrm{H_2} \tag{2}$$

where the O/Zr ratio in the metal at the interface is the final solubility of oxygen in αZr to βZr. During this regime, oxide growth is controlled by oxygen diffusion inside the oxide layer. This phenomenon also follows Fick's law so that the diffusion rate is proportional to the concentration gradient.

Then, the oxide layer loses its protectiveness for a critical thickness, whose value depends on the initial state of the cladding, the composition of the atmosphere, and temperature [3]. According to Duriez et al. [11], there are breaks at the surface layers of the oxide, due to the accumulation of stress and change of solid phase of Zr. In other words, there is an interrelationship between the change in density of the phase shift (αZr to βZr) and the difference of thermal expansion for the growth of the oxide layer and metal [4, 12]. Additionally, zirconia thus obtained is not pure, derived from the composition of Zry-4 and the rapid transition in the conditions that occurs during a severe accident: the crystalline phase changes of the oxide formed, monoclinic to tetragonal between 1133 K and 1473 K, and tetragonal to cubic between 1773 K and 2723 K [13]. Then, the oxide layer loses its protectiveness as a function of the cladding initial state (if an oxide layer is already exists), atmosphere composition, and temperature. Then, the stoichiometric oxidation reaction is

$$\beta\mathrm{Zr} + 2\mathrm{H_2O}_g \longrightarrow \mathrm{ZrO_2} + 2\mathrm{H}_{2,g}; \quad \Delta H_r = -586\,\mathrm{kJ/mol}. \tag{3}$$

The chemical equilibrium of this reaction shows a mechanism in which there exists a first-phase component of $\mathrm{ZrO(OH)_2}$ near to the ambient temperature.

At breakaway transition, the oxide rate increase after reached a minimum, and then inside the crack formed during this step, there is a fast oxidation inside the cladding, which contributed to form porosities [11]. The oxidizable surface is then increased for those cracks and also for the cladding distortion and so called ballooning. This last step is known as the postbreakaway regime [4].

In Figure 1, we show the computed chemical equilibrium data in the presence of ZrO_2. We notice that the data is only stable at high temperatures. Hydrogen is produced at low temperatures, although with a very slow kinetics.

The heat of the reaction given by (1) is expressed as a function of temperature as:

$$\begin{aligned}
&\Delta H_r \\
&= -6.304940 \times 10^2 + 2.996279 \times 10^{-2} T - 2.179432 \times 10^{-6} T^2, \\
&\qquad \text{for } 298.15\,\mathrm{K} \le T < 1445.15\,\mathrm{K}, \\
&\Delta H_r \\
&= -6.318406 \times 10^2 + 4.755655 \times 10^{-2} T - 9.785421 \times 10^{-6} T^2 \\
&\qquad \text{for } 1445.15\,\mathrm{K} \le T \le 2273.15\,\mathrm{K}.
\end{aligned} \tag{4}$$

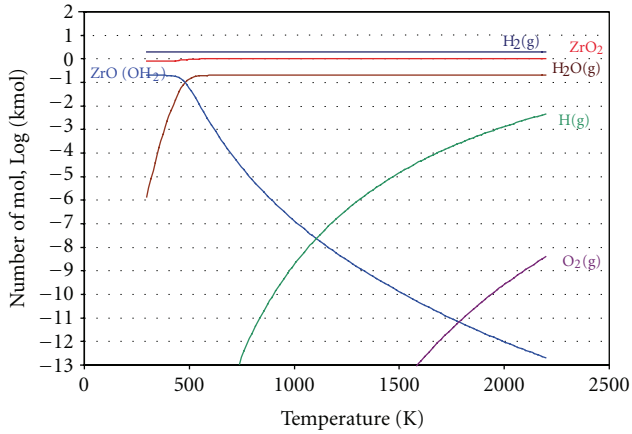

Figure 1: Chemical equilibrium for Zry oxidation with steam.

The transition solid phase enthalpy is $\Delta H_t = 8.4\,\text{kJ/mol}$ at 1445 K. These expressions for the enthalpy are used in the following section to take into account the heat generated at the solid-fluid interface.

The reaction of Zry with steam at elevated temperatures involves the growth of discrete layers of oxides and oxygen rich phase from parent β-phase [1]. The main experimental data obtained in laboratory experiments includes oxide scale growth (k_{ox}), which accordingly with the chemical equilibrium is $ZrO(OH)_2$ and total oxygen mass gain (k_T). These quantities can be defined through

$$l_{ox}^2 = k_{ox}^2 t, \qquad W^2 = k_T^2 t, \tag{5}$$

where l_{ox} is the thickness of the layers, W is the mass of oxygen absorbed by Zry per unit area, and t is the reaction time.

Parabolic correlation k is given as temperature-dependent Arrhenius-type function with constant activation energy E_a and a factor A:

$$k = A \exp\left(\frac{E_a}{RT}\right). \tag{6}$$

There are several classical parabolic correlations used to calculate the reaction rate in cladding oxidation at elevated temperatures. The kinetics evaluation of the growth of ZrO_2 and $\alpha - Zr(O)$ layers was evaluated by several authors, nevertheless Urbanic and Heidrick [14] were the first to identify a discontinuity in the Arrhenius plot of the rate coefficients for mass increase and ZrO_2 scale grows at the beginning of tetragonal to cubic transition zirconia. More recently, Shantz et al. [1] made a kinetics evaluation of ZrO_2 and $\alpha - Zr(O)$ in the temperature range 1273–1773 K by calculated approximation of oxygen uptake comparing with some measurements. Other authors have also studied the kinetics of this reaction; nevertheless, we only consider those formulated by Leistikow and Schanz [15], Prater et al. [16], and Volchek [17].

The kinetics of the oxidation reaction is divided in three parts, in each one, a phase transition of the zirconium and zirconia from α to β and monoclinic to tetragonal and to cubic, respectively is involved. Leistikow and Schanz correlations were obtained from experimental sets, over the temperature range 973 to 1873 K. Weight gain and many specimens for growth of ZrO_2 and $\alpha - Zr(O)$ were measured gravimetrically. These correlations correspond to a temperature range of 973 K to 1873 K:

$$K_T = 7.24 \exp\left(\frac{-0.871 \times 10^5}{RT}\right), \qquad K_{ox} = 2.80 \times 10^{-3} \exp\left(\frac{-0.840 \times 10^5}{RT}\right), \tag{7}$$

where K_T is the parabolic coefficient of total oxygen mass gain ($\text{kg/m}^2\text{s}^{0.5}$), K_{ox} is the coefficient of oxide scale growth ($\text{m/s}^{0.5}$).

According to Veshchunov et al. [18], the oxide layer consists of two sublayers in the temperature range of 1800 K to 2650 K: the tetragonal phase outside and the cubic phase inside. Later, the best-fit correlations were made at high temperature $T > 1800$ K and verified the applicability to different of temperature transient based in its experiments [9] and also reported by Shi and Cao [10]. Then, the next equations can be applied to compute the K_{ox} kinetics parameter for the superficial oxidation that is predominant in these phenomena:

$$K_{ox} = 0.093 \exp\left[\frac{-1.286 \times 10^5}{RT} - 6.16 \times 10^8 \left(\frac{1}{T} - \frac{1}{1900}\right)^2\right], \quad \text{for } 1800\,\text{K} < T < 1900\,\text{K},$$

$$K_{ox} = 0.093 \exp\left(\frac{-1.286 \times 10^5}{RT}\right), \quad \text{for } T > 1900\,\text{K}, \tag{8}$$

Urbanic and Heidrick [14] correlation for mass gain rate have two turning points: at $T = 1853$ K and $T = 1873$ K, because the authors consider the tetragonal to cubic transition temperature as $T = 1853$ K. Meanwhile, Fichot et al. [9] consider that the transition temperature is lower and at the beginning of the tetragonal to cubic transition $T \approx 1800$ K oxidation behavior runs gently and rates increase smoothly. The oxidation rates calculated by Prater and Courtright [16] and Urbanic and Heidrick [14] agree with the best-fitted values and the errors are very small at $T > 1900$ K. Nevertheless, the values calculated by Prater et al. [16] are better than other two correlations at $T > 1900$ K [10]. For this reason, in this work, we consider the temperature ranges as $T < 1800$ K; $1800 < T < 1900$; $T > 1900$ K.

The oxygen flux available at the cladding surface F_{gas} strongly depends on the steam mass fraction in the bulk and properties of neighboring boundary layer:

$$F_{gas} = k_{gas}(C_{bulk} - C_{surf}), \tag{9}$$

where k_{gas} is the mass transfer coefficient, C_{bulk} and C_{surf} are steam mole fraction in the bulk and on the solid surface, respectively.

Assuming identity between Sherwood (Sh) and Nusselt (Nu) numbers, k_{gas} at outer cladding surface can be estimated as

$$k_{\text{gas}} = \frac{\text{Nu}D_g}{L_h}, \tag{10}$$

where D_g is the diffusion coefficient in boundary layer, and L_h is the equivalent hydraulic diameter of fluid channels associated with a single rod.

The maximum steam flux is obtained with $C_{\text{surf}} = 0$, which means that all steam is consumed at the surface. Then, F_{gas} can be rewritten as

$$F_{\text{gas}} = k_{\text{gas}} C_{\text{bulk}}. \tag{11}$$

According with Olander [8], for an axial steaming velocity of $v_{\text{steam}} \cong 0.1$ m/s, ideal gas densities corresponding to typical total pressure and temperature in the event, an $L_h \cong 0.01$ m, the Reynolds number is lower than 2000. For this regime, the Nusselt number is 3.66. Then, it is possible to assume, as made by Olander, that D_g is the binary diffusivity of steam in H_2O(g)-H_2 mixture. The expressions for these coefficients are [1]

$$\begin{aligned} D_{H_2} &= 2.15 \times 10^{-5} \frac{T^{2.33}}{P_T}, \\ D_{\text{bin}} &= 6.262 \times 10^{-4} \frac{T^{2.33}}{P_T}. \end{aligned} \tag{12}$$

Densities (international units) used in this work of pure materials are [19]

$$\begin{aligned} &\beta\text{Zr} : \rho(T) = 6434 \times \left(1 + 9.7 \times 10^{-6} \times T\right)^{-3}, \\ &\text{ZrO}_2 : \rho(T) = 5640 \times \left(1 + 7.8 \times 10^{-6} \times T - 2.34 \times 10^{-3}\right)^{-3} \\ &\qquad \text{for } T < 1478\,\text{K} \\ &\text{ZrO}_2 : \rho(T) = 5640 \times \left(1 + 1.3 \times 10^{-5} \times T - 3.338 \times 10^{-3}\right)^{-3} \\ &\qquad \text{for } T > 1478\,\text{K}. \end{aligned} \tag{13}$$

The heat capacity is computed by means of the coefficients of the polynomial formula [20]: $Cp = A + BT + CT^{-2} + DT^2$, the coefficients for the materials used are presented in Table 1.

Table 1: Coefficients for Cp calculations for materials in rods and cladding [20].

Specie	A	B	C	D	Temperature range (K)
βZr	6.15	−0.227	−0.173	1.533	298.15–800
	10.076	−6.404	0.008	3.076	800–1135
	7.745	−2.301	−0.008	1.272	1135–2125
	7.848	−2.357	−1.031	1.280	2125–2600
ZrO_2	16.331	2.171	−3.212	0	298.15–1445
	18.666	0	0	0	1445–2620
H_2(g)	6.180	1.156	0.379	−0.089	298.15–5000
H_2O	6.790	2.982	0.307	0.086	298.15–1100
	7.514	3.371	−5.964	−0.438	1100–2800

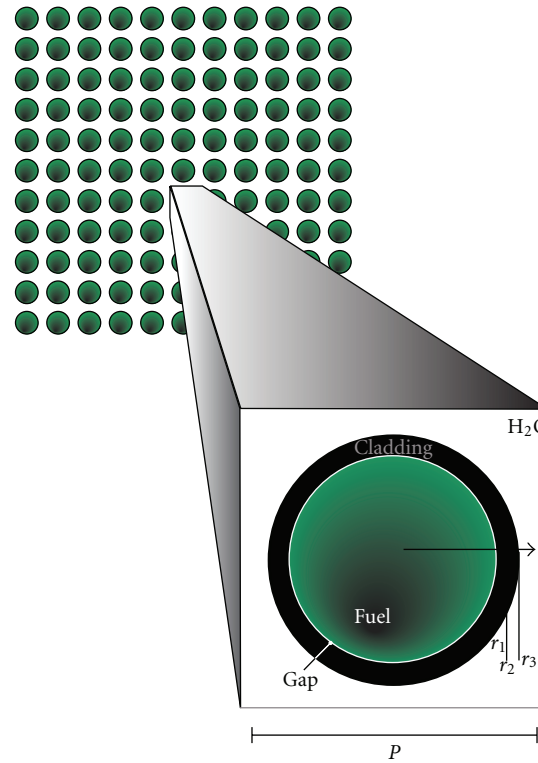

Figure 2: Unit cell for the system solution, $r_1 = 5.207$ mm, $r_2 = 5.321$ mm, $r_3 = 6.234$ mm, and $P = 16.2$ mm.

3. Mathematical Model in Reactor Fuel Elements

The system under consideration is depicted in Figure 2, which consists of an array of fuel cylinder bars, each coated with a cladding and a current of steam flowing outside the cylinders. In the same figure, we also show a representative periodic unit cell where the initial and boundary-value problems for heat and mass transfer are to be solved.

In this way, we can identify four regions of interest, where the problem under study has a characteristic length of the order of P, that is, 16.2 mm, in contrast with the fuel assembly that is ten times larger as illustrated in Figure 3(b) (large scale). Accordingly, the unit cell regarding the core of the BWR is hundreds of times smaller (Figure 3(a)). Then, we can say that the study presented in this work takes place in a small length scale (Figure 3(c)).

Let us identify four regions in the unit cell, representative of the fuel element and coolant:

(i) Region I: Fuel, $0 \le r \le r_1$,

(ii) Region II: Gap, $r_1 \le r \le r_2$,

(iii) Region III: Cladding, $r_2 \le r \le r_3$,

(iv) Region IV: Fluid (coolant), $r_3 \le r \le r_4$.

Since $r_2/r_1 = 0.005321/0.005207 = 1.021894 \approx 1$ and con-

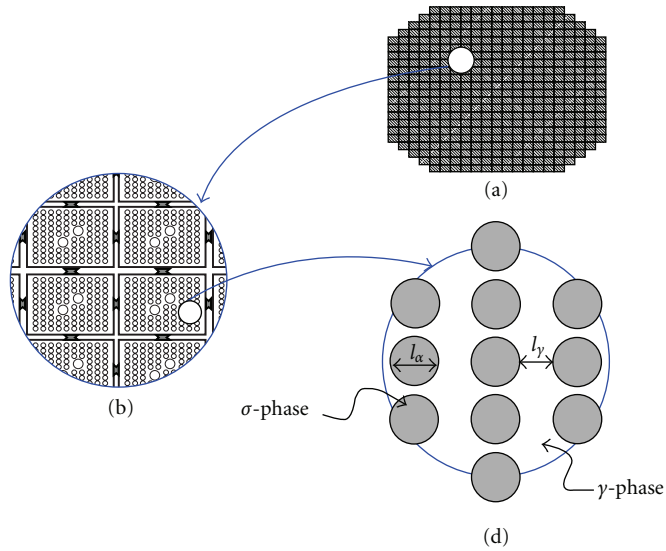

Figure 3: Characteristic lengths of the system [21]. (a) Nuclear reactor core; (b) Large scale (showing four fuel assemblies); (c) Small scale; σ-phase is the fuel element and γ-phase is the coolant.

tinuity conditions of heat transfer can be assumed; we may neglect Region II overall. In this way, the differential equations for heat and mass transfer to be solved taking into account only three regions.

3.1. Heat Transfer Process. The fuel element temperature distribution was obtained considering each radial node at each of the twelve hydraulic axial nodes in the core. The fuel heat transfer formulation is based on the following fundamental assumptions: (i) axis-symmetric radial heat transfer, (ii) the heat conduction in the axial direction is negligible with respect to the heat conduction in the radial direction, (iii) the volumetric heat rate generation in the fuel is uniform in each radial node, (iv) storage of heat in the fuel cladding and gap is negligible, and (v) periodic boundary condition at entrances and exits of the unit cell.

Under these assumptions, the transient temperature distribution in the fuel element, initial and boundary conditions are given by each region:

Region I:

$$\begin{aligned}
&(\rho Cp)_f \frac{\partial \left\langle T_f \right\rangle_f}{\partial t} = K_f \nabla^2 \left\langle T_f \right\rangle_f + q''', \\
&r = 0, \quad -\mathbf{n} \cdot K_f \nabla \left\langle T_f \right\rangle_f = 0, \\
&r = r_2, \quad -\mathbf{n} \cdot \nabla K_f \left\langle T_f \right\rangle_f = -\mathbf{n} \cdot K_c \nabla T_c;
\end{aligned} \tag{14}$$

Region II: continuity conditions of heat transfer are assumed;

Region III:

$$(\rho Cp)_c \frac{\partial T_c}{\partial t} = K_c \nabla^2 T_c, \tag{15}$$

$$r = r_2, \quad \left\langle T_f \right\rangle_f = T_c, \tag{16}$$

$$r = r_3, \quad -\mathbf{n} \cdot K_c \nabla T_c = -\mathbf{n} \cdot K_{fl} \nabla T_{fl} + \Delta H_r (k c_{H_2}); \tag{17}$$

Region IV:

$$\begin{aligned}
&(\rho Cp)_{fl} \left(\frac{\partial T_{fl}}{\partial t} + \langle \mathbf{v} \rangle \cdot \nabla T_{fl} \right) = K_{fl} \nabla^2 T_{fl}, \\
&r = r_3, \quad T_c = T_{fl};
\end{aligned} \tag{18}$$

Periodicity:

$$\begin{aligned}
T = {} & \mathbf{h} \cdot \mathbf{r} + \Im(\mathbf{r}) \\
& + T_0, \quad \text{at entrances and exits of the unit cell.}
\end{aligned} \tag{19}$$

In these equations, the subscripts f, c, and fl are used for denoting the fuel region, cladding region, and coolant region, respectively; T is the temperature, ρ is the density, Cp is the heat capacity, K is the conductivity, q''' is the neutronic power per unit volume (which is calculated by standard law of the decay heat), and $\mathbf{n}$ is the unit normal vector. We used the symbol $\langle \cdot \rangle$ to represent the volume-averaged variables, that is, $\langle T_f \rangle_f$ is the average fuel temperature and $\langle \mathbf{v} \rangle$ is the average velocity of the coolant. Clearly, the averaging domains for $\langle T_f \rangle_f$ and $\langle \mathbf{v} \rangle$ are not the same. Furthermore, (17) considers that the reaction heat due to chemical reaction between the Zr and coolant is represented by ΔH_r, which is given by (4) as a function of temperature. The periodic boundary conditions for unit cell which consider each

regions is represented by (19), where $\mathbf{h}$ and T_0 are constants and $\Im(\mathbf{r})$ is a periodic function whose characteristic is zero mean [22]. Finally, at $t = 0$ each section is assumed to be at different constant temperatures.

3.2. Mass Transfer Process. The mass transfer phenomena were discussed in Section 2, in this work, we consider that the hydrogen generated diffuses in the coolant by convection and diffusion. Then, the governing equation and boundary conditions for mass transfer are given by:

$$\frac{\partial c_{H_2}}{\partial t} + \langle \mathbf{v} \rangle \cdot \nabla c_{H_2} = D\nabla^2 c_{H_2},$$
$$r = r_3, \quad -\mathbf{n} \cdot D\nabla c_{H_2} = k c_{H_2}; \tag{20}$$

Periodicity:

$$c_{H_2} = \mathbf{i} \cdot \mathbf{r} + \Im(\mathbf{r}) + c_0, \quad \text{at entrances and exits of the unit cell,} \tag{21}$$

where c_{H_2} is the hydrogen concentration, D is the diffusion coefficient, k reaction rate coefficient, and $\mathbf{i}$ and c_0 are constant. The hydrogen concentration at the initial time is assumed to be constants. Actually, for the developments that follow, the concentration is made dimensionless with this initial value.

The heat transfer processes are coupled with the mass transfer process through reaction rate and heat reaction at the interface, which are a functions of the temperature. Thus, in this work the simultaneous transfer of heat and mass is considered.

3.3. Decay Heat. Evaluation of the heat generated in a reactor after shutdown is important for determining cooling requirements under normal conditions and accident consequences. Reactor shutdown heat generation is the sum of heat produced from fission due to delayed neutron or photoneutron emissions, decay of fission products fertile materials, and activation products. The heat decay level used in this work is given by [23]

$$\frac{q'''}{q'''_0} = 0.066\left[(\tau - \tau_s)^{-0.2} - \tau^{-0.2}\right], \tag{22}$$

where q'''_0 is the steady-state volumetric heat-generation rate, $(\tau - \tau_s)$ is time after shutdown, and τ is the time after reactor startup. Equation (22) is used in the heat transfer process in the fuel (14).

4. Numerical Experiments and Discussions

In order to solve the boundary-value problem presented in the previous section, we used the commercial finite-element solver Comsol multiphysics 4.2. The space and temporal meshing were adapted depending of the range of time of interest. Standard meshing and convergence analyses were performed in order to ensure the accuracy and exactness of the numerical results. The numerical solution was easily adapted to study each of the 12 nodes of the system. In the following paragraphs, we will present the numerical simulations for a particular node (node 3) that was arbitrarily chosen for illustration purposes. In order to gain some insight about the influence of the initial temperature distributions over the system transient performance, we computed four types of average temperatures, three corresponding to regions I, III, and IV and the fourth one for the whole unit cell. In the following paragraphs we discuss our results.

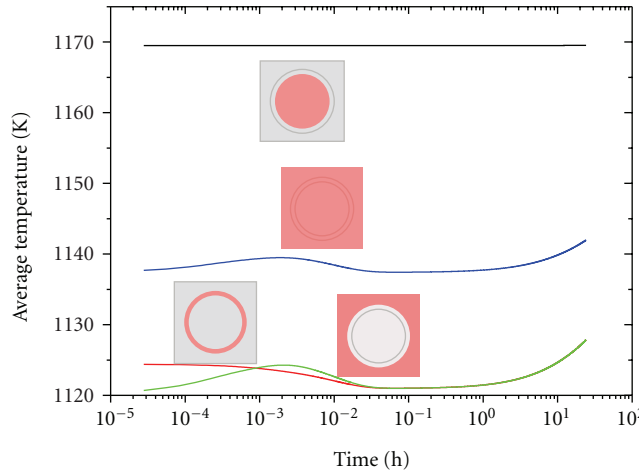

FIGURE 4: Temporal evolution of the average temperatures in the system taking initial temperature distributions of 1115 K, 1126 K and 1169.5 K for the coolant, cladding, and fuel regions, respectively. The heat source term was fixed as 3403.569 W/m^3; the average fluid velocity is 0.7045 m/s.

4.1. Average Temperatures. In Figure 4, we present the evolution of the average temperatures for the four types of averages mentioned above. We observe that the fuel temperature is practically unaffected by the heat transfer processes taking place in the other parts of the system. However, the average temperatures in the cladding and in the coolant exhibit more plausible oscillations in the temperature. It is interesting to notice that the average temperatures corresponding to the cladding and water regions fluctuate until reaching equilibrium at about 0.1 h. Furthermore, after the first hour is elapsed, the exothermic reaction and the heat source in the fuel make the average temperatures in the cladding and water regions to increase, and eventually the whole system will reach equilibrium. Overall, the whole system did not exhibit drastic temperature variations in the time range studied. This is to be expected since the maximum initial temperature differences are about 50 K. Let us also note that the average temperatures in the cladding and in the coolant regions tend to increase rapidly after about 10 hours. Certainly, if the heat source within the fuel section overcomes the heat generated by the chemical reaction at the solid-fluid interface, the steady state solution (not shown in the figure) should consist in a thermal equilibrium condition with respect to the fuel temperature.

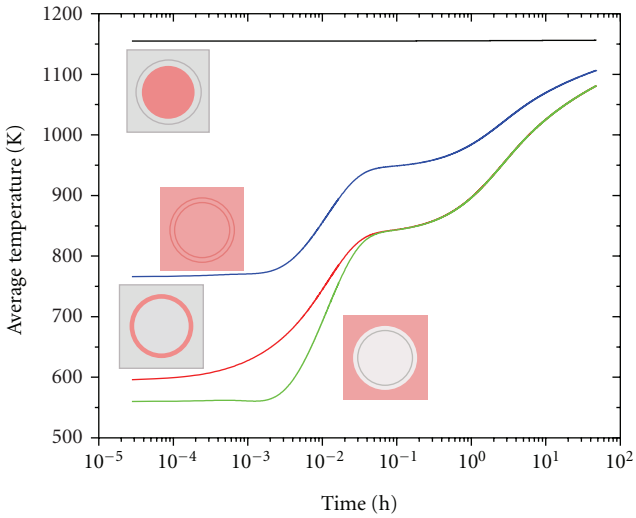

Figure 5: Temporal evolution of the average temperatures in the system taking initial temperature distributions of 557.5 K, 563 K and 1169.5 K for the coolant, cladding, and fuel regions, respectively. The heat source term was fixed as 3403.569 W/m^3; the average fluid velocity is 0.7045 m/s.

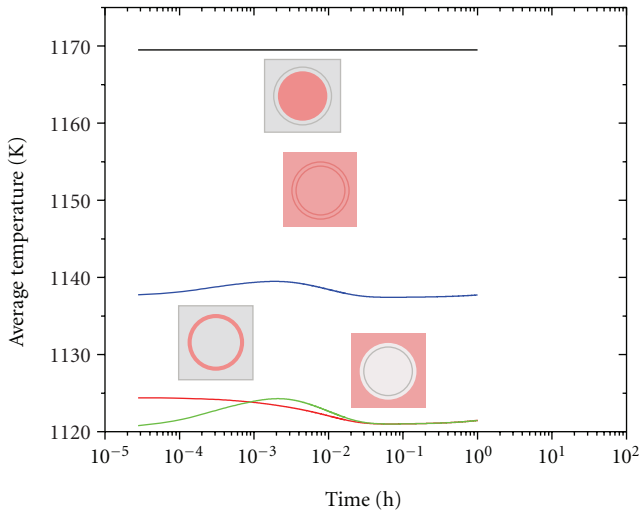

Figure 6: Same case as Figure 4 but with the velocity increased 10 times.

In Figure 5, we compare the same average temperature transient profiles but imposing a larger initial heat flux driving force, that is, the initial temperatures in the cladding and in the coolant were taken to be half the values used in Figure 4. Now, we observe that the average temperatures corresponding to the cladding and the water exhibit a stepwise time evolution, reaching equilibrium at approximately the same time range as in the previous case. Interestingly, the values of the temperatures in these regions at the last computed times (corresponding to a 48 h simulation) approach the range of initial values shown in Figure 4. It is also worth noticing that the temperatures from the cladding and the coolant approach the one corresponding to the whole unit cell at a faster rate than in the previous case.

Another degree of freedom that we explored in our simulations was the fluid flow, which impacts the convective heat and mass transfer. Taking as reference the conditions used in Figure 4 and increasing the fluid velocity by a factor of 10, we obtained the results shown in Figure 6. In this case, the analysis had to be stopped at 3600 s due to problems in solution convergence generated by the large convective effects. Despite this drawback, we can observe that the time required for the first stabilization of temperatures is reached sooner than under the conditions used in Figure 4.

To gain a better insight of the transport phenomena taking place in the system, we provide in Figure 7 surface plots with the spatial temperature distribution for certain times. The conditions under which these figures were obtained correspond to those used in Figure 5. Here, we observe that the most dramatic changes of temperature take place near the boundaries of the system regions. For shorter times (i.e., at the first hour), the temperature variations are quite steep near the fuel and cladding boundary, whereas after ten hours these profiles become shallower. In addition, let us notice that the temperature profiles in the cooling steam region do not change very drastically with position but the same is not true for the time dependence. This means that the results from taking the spatial average of the temperature are justifiable since they provide, at the very least, a qualitative assessment of the physical phenomena taking place in the system.

4.2. Hydrogen Average Concentration. To finalize this section, we present in Figure 8 the average concentration profiles for the three cases considered above. In this context, Case A corresponds to the parameters used to obtain Figure 4, Case B for those in Figure 5, and Case C for those corresponding to Figure 6. The hydrogen concentration is displayed dimensionless with respect to its initial value. We observe that the initial temperature distributions do not play a role as relevant as that played by convection, since the characteristic times at which the concentration rapidly departs from its initial values are defaced in two orders of magnitude when the velocity is increased in only one order of magnitude. In other words, an increment in the velocity influences more drastically convective mass transfer than convective heat transfer. This is reasonable since heat transfer is mainly driven by the source in the fuel region, whereas mass transfer is driven by the interfacial reaction at the solid-fluid interface.

5. Conclusions

In this work, we carried out numerical simulations in a periodic unit cell that represents a fuel rod with its cladding and cooling steam of a BWR. Our main simulation variables were the initial heat distributions and the flow rate. We found that the temperature is more sensitive to changes on the initial distribution than over the flow rate. This follows from the fact that a larger temperature difference is established thus promoting heat transfer over time. Our main result is the prediction of the hydrogen generation that is carried with the cooling steam. In this case, we found that an increment in

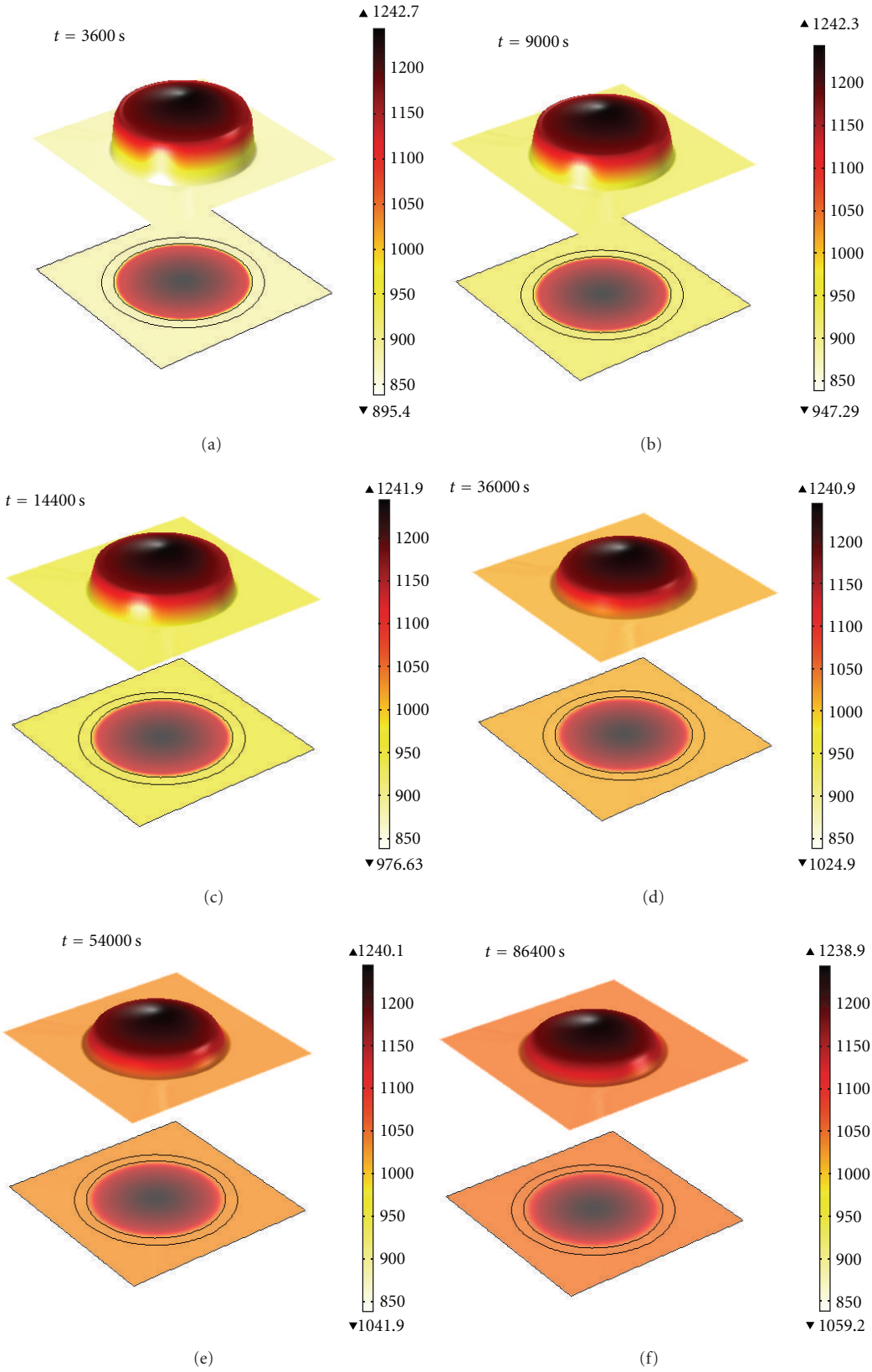

Figure 7: Evolution of the temperature profiles in the unit cell for the conditions used in Figure 5.

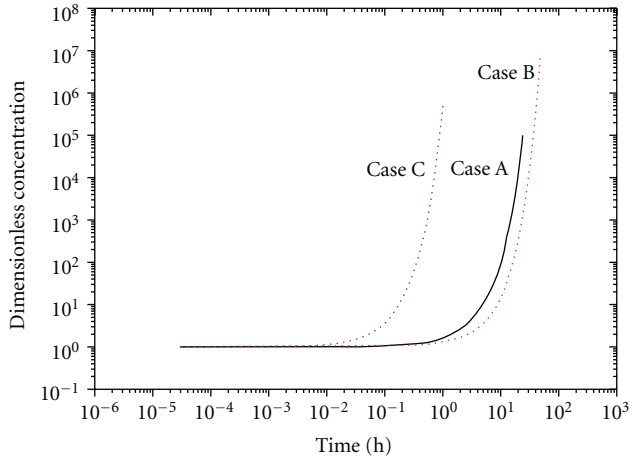

Figure 8: Temporal evolution of the hydrogen average concentration for the three study cases.

the flow rate resulted in a plausible decrement of the characteristic times at which the hydrogen generation exponentially increases. In addition, a change of the initial temperature distributions did not provide such drastic time variations.

These results can be used in further upscalings for decision making in terms of risk analysis. As shown in Figure 3, the real system under consideration is hierarchical in nature. This means that the results of this work can be used in conjunction with an appropriate upscaling technique in order to derive mathematical models at other levels of scale of the nuclear reactor. This type of modelling consisting of linking averaging and pointwise numerical simulations is currently known as hybrid upscaling and will be pursued in future works.

References

[1] G. Schanz, B. Adroguer, and A. Volchek, "Advanced treatment of zircaloy cladding high-temperature oxidation in severe accident code calculations Part I. Experimental database and basic modeling," *Nuclear Engineering and Design*, vol. 232, no. 1, pp. 75–84, 2004.

[2] C. Duriez, M. Steinbrück, D. Ohai, T. Meleg, J. Birchley, and T. Haste, "Separate-effect tests on zirconium cladding degradation in air ingress situations," *Nuclear Engineering and Design*, vol. 239, no. 2, pp. 244–253, 2009.

[3] M. Steinbrück, "Prototypical experiments relating to air oxidation of Zircaloy-4 at high temperatures," *Journal of Nuclear Materials*, vol. 392, no. 3, pp. 531–544, 2009.

[4] E. Beuzet, J.-S. Lamy, A. Bretault, and E. Simoni, "Modelling of Zry-4 cladding oxidation by air, under severe accident conditions using the MAAP4 code," *Nuclear Engineering and Design*, vol. 241, no. 4, pp. 1217–1224, 2011.

[5] W. Breitung and P. Royl, "Procedure and tools for deterministic analysis and control of hydrogen behavior in severe accidents," *Nuclear Engineering and Design*, vol. 202, no. 2-3, pp. 249–268, 2000.

[6] X. G. Huang, Y. H. Yang, and S. X. Zhang, "Analysis of hydrogen risk mitigation with passive autocatalytic recombiner system in CPR1000 NPP during a hypothetical station blackout," *Annals of Nuclear Energy*, vol. 38, no. 12, pp. 2762–2769, 2011.

[7] P. Royl, H. Rochholz, W. Breitung, J. R. Travis, and G. Necker, "Analysis of steam and hydrogen distributions with PAR mitigation in NPP containments," *Nuclear Engineering and Design*, vol. 202, no. 2-3, pp. 231–248, 2000.

[8] D. R. Olander, "Materials chemistry and transport modeling for severe accident analyses in light-water reactors I: external cladding oxidation," *Nuclear Engineering and Design*, vol. 148, no. 2-3, pp. 253–271, 1994.

[9] F. Fichot, B. Adroguer, A. Volchek, and Y. Zvonarev, "Advanced treatment of zircaloy cladding high-temperature oxidation in severe accident code calculations Part III. Verification against representative transient tests," *Nuclear Engineering and Design*, vol. 232, no. 1, pp. 97–109, 2004.

[10] X. Shi and X. Cao, "Study and assessment of Zry cladding oxidation model under severe accident in PWR," in *Proceedings of the Asia-Pacific Power and Energy Engineering Conference (APPEEC '11)*, pp. 1–5, Wuhan, China, March 2011.

[11] C. Duriez, T. Dupont, B. Schmet, and F. Enoch, "Zircaloy-4 and M5 high temperature oxidation and nitriding in air," *Journal of Nuclear Materials*, vol. 380, no. 1–3, pp. 30–45, 2008.

[12] L. Gosmain, C. Valot, D. Ciosmak, and O. Sicardy, "Study of stress effects in the oxidation of Zircaloy-4," *Solid State Ionics*, vol. 141-142, pp. 633–640, 2001.

[13] V. Lacour, *Modélisation de la production d'hydrogène lors de la phase de renoyage des coeurs de réacteurs nucléaires en situation d'accidents graves*, Ph.D. thesis, Ecole Nationale Supérieure des Mines de Paris, November 2001.

[14] V. F. Urbanic and T. R. Heidrick, "High-temperature oxidation of zircaloy-2 and zircaloy-4 in steam," *Journal of Nuclear Materials*, vol. 75, no. 2, pp. 251–261, 1978.

[15] S. Leistikow and G. Schanz, "Oxidation kinetics and related phenomena of zircaloy-4 fuel cladding exposed to high temperature steam and hydrogen-steam mixtures under PWR accident conditions," *Nuclear Engineering and Design*, vol. 103, no. 1, pp. 65–84, 1987.

[16] J. T. Prater, E. L. Courtright et al., "Oxidation of Zircaloy-4 in steam at 1300 to 2400°C Zirconium in the nuclear industry," in *Proceedings of the 7th International Symposium*, vol. 939 of *ASTM STP*, pp. 489–303, Adamson R. B., Van Swan L. F. P., Philadelphia, Pa, USA, 1987.

[17] A. Volchek, Y. Zvonarev, and G. Schanz, "Advanced treatment of Zircaloy cladding high-temperature oxidation in severe accident code calculations PART II. Best-fitted parabolic correlations," *Nuclear Engineering and Design*, vol. 232, no. 1, pp. 85–96, 2004.

[18] M. S. Veshchunov, A. V. Berdyshev, A. V. Boldyrev, L. V. Matweev, A. V. Palagin, and V. E. Shestak, "Physico-chemical behavior of Zircaloy fuel rod cladding tubes during lwr severe accident reflood. Part II: modelling of quench phenomena," FZKA 5864, Forschungszentrum Karlsruhe, 1997.

[19] C. M. Allison et al., *SCDAP/RELAP5/MOD 3.1 Code Manual, MATPRO—a Library of Material Properties for Light Water Reactors Accident Analysis, NUREG/CR – 6150, EGG-2720*, vol. 4, EG&G Idaho, Idaho Falls, Idaho, USA, 1995.

[20] A. Roine, *HSC Chemistry 7.11*, Outokumpu Research, Oy, Pori, Finland, 2006.

[21] G. Espinosa-Paredes, J. B. Morales-Sandoval, R. Vázquez-Rodríguez, and E. G. Espinosa-Martínez, "Constitutive laws for the neutron density current," *Annals of Nuclear Energy*, vol. 35, no. 10, pp. 1963–1967, 2008.

[22] M. Quintard and S. Whitaker, "One- and Two-Equation Models for Transient Diffusion Processes in Two-Phase Systems," *Advances in Heat Transfer*, vol. 23, no. C, pp. 369–464, 1993.

[23] N. E. Todreas and M. S. Kazimi, *Nuclear Systems I: Thermal Hydraulic Fundamentals*, Hemisphere, Washington, DC, USA, 1990.

Hindawi Publishing Corporation
Science and Technology of Nuclear Installations
Volume 2012, Article ID 943197, 20 pages
doi:10.1155/2012/943197

Research Article

Large-Scale Containment Cooler Performance Experiments under Accident Conditions

Ralf Kapulla, Guillaume Mignot, and Domenico Paladino

Laboratory for Thermalhydraulics (LTH), Paul Scherrer Institut, 5232 Villigen, Switzerland

Correspondence should be addressed to Ralf Kapulla, ralf.kapulla@psi.ch

Received 8 December 2011; Accepted 27 February 2012

Academic Editor: Jun Sugimoto

Computational Fluid Dynamics codes are increasingly used to simulate containment conditions after various transient accident scenarios. This paper presents validation experiments, conducted in the frame of the OECD/SETH-2 project. These experiments address the combined effects of mass sources and heat sinks related to gas mixing and hydrogen transport within containment compartments. A wall jet interacts with an operating containment cooler located in the middle (M-configuration) and the top (T-configuration) of the containment vessel. The experiments are characterized by a 3-phase injection scenario. In Phase I, pure steam is injected, while in Phase II, a helium-steam mixture is injected. Finally, in Phase III, pure steam is injected again. Results for the M-configuration show helium stratification build up during Phase II. During Phase III, a positively buoyant plume emerging from the cooler housing becomes negatively buoyant once it reaches the helium-steam layer and continuously erodes the layer. For the M-configuration, a strong degradation of the cooler performance was observed during the injection of the helium/steam mixture (Phase II). For the T-configuration, we observe a mainly downwards acting cooler resulting in a combination of forced and natural convection flow patterns. The cooler performance degradation was much weaker compared with the M-configuration and a good mixing was ensured by the operation of the cooler.

1. Introduction

Three-dimensional computational fluid dynamics (CFD) codes as well as advanced lumped parameter (LP) codes are increasingly used for safety analysis to simulate transient containment conditions after various accident scenarios for present [1] and upcoming generations of nuclear power plants [2]. Consequently, the reliability of such codes must be tested against experimental data collected under prototypical thermal hydraulic conditions. Large-scale test facilities [3] are used to minimize distortional effects that might arise from geometrical scaling [4]. For example, power upgrades may require reducing conservative criteria in the evaluation of safety margins by using more accurate simulation models, which properly account for inhomogeneities in the distribution of steam and gases within the containment. In the frame of the OECD/SETH project (Phase I), the Large-scale PANDA facility built at the Paul Scherrer Institut (PSI) in Switzerland was used to perform such experiments relevant for light water reactor (LWR) containment safety issues. The applications of the PANDA facility in the past, present, and future programs cover integral containment response tests, component tests, primary system tests, and separate effect tests. These tests have been and will be embedded in international projects, most of which under the auspices of the EU and OECD and with the support of a large number of organizations (regulatory bodies, technical support organizations, national laboratories, electrical utilities, and industries) worldwide. For an overview of these projects, see [5].

The separate effect experiments conducted in Phase I of the OECD/SETH project can be briefly characterized as the transient build up of a stratified environment by wall plumes [6, 7], free plumes [8, 9], and horizontal high momentum jets [10]. Post-test analytical activities performed by the project participants were aimed at assessing the strengths and drawbacks of different codes in analyzing the phenomena occurring in these PANDA tests [11–13]. The analytical activities revealed a number of code challenges related to (i) gas transport, (ii) stratification build up, (iii) prediction of peak

gas temperature, and (iv) stratification disruption and erosion. In response to this, an experimental program using the PANDA and MISTRA facilities [14, 15] was conducted in the frame of the OECD/SETH-2 project which addresses some of the above-mentioned issues including both fundamental phenomena and component tests with increasing complexity such as gas mixing, hydrogen transport, and the erosion of hydrogen stratifications within containment compartments [16–23]. For safety reasons, helium is used to simulate the expected hydrogen release from the oxidation reaction between cladding metal and water during a severe accident. It was shown in the OECD THAI project that "thermal-hydraulic processes in the containment atmosphere, in particular the stratification and mixing phenomena, are primarily governed by the density differences in the atmosphere" and not by the gas species used [24]. Consequently, one can substitute hydrogen by helium. The experiments within the OECD/SETH-2 project focus on the characterization of the erosion and/or break-up mechanisms of a postulated already present stratified layer located in the upper part of an NPP containment. These breakup mechanisms could be activated by means of a mass source, a heat source or a heat sink. The main phenomena studied in the OECD/SETH-2 PANDA tests cover phenomena such as

(i) gas mixing under natural/forced convection induced by the direct vertical impingement on a stratified layer [17, 18],

(ii) gas mixing/stratification under natural/forced convection induced by a horizontal jet [19],

(iii) effect of hydrogen mitigation system such as spray [22] or recombiner systems (modeled by a heat source) on a stratified layer,

(iv) performance of a containment cooler in the presence of noncondensable light gas and its effect on gas and temperature distribution [16, 23],

(v) pressure, temperature, and gas distributions following a sudden opening of a hatch separating two large volumes with different initial pressure [21].

The experiments presented in this paper address the combined effects of a mass source and a heat sink (a containment cooler similar to those described in [25, 26]) in the case of a generic severe accident scenario with the possible release of hydrogen. They highlight the influence of the condensation of steam, as well as the convective flow caused by the operating cooler, on the gas transport and the hydrogen distribution in the containment. It must be stressed that the main objective of the SETH-2 experiments was to generate an experimental database for the validation of CFD as well as LP codes. Therefore, the SETH-2 experiments do not include a scaling of the accident scenario. This is subject of the ongoing project ERCOSAM/SAMARA which addresses "whether in a test sequence representative of a severe accident in an LWR a hydrogen (helium) stratification can be established during part of the transient starting from the initiation of the loss of coolant accident (LOCA) blowdown until the end of bulk hydrogen release from the reactor vessel into the containment, and [...] how this stratification can be broken down by the operation of severe accident management systems (SAMs); sprays, coolers, and passive autocatalytic recombiners." [27].

The experimental series discussed in this paper consist of a total of four tests plus one additional test. The latter was conducted to test for the repeatability of the phenomena for the reference experiment. Initial conditions and test scenarios were kept identical for all tests whereas (1) the position of the cooler, (2) the presence of a duct (acting as a downward chimney), and (3) the pressure control have been varied.

The paper is organized as follows. In Section 2 the PANDA facility and the instrumentation are briefly described. This is followed by a description of the entire test matrix and the experimental procedure including the preconditioning of the facility in Section 3. The qualitative and quantitative discussion of the results in Section 4 will focus on the phenomenology of the dominating flow patterns. Additional results depicting the mixing and the transport in the vessel which are necessary to understand the velocity fields will be presented in terms of density evolutions, temperature maps, and velocity fields. For the sake of brevity we omit in this paper a detailed discussion of the concentration results. They are subject of separate publications.

Some of the axis scales in the figures of the paper are not shown or are presented in nondimensional form to keep a conservative position with respect to the release of the experimental data. The data will be opened for the public in December 2013. Nevertheless, the present overview should allow the reader to follow and understand the main phenomena characterizing the evolution of the tests. For those interested to use these data as well as the technical information, both can be obtained through the participating agencies as documented in [28].

2. Facility and Instrumentation

This section provides a brief overview of the PANDA facility and the PANDA instrumentation used for the containment cooler experiments. The containment compartments and the reactor pressure vessel (RPV) are simulated in the PANDA facility by six cylindrical pressure vessels, Figure 1. For a comparison of the main components of a european simplified boiling water reactor (ESBWR) and the PANDA facility see [5]. The overall height of the facility is 25 m, the total volume of the vessels is about 530 m^3, and the maximum operating conditions are 10 bar at 200°C. The reactor pressure vessel (RPV) is electrically heated with a maximum power of 1.5 MW. Various auxiliary systems are available to maintain and control the necessary initial and boundary conditions during each test.

The experiments for the containment cooler series were carried out in a large double compartment with 183.3 m^3 total volume consisting of the two identical drywell vessels (referred to as vessel 1 and vessel 2 in the SETH-2 project) having a height of 8 m and a diameter of 4 m each. Both vessels are shown in the upper part of Figure 1 and are marked in red. Vessel 1 and 2 are connected by a large interconnecting

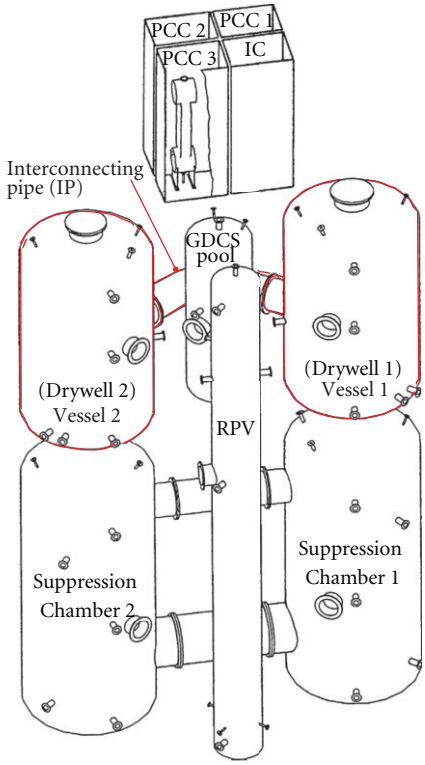

Figure 1: Schematic of the PANDA facility.

pipe (IP) with a diameter of 1 m. The RPV is used as a steam source. The steam was used to precondition the facility. To minimize heat losses, the entire facility is thermally insulated with 20 cm thick rock-wool mat. The cooler was installed at two different locations in Vessel 1 of the PANDA facility as presented in Figure 4 with the dashed thick green lines. The cooler consists of the cooler head and the cooler duct or chimney with a length of 1500 mm, Figure 2(b). The cooler head has one open side which is oriented towards the interconnecting pipe (IP). The array of 224 cooling tubes is composed of eight vertical tube serpentines. Behind this tube array, one finds a space not filled with cooling tubes and the duct is connected at the bottom of this empty space.

The three main measurement systems used in the PANDA Vessels 1 and 2 are (1) temperature sensors, (2) concentration, and (3) velocity measurements devices. In addition to the recording of these main quantities, the data acquisition allows for the recording of absolute and differential pressures, flow rates, heating power, water level, and automatic valve status. The measurement sensors are distributed over all facility compartments, the system lines, and the auxiliary systems. The spatial resolution of the sensor grid for the temperature and concentration measurements in Vessel 1 and in Vessel 2 has a high spatial resolution well suited for the envisaged code validation purposes. The instrumentation installed for the cooler series is introduced and explained in the following sections.

2.1. Temperature. Up to 374 K-type thermocouples (TCs) were used for measuring fluid as well as inside and outside wall temperatures of Vessel 1, Vessel 2, and the IP. An addition of 26 K-Type TCs was used for the instrumentation of the cooler component. Through calibration of these thermocouples, an accuracy of $\pm 0.7^{\circ}$C was assessed. Temperature sensors are installed in the vessels at different heights identified as level A (near the top of the vessels) to level T (near the bottom of the vessel) and at different radial distances from the vessel axis, Figure 4. A schematic of the cooler with the TCs is depicted in Figure 2. Particular attention was paid to ensure good spatial resolution of temperature measurement in front of the cooler as well as inside the cooler. One thermocouple and capillary was installed at the exit of the duct to measure the temperature and composition of the exhaust gas mixture, CO_1. Three more locations were chosen inside the cooler casing, one in the empty space behind the cooling tubes, CO_2, and two within the cooling tube array itself. For the latter, one was located at the top of the tube array, CO_3, and one at the bottom, CO_4, to observe any concentration inhomogeneities. In front of the cooler outlet, a vertical array of five thermocouples/capillaries was installed to monitor possible nonuniformities of the gas entering or leaving the cooler, CO_5 to CO_9. Finally, two horizontal thermocouple arrays (CO_10 to CO_15) located at the top and the bottom of the cooler open side were installed to monitor the cooler inflow conditions. All these sensors were aligned with the symmetric plane of the cooler. The main inlet and outlet cooling water lines as well as each cooling line outlets were instrumented with thermocouples to monitor the presence of inhomogeneities in the heat removal of the cooler during operation, MTF_D1CO_1 to MTF_D1CO_10, Figure 3.

2.2. Concentration Measurements. The gas concentration was measured in the PANDA facility by mean of two mass spectrometers (MSs). Gas was continuously sampled through capillaries and sent to the MS systems through heated tubes to avoid any condensation. The measurement is sequential and only one line can be selected at a time via a multiport rotating valve per mass spectrometer. When selected, the sampled gas is sent to a quadrupole mass spectrometer which gives the partial pressure of the selected gas (steam, air, or helium). From these partial pressures, the concentrations were calculated.

Up to 118 sampling lines can be connected to the two MS. Once calibrated, the system can measure any gas concentration and composition. The gas mixtures used for the SETH-2 tests in PANDA are either helium/air, steam/helium, or steam/air/helium. The number of sampling lines used for measurements varies in each test and during the test evolution. Different scanning sequences are programmed in the MS to monitor facility preconditioning, initial test conditions, test evolution, and so forth. A thermocouple is placed a few millimeters apart from each sampling line tip such that gas concentration and temperature measurements are available at almost the same spatial location. For steam/helium mixtures, an absolute error on the measured steam/helium

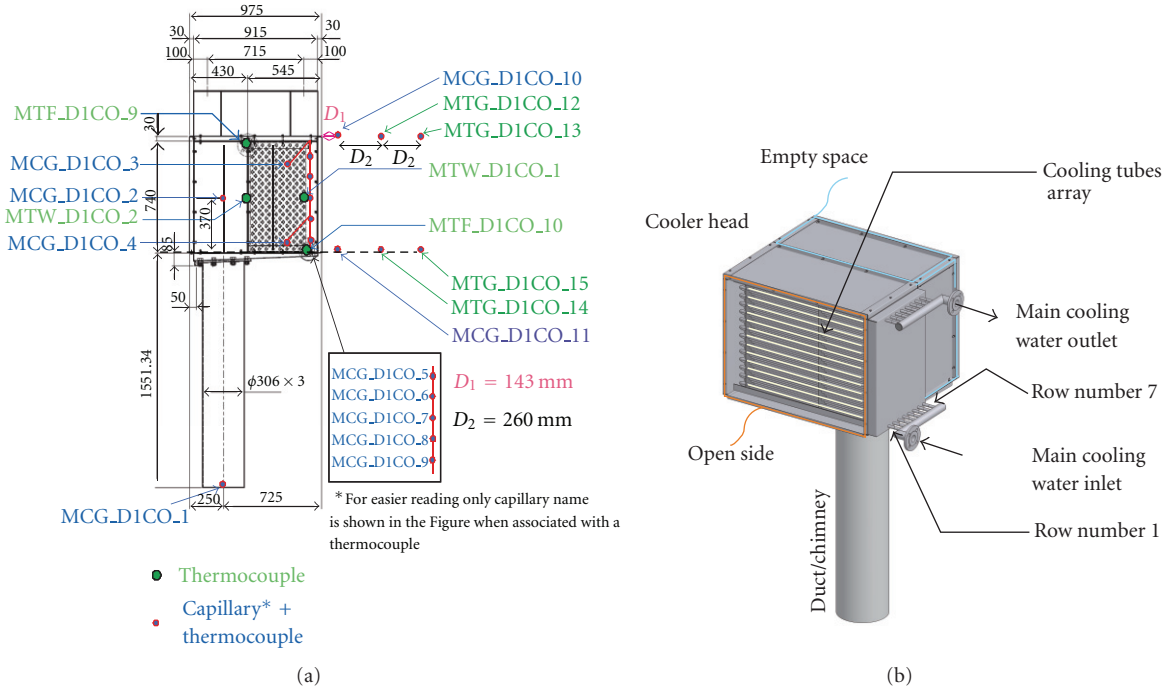

Figure 2: Sensor locations for mass spectrometer sampling lines and TCs in the cooler.

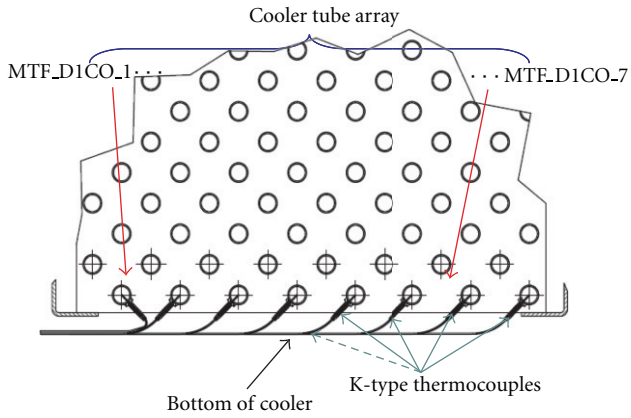

Figure 3: Schematic of the installed TCs in the cooler outlet subchannels.

molar fraction of ±1.5% is assessed. The main sampling locations mentioned in this paper are presented in Figures 2 and 4. Note that depending on the position of the cooler, the sensors that overlapped with the cooler had to be removed (i.e., CD1.20, CD2.20, and D.20 for top position or I.20 for middle position).

2.3. Velocity Field. Particle image velocimetry (PIV) is a measurement technique, which allows for capturing instantaneous velocity information of whole flow fields [29]. For the current test series, a commercial particle image velocimetry (PIV) system was used to measure the 2D velocity fields in Vessel 1 in a vertical plane aligned with the vertical mid plane of the injection pipe. Olive oil, dispersed into small particles by a spray nozzle, was used as seeding particles for the PIV technique. The oil particles were injected into the steam/helium flow that was directed into Vessel 1 through the injection line. The PIV system provides 2D velocity fields with a typical acquisition rate of 5 Hz. For the cooler series, two configurations were used depending on the position of the cooler in Vessel 1, see Figure 5. For the M-configuration, velocity measurements were conducted in the field of view (FOV) denoted G, whereas for the T-configuration, the FOV denoted as B in Figure 5 could be captured.

3. Test Specifications and Preconditioning

The cooler test series (ST4) addresses the effect of the cooler activation on the gas distribution. Additionally, these tests provide insight into the performance alteration of a containment cooler during an accident sequence scenario involving light noncondensable gas. In the ST4 test series, the operation of the cooler during a scenario involving successive injection of steam, steam-helium mixture, and steam in a hot air environment is studied.

The SETH-2 PANDA tests are identified using the abbreviation:

$$\mathrm{ST}x\_y\_z, \tag{1}$$

where ST denotes SETH-2 test, x depicts the series number, that is, ST4_y_z, y denotes the test number, and z indicates a possible repetition of the experiment.

Two facility configurations were used for the ST4 experiments. The main differences are the location of the containment cooler in Vessel 1. Two positions for the cooler, shown

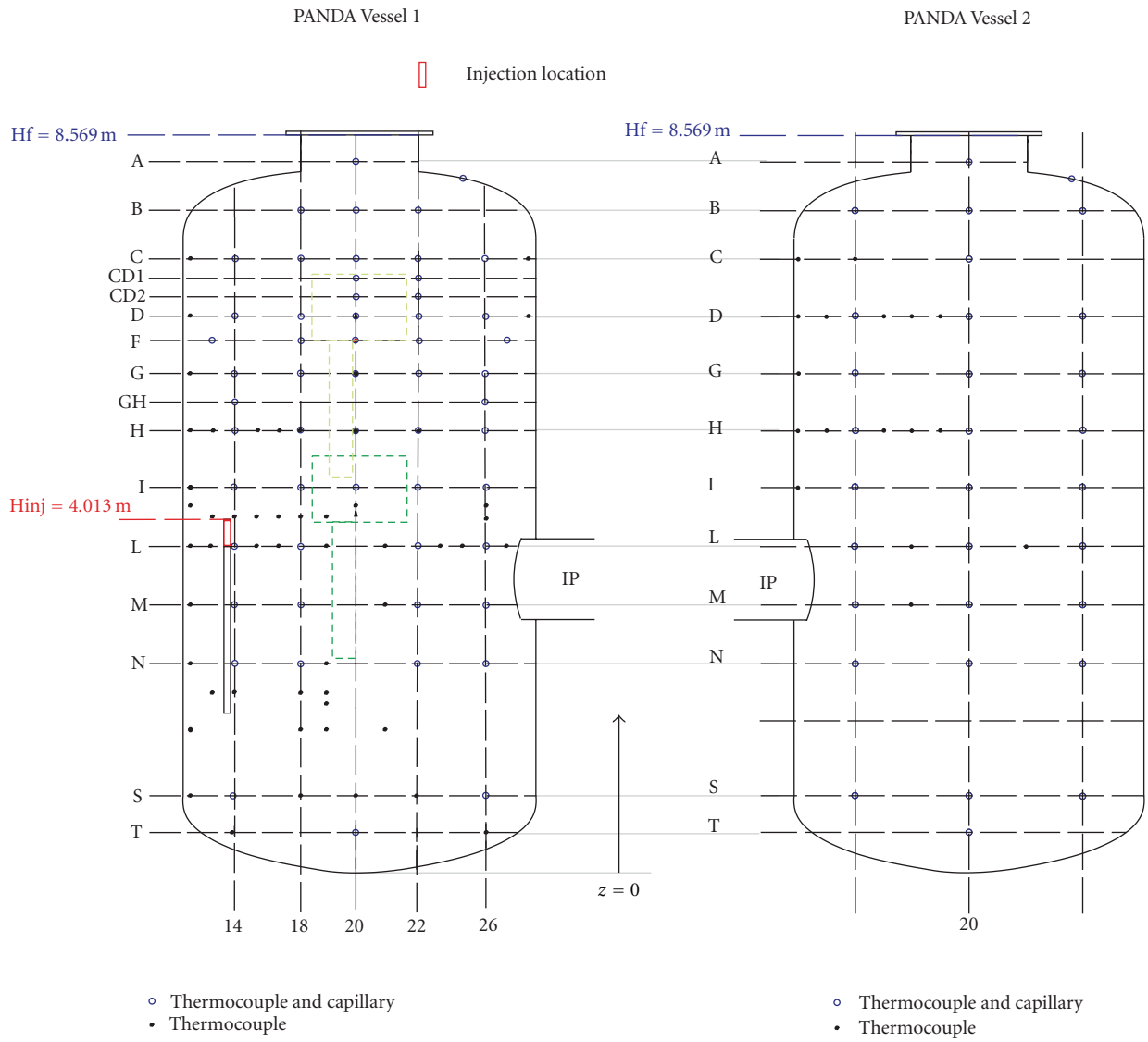

FIGURE 4: Sensor locations for mass spectrometer sampling lines and temperatures in the main measurement plane of Vessel 1 and Vessel 2 and cooler locations (middle and top position).

in Figure 5, were used. For the M-configuration, the cooler was located 3900 mm from the bottom of Vessel 1 and the injection tube was located 500 mm away from the vessel side wall, Figure 4. For the T-configuration, the cooler was located 6000 mm from the bottom of Vessel 1 and the injection tube was at the same positions as for the M-configuration, Figure 4. The injection tube outlet was located 4013 mm above the bottom of Vessel 1. In addition, one should note that the injection tube is a double walled with reduced pressure in between the walls to reduce the heat transfer between the fluid in the tube and the ambient fluid. For all the tests of the ST4 series, the injection was in Vessel 1 and venting at the top of Vessel 2 to ensure constant pressure for the duration of the tests when required.

All the experiments within the ST4 series are characterized by an identical test scenario. Following the stabilization phase of the operating cooler in ambient hot air, each experiment was then divided into three injection phases, Figure 6 lower part. In Phase I, steam was injected for 3600 s at a mass flow rate of $40\,g\cdot s^{-1}$. In Phase II, $2\,g\cdot s^{-1}$ helium was added for 1800 s to the $40\,g\cdot s^{-1}$ steam flow. In Phase III, pure steam was again injected for 3600 s at a mass flow rate of $40\,g\cdot s^{-1}$.

There are three main experimental parameters for the ST4 test series: (1) the cooler position inside Vessel 1, (2) whether the connected vessels were vented through Vessel 2 or not, and (3) the presence or absence of the duct (downward chimney) the relevant parameters for the experiments discussed in the present paper can be found in Table 1. In this table, one finds the abbreviation of the experiments (Test) where ST4_*X*_2 depicts a repetition, the location of the cooler (loc.), the venting status (vent.), and the presence of the duct (duct). These parameters were varied to observe different aspects of the operating cooler during the previously

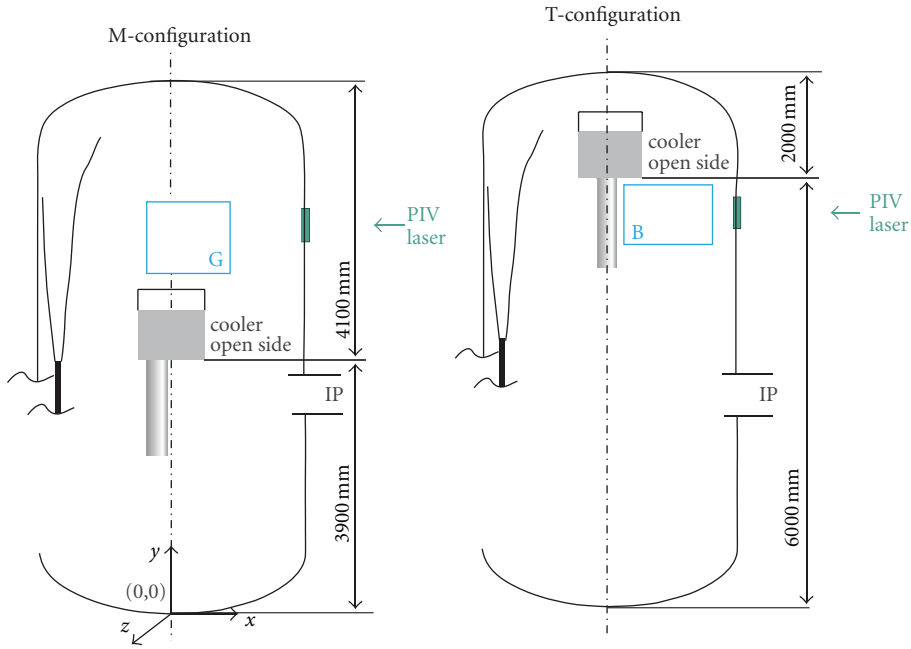

Figure 5: Schematic representation of field of view locations used.

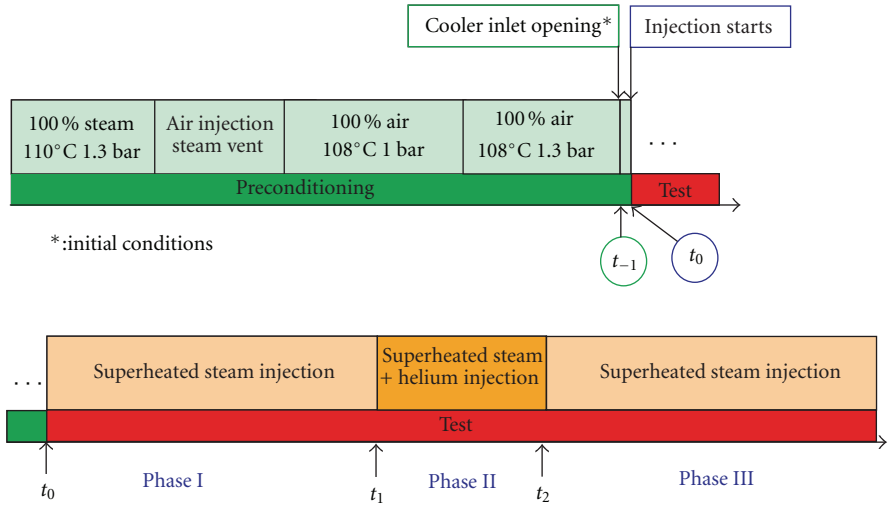

Figure 6: Schematic of the timeframe for the ST4 series.

described scenario. During the injection phases, gas lighter than the initial ambient air was expected to accumulate at the top of the facility leading to gas stratification. The rationale behind the location of the cooler was to test for the influence of the cooler on the possible stratification process with particular attention put on the possible accumulation of light noncondensable gas inside and outside of the cooler. Except for experiment ST4_1, the pressure was kept constant during the entire test. For ST4_1 the facility was disconnected from the environment in order to observe the possible pressurization of the system and its impact on both the cooler performance and the gas distribution in the vessels. The design of the cooler included the presence of a duct directing downwards. The rationale behind the presence of such a duct was to create a suction effect by exhausting the cold gas mixture through it, therefore, enhancing the inlet flow entering through the open side of the cooler into the cooler tubes. The duct was always mounted to the cooler casing except for test ST4_3.

The entire preconditioning and test time sequence which is identical for all the experiments is presented schematically in Figure 6 and consists in the following steps. At the beginning of each experiment, the vessels are heated up with pure steam to ≈112°C and pressurized to the corresponding steam saturation pressure. The temperature used for preconditioning was slightly higher than the specified temperature of 108°C to compensate for the facility's heat loss expected during the remaining time of the preconditioning.

Table 1: Main parameters for the different runs.

Test	Loc.*	Vent.	Duct	Temp.	Conc.	PIV	
ST4_1	Middle	Yes	Yes	√	√	√	Reference experiment and repetition
ST4_2	Middle	No	Yes	√	√	√	
ST4_2_2	Middle	No	Yes	√	√	√	
ST4_3	Middle	No	No	√	√	√	
ST4_4	Top	No	Yes	√	√	√	
Experimental parameters				Recorded data			

This heating phase of the facility lasted about one day, after which the facility was depressurized to atmospheric pressure. Afterwards, the steam was purged out of the facility by injecting hot air using fans located at the top of each vessel. This phase lasted about 90 min. When the air content reached a molar concentration of >98%, the air injection was stopped and the facility was disconnected from the environment. Finally, the facility was pressurized by injecting air through a compressor until the pressure reached the specified conditions of 130 kPa. This took about 40 min. The aim of the above, described facility preconditioning procedure was to obtain a well defined and reproducible initial gas concentration, pressure, and temperature conditions.

4. Results and Discussion

The coordinate system origin used to describe the measurements locations for the concentration, temperature, as well as velocity measurements is located at the bottom of Vessel 1, while the axis coincides with the symmetric axis of Vessel 1, Figure 5.

Results depicting the mixing, transport, and stratification are presented in terms of concentration and temperature maps. Additionally, PIV results are used to provide better insight into the flow velocity pattern around the cooler. The cooling power of the system as well as the condensation rate of the steam inside the cooler is also discussed. A particular interest was to verify the possibility of accumulation of light noncondensable gas (helium) in the two connected vessels (Figure 4) as well as to verify the possibility of unstable operating conditions and the resulting gas concentration patterns inside and outside of the cooler.

According to the test matrix presented in Table 1, only one of the three test parameters—venting, duct, and cooler position—changes from the reference experiment ST4_2 to each of the other tests in the series. Due to the intricacy of the physical phenomena involved, each test results are presented separately in this chapter, starting with the reference test ST4_2 and its repetition. Then, the main differences obtained for the pressurized tests, ST4_1, the cooler without duct test, ST4_3, and the top position cooler test ST4_4 are presented.

4.1. Experiments ST4_2 and ST4_2_2. In this section, a detailed description of the cooler performance, temperature distribution, and the flow pattern by means of PIV results for the reference experiment ST4_2 are presented. Selected results are also shown to confirm the successful repeatability of the test (ST4_2_2). A more in-depth discussion of these results can be found in [16, 23].

4.1.1. Cooler Performance. The performance of the cooler is discussed in terms of heat removed and individual cooler row water outlet temperatures in this section. The cooler performance is calculated from the water feed line inlet temperature measured *outside* Vessel 1 and the main cooler outlet water temperature together with the mass flow rate passing through the cooler. To account for the heat removed from the original ambient prior to the steam injection, the measured heat removal before $t = 0$ s was treated as an offset and subtracted from the measured value during the experiment. The resulting value was then normalized with the heat corresponding to the condensation of the entire injected superheated steam. The normalized heat removal is presented with a blue line in Figure 7(a). The horizontal black line in Figure 7(a) depicts a virtual equilibrium between the heat extracted by the cooler and the heat transported by the steam where all the injected steam condenses. This corresponds to a normalized heat removal of 1.

During the initial part of Phase I (pure steam injection), the steam which is lighter than the ambient air accumulates at the top of the Vessel 1. The interface between high and low steam content zone moves downwards until it reaches the cooler open side. During the remaining part of Phase I, the cooling power continuously increases and reached almost 0.9 at the end, Figure 7(a).

During the first part of Phase II, (steam and helium injection), we find a remarkable continuous decrease of the cooling power down to less than 0.2. Still in Phase II, the cooling power recovered very quickly and resulted in a maximum of approximately 1.14. Finally, a short time after the beginning of Phase III (again pure steam injection), the cooling power remained almost constant at ≈0.9, Figure 7(a). The final steady value lower than 1 suggests that the cooler could not remove all the heat injected in the facility. This would lead to a pressurization of the facility if not vented.

To explain the somewhat surprising cooler performance deterioration during Phase II, one must take a local perspective. Five out of seven outlet water temperatures are presented in Figure 7(b). Row number 1 (MTF_D1C0_1, Figure 2) corresponds to the front sub channel. During Phase I, the outlet temperature difference across the cooling array (#1 to #7) was about 10°C. At the beginning of Phase II, the outlet water temperature of the front subchannel array increased slightly whereas the temperatures

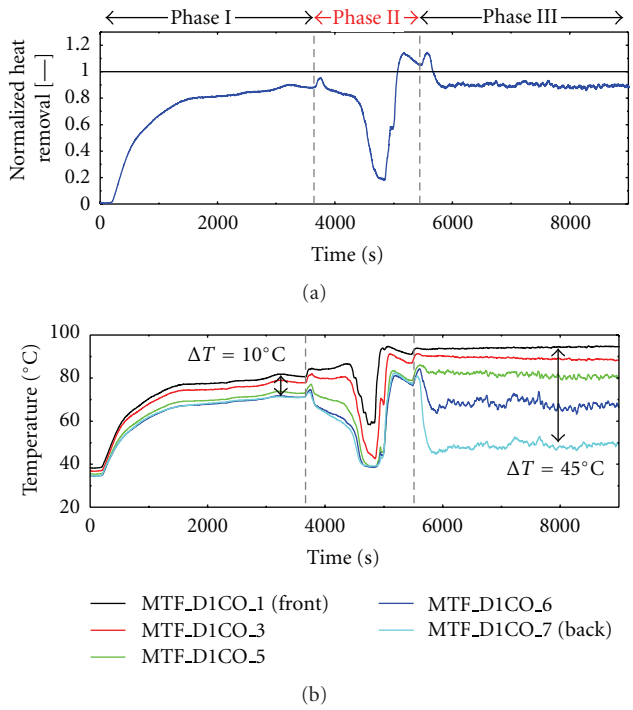

FIGURE 7: Normalized heat removal and water outlet temperature of the subchannels for test ST4_2(_2).

decreased rapidly for the back rows (#6 and #7) such that the temperature difference between front and back tubes increased. Later, we find the temperatures for the front tubes also decreasing ($t \approx 4500$ s). This suggests that the accumulation of helium in the rear part of the cooler (subchannel #7) increasingly hindered the flow passage of steam. This would reduce the condensation rate and, correspondingly, the heat removed by the cooler. This process started at sub-channel #7 and propagated to the front of the cooler. Finally, during Phase III, the outlet temperature difference was about 45°C between the front (#1) and the back rows (#7), which suggests that the condensation of steam occurred mainly in the first rows of the tube array. During Phase I, the heat released by the condensation of steam was almost equally distributed over the depth of the tube array whereas in Phase III, it was unequally divided over the depth resulting in an outlet temperature increase for the front cooler tubes and a large decrease for the back tubes. Nonetheless, the overall energy removed was the same, Figure 7(a). The excellent repeatability of the cooler performance can be seen in Figure 23, ST4_2 versus ST4_2_2.

4.1.2. Gas Transport in Vessel 1. The transport phenomena occurring inside and outside the cooler in Vessel 1 are discussed in this section with the support of six temperature contour maps, Figure 8, and four mean velocity fields with stream lines, Figure 10. The black crosses in the temperature contour maps represent temperature measurement locations. A linear interpolation between the closest neighboring points was calculated to obtain the contour maps. The corresponding temperature contour maps for ST4_2_2 are presented in Figure 9 to show the very good repeatability of the phenomena. Note that the times given in Figure 9 are delayed by 242 s after the beginning of Phase II when compared with Figure 8.

During Phase I, superheated steam appearing in red is filling the top of the vessel through the injection pipe located in the lower left part of the vessel, Figure 8 at $t = 2500$ s. The containment cooler appears in blue. The condensation of the steam in the cooler creates a suction effect, which is further enhanced by the presence of the downward chimney. The colder temperature measured at the chimney exit and below the chimney in Vessel 1 suggests the presence of flow through the duct. The higher temperature above the cooler and the temperature transition from warm to colder (for details see [23]), suggests that the steam mixture remains confined above the cooler. Still in Phase I, the flow passes most probably through the entire depth of the cooler tube array as confirmed by the small outlet temperature differences, Figure 7, and leaves through the duct. The mean velocity field obtained at the end of Phase I above the cooler shows a slightly upward oriented flow whose direction points toward the injection jet, Figure 10(a). This suggests the presence of a large clockwise rotating circulation driven by the steam injection in the upper part of Vessel 1 above the cooler. The velocity field is almost perpendicularly oriented towards the open side of the cooler ensuring a good transport of the steam into the cooler. This stable flow field was observed during the entire Phase I and at the beginning of Phase II.

The temperature maps which correspond to the beginning of Phase II are presented in Figures 8 and 9 at $t = 4742$ s and $t = 4500$ s, respectively. The duct outlet temperature is now similar to its surrounding. Thus, it is concluded that the accumulation of helium has led to a partial blockage of the flow passage such that the flow through the duct is considerably hindered or even stopped. The steam/air/helium mixture flowing through the cooler cannot penetrate the entire depth of the array due to the resistance of a helium rich mixture confined in the casing. This explains the deterioration of the heat removal beginning from the back end of the array. The cooled gas mixture exits the cooler through the bottom part of the cooler open side, which explains the rapid drop in density observed at L level, $y = 3676$ mm, Figure 11(a) mark B. The accumulation of helium during Phase II (at $t = 4942$ s and $t = 4700$ s for experiment ST4_2 and ST4_2_2, resp.) is probably large enough that almost no flow can pass through the cooler array; this corresponds to the minimum heat removal observed in Figure 7.

During Phase II, the hot helium/steam rich mixture accumulates at the top of the vessel and the interface towards the helium/steam poor mixture in the lower part of the vessel moves continuously downwards up to a level below the cooler inlet, Figure 8 at $t = 4942$ s. This downward movement of the interface was captured by plotting the vertical density in Vessel 1, Figure 11(a). The density profiles are given as a function of elevation within Vessel 1 at four selected times during Phases I and II. The open side of the cooler is marked with a blue dashed lines.

During Phase I, we find a transition between the less dense upper part and the denser lower part of the gas in

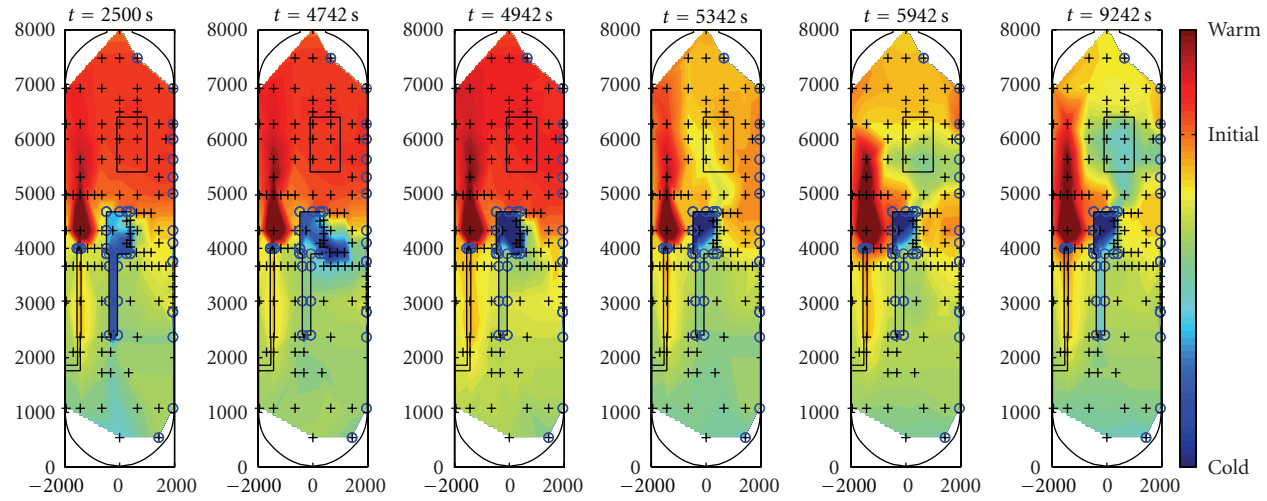

Figure 8: Temperature contour maps in Vessel 1 for experiment ST4_2 for different instances in time.

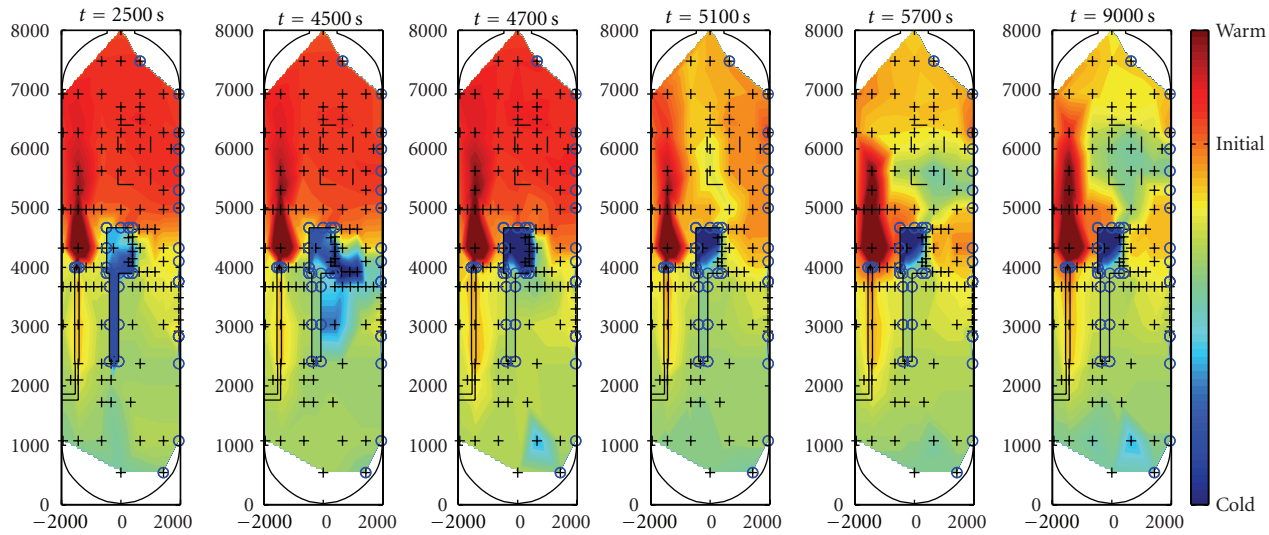

Figure 9: Temperature contour maps in Vessel 1 for experiment ST4_2_2 for different instances in time.

Vessel 1. This gradient begins at the upper part of the cooler open side, mark A in Figure 11(a) at $t \approx 3000$ s, with the density gradient confined between 4500 mm and 5000 mm. During Phase II (steam and helium injection), the density in the upper part decreases, while the density in the lower part of the vessel remains almost constant. Consequently, the density gradient becomes steeper. This process continues until the additional downward movement of the less dense upper part of the gas at $t = 4800$ s surrounds the entire cooler head, Figure 11(a) mark B. This observation is confirmed by the density measurement in front of the cooler, Figure 11(c). The density gradient measured at $t = 3000$ s disappears and the vertical density profile flattens at a much lower level across the open side of the cooler for $t > 4800$ s. The flat density profile in front of the cooler at $t = 4800$ s coincides with the maximum cooler performance deterioration, Figure 7. Later in time, during Phase II, the density gradient has slightly moved upwards again, Figure 11(a) at $t = 5400$ s mark C, which coincides with the cooler performance recovery, Figure 7.

These observations now allow a full explanation of the cooler performance recovery during Phase II of the injection. The helium/steam mixture density inside the cooler, Figure 11(b), which was higher than the surrounding during the first part of Phase II, now reaches levels similar to the one measured outside the cooler such that gas from the surrounding finally finds its way through the bottom of the cooler tube array, which increases the condensation rate again, Figure 8 at $t = 5342$ s and Figure 7. The breakup of an unstable density stratification between the inside and outside part of the cooler seems to trigger the cooler recovery phase. The heavier hot gas mixture outside the cooler pushes the lighter colder helium rich mixture out of the cooler case creating a new flow circulation pattern through the tube

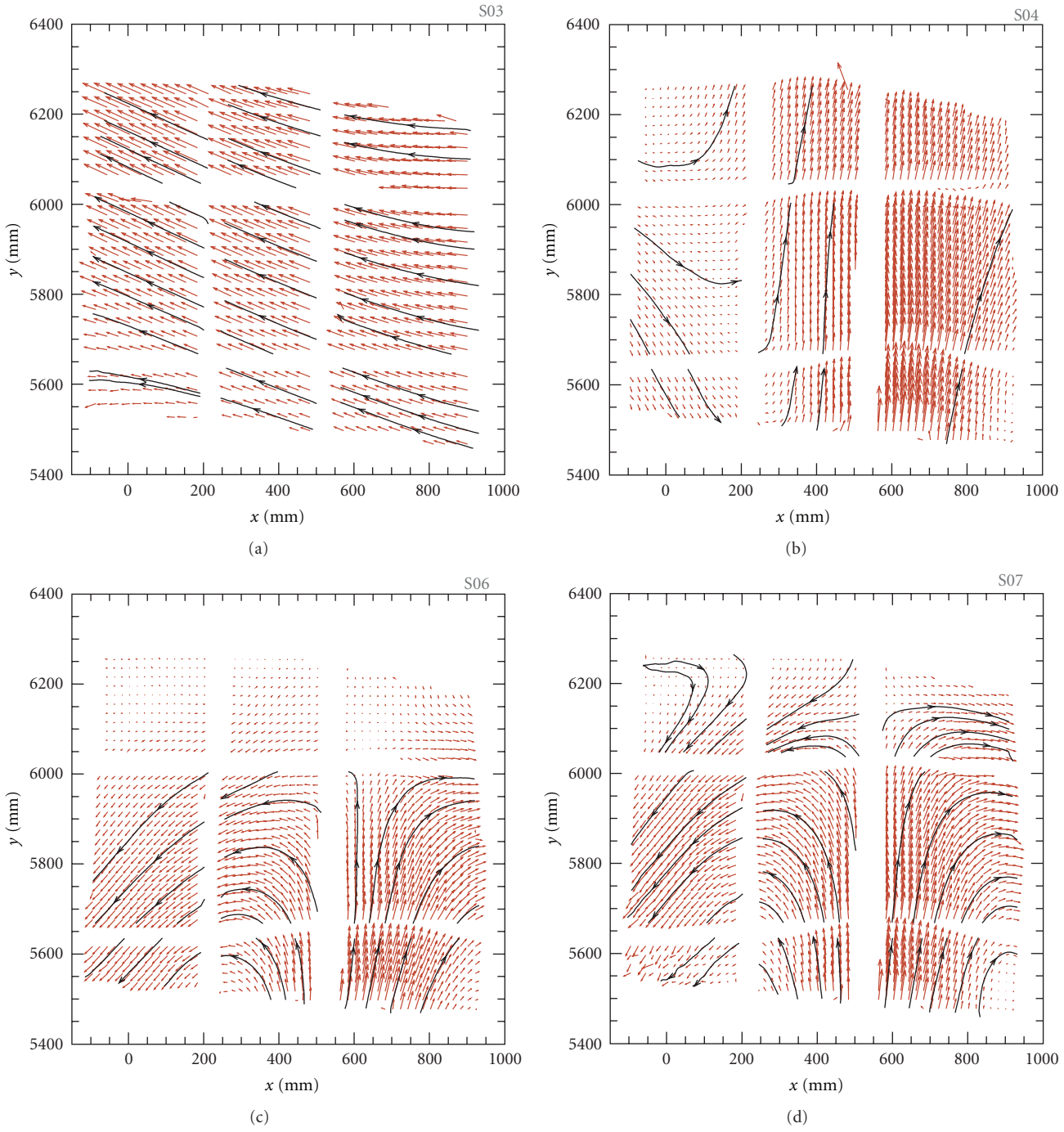

FIGURE 10: Selected mean velocity fields for ST4_2(_2) for (a) 3541 s < t < 3746 s, (b) 5384 s < t < 5896 s, (c) 7135 s < t < 7340 s, and (d) 7517 s < t < 8541 s.

array. However, this flow pattern in the cooler is confined to the first few cooler rows located close to the front of the tube array as discussed previously, Figure 7. The lighter colder helium rich mixture leaving the cooler now alters the flow pattern above the cooler considerably. Initially, we find a strong vertical flow which reaches the top of Vessel 1 as suggested by the colder zone observed at the center of the Vessel 1 above the cooler in the temperature contour map, Figure 8 at t = 5342 s. This is confirmed by the velocity field. A strong vertical flow coming from the cooler is observed in the mean velocity field after the recovery, Figure 10(b). This initial release of gas from the cooler is so strong that it reaches the Vessel 1 ceiling.

After the cooler performance recovery, we again find a new flow configuration above the cooler during Phase III (pure steam injection). The system consists now of a light gas

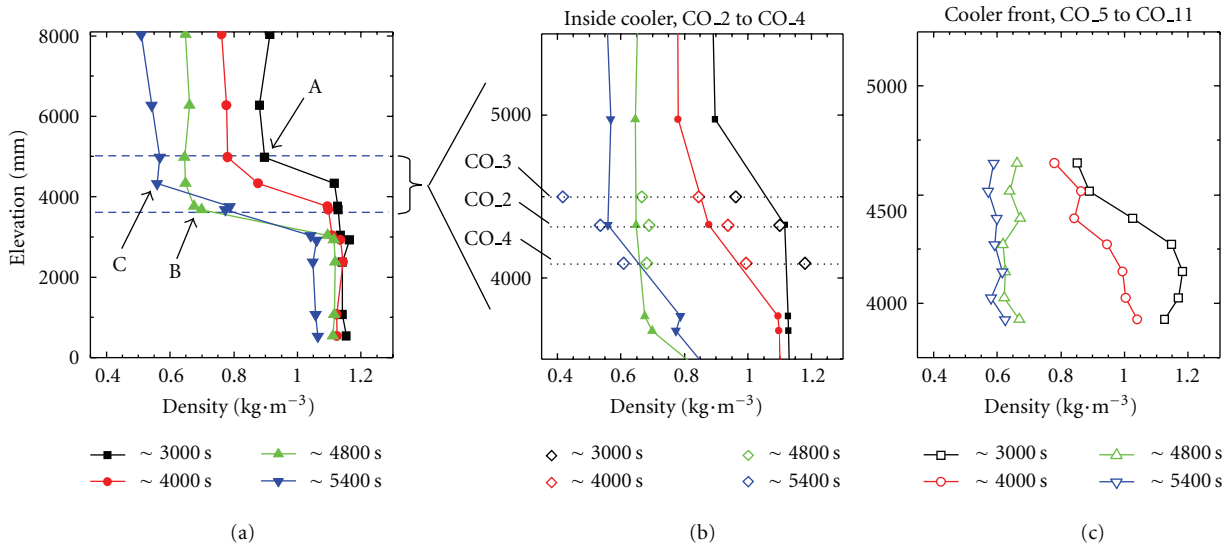

Figure 11: Density profile in Vessel 1 recorded for ST4_2 (a), inside (b) and in front of the cooler (c) with the time as parameter.

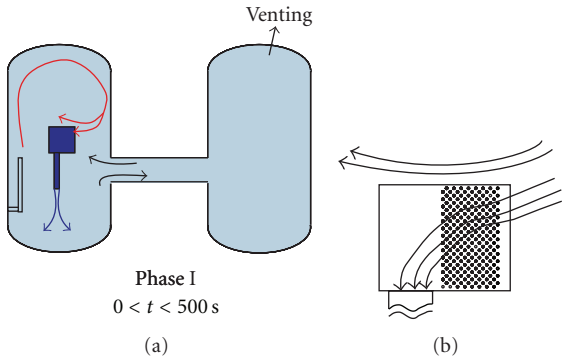

Figure 12: Suggested flow pattern for $0 < t < 500$ s.

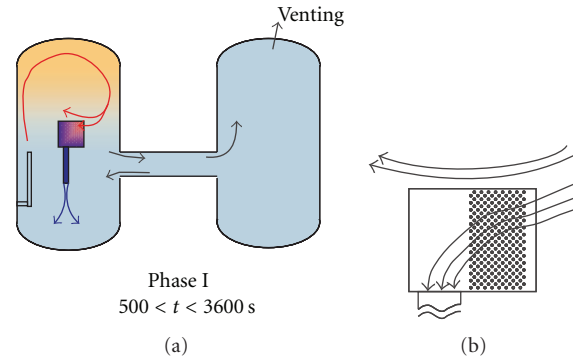

Figure 13: Suggested flow pattern for $500 < t < 3600$ s.

layer located at the top of Vessel1 onto which a steam jet and a cold helium rich plume impinge. This is shown on the temperature contour map, Figure 8, at $t = 5942$ s. On the left side of the vessel, the hot steam (dark red) jet is confined between the upper light layer on the top, the cold pocket (blue green) fed by the plume leaving the cooler casing on the right, and the wall on the left. Note that the penetration depth of the jet and the plume in the upper layer increases with time as confirmed by the temperature and the velocity maps, Figure 8 at $t = 5942$ s versus $t = 9242$ s and Figure 10(c) versus Figure 10(d). Both the steam jet and the gas mixture plume are subject to the effect of negative buoyancy when impacting the upper layer, which leads to the mixing around the impact zone resulting in an erosion of the upper layer.

4.1.3. Synthesis Discussion ST4_2. Possible global and local flow patterns derived from the previously presented results are discussed in this section. Each of the following figures consists of a suggestion for the Large-scale flow pattern in both vessels, the IP, and inside the cooler. Note that the representation is only 2D and that no attempt was made to consider the 3D transport phenomena. At the beginning of Phase I, $0 < t < 500$ s, the steam injected accumulates at the top of Vessel 1 forming a large clockwise circulation vortex above the cooler, Figure 12(a). Cold gas flows through the duct to the bottom of Vessel 1, which leads to a gas flow from Vessel 1 to Vessel 2 through the bottom of the IP. This was measured with an array of thermal anemometers [30] installed in the IP. These anemometer results are beyond the scope of this paper.

A counter flow is observed towards Vessel 1 at the top of the IP. Inside the cooler Figure 12(b), the steam flows through the entire cooling tube array. Later in time, the concentration of steam increases at the top of Vessel 1 and the power removed by the cooler increases accordingly. The noncondensed steam transported through the duct leads to a decrease of the density at the bottom of Vessel 1. During the remaining part of Phase I, $500 < t < 3600$ s, the flow patterns in the vessels and the cooler are similar to the one described above for the earlier phase but with a reversed flow through the IP, Figure 13.

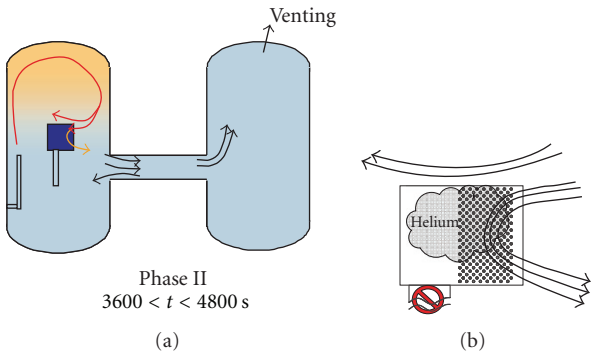

Figure 14: Suggested flow pattern for $3600 < t < 4800$ s.

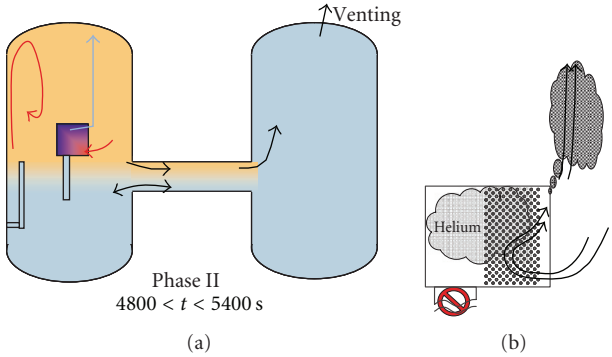

Figure 15: Suggested flow pattern for $4800 < t < 5400$ s.

The gas mixture now leaves Vessel 1 through the top of the IP to Vessel 2 where it moves upwards under the effect of buoyancy and starts accumulating at the top. At the beginning of Phase II, $3600 < t < 4800$ s, the injected helium mixes with the steam and is transported into the cooler where its concentration increases due to the steam condensation. Caused by the accumulation of a helium rich gas mixture in the cooler casing, the flow passage through the duct is blocked and part of the cold gas mixture leaves the cooler through the open front, orange arrow in Figure 14(a). The flow through the IP increases rapidly and a steam/helium rich mixture is transported to the top of Vessel 2. The flow pattern within the tube array changes and the flow is expected to be mainly directed vertically downward, Figure 14(b). Ultimately, the accumulation of helium is such that the flow through the cooler is very limited. It corresponds to the maximum deterioration of the cooler performance observed at $t \approx 4800$ s. At the end of Phase II, $4800 < t < 5400$ s, the steam/helium-rich mixture accumulates at the top of Vessel 1 and the interface between the steam/helium-rich mixture and the steam/helium-poor mixture moves continuously downward up to a level below the cooler inlet, Figure 15(a).

The cold helium-rich mixture in the cooler reaches a density lighter than the surrounding gas mixture outside the cooler. Part of the trapped gas inside the cooler housing can now leave the cooler. This triggers the cooler performance recovery associated with the steam reentering and condensing in the cooler while a cold helium-rich gas mixture is released from the upper part of the cooler open side. The released helium-rich mixture initially reaches the top of Vessel 1 leading to the formation of a light stratified layer. After the strong initial release from the cooler, the release becomes weaker. As the steam condenses, the helium rich mixture is continuously produced in the cooler. Its potential buoyancy, however, is smaller than that of the mixture build up at the beginning of Phase II and not strong enough to move all the way up to the vessel ceiling anymore. During Phase III, $5400 < t < 9000$ s, the cooler reaches stable operation conditions, Figure 16. The previously build up of a helium-rich layer is not penetrated by the injected steam. The injected steam stays, therefore, confined between the wall and the upper layer and must find its way around to reach the open side of the cooler—here one cannot neglect the presence of 3D effect to explain the transport phenomena involved. Through the condensation of steam, the steam/helium mixture entering the cooler creates a helium rich buoyant plume that escapes the top of the cooler. Similar to the steam jet, the plume cannot penetrate the lighter gas layer located above. The impingements of both the jet and the plume lead to a complex situation where the layer gets slowly eroded by two different sources.

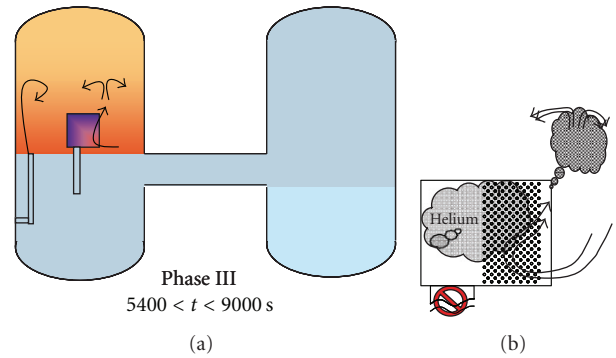

Figure 16: Suggested flow pattern for $5400 < t < 9000$ s.

4.2. Experiment ST4_1. The main differences to the reference experiment ST4_2 that give insights into the gas transport and distribution in the vessels during the test scenario are presented in this section. Test ST4_1 was characterized by the absence of the venting through Vessel 2 which leads to the pressurization of the facility.

4.2.1. Cooler Performance. The cooler performance is presented in terms of normalized heat removal together with the pressure time history in Figure 17.

The heat removal was calculated as described in the previous section for experiment ST4_2. During Phase I (pure steam injection), the normalized heat removal increases similar to experiment ST4_2. The first difference to the reference test ST4_2 occurs at the end of Phase II. The recovery does not occur in Phase II but at the beginning of Phase III, $t \approx 5600$ s, even though the cooler performance deterioration down to 0.4 is observed. The second and more important difference compared with ST4_2 occurs in Phase III, where

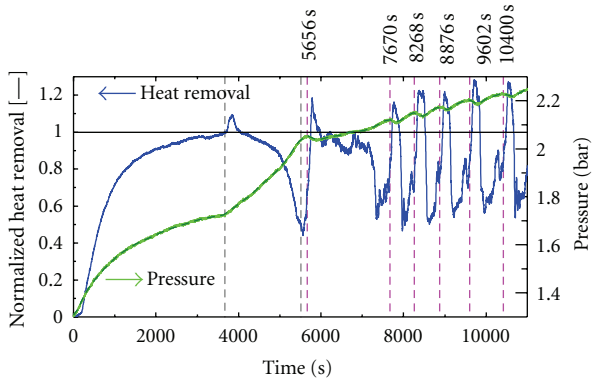

FIGURE 17: Normalized heat removal together with pressure trace for test ST4_1.

oscillations of the heat removal are observed. The periodic deterioration/recovery of the heat removal during Phase III of experiment ST4_1 is believed to be similar to the single recovery during Phase II of the reference experiment ST4_2. This is discussed in more details in the following sections. Overall, the pressure in the vessels continuously increase during the test. Going into the details of the pressure time history during Phase III one finds a small but periodic pressure decay, marked with pink dashed lines in Figure 17, which are in agreement with those instances in time where the normalized heat removal is above 1. During a power recovery period, the cooler removes more heat than transported into the system, leading to a decrease in pressure. When a deterioration occurs, the pressure increases again.

4.2.2. Gas Transport in Vessel 1. To describe the gas transport occurring in the entire Vessel 1 for test ST4_1, 12 temperature contour maps are presented in Figures 18 and 19.

Additionally, four mean velocity fields recorded above the cooler are presented in Figure 20. The first five temperature maps, Figure 18 $t = 2500$ s, 4500 s, 5500 s, 5580 s, and 5746 s, represent a sequence quite similar to the one presented for ST4_2, Figure 8. The timing, however, differs. Test ST4_1 is delayed compared to test ST4_2. During Phase I, at $t = 2500$ s, the steam-rich mixture accumulates at the top of Vessel 1 and reaches the top of the cooler where steam condenses similar to ST4_2. The resulting steam depleted cold mixture leaves through the duct to the bottom of Vessel 1.

The cold mixture with a higher helium content has a density too low to sustain the flow through the duct during Phase II similar to experiment ST4_2, Figure 18 $t = 4500$ s. The cold gas mixture now leaves through the open side of the cooler as suggested by the presence of cold fluid between the cooler and the vessel wall.

In contrast to experiment ST4_2, the flow pattern described above remains the same during the entire Phase II and at the beginning of Phase III. At $t = 5500$ s, for example, the flow leaving from the cooler is even colder compared with ST4_2. At that time the warm gas mixture does not enter the cooler anymore as suggested by the cold temperature measured in every location inside the cooler (appearing in dark blue). The mean velocity field presented in Figure 20(a) at the end of Phase II for ST4_1 shows a remarkable agreement with the one presented in Figure 10(a) at the end of Phase I for ST4_2. The large vortex structure above the cooler is still active during Phase II for ST4_1.

The temperature contour map observed 80 s later, at $t = 5580$ s, corresponds to the minimum heat removal of the cooler. No flow is observed either through the duct or through the open side of the cooler that appears homogeneously cold. As mentioned previously, in contrast to test ST4_2, the recovery does not occur in Phase II, which might be due to the pressurization of the vessels that keeps the helium-rich gas mixture longer confined in the cooler casing. Previously, it was suggested that the heat removal recovery was caused by the cold helium-rich mixture in the cooler reaching a density lower than the surrounding warm gas mixture. Due to pressurization, the front representing the density gradient moves slower downward than without pressurization. More steam can be stored above the cooler when pressurizing. Therefore, situations observed at $t = 5500$ s and $t = 5580$ s for ST4_1, Figure 18, correspond to the ones observed at $t = 4742$ s and $t = 4942$ s for test ST4_2, Figure 8.

At $t = 5746$ s, the recovery occurred, the steam-rich mixture reentered the cooler through the bottom of the open side as the helium rich mixture leaves the cooler casing. This is represented by a large orange/yellow area above the cooler in Figure 18. The plume released by the cooler moves upwards to the top of Vessel 1. The mean velocity field, presented in Figure 20(b), has changed when compared to the one of Phase II, Figure 20(a). Up to that point, the gas transport sequence inside and outside the cooler is very similar to the one of ST4_2.

In contrast to ST4_2, the cooler performance does not reach steady-state conditions during experiment ST4_1, Figure 17 versus Figure 7(a). Between $t = 5746$ s and $t = 7350$ s, the helium concentration builds up again in the cooler casing and at $t = 7350$ s, a second deterioration of the cooler performance occurs. The 6 temperature contour maps presented in Figure 19 show the oscillations observed in the cooler performance from a temperature point of view. Successively, the flow inside the cooler is blocked (all the TCs inside the cooler indicate cold temperatures in blue) and then restored together with a release of helium-rich mixture that behaves like a plume (the TCs at the bottom of the cooler show higher temperatures in yellow). The plume-like behavior of the helium-rich mixture released from the cooler was also observed via PIV measurements, obtained above the cooler, Figure 20(c). Two mean velocity fields were extracted to illustrate the change in the flow field when transitioning from a normal operating cooler period, Figure 20(c), to a deterioration period, Figure 20(d). At $t \approx 8475$ s, the flow field appears similar to the one of a plume impinging on a lighter gas layer [17, 18]. The impingement zone is characterized by a core of velocity vector oriented vertically upward that are deflected downward when penetrating the lighter gas layer. This leads to the formation of recirculation cells surrounding the head of the plume at the impingement location. After the helium build up in the cooler is high enough to

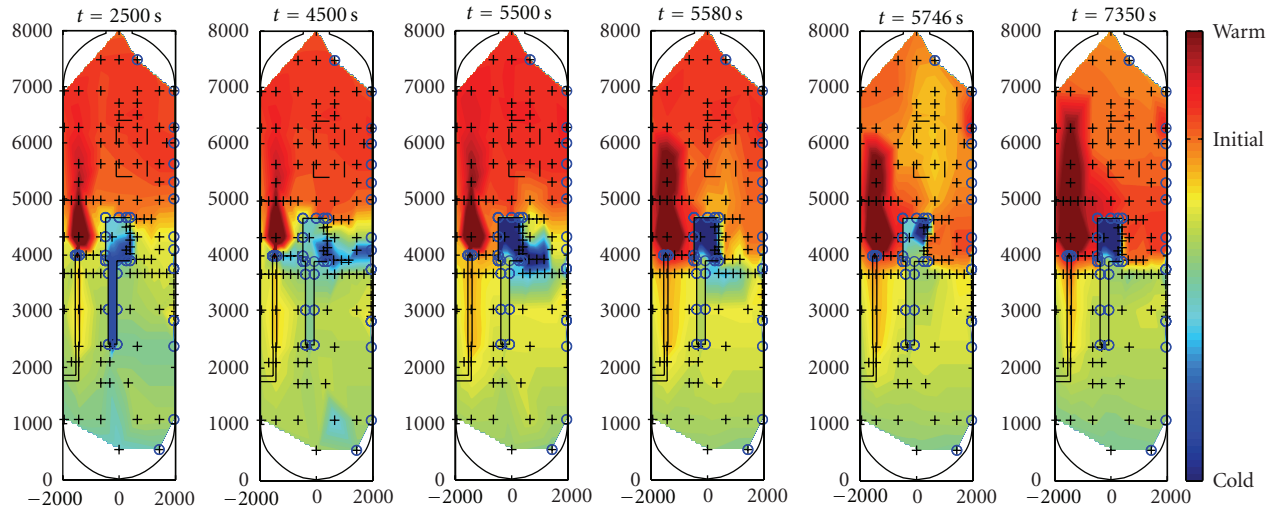

Figure 18: Temperature contour maps in Vessel 1 for experiment ST4_1 for different instances in time $0 < t < 7350$ s.

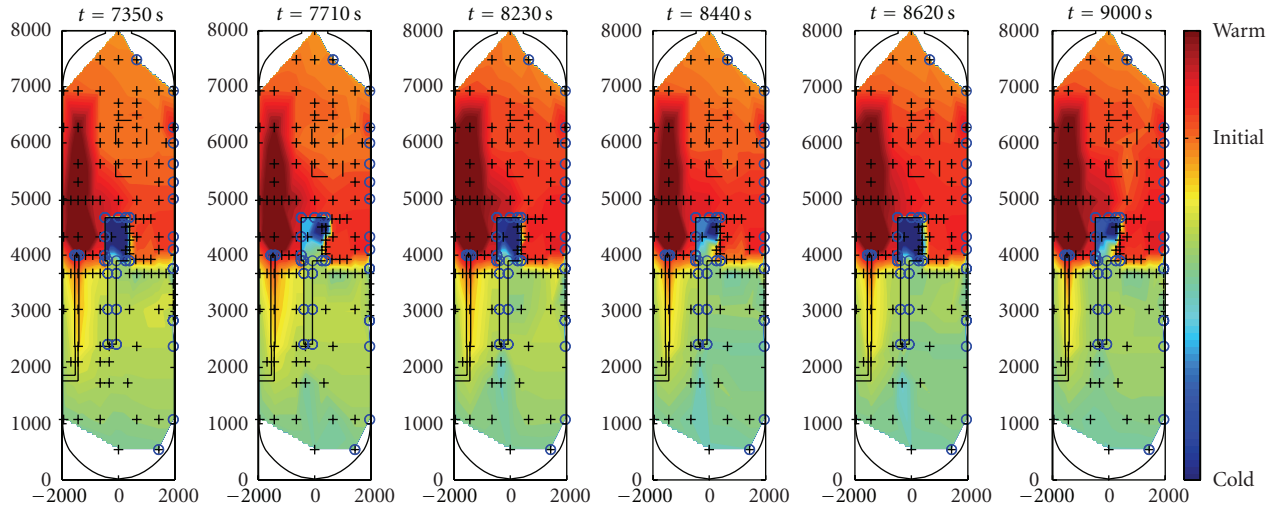

Figure 19: Temperature contour maps in Vessel 1 for experiment ST4_1 for different instances in time $7350 < t < 9000$ s.

hinder the inlet flow in the cooler, the release of helium-rich mixture is interrupted.

The resulting mean velocity field obtained after this transition, at $t \approx 8625$ s, is shown in Figure 20(d). Despite the absence of helium release, the flow field is completely different to the one during Phases I and II, Figures 20(a) and 20(b). The velocity magnitudes are very low and the vectors are mostly oriented downwards with some small recirculation.

4.2.3. Synthesis Discussion for ST4_1. An attempt to summarize the flow patterns that have been discussed previously is presented in this section in a schematic form. Compared with the reference experiment ST4_2, the pressurization of the vessels leads to a delay in the change of flow patterns for ST4_1 even though the scenario is very similar.

The initial part of Phase I with gas flowing towards Vessel 1 at the top of the IP is extended to ≈750 s (ST4_1) instead of ≈500 s (ST4_2), Figure 12 (here and in the following with the vent line now neglected). In the flow patterns observed during the remaining time of Phase I, the steam mixture enters the cooler where steam condenses. The resulting cold-steam depleted gas mixture flows to the bottom of Vessel 1 through the duct, Figure 13. Shortly after the beginning of the helium injection in Phase II, the flow through the duct is interrupted and the steam-depleted mixture leaves the cooler through the bottom of the open side, Figure 14.

Whereas the flow patterns change in Phase II for ST4_2, they remain unchanged until the beginning of Phase III, at $t = 5600$ s (ST4_1) instead $4800 < t < 5400$ s for ST4_2. The flow through the cooler is blocked and its cooling performance is deteriorated to about 50%, Figure 21. This repeats for each of the deterioration/recovery cycle observed until the end of Phase III. As the steam-rich mixture reenters the cooler through the lower part of the open side, helium

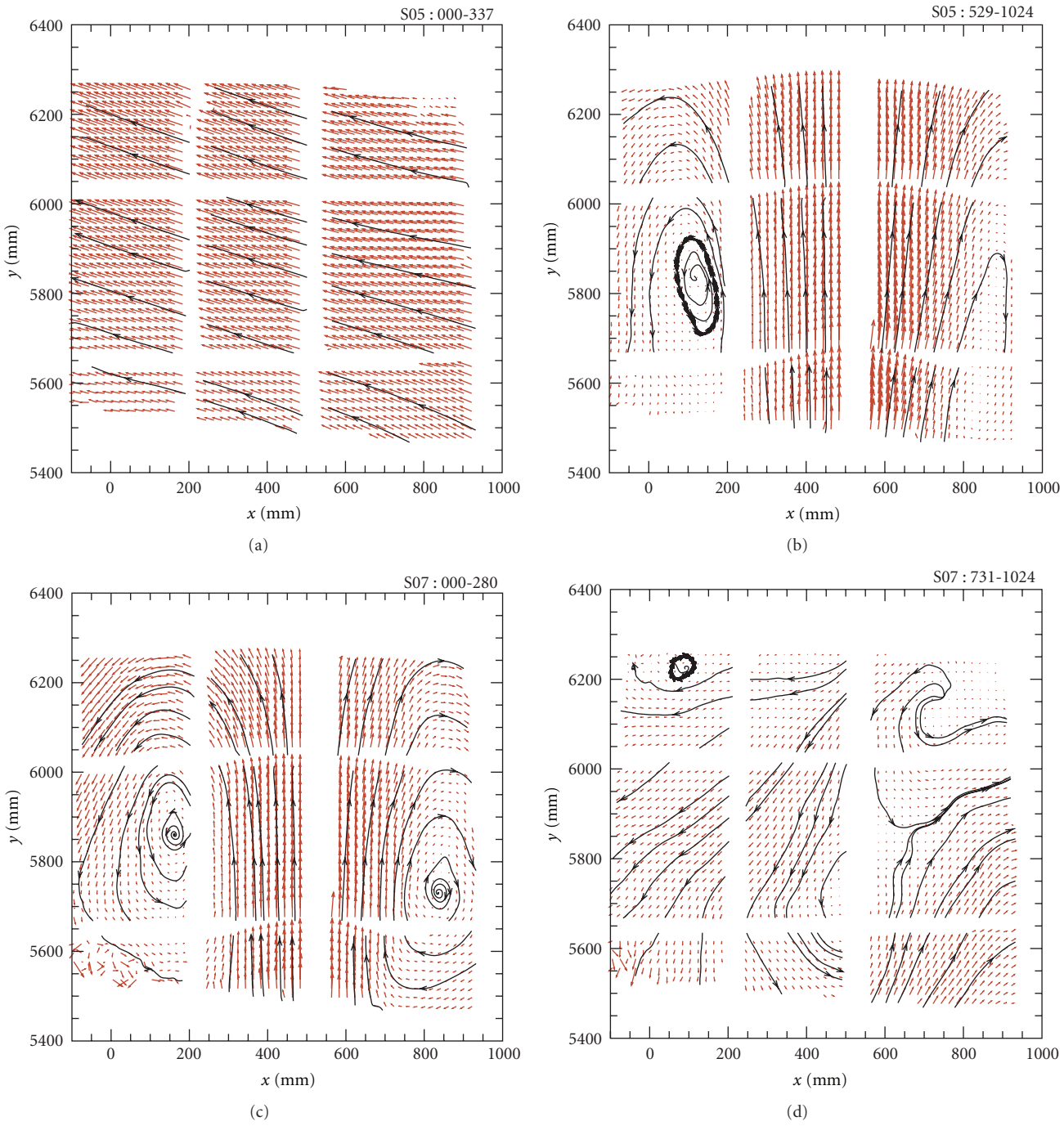

Figure 20: Selected mean velocity fields for ST4_1 for (a) 5410 s < t < 5560 s, (b) 5656 s < t < 5904 s, (c) 8444 s < t < 8500 s, and (d) 8590 s < t < 8649 s.

rich mixture is released out of the cooler casing, Figure 15, which results in the formation of a helium rich layer in the upper part of Vessel 1. The helium mixture release initiates again the recovery of the heat removal capacity of the cooler, strong enough to create a temporary decrease in pressure. This results in a suction effect of the gas from Vessel 2 to Vessel 1, Figure 22. This deterioration/recovery sequence was repeated with a period of about 600–800 s throughout the remaining of the experiment.

4.3. Experiment ST4_3. For the ST4_3 experiment, the duct was removed and replaced with a blind flange. This change in the cooler configuration, however, did not lead to any significant change of the flow pattern when compared with ST4_2.

4.3.1. Cooler Performance. A comparison of the cooler performance for experiments ST4_3, ST4_2 and the repetition

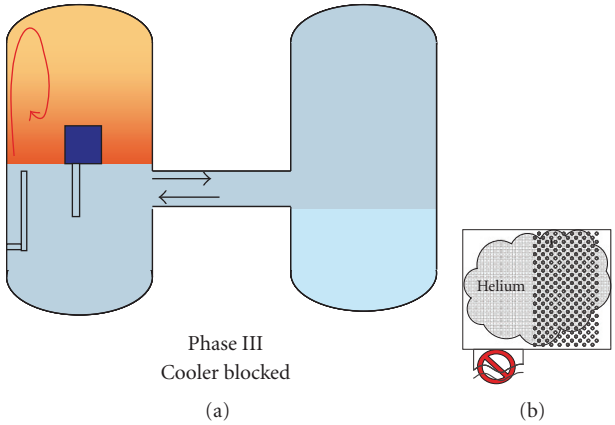

Figure 21: Suggested flow pattern during the cooler performance deterioration configuration.

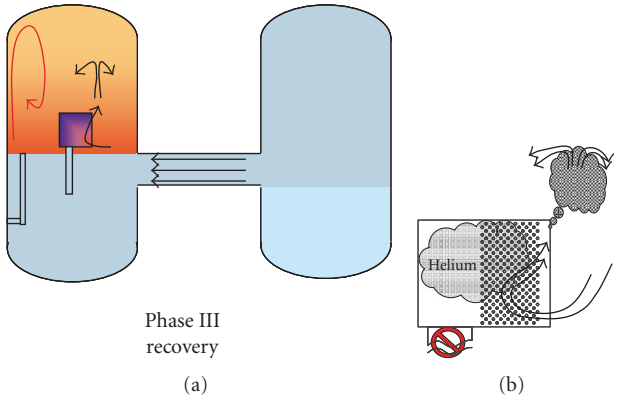

Figure 22: Suggested flow pattern during the cooler performance recovery configuration.

experiment ST4_2_2 can be found in Figure 23. The comparison demonstrates an almost perfect similarity with respect to the shape and scale if one considers the complexity of the geometry and the test scenario.

One can conclude that the presence of the duct does not affect the cooler performance for the M-configuration.

4.3.2. Gas Transport in Vessel 1. Except for the initial outflow through the duct, the gas transport in Vessel 1 for experiment ST4_3 is almost identical to the one already discussed for ST4_2, Figure 8. Also, the flow patterns as recorded with the PIV system are so similar to the ones recorded during experiment ST4_2 that we have decided not to present them. For the synthesis discussion, the reader is referred to the corresponding discussion of experiment ST4_2.

4.4. Experiment ST4_4. Test ST4_4 was conducted with the cooler located at $y = 6000$ mm. Due to the position of the cooler in a region where light gas accumulates, compared with the previous experiments, different flow patterns and gas distributions were expected.

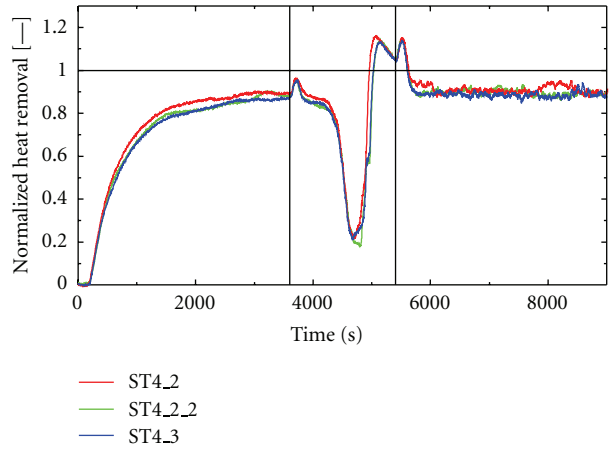

Figure 23: Power removed by the cooler during test ST4_3 compared with ST4_2 (ST4_2_2).

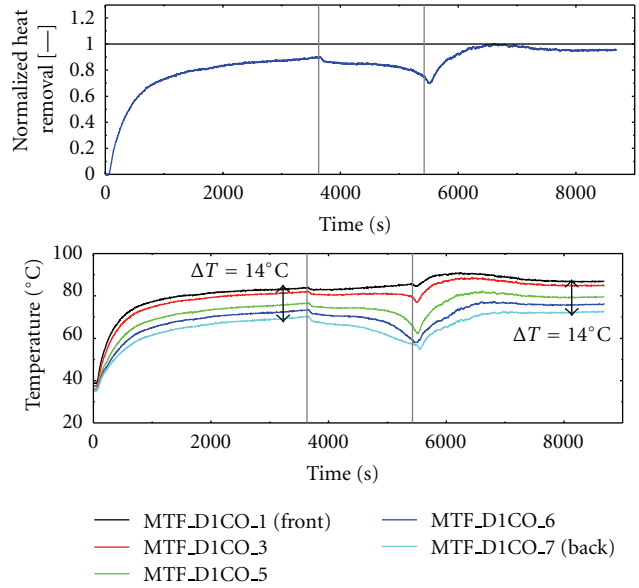

Figure 24: Normalized heat removal and water outlet temperature of the subchannels for experiment ST4_4.

4.4.1. Cooler Performance. The cooler performance is discussed in terms of heat removal and outlet cooling water temperatures of the subchannels in Figure 24.

In Phase I, the nondimensional heat removal increases continuously to 0.9. In Phase II, it decreases to ≈0.7. This deterioration of the heat removal is much less compared with experiment ST4_2 (to ≈0.2 in Phase II). Additionally, the recovery occurs later after the beginning of Phase III. At the end of ST4_4, the heat removal reaches an asymptotic value of ≈0.95.

From another point of view, the temperature gradient between the front rows (MTF_D1CO_1) and the back row (MTF_D1CO_7) of the cooling array remains almost constant with ≈14°C. Only a slight increase was observed in Phase II which reaches a maximum of ≈30°C at the beginning of Phase III. Almost the entire cooling tube array seems

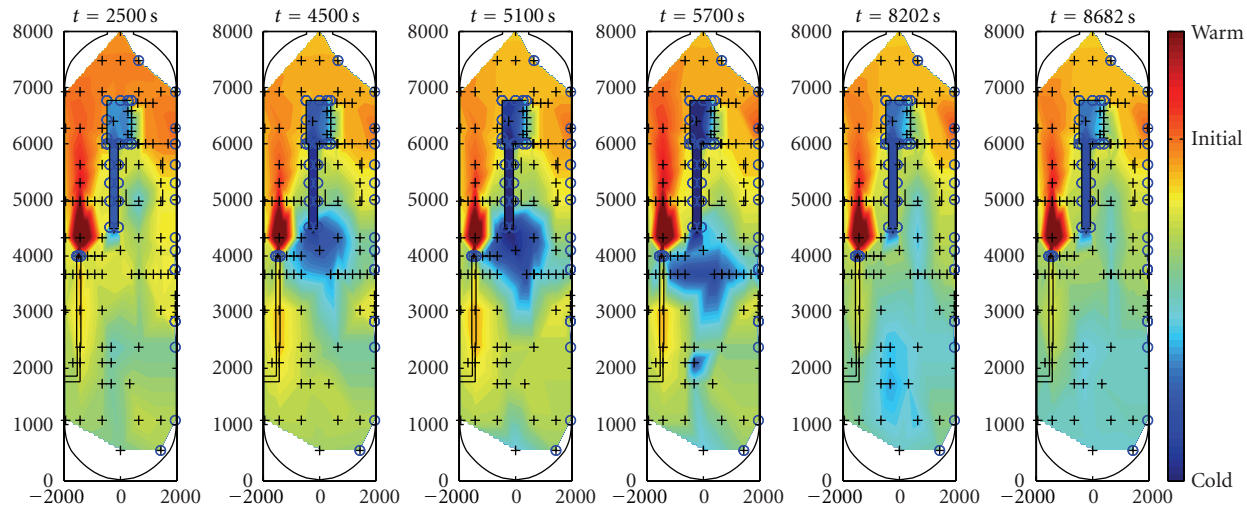

Figure 25: Temperature contour maps in Vessel 1 for experiment ST4_4 for different instances in time.

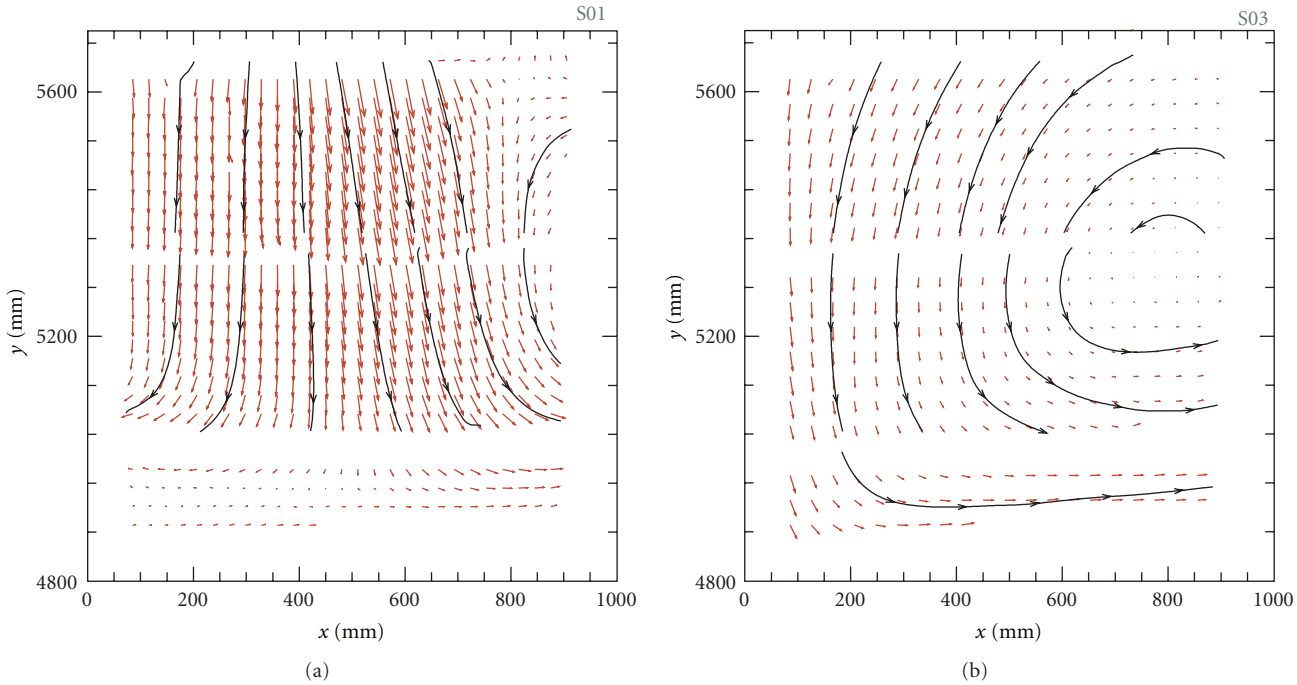

Figure 26: Selected mean velocity fields at position B for ST4_4 for (a) 1254 s < t < 1459 s and (b) 6456 s < t < 6661 s.

to contribute to the condensation process in contrast to ST4_2, where only the first few rows were effectively working during the end of Phases II and III, Figure 7 versus Figure 24. The heat removal of the cooler is much more homogeneously distributed across the single cooler rods for ST4_4 than for ST4_2. This suggests a more homogeneous gas mixture flowing through the cooler for ST4_4.

4.4.2. Gas Transport in Vessel 1. The gas transport in Vessel 1 is discussed in terms of temperature and velocity fields in this section.

During Phase I (pure steam injection), the hot steam (orange color) is flowing to the top of Vessel 1, Figure 25 t = 2500 s. In contrast to ST4_2 where the rich-to-poor steam mixture interface remained above the cooler, the steam-rich mixture now surrounds the cooler right from the beginning of the injection phases. Therefore, steam is expected to enter through *most* of the height of the cooler open side. *Most* is emphasized since some outflow was also observed from the cooler open side. It is depicted in the temperature contour maps with colder zones located below the cooler at $y \approx$ 5000 mm on the right side of the duct, Figure 25, t = 2500 s. This observation is confirmed by the mean velocity field recorded with the PIV system ($t \approx$ 1350 s) right below the cooler, Figure 26(a). For the position of the FOV, see Figure 5. We find an outflow from the cooler to the bottom of Vessel 1.

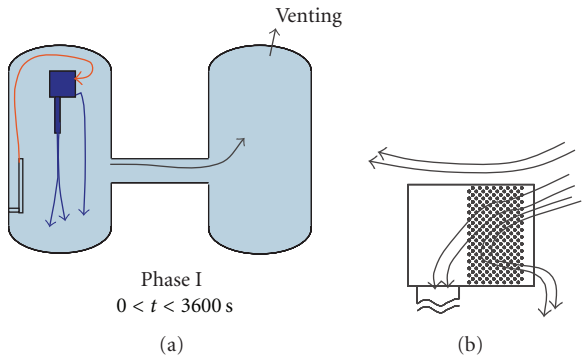

Figure 27: Suggested flow pattern for $0 < t < 3600$ s.

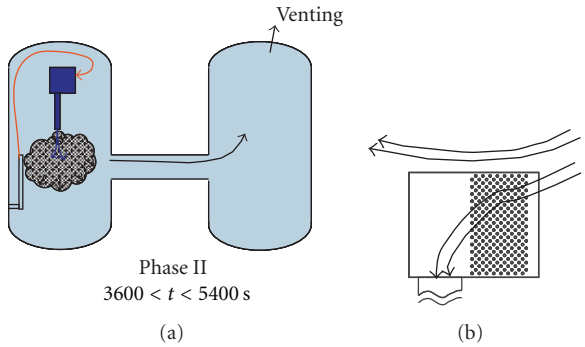

Figure 28: Suggested flow pattern for $3600 < t < 5400$ s.

Still during Phase II, we monitor a flow through the duct as suggested by the cold outlet temperature. The cold gas mixture leaving from both the duct and the open side of the cooler falls to the lower part of Vessel 1 as suggested by the temperature measured around $y \approx 1000$ mm, Figure 25, $t = 2500$ s.

In Phase II, the flow through the cooler duct enhances, Figure 25, $t = 4500$ s, and $t = 5100$ s. The presence of helium in the cold exhausted mixture flowing through the duct results in a density decrease and the cold gas mixture accumulates below the duct exit at intermediate level, $3500 < y < 4500$ mm.

During Phase III the helium content of the duct outflow gas mixture decreases and consequently its density increases, Figure 25 $t = 5700$ s. The cold gas mixture fills the lower part of Vessel 1, $t = 8202$ s such that the entire lower part becomes colder at the end of Phase III, Figure 25, $t = 8202$ s.

The mean velocity field recorded at $6456 < t < 6661$ s depicts a strong natural circulation loop on the right side of the cooler duct which is caused by the temperature difference between the cold duct and the surrounding warm gas, Figure 26(b). This observation confirms the absence of flow from the open side of the cooler at that time.

4.4.3. Synthesis Discussion ST4_4. The flow patterns that were deduced from the results discussed previously are presented in this section.

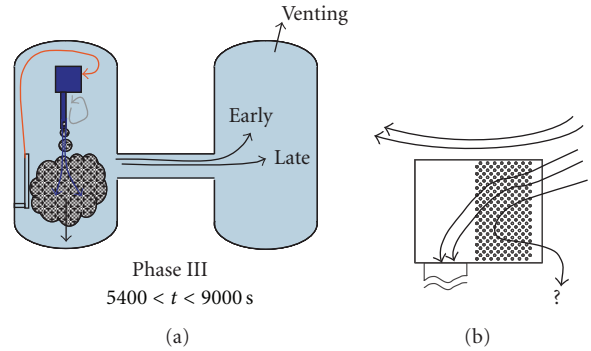

Figure 29: Suggested flow pattern for $5400 < t < 9000$ s.

During Phase I of experiment ST4_4, the injected steam accumulates at the top of Vessel 1, Figure 27(a). The cooler is immersed in the steam rich layer which enters the cooler through almost the entire open side. Gas leaves the cooler through the duct and the bottom part of the cooler open side and drops to the bottom of Vessel 1. Within the cooler, the exact flow patterns were not clearly observed and one can just assume that part of the flow goes through the array and part deflects from this path to leave through the open side, Figure 27(b). During Phase II, the outlet flow through the cooler open side is stopped.

The cold gas mixture which contains helium leaves continuously through the duct which contrasts the findings for the M-configuration. Accordingly, the cooler performance degradation is much weaker compared with the other experiments. Because of a lighter density, the mixture leaving the duct stays at an intermediate level within Vessel 1. The flow enters the cooler from the bottom of the open side, as suggested by the interruption of the outflow at this location, Figure 28(b). In Phase III, the density of the duct outflow increases as helium content decreases.

The outflow can reach a lower level within the heavier gas layer located in the bottom part of Vessel 1 until $t \approx 8200$ s. In the early part of Phase III, below the cooler and next to the duct, natural convection circulation was observed suggesting a quiet undisturbed flow.

Finally, for most of Phase III, the flow pattern in the cooler is similar to the one observed in Phase II. At the end of Phase III, the flow patterns within the cooler is assumed to be similar to the one of Phase I, Figure 29(b).

5. Conclusions

A series of experiments and a repetition experiment were conducted in the PANDA facility with a wall jet of different compositions interacting with an operating containment cooler located either in the middle (M-configuration) or at the top (T-configuration) of a containment vessel. The experiments were characterized by three phase injection scenario where the cooler was kept running during all the phases. In the first phase, pure steam was injected, while in the second phase, a helium-steam mixture was injected. Finally, in the third phase pure steam was injected again.

The cooler performance during the different phases of the experiment and the overall flow patterns within the vessel containing the cooler were studied for two different configurations. The middle configuration experiment was conducted with and without pressurization as well as with and without exhaust duct. The test without pressurization and with duct in the middle configuration was considered as reference test.

(i) For all configurations, the pure steam injection during Phase I leads through a transient process to an equilibrium where the heat removed by the cooler tends to balance the heat injected through the jet.

(ii) For the M-configuration without pressurization (ST4_2 and ST4_3), a strong degradation of the cooler performance was observed during the injection of a helium/steam mixture (Phase II), which was caused by an accumulation of helium rich gas mixture in the cooler housing. The helium rich gas accumulation blocked the flow through the exhaust duct when installed. Still during Phase II, the cooler performance recovers; despite the fact that the duct flow remains blocked for the rest of the test ST4_2. The recovery was associated with a continuous release of helium rich gas mixture from the cooler open side that adds to the strong density stratification on top of the vessel. In Phase III, neither the injected steam jet nor the escaping helium gas mixture plume were strong enough to break through the helium-rich layer. Instead, an erosion process is observed by which helium is successively entrained and mixed into the lower parts of Vessel 1, but not to the bottom of the vessel. For ST4_3, no additional effect of the duct absence was observed during Phases II and III with gas distribution and flow pattern almost identical to the ones observed with duct presence (ST4_2). Interestingly, the overall cooler performance for experiment ST4_3 with the blockage of the duct with a blind flange shows the same characteristics with respect to the shape and scale if one considers the complexity of the geometry and the test scenario.

(iii) We found an excellent repeatability of experiment ST4_2 highlighting the careful preparation of the experiments.

(iv) For the M-configuration, with pressurization (ST4_1), the cooler performance degradation occurs in Phase II and at the beginning of Phase III. The recovery is delayed at the beginning of Phase III when compared with ST4_2. The observed flow patterns and gas distributions were similar to experiment ST4_2. The main difference to the nonpressurized test resides in a periodic degradation of the cooler performance followed by a recovery. Each of this cycle is accompanied with an interruption of the helium release from the cooler. When the cooler performance recovers, a helium release, a pressure drop, and an inversion of the flow in the upper part of the IP were observed.

(v) During Phase III for the T-configuration (ST4_4), an accumulation of helium was also observed in the cooler casing but to a smaller extent compared to the cooler M-configuration, such that the performance degradation remained smaller. Additionally, the flow through the duct was enhanced leading to the formation of a helium rich gas mixture accumulation at the middle elevation of the vessel.

In summary, the top configuration allows for a better performance of the cooler in the presence of light noncondensable gas and a better overall mixing compared to the middle configuration.

Acknowledgments

The authors gratefully acknowledge the support of all of the countries and international organizations participating in the OECD/SETH-2 project as well as the members of the Management Board and the Program Review Group of the SETH-2 projects. In particular, they would like to thank Robert Zboray, Nejdet Erkan, Max Fehlmann, and Chantal Wellauer for their engaged support in conducting these experiments.

References

[1] M. Houkema, N. B. Siccama, J. A. Lycklama à Nijeholt, and E. M. J. Komen, "Validation of the CFX4 CFD code for containment thermal-hydraulics," *Nuclear Engineering and Design*, vol. 238, no. 3, pp. 590–599, 2008.

[2] A. Epiney, K. Mikityuk, and R. Chawla, "Heavy-gas injection in the generation IV gas-cooled fast reactor for improved decay heat removal under depressurized conditions," *Nuclear Engineering and Design*, vol. 240, no. 10, pp. 3115–3125, 2010.

[3] M. Andreani, K. Haller, M. Heitsch et al., "A benchmark exercise on the use of CFD codes for containment issues using best practice guidelines: a computational challenge," *Nuclear Engineering and Design*, vol. 238, no. 3, pp. 502–513, 2008.

[4] G. Yadigaroglu, M. Andreani, J. Dreier, and P. Coddington, "Trends and needs in experimentation and numerical simulation for LWR safety," *Nuclear Engineering and Design*, vol. 221, no. 1–3, pp. 205–223, 2003.

[5] D. Paladino and J. Dreier, "PANDA: a multipurpose integral test facility for LWR safety investigations," *Science and Technology of Nuclear Installations*, vol. 2012, Article ID 239319, 9 pages, 2012.

[6] O. Auban, R. Zboray, and D. Paladino, "Investigation of large-scale gas mixing and stratification phenomena related to LWR containment studies in the PANDA facility," *Nuclear Engineering and Design*, vol. 237, no. 4, pp. 409–419, 2007.

[7] D. Paladino, R. Zboray, and O. Auban, "The panda tests 9 and 9bis investigating gas mixing and stratification triggered by low momentum plumes," *Nuclear Engineering and Design*, vol. 240, no. 5, pp. 1262–1270, 2010.

[8] D. Paladino, R. Zboray, P. Benz, and M. Andreani, "Three-gas mixture plume inducing mixing and stratification in a multi-compartment containment," *Nuclear Engineering and Design*, vol. 240, no. 2, pp. 210–220, 2010.

[9] R. Zboray and D. Paladino, "Experiments on basic thermal-hydraulic phenomena relevant for LWR containments: gas

mixing and transport induced by buoyant jets in a multi-compartment geometry," *Nuclear Engineering and Design*, vol. 240, no. 10, pp. 3158–3169, 2010.

[10] D. Paladino, R. Zboray, M. Andreani, and J. Dreier, "Flow transport and mixing induced by horizontal jets impinging on a vertical wall of the multi-compartment PANDA facility," *Nuclear Engineering and Design*, vol. 240, no. 8, pp. 2054–2065, 2010.

[11] P. Royl, J.-R. Travis, W. Breitung, J. Kim, and B. K. Sang, "GASFLOW validation with PANDA tests from the OECD SETH benchmark covering steam/air and steam/helium/air mixtures," *Science and Technology of Nuclear Installations*, vol. 2009, Article ID 759878, 13 pages, 2009.

[12] M. Andreani, D. Paladino, and T. George, "Simulation of basic gas mixing tests with condensation in the PANDA facility using the GOTHIC code," *Nuclear Engineering and Design*, vol. 240, no. 6, pp. 1528–1547, 2010.

[13] M. Andreani and D. Paladino, "Simulation of gas mixing and transport in a multi-compartment geometry using the GOTHIC containment code and relatively coarse meshes," *Nuclear Engineering and Design*, vol. 240, no. 6, pp. 1506–1527, 2010.

[14] E. Studer, F. Dabbene, J.-P. Magnaud, L. Blumenfeld, J. Quillico, and H. Paillere, "On the use of the MISTRA coupled effect test facility for the validation of containment thermal hydraulics codes," in *Proceedings of the 10th International Topical Meeting on Nuclear Thermal-Hydraulics (NURETH-10 '03)*, Seoul, Korea, October 2003.

[15] I. Tkatschenko, H. Studer, and E. Paillère, "Status of the MISTRA programme for the validation of containment thermal-hydraulics codes," in *Proceedings of the 11th International Topical Meeting on Nuclear Thermal-Hydraulics (NURETH-11 '05)*, American Nuclear Society, Pittsburgh, Pa, USA, October 2005.

[16] R. Kapulla, G. Mignot, D. Paladino, N. Erkan, and R. Zboray, "Thermal hydraulic phenomena caused by the interaction of steam and steam-helium mixture wall jets with a containment cooler," in *Proceedings of the International Congress on Advances in Nuclear Power Plants (ICAPP '11)*, Paper 11093, Nice, France, May 2011.

[17] R. Kapulla, D. Paladino, G. Mignot, R. Zboray, and S. Gupta, "Break-up of gas stratification in LWR containment induced by negatively buoyant jets and plumes," in *Proceedings of the 17th International Conference on Nuclear Engineering (ICONE-17 '09)*, vol. 2 of *Proceedings of ASME*, pp. 657–666, Brussels, Belgium, July 2009.

[18] G. Mignot, R. Kapulla, R. Zboray, N. Erkan, and D. Paladino, "Parametric study of containment gas stratification break-up by vertical fluid release," in *Proceedings of the 13th International Topical Meeting on Nuclear Reactor Thermal Hydraulics (NURETH-13 '09)*, Paper NURETH13-1087, Kanazawa City, Japan, September/October 2009.

[19] R. Zboray, D. Paladino, G. Mignot, R. Kapulla, N. Erkan, and M. Andreani, "Mixing of density stratified containment atmosphere by horizontal jet release," in *Nuclear Energy for New Europe*, paper 403, Bled, Slovenia, September 2009.

[20] M. Andreani, R. Kapulla, and R. Zboray, "Gas stratification break-up by a vertical jet: simulations using the GOTHIC code," *Nuclear Engineering and Design*. In press.

[21] D. Paladino, G. Mignot, N. Erkan, R. Zboray, R. Kapulla, and M. Andreani, "Three gas mixture distribution in two large compartments after sudden opening of interconnecting line," in *Proceedings of the 14th International Topical Meeting on Nuclear Reactor Thermalhydraulics (NURETH-14 '11)*, NURETH-14-90, Ontario, Canada, September 2011.

[22] N. Erkan, R. Kapulla, G. Mignot, R. Zboray, and D. Paladino, "Experimental investigation of spray induced gas stratification break-up and mixing in two interconnected vessels," *Nuclear Engineering and Design*, vol. 241, no. 9, pp. 3935–3944, 2011.

[23] G. Mignot, R. Kapulla, N. Erkan, R. Zboray, and D. Paladino, "Containment cooler performance in the presence of light non condendable gas with cooler location as a primary parameter," in *Proceedings of the 14th International Topical Meeting on Nuclear Reactor Thermalhydraulics (NURETH-14 '11)*, Paper NURETH14-239, Ontario, Canada, September 2011.

[24] OECD/CSNI, "OECD/THAI project, hydrogen and fission product issues relevant for containment safety assessment under severe accident conditions," 2010.

[25] H. Nagasaka, T. Tobimatsu, M. Tahara, S. Yokobori, and M. Akinaga, "System transient tests with a BWR dry well cooler used as a countermeasure in severe accidents," *Transactions of the Japan Atomic Energy Society*, vol. 2, no. 3, pp. 240–250, 2003.

[26] S. Yokobori, T. Tobimatsu, M. Akinaga, M. Fukusawa, and H. Nagasaka, "Containment vessel cooling test by bwr drywell cooler under severe accident conditions," *Transactions of the Japan Atomic Energy Society*, vol. 2, no. 3, pp. 230–239, 2003.

[27] ERCOSAM, Containment thermal-hydraulics of current and future LWRs for severe accident management (ERCOSAM),. SP5-Euratom, Collaborative Project, Small or medium-scale focused research project, FP7-Fission-2009, Grant Agreement No 249691, 26.10.2010.

[28] OECD-NEA, Agreement on the OECD-NEA SETH-2 project to resolve key computational issues for the simulation of thermal-hydraulic conditions in water reactor containments, 7 2007.

[29] M. Raffel, C. Willert, and J. Kompenhans, *Particle Image Velocimetry*, Springer, New York, NY, USA, 1998.

[30] M. Ritterath, P. Voser, W. Dietze, H. M. Prasser, and D. Paladino, "Robust thermal flow sensor for a containment test facility," in *Proceedings of the IEEE Sensors Conference (SENSORS '09)*, pp. 1419–1422, Christchurch, New Zealand, October 2009.

Hindawi Publishing Corporation
Science and Technology of Nuclear Installations
Volume 2012, Article ID 686945, 12 pages
doi:10.1155/2012/686945

Research Article

The European Research on Severe Accidents in Generation-II and -III Nuclear Power Plants

Jean-Pierre Van Dorsselaere,[1] Ari Auvinen,[2] David Beraha,[3] Patrick Chatelard,[1] Christophe Journeau,[4] Ivo Kljenak,[5] Alexei Miassoedov,[6] Sandro Paci,[7] Th. Walter Tromm,[6] and Roland Zeyen[8]

[1] *Institut de Radioprotection et de Sûreté Nucléaire (IRSN), Cadarache, BP3 13115, Saint-Paul-lez-Durance, Cedex, France*
[2] *VTT Technical Research Centre, Vuorimiehentie 5, Espoo, Finland*
[3] *Gesellschaft für Anlagen- und Reacktorsicherheit mbH (GRS), Forschungsinstitute, 85748 Garching, Germany*
[4] *Commissariat à l'Energie Atomique et aux Energies Alternatives (CEA), DEN/STRI/LMA, 13108 Saint-Paul-lez-Durance, Cedex, France*
[5] *Jozef Stefan Institute (JSI), Jamova cesta 39, Sl-1000, Ljubljana, Slovenia*
[6] *Karlsruhe Institute of Technology (KIT), Hermann-von-Helmholtz-Platz 1, 76344 Eggenstein-Leopoldshafen, Germany*
[7] *Dipartimento di Ingegneria Meccanica, Università di Pisa, Via Diotisalvi 2, 56126, Pisa, Italy*
[8] *European Commission Joint Research Centre, Institute for Energy and Transport (JRC/IET), Westerduinweg 3, P.O. Box 2, 1755 ZG Petten, The Netherlands*

Correspondence should be addressed to Jean-Pierre Van Dorsselaere, jean-pierre.van-dorsselaere@irsn.fr

Received 23 December 2011; Accepted 10 February 2012

Academic Editor: Gilberto Espinosa-Paredes

Forty-three organisations from 22 countries network their capacities of research in SARNET (Severe Accident Research NETwork of excellence) to resolve the most important remaining uncertainties and safety issues on severe accidents in existing and future water-cooled nuclear power plants (NPP). After a first project in the 6th Framework Programme (FP6) of the European Commission, the SARNET2 project, coordinated by IRSN, started in April 2009 for 4 years in the FP7 frame. After 2,5 years, some main outcomes of joint research (modelling and experiments) by the network members on the highest priority issues are presented: in-vessel degraded core coolability, molten-corium-concrete-interaction, containment phenomena (water spray, hydrogen combustion…), source term issues (mainly iodine behaviour). The ASTEC integral computer code, jointly developed by IRSN and GRS to predict the NPP SA behaviour, capitalizes in terms of models the knowledge produced in the network: a few validation results are presented. For dissemination of knowledge, an educational 1-week course was organized for young researchers or students in January 2011, and a two-day course is planned mid-2012 for senior staff. Mobility of young researchers or students between the European partners is being promoted. The ERMSAR conference is becoming the major worldwide conference on SA research.

1. Introduction

Despite the accident prevention measures adopted in nuclear power plants (NPPs), some accident scenarios, in very low probability circumstances, may result in severe accidents (SA) with core melting and plant damage and to dispersal of radioactive materials into the environment, thus constituting a hazard for the public health and for the environment. This was unfortunately underlined by the accidents in the Japanese Fukushima-Daiichi NPPs in March 2011. After 4 years in the 6th Framework Programme (FP6) of the European Commission, the SARNET (Severe Accident Research NETwork of Excellence) network (http://www.sar-net.eu), coordinated by the French Institut de Radioprotection et de Sûreté Nucléaire (IRSN), is continuing to operate in FP7 [1] for 4 years since April 2009. The objective is to enhance the coordination of the national efforts in order to optimise the use of the available expertise and the experimental facilities

for resolving the remaining issues for enhancing the safety of existing and future NPPs.

The work focuses on the highest priority safety issues still to be resolved [2], including the realization of experiments and the assessment of the ASTEC integral computer code [3], jointly developed by IRSN and the German Gesellschaft für Anlagen und Reaktorsicherheit mbH (GRS) to simulate the NPP behaviour during a postulated SA. The present paper shows some R&D selected results at midterm of the project.

2. THE Sarent Network

The network gathers 43 partners from 22 countries in Europe, Canada, Korea, United States, and India (see Table 1).

A Steering Committee of 10 members is in charge of strategy and decisions, advised by an Advisory Committee, composed of external end-user organisations (utilities or safety authorities). A General Assembly, composed of one representative of each SARNET partner, plus the EC representative, is called periodically for information and consultation on the progress of the activities, the work orientations and the Steering Committee decisions. A Management Team, composed of the network coordinator and of the work-package leaders, is entrusted with the day-to-day management of the network. The Joint Programme of Activities (JPA) is broken down into 8 work-packages pertaining to the three following types of activities:

(i) integrating activities, aiming at strengthening links between the partner organizations,

(ii) spreading of excellence,

(iii) joint research activities.

In the SARNET FP6 project, an approach based on the Phenomena Identification and Ranking Table (PIRT) was carried to rank the priority of R&D issues. The following issues have been selected as highest priority: in-vessel corium and debris coolability, molten corium concrete interaction (MCCI), fuel-coolant interaction, hydrogen mixing and combustion in containment, impact of oxidising conditions on source term, and iodine chemistry.

A review and update of these priorities will be performed in 2012 by a group of ad-hoc experts. Based on the analysis of R&D progress since 4 or 5 years and on results from Level 2 Probabilistic Safety Assessment (PSA2) studies, it may reorient priorities and identify potential new experimental and theoretical programmes to address these issues. It should also account for the impact of the Fukushima-Daiichi accidents.

As an important integrating activity, the ASTEC integral computer code, jointly developed by IRSN and GRS to predict NPP behaviour during a postulated SA, plays a key role in the network by capitalizing the SA knowledge through new physical models. Besides, efforts are currently underway for the extension of its applicability to BWR and CANDU NPP types (see Section 7.1).

3. Corium and Debris Coolability

The major objective of the work on corium and debris coolability is to reduce or possibly solve the remaining uncertainties on the ability of cooling structures and materials during SA, either in the core or in the vessel lower head or in the reactor cavity, in order to limit the progression of the accident. The work comprises experimental and modelling activities, with strong crosscoordination between tasks. Substantial knowledge now exists concerning cooling of a large intact and rod-like geometry. A large part of the effort is being directed now on cooling of a debris bed, in order to demonstrate effective cooling modes and to establish cooling rates and limits.

The analysis of data on degraded core reflooding indicates that major gaps in knowledge till remain in the areas of debris and molten pool. To address these issues, POMECO (KTH) [4] and DEBRIS (IKE) [5] analytical experiments with debris beds are performed to support the quantification of basic laws and coolability behaviour. Top and bottom flooding (quenching) of hot debris (up to 900°C) can be investigated in the DEBRIS facility, also at elevated pressures. New POMECO test facilities are constructed to perform isothermal and boiling two-phase flow experiments with better instrumentation and flexibility to accommodate various prototypical conditions. POMECO aims at analyses under boil-off conditions with emphasis on basic laws and specific 2D effects (downcomers), more oriented at lower head or exvessel situations but also addressing basically the situation in the degrading core. Both DEBRIS and POMECO deal with irregular particles aiming at representing realistic debris.

IRSN is planning larger size quenching experiments [6, 7] with 2D porous media, which allows a multidimensional progression of the quench front in the PEARL programme. Preliminary reflooding experiments were carried in the PRELUDE facility, involving a debris bed of 4 mm particles inside a 110 mm external diameter and 100 mm height test section, at atmospheric pressure. Parameters investigated were

(i) inlet water velocity between 1 and 8 mm/s (4 to 30 $m^3/h/m^2$), in the range foreseen in PEARL test matrix,

(ii) power at 300 W/kg (maintained or not during the reflooding phase),

(iii) initial temperature before reflooding at 420 K, 500 K, 600 K and 1000 K.

Additional PRELUDE experiments were performed to evaluate the power distribution inside a larger debris bed diameter (from 110 to 280 mm) using stainless amagnetic steel particles, 2 and 4 mm in diameter, up to 300 W/kg. This campaign ended with two experiments with a heating sequence of a debris bed (test section diameter 180 mm, particles 4 mm) up to 1000 K at about 140 and 200 W/kg before the water injection. Those experiments were well instrumented with lot of thermocouples inside the debris bed (different radial and axial positions) to follow the water front propagation along time (Figure 1, where thermocouples measurements at different axial levels are shown).

Table 1: List of SARENT partners.

Partner	Short name	Country
Institut de Radioprotection et de Sûreté Nucléaire	IRSN	France
KFKI Atomic Energy Research Institute	AEKI	Hungary
AREVA NP GmbH	AREVA GmbH	Germany
AREVA NP SAS	AREVA NP SAS	France
Budapest University of Technology and Economics	BME	Hungary
Commissariat à l'Energie Atomique et aux Energies Allternatives	CEA	France
Ricerca Sul Sistema Energetico—RSE SpA	RSE	Italy
Chalmers tekniska högskola AB	CHALMERS	Sweden
Centro de Investigaciones Energeticas MedioAmbientales y Tecnologicas	CIEMAT	Spain
National Centre for Scientific Research "DEMOKRITOS"	DEMOKRITOS	Greece
Electricité de France SA	EDF	France
Energy Institute JSC Sofia	EI	Bulgaria
Agenzia Nazionale per le Nuove Tecnologie, l'Energia e lo Sviluppo Economico Sostenibile	ENEA	Italy
Forschungszentrum Juelich GmbH	JÜLICH	Germany
Karlsruher Institut fuer Technologie	KIT	Germany
Gesellschaft für Anlagen—und Reaktorsicherheit mbH	GRS	Germany
National Autonomous Company for Nuclear Activities Nuclear Research Subsidiary Pitesti	INR	Romania
Institute for Nuclear Research and Nuclear Energy	INRNE	Bulgaria
Inzinierska Vypoctova Spolocnost Trnava s.r.o.	IVS	Slovakia
Jozef Stefan Institute	JSI	Slovenia
Kungl Tekniska Högskolan	KTH	Sweden
Lithuanian Energy Institute	LEI	Lithuania
National Nuclear Laboratory	NNL	UK
Nuclear Research & Consultancy Group v.o.f.	NRG	Netherlands
Paul Scherrer Institut	PSI	Switzerland
Ruhr-Universität Bochum	RUB-LEE	Germany
Tractebel Engineering SA	TRACTEBEL	Belgium
Thermodata	THERMODATA	France
Technical University of Sofia	TUS	Bulgaria
Urad Jadroveho Dozoru Slovenskej Republiky	UJD SR	Slovakia
Ustav Jaderneho Vyzkumu Rez a.s.	UJV	Czech Rep.
University of Newcastle upon Tyne	UNEW	UK
Dipartimento di Ingegneria Meccanica, Nucleare e della Produzione—Università di Pisa	UNIPI	Italy
Universität Stuttgart	IKE	Germany
NUBIKI Nuclear Safety Research Institute	NUBIKI	Hungary
VTT Technical Research Centre of Finland	VTT	Finland
VUJE Trnava, a.s.–Inzinierska, Projektova a Vyskumna Organizacia	VUJE	Slovakia
Commission of the European Communities—Joint Research Centres	JRCs	EU
Atomic Energy Canada Limited	AECL	Canada
Korea Atomic Energy Research Institute	KAERI	Korea
United States Nuclear Regulatory Commission	USNRC	USA
Korea Institute of Nuclear Safety	KINS	Korea
Bhabha Atomic Research Centre	BARC	India

The measurements of the injected water flow, as well as the steam flow rate generated during reflooding, were accurately obtained by mean of adapted sensors to reach a very good water/steam balance.

The PEARL programme will simulate the reflooding of a debris bed, characteristic of an in-core debris bed, surrounded by a more permeable medium (such as intact structures and rods). PEARL goes beyond DEBRIS and PRELUDE quenching analyses by the larger facility size and thus the possibility to perform extended analyses on multidimensional effects. It will also provide a general basis for the assessment of the overall behaviour described in the codes (both in- and exvessel phenomena).

Modelling of the coolability of porous media has indicated the importance of multidimensional effects. Different quenching analyses by the partners showed agreement concerning a strongly favoured coolability by inflow of water from lateral water-filled regions of the core with higher porosities. Since lateral water inflow, especially via lower regions, strongly improves coolability, in general the coolability is much better than concluded from 1D analyses with top flooding, and 2D/3D computer codes including adequate descriptions of constitutive laws are required to analyse the real coolability situation [8]. The mechanistic codes ATHLET-CD/WABE (GRS, IKE) and ICARE/CATHARE (IRSN) codes are being validated on the above-quenching experiments. This should help to improve their models with the ultimate objective to propose an adequate model for the ASTEC integral code.

Also, it is necessary to improve the modelling of formation of porous media in the core. Alternatively, for assumed configurations, degradation and melting, pool formation and melt release must be analysed to reveal major trends taking into account water supply (cooling versus melt pool formation).

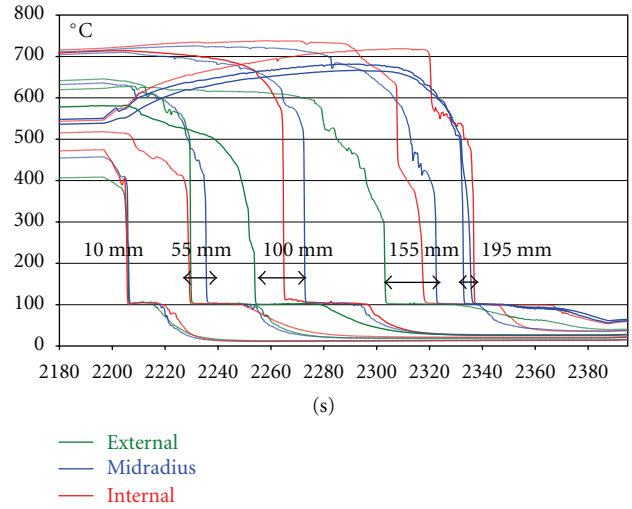

Figure 1: PRELUDE measurements of the water front evolution along time.

Figure 2: Pictures of VULCANO VB-ES-U2 test during corium pouring phase. Left: Corium pouring from the plasma arc rotating furnace (upper right) to the concrete cavity (lower left). Right: Zoom on the concrete hemicylindrical cavity.

4. Molten Corium Concrete Interaction

MCCI can eventually lead to containment basemat melt-through and thus has been considered as high priority SA research topic. A significant programme of joint activities is organized within SARNET on this issue with the participation of 17 organizations.

4.1. 2D Ablation Profiles. Contrary to what was previously expected, the 2D MCCI experiments performed at Argonne National Laboratory [9] and at CEA Cadarache [10, 11] have shown that, except for limestone-rich concretes, the concrete ablation is anisotropic: lateral ablation is significantly larger than axial ablation. Anisotropic ablation has also been observed in the under-reactor room of the Chernobyl-4 reactor [12], where a marked lateral ablation of the (silica-rich) granitic concrete has been observed. So the experimental observations of ablation anisotropy should not be attributed solely to scale or heating technique artefacts and must be understood in order to achieve predictive modelling of concrete ablation during a postulated SA.

To contribute to the understanding of this phenomenon, CEA has launched, with SARNET and national supports, a series of Separate-Effect-Tests in the VULCANO facility. Two experiments have been performed (Figure 2) with respectively a concrete made of decarbonated limestone (VB-ES-U2), which presented anisotropic ablation and with a siliceous mortar (i.e., a "concrete" without the aggregates above 2 mm) which is still awaiting post test examinations (VB-ES-U3).

The VB-ES-U2 experiment clearly showed that neither the molten concrete physical properties nor the physico-chemical properties cause the transition from anisotropy to isotropy, since two concretes having the same melt composition (after decarbonation) present very different ablation patterns. It is also very unlikely that the gas superficial velocity is the cause of isotropy, since these parameters were close in the VULCANO experiments with limestone and clinker concretes while the ablation patterns were different. Three remaining effects need to be considered: effect of large unmelted gravel, effect of concrete shrinkage, effect of the gas superficial momentum (or mass flow rate). The analysis of the latest experiment and of one or two further experiments should allow narrowing the investigations on the origin

of ablation anisotropy. Temperatures in the pool, in the concrete and on the pool surface are monitored throughout the experiment to be compared with code calculations.

Since MCCI thermalhydraulics is strongly coupled with thermochemistry, some analytical experiments are conducted to determine melt liquidus composition at UJV and ITU. They contribute, with the assessment of all the material analyses, to the validation or improvement of the NUCLEA thermodynamic database [13]. The CLARA facility in CEA provides new thermalhydraulic data on convection with gas sparging in the bottom and on the sides of the pool. These experiments are important to derive empirical models for prediction of MCCI ablation profiles.

In parallel, a benchmark exercise between several computer codes is under way on 2 earlier VULCANO experiments.

4.2. Effect of the Metallic Phase. The effect of the metallic phase must be considered, especially because models indicate that a heavy metallic layer would concentrate the heat fluxes towards the bottom. The MOCKA large scale (~1 ton of corium) facility is under construction at KIT to study the effect of the metallic phase with high temperature simulant materials. Experiments with prototypic materials (oxidic corium and steel) were performed in the VULCANO facility [14] at the 50 kg scale and in the SICOPS facility (in AREVA-NP GmbH) [15] at a smaller scale. Both experiments showed a significant metal oxidation. The next planned experiments will last shorter so that a sufficient volume of metal remains in order to analyze its spatial repartition during Posttest examinations. Interpretation work of all available metal-oxide tests using both stimulant and prototypical materials has been performed, which led to review the metal/oxide stratification criterion. Reactor MCCI studies have been performed with the ASTEC code using this more realistic criterion: it led to the melt-trough of a 4 m thick basemat in more than 5 days and only 1 day for an unrealistic fixed configuration with the metallic phase under the oxide one. Further experimental and theoretical investigations are necessary, especially for cases with siliceous concrete that will promote stratification due to the low gas production of its ablation. They will be devoted to the metal oxidation kinetics but also to determine the effects of a stratified configuration. For this last issue, information will be obtained in particular from Direct Numerical Simulation of heat transfer due to sparging of gas bubbles through the interface between a heavy metallic layer and a lighter heated oxide layer [16]. Figure 3 shows the temperature field in an IRSN calculation.

4.3. Late Water Cooling of MCCI. Research activities are underway to assess the capability of water cooling starting after the pouring of corium in the cavity. Although CCI-6 results [17] suggest that early water flooding (i.e., at a time when the concrete molten fraction is low) has a good coolability potential that must be confirmed by further experiments, the efficiency of late top flooding seems more doubtful, especially for siliceous concretes. Bottom flooding, for example, using the COMET concept [18], is being studied as an efficient alternative to top flooding. IKE is conducting modelling and interpretation of the VULCANO COMET experiment and reactor scale calculations. The porosity formation in the melt layer and the cooling process due to the injection of water via porous concrete at bottom is calculated with the MEWA code. Figure 4 shows the status of quenching after about 300 s (melt temperature field) together with water and steam velocities.

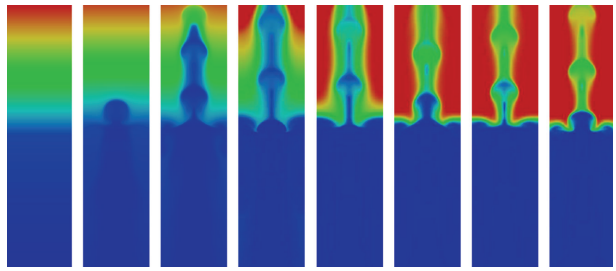

Figure 3: Direct Numerical Simulation of heat transfer induced by a bubble swarm at the metal-oxide interface.

4.4. Bringing Research to Reactor Applications. The research activities conducted with SARNET are always linked to reactor applications. For MCCI, these applications are organized around benchmarks between different computer codes. A benchmark of a generic VVER-1000 MCCI is under way. Lessons from the MCCI which took place during Chernobyl accident are also being considered.

5. Containment Issues

The considered safety issue is the threat to the containment integrity due to two types of highly energetic phenomena: steam explosion and hydrogen combustion. Several benchmarks were launched involving simulation codes (Lumped-Parameter (LP) or Computational Fluid Dynamics (CFD)) on different physical phenomena or safety systems, such as containment sprays, hydrogen combustion, steam condensation, interaction between Passive Autocatalytic Recombiners and containment atmosphere, plus a theoretical benchmark on a generic NPP containment including the most important components. Some benchmarks already achieved significant results.

5.1. Benchmark on Containment Sprays. The first part of the spray benchmark [19] consisted in simulating an elementary heat and mass transfer experiment, done in IRSN: separate uniform droplets were generated and observed in a vessel with a controlled atmosphere. For this exercise, both LP and CFD codes were used. Apart from the organizer IRSN, the following organizations participated in the benchmark: EDF, RSE, GRS, KIT, LEI, NRG, UJV, UJD SR, and UNIPI. Five droplet evaporation and four droplet condensation experiments were simulated. The comparison of code results with the vertical evolutions of the droplet temperature, droplet diameter and vertical velocity, enabled the assessment of droplet models in different codes, as the results were not

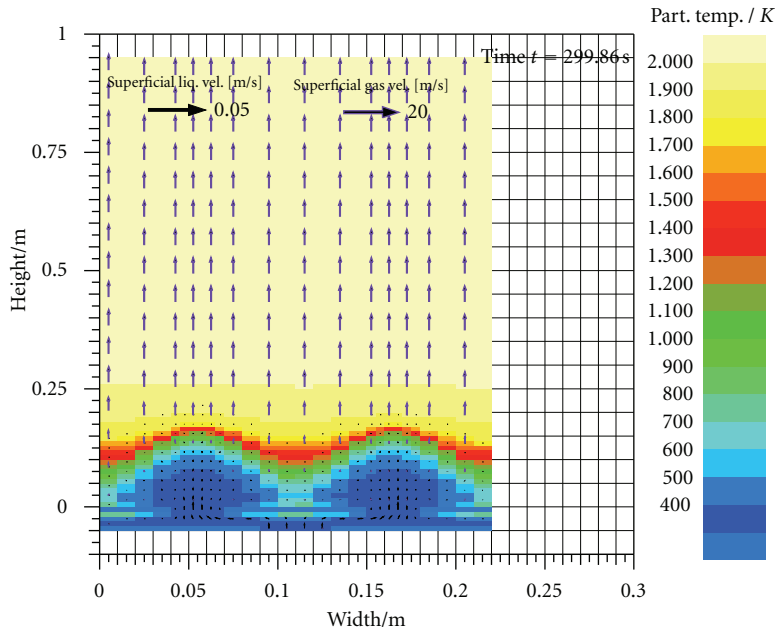

Figure 4: MEWA calculation of the velocities and temperatures in the VULCANO COMET experiment.

distorted by the influence of other simulated phenomena. In particular, it appeared that the calculated evaporation rate is mostly too high at ambient conditions.

5.2. Benchmark on Hydrogen Combustion. The benchmark on flame acceleration during hydrogen combustion [20] consists in simulating experiments performed in the ENACCEF 0,8 m^3 facility (Figure 5), located at the Centre National de la Recherche Scientifique (CNRS) in Orléans (France). The following organizations have participated in the benchmark: IRSN (organizer and joint owner of the facility), AREVA NP GmbH, GRS, KAERI, LEI, NUBIKI and RUB. Three experiments were simulated, one without obstacles in the acceleration tube and two with obstacles, with different blockage ratios. In all cases, the flame propagation was much better simulated in the later parts of the tube (in the region with obstacles and further) than in the initial part (between the ignition point and the first obstacle). The pressure increase was also mostly well calculated.

5.3. Benchmark on Steam Condensation. Although research of condensation as such does not fall in the field of severe accidents, the modelling of condensation may significantly affect the results of CFD simulations of containment atmosphere mixing and stratification. The purpose of the benchmark [21], which consists in simulating experiments that were performed in the CONAN facility (at UNIPI) with CFD codes, is to compare different existing models with the purpose to identify the most adequate ones. The following organizations have participated: UNIPI (organizer), CEA, FZ Jülich, JSI, KIT, NUBIKI, UJV and AECL. So far, experiments involving condensation during downward forced flow of a steam-air mixture near a condensing vertical plate were

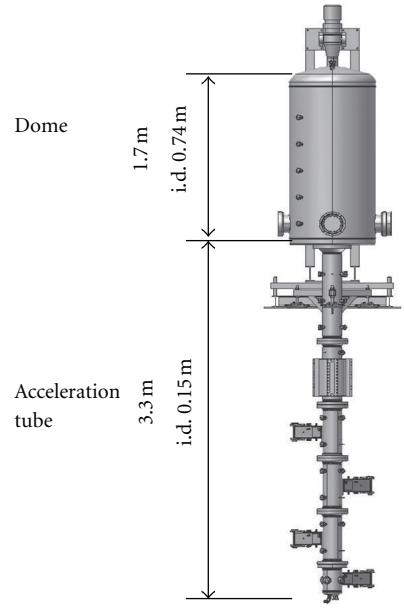

Figure 5: ENACCEF experimental facility for performing experiments on hydrogen combustion.

simulated. In general, a good agreement of measured and calculated condensation rates, heat fluxes and plate temperatures was obtained by most participants. In the next phase of the benchmark, experiments and simulations are planned to involve natural convection, which will be closer to the expected physical conditions during a severe accident.

5.4. Benchmark on Generic Containment. When comparing simulation results of severe accidents in actual NPPs,

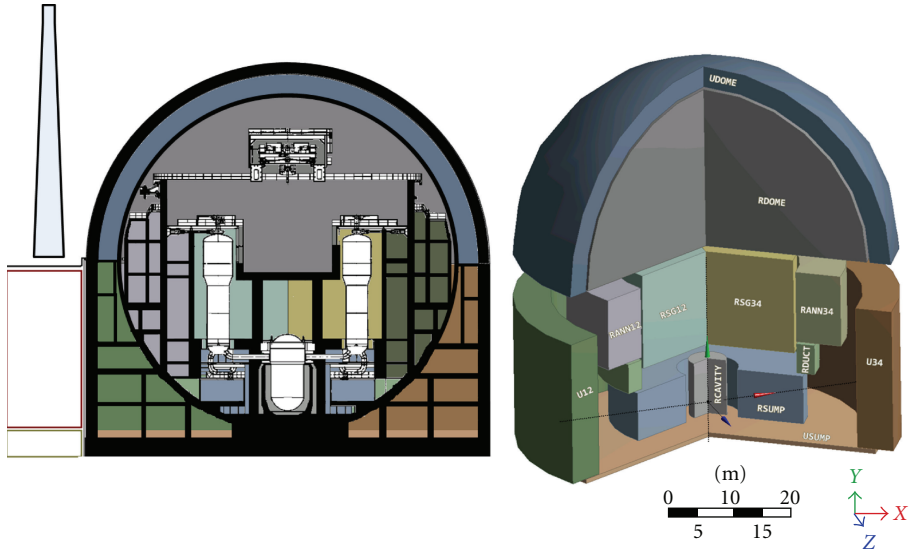

Figure 6: Schematic view of the "generic" NPP containment.

obtained by different LP codes, the differences are often distorted by different assumptions and modelling, adopted by different users. The basic idea of the benchmark on "generic" containment is to compare code results by simulating a transient in a precise and unique containment model, based on the containment of a German NPP [22] (Figure 6). Apart from the organizer FZ Jülich, the following organizations have participated in the first phase: AREVA GmbH, ENEA, RSE, JSI, GRS, IRSN, NRG, NUBIKI, RUB, TUS, UJV, UNIPI and VTT. Although most calculated results were similar, an interesting outcome of the 1st phase of the benchmark is that significant differences may still be observed, due mainly to:

(i) differences in applied thermal-hydraulic models,

(ii) prediction of different flow patterns by different codes.

6. Source Term Issues

In the source term area, collaboration has been especially active concerning iodine behaviour in the containment. Experimental and analytical studies focused on volatile iodine formation from iodine-loaded paints and possible destruction of gaseous iodine species by their reactions with air radiolysis products. Some examples of the extensive work performed are summarized here.

The EPICUR S2-6 analytical test series was launched by IRSN to validate and develop models for gaseous organic iodide formation from a painted surface loaded with iodine [20]. Iodine is assumed to be adsorbed onto a painted coupon, and then to react with the organics in the paints. In these experiments, the influence of the temperature, humidity, and iodine surfacic concentration was studied. One objective was also to study the effect of residence time in the irradiation vessel on the nature and proportions of volatile species formed and the duration of the irradiation in order to quantify the release kinetics from the coupon after 8 h of irradiation. Before the experiments the coupons were loaded with labelled molecular iodine (^{131}I) by Dushman's reaction. Then the coupons were irradiated in a vessel and the volatilised iodine species were swept to a May-Pack. The May-Pack is composed of selective filters which allow speciation between molecular and organic iodide. The iodine compounds trapped in the different filters are γ-counted on-line with NaI-probes set above each filter group.

The S2-6 series revealed two important and partly surprising facts. The fraction of iodine volatilised as organic iodide decreased when iodine loading on painted coupons increased. A 30-hour experiment also revealed that there was still release of iodine after 8 hours of irradiation, but the volatilisation was slower. IRSN and NNL have proposed a joint preliminary interpretation of the S2-6 test series based on mechanistic considerations. Mechanisms of interaction between iodine and main functions of polymeric paint molecules have been identified and ranked according to their influence in organic iodine production. Then an explanation of the influence of the most influent parameters, that is, the iodine loading, temperature and relative humidity, has been proposed in the light of those mechanisms. The development of a new ASTEC model of iodine interaction with paint is under way by determining the kinetic constants of those mechanisms.

Experimental studies on radiolytic oxidation of elemental iodine and methyl iodide were carried out in the EXSI facility by VTT and Chalmers University [23]. The aim was to verify the possible formation of iodine-containing aerosol species, when gaseous iodine is exposed to air radiolysis products. The reactions take place in a flow furnace with temperature varying from 50°C to 120°C and residence time from 2 to 7 seconds. Up to four ultra-violet C (UVC) lamps were used as a source of ionizing radiation and to produce ozone in various oxygen concentrations. Ozone was also

produced with an ozone generator. The effect of humidity on oxidation of iodine was also studied.

The aerosol particles formed were collected on plane filters, after which gaseous iodine was trapped in a NaOH-water solution. The amount of iodine in both filters and trapping bottles was analysed using an Inductively Coupled Plasma-Mass Spectrometer (ICP-MS). Particle mass flow rates, number concentrations and size distributions were measured on-line using aerosol instrumentation. Speciation of gaseous reaction products was measured also on-line with Fourier Transform Infrared Spectroscopy (FTIR). The morphology as well as the elemental composition of the particles was determined with Scanning Electron Microscope Energy Dispersive X-Ray Analysis (SEM-EDX).

It was found that the formation of aerosol particles was very rapid when ozone was present with either elemental iodine or methyl iodide. A similar increase in aerosol mass concentration was found with increasing UV radiation intensity. Regardless of the ozone generation technique, increasing reaction temperature also increased aerosol mass concentration. Particle mass concentrations measured in CH_3I experiments are presented in Figure 7 as a function of radiation intensity and temperature.

The diameter of the primary particles varied between 5–10 nm. Due to the very high number concentration, particles grew by agglomeration. Agglomerate size distribution was log-normal with number median diameter (NMD) varying between 60–120 nm. The size of the agglomerates increased and the number concentration decreased with increasing residence time. The agglomerate size also increased with iodine concentration. SEM-EDX analysis showed that particles contained iodine and oxygen. According to a literature study, the most likely iodine oxide species would be I_2O_4, I_2O_5 and I_4O_9. Depending on experimental conditions, both liquid and solid particles were observed. Iodine oxides in contact with water form hydrated species and the final product is likely to be iodic acid [24, 25].

The transport of elemental iodine through the facility was very low when ozone was present, whereas a part of methyl iodide was always detected at the outlet of the system. The presence of ozone promoted retention of iodine in the facility probably by surface reaction. Some deposited iodine evaporated later during the experiments and formed particles in the gas stream. The main gaseous reaction products of organic iodides were methanol and formaldehyde. Especially at elevated temperature other reaction products, such as formic acid and methyl formate, became important as well. The decomposition of CH_3I and subsequent formation of reaction products was much faster than what is considered in previous studies.

NNL analysed the EXSI methyl iodide experiments with the mechanistic IODAIR code. Methyl iodide decomposition in UV tests was probably due to direct photolysis and reactions with O atoms. Direct photolysis would favour production of gaseous iodine, whereas reaction with O atoms would lead to formation of iodine oxide particles. According to modelling, ozone formation was expected to be insignificant, which was confirmed by measurements. Methyl iodide decomposition in experiments with ozone feed was much higher than predicted by the model. Such result cannot be accounted for only by thermal decomposition of ozone. The test results indicate a direct reaction between methyl iodide and ozone.

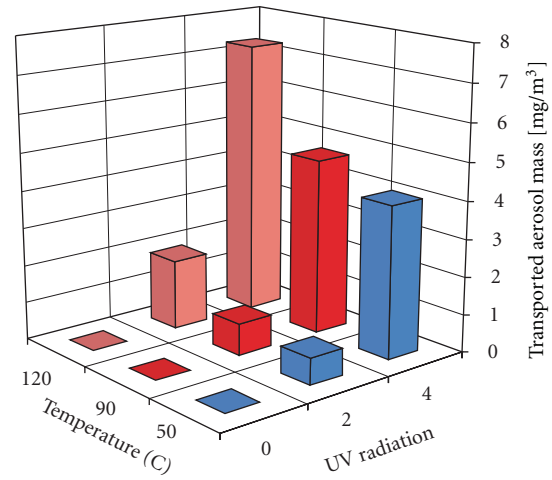

Figure 7: Particle mass concentration in CH_3I experiments as a function of radiation intensity and temperature.

To apply the results obtained with UV radiation in reactor safety, further EXSI experiments on methyl iodide oxidation are being carried out using a 20 kGy/h ^{60}Co source in Chalmers Technical University.

7. Integrating Activities

7.1. ASTEC Code Assessment and Improvements. IRSN and GRS jointly develop the ASTEC code to describe the complete evolution of a SA in a nuclear water-cooled reactor [3]. The new series of versions V2 can simulate the EPR (European Pressurised Reactor), especially its external core-catcher, and it includes the advanced core degradation models of the ICARE2 IRSN mechanistic code. Twenty-eight organizations contribute to the assessment of the successive ASTEC versions in the SARNET frame, through validation on reference experiments and through reactor applications for the most important SA scenarios in PWR, VVER and CANDU.

A first revision of the V2.0 version, released in June 2010, included mainly model improvements in the modules ICARE (about corium behaviour in the lower head), MEDICIS (about MCCI in EPR), and CESAR (about thermal-hydraulics in the primary and secondary circuits). CESAR uses 0-D components to represent the pressuriser, the vessel upper head or the steam generator (SG) cavity (separator): these volumes may contain a water level, with gas above the water level close to the saturation temperature. Two distinct zones, a lower water/steam zone and an upper gas region, have been modelled in these volumes: in both zones, different pressures (for a correct account for the hydrostatic pressure), wall temperatures (for a correct distribution of heat from walls) and gas temperatures (for a right interface/steam transfer) are now considered. A second revision of the V2.0

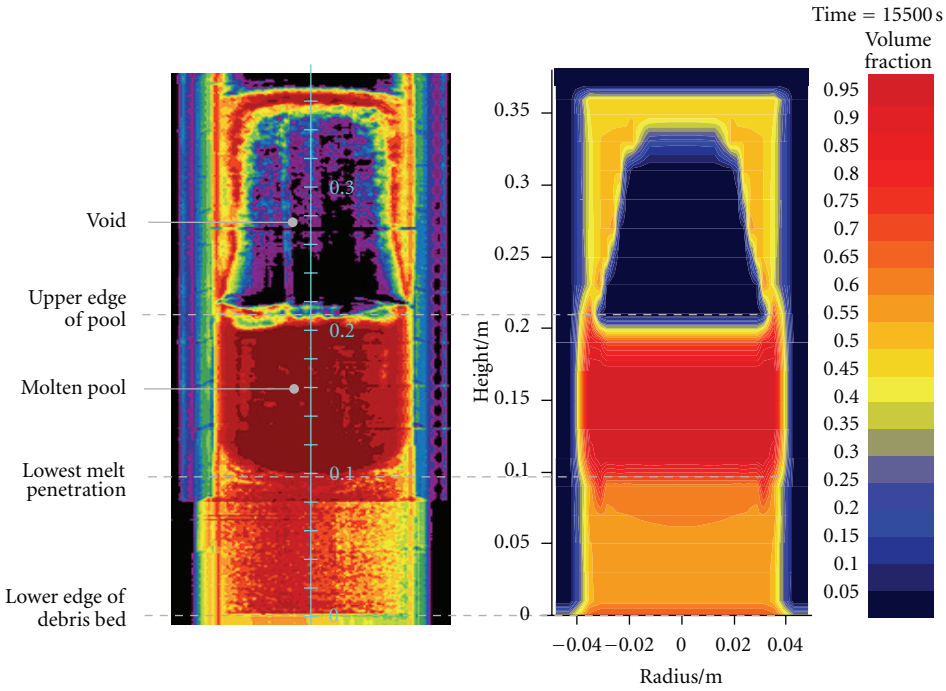

Figure 8: Comparison of Phébus FPT4 post-test radiography (left) with calculated volume fraction of material (right).

version was released in December 2011, accounting for the feedback of the maintenance efforts.

As one example of V2 validation, IKE (Germany) applied ICARE2 to the Phébus FPT4 experiment on melting of a debris bed, made of UO_2 and ZrO_2 particles of 2 to 5 mm size. The calculated temperatures are in very good agreement with the measurements, which indicates that the heat transport phenomena in the dry debris bed are well described by the chosen Imura/Yagi correlation for the effective heat conductivity and the Gunn correlation for the convective heat transfer. The final material distribution is also very well captured (Figure 8), indicating a very good behaviour of the 2D magma model. As concerns fission products, the ASTEC V2 prediction is very good for the release of volatile species while a tendency to over-predict the release of medium volatile species is observed.

As another example of V2 assessment, AREVA NP SAS (France) performed a benchmark between the ASTEC V2.0 and MAAP4.07 codes on a transient of failure of SG feed-water system in a PWR 900 MWe. It is additionally supposed here that the active emergency core cooling systems are unavailable: only passive cooling systems (hydro-accumulators) are available. Two ASTEC calculations were performed: the one named CAND using the candling 1D model of corium relocation along the rods and the one named MAGMA using the 2D corium relocation model within the core. The timing of calculated events is similar between both codes during the core degradation phase except for the vessel lower head rupture that occurs sooner with ASTEC. The corium masses in the vessel lower head are close at time of vessel rupture. Figure 9 shows the comparison of the in-vessel hydrogen cumulated release mass: though the

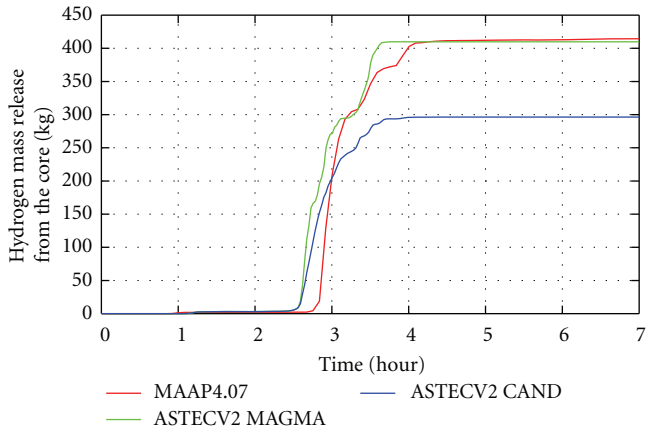

Figure 9: Comparison ASTEC-MAAP of produced in-vessel hydrogen in a reactor benchmark.

core degradation phase starts a little bit earlier with ASTEC than with MAAP, a very good agreement is obtained between both codes when using the MAGMA model in ASTEC V2. This comparison will focus in the next months on the ex-vessel phase and on the behaviour of fission products.

The work done in the SARNET FP6 and FP7 projects has shown that ASTEC models were applicable to BWR and CANDU reactors except for the core degradation phenomena, mainly due to the specific core geometry with metallic boxes around the fuel bundles, like square canisters in BWR and pressure tubes in CANDU. IRSN is currently restructuring the ICARE module to account for these new

components and for the associated multi-channels thermal-hydraulics with coolant flows inside these boxes and between them. Partners also specify new BWR models for the impact of control rod guide tubes and instrument tube structures on corium behaviour in the vessel lower head, as well as for the formation of debris due to corium ejection in a cavity filled with water. New models of CANDU pressure tube thermal creep deformation have also been implemented in the ASTEC development version.

7.2. Storage in DATANET of Experimental Data. The objective of the DATANET database [26] is to collect the available experimental data in a common format in order to ensure preservation, exchange and processing of SA experimental data, including all related documentation on an internet based protected site. The data are both previous experimental data that SARNET partners are willing to share within the network and all new data produced within SARNET. DATANET is based on the STRESA tool developed by the Joint Research Centre (JRC) in Ispra (Italy) and now managed by JRC IET (Institute for Energy) in Petten (The Netherlands). It consists of a network with several local databases where all access rights are managed in accordance with the rules adopted in the SARNET consortium. The protection of confidential data is an important feature that is taken into account as the information security of the database.

In SARNET FP7, three new STRESA nodes were opened and the results of about 270 experiments from more than 20 facilities have now been implemented. The storage by partners of new experiments will continue. JRC IET will also create new local STRESA nodes for partners with a small volume of experimental data and support the users through training sessions when necessary.

8. Spreading of Excellence

The existing public website (http://www.sar-net.eu) is being continuously improved to make it more attractive and to provide more information on the SA research field to the general public. For communication between all network members, the e-collaborative Internet Advanced Communication Tool (ACT) is used like in SARNET FP6 project but with substantially improved features.

About 320 papers related to SARNET work in the last 5 years have been presented in conferences or published in scientific journals. Efforts will continue in that direction. The dissemination of information is also done through periodic newsletters or participation to public events.

Three conferences ERMSAR (European Review Meetings on Severe Accident Research) have been organized during the last 5 years successively in France, Germany and Bulgaria as a forum for the SA community. They are becoming one of the major yearly events in the world on this topic. The 4th one was hosted by ENEA (Italy) on May 11-12, 2010 in Bologna (Italy). The next one will be hosted by GRS in Cologne (Germany) on 21–23 March 2012.

The Education and Training programme is focusing on raising the competence level of the university students (Master and PhD) and researchers engaged in SA research. Towards this purpose, in the wake of SARNET FP6 project, education courses are being developed on the SA phenomenology. The teaching will not be a survey but an in-depth treatment so that the students and researchers will be able to understand the methodology in the topics further and use analysis computer codes, mainly ASTEC, more effectively for any type of European NPP. The best-estimate analysis will be supplemented with an uncertainty analysis. Links with the European ENEN association (European Nuclear Education Network) will be maintained and strengthened. Besides, training courses will be proposed for plant operators and for researchers who are interested in the severe accident management procedures. Here, the emphasis should be in identifying what these procedures are based on and why they are effective. Three one-week educational courses were organised during the last 5 years, gathering from 40 to 100 persons. A 4th course was organised by University of Pisa and CEA in Pisa in January 2011. The next one, organized by KIT and AREVA GmbH, will take place in Karlsruhe (Germany) mid-2012 for staff in regulatory authorities, utilities or NPPs.

The textbook on SA phenomenology was drafted during the SARNET FP6 project. It covers historical aspects of water-cooled reactors safety principles and phenomena concerning in-vessel accident progression, early and late containment failure, fission product release and transport. It contains also a description of analysis tools or codes, of management and termination of SA, as well as environmental management. It gives elements on Generation III reactors. After the final review done in 2011, the publication is planned in early 2012.

A programme enables university students and researchers to go into different laboratories for education and training in the SA area. Some stages for master thesis may be organised in the ENEN framework to obtain the 20 credits (ECTS) necessary for the achievement of the European EMSNE (European Master of Science in Nuclear Engineering) certification. The staff deputation programme is continuing: a researcher from one laboratory can spend several months in another European Laboratory where he/she would participate in an area of the SA research ongoing there.

9. Conclusion

After a first phase of four and a half years, the SARNET network of excellence is continuing from April 2009 for four years more. A significant progress is foreseen in the last 18 months of the project towards solving the pending issues for current NPP SA through new experiments and modelling, in particular in the ASTEC integral code used as European reference code. An important task in 2012 will be the update of the SA R&D priorities, notably using the results of all international programmes (OECD/NEA, ISTP, ISTC. . .etc) and accounting for the impact of the Fukushima-Daiichi accidents. Efforts will continue on the transfer of knowledge to younger generations through the ERMSAR periodic international conferences, educational courses and delegations in laboratories.

A first step towards a sustainable integration of the European SA research capacities has been reached. A strong link must be kept with the "PSA2 community," in continuation of the ASAMPSA2 EC FP7 project on PSA2 best-practice guidelines [27].

The European SNETP (Sustainable Nuclear Energy Technology Platform), that gathers all nuclear fission actors and aims at providing the stakeholders and the public with a 2020–2050 vision on R&D, has delegated to SARNET the R&D SA coordination for Gen.II-III NPPs. The challenge is to prepare the network self-sustainability after the end of EC funding after 2013: such a living and unique pool of experts should assess the remaining issues on SA and propose relevant R&D programmes to address them.

Acknowledgment

The authors thank the European Commission for funding the SARNET network in FP7 (project SARNET2 N°231747 in the area "Nuclear Fission and Radiation Protection").

References

[1] J. P. Van Dorsselaere, A. Auvinen, D. Beraha et al., "Status of the SARNET network on severe accidents," in *Proceedings of the International Congress on Advances in Nuclear Power Plants (ICAPP '10)*, pp. 1029–1043, June 2010.

[2] B. Schwinges, C. Journeau, T. Haste, L. Meyer, W. Tromm, and K. Trambauer, "Ranking of severe accident research priorities," *Progress in Nuclear Energy*, vol. 52, no. 1, pp. 11–18, 2010.

[3] J. P. Van Dorsselaere, C. Seropian, P. Chatelard et al., "The ASTEC integral code for severe accident simulation," *Nuclear Technology*, vol. 165, no. 3, pp. 293–307, 2009.

[4] L. Li, S. Thakre, and W. Ma, "An experimental study on two-phase flow and coolability of particulate beds packed with multi-size particles," in *Proceedings of the 14th International Topical Meeting on Nuclear Reactor Thermal Hydraulics (NURETH '11)*, Toronto, Ontario, Canada, 2011.

[5] M. Rashid, S. Rahman, R. Kulenovic, M. Bürger, and E. Laurien, "Quenching experiments: coolability of debris bed," in *Proceedings of the 14th International Topical Meeting on Nuclear Reactor Thermal Hydraulics (NURETH '11)*, Toronto, Ontario, Canada, 2011.

[6] N. Stenne, F. Fichot, and J. P. van Dorsselaere, "R&D on reflooding of degraded cores in SARNET—focus on PEARL new IRSN facility," in *Proceedings of the EUROSAFE Forum*, Brussels, Belgium, 2009.

[7] G. Repetto, T. Garcin, S. Eymery, P. March, and F. Fichot, "Experimental program on debris reflooding (PEARL) results on PRELUDE facility," in *Proceedings of the 14th International Topical Meeting on Nuclear Reactor Thermal Hydraulics (NURETH '11)*, Toronto, Ontario, Canada, 2011.

[8] F. Fichot et al., "Understanding the effects of reflooding in a reactor core beyond LOCA conditions," in *Proceedings of the 4th ERMSAR Conference*, Bologna, Italy, 2010.

[9] M. T. Farmer, R. W. Aeschlimann, D. J. Kilsdonk, and S. Lompersky, "A summary of findings from the 2D Core-Concrete Interaction (CCI) test series," in *Proceedings of the OECD MCCI-2 Project Seminar*, Cadarache, France, 2010.

[10] C. Journeau, P. Piluso, J. F. Haquet et al., "Two-dimensional interaction of oxidic corium with concretes: the VULCANO VB test series," *Annals of Nuclear Energy*, vol. 36, no. 10, pp. 1597–1613, 2009.

[11] C. Journeau et al., "Two EU-funded tests in VULCANO to assess the effects of concrete nature on its ablation by molten corium," in *Proceedings of the 4th ERMSAR Conference*, Bologna, Italy, 2010.

[12] S. A. Bogatov et al., "Database on the location and status of nuclear fuel at Unit4 of Chernobyl NPP before and after the accident," Preprint, *RRC Kurchatov Institute*.

[13] S. Bakardjieva, M. Barrachin, S. Bechta et al., "Improvement of the European thermodynamic database NUCLEA," *Progress in Nuclear Energy*, vol. 52, no. 1, pp. 84–96, 2010.

[14] C. Journeau, P. Piluso, J. F. Haquet et al., "Oxide-metal corium concrete interaction tests in the VULCANO facility," in *Proceedings of the OECD MCCI-2 Project Seminar*, Cadarache, France, 2010.

[15] G. Langrock and S. Hellmann, "An overview of AREVA's MCCI laboratory-scale tests with prototypic corium (1D/2D, including mixed metallic/oxidic melts)," in *Proceedings of the OECD MCCI-2 Project Seminar*, Cadarache, France, 2010.

[16] B. Michel, F. Duval, C. Lapuerta, M. Quintard, and M. Cranga, "Oxide/metal convective heat transfer during MCCI: state of the art and multi-scale modelling using detailed simulation," in *Proceedings of the OECD MCCI-2 Project Seminar*, Cadarache, France, 2010.

[17] M. T. Farmer, R. W. Aeschlimann, D. J. Kilsdonk, and S. Lompersky, "The CCI-6 large scale core-concrete interaction experiment examining debris coolability under early cavity flooding conditions," in *Proceedings of the OECD MCCI-2 Project Seminar*, Cadarache, France, 2010.

[18] J. J. Foit, M. Bürger, C. Journeau, H. Alsmeyer, and W. Tromm, "Quenching of melt layers by bottom injection of water in the COMET core-catcher concept," in *Proceedings of the 3rd ERMSAR Conference*, Nesseber, Bulgaria, 2010.

[19] J. Malet, T. Gelain, S. Mimouni et al., "Single droplet heat and mass transfer modelling for nuclear containment spray applications—SARNET2 benchmark," in *Proceedings of the 5th ERMSAR Conference*, Cologne, Germany, 2012.

[20] J. Colombani, S. Fillet, C. Pascal, L. Martinet, C. Gomez, and L. Bosland, "Experimental study of organic iodide formation in the containment during a severe accident," in *Proceedings of the ICAPP*, Nice, France, 2011.

[21] W. Ambrosini, M. Bucci, N. Forgione, F. Oriolo, and S. Paci, "Quick look report on SARNET2 condensation benchmark-2 results," Report DIMNP RL 1252, University of Pisa, 2010.

[22] S. Kelm, P. Broxtermann, S. Krajewski, and H.-J. Allelein, "Report on the generic containment code-to-code comparison—run0," Forschungszentrum Jülich, 2010.

[23] T. Kärkelä, J. Holm, A. Auvinen et al., "Gas phase reactions of organic iodine in containment conditions," in *Proceedings of the International Congress on Advances in Nuclear Power Plants (ICAPP '10)*, pp. 1084–1091, June 2010.

[24] G. Daehlie and A. Kjekshus, "Iodine oxides, I. I2O3.SO3, I2O3.4SO3.H2O, I2O3.SeO3, and I2O4," *Acta Chemica Scandinavica*, vol. 18, no. 1, pp. 144–156, 1964.

[25] M. W. Chase, "NIST-JANAF thermochemical tables for the iodine oxides," *Journal of Physical and Chemical Reference Data*, vol. 25, no. 5, pp. 1229–1339, 1996.

[26] R. Zeyen, "European approach for a perennial storage of severe accident research experimental data, as resulting from EU projects like SARNET, Phébus FP and ISTP," in *Proceedings of the ANS Winter Meeting*, Washington, DC, USA, 2009.

[27] FP7 project ASAMPSA2, "Advanced safety Assessment Methodologies: level 2 Probabilistic Safety Assessment," 2007, http://www.asampsa2.eu/.